UNIVERSITY OF CALIFORNIA
RIVERSIDE

Electrochemical Synthesis of Tellurium & Lead Telluride from Alkaline Baths and Their Thermoelectric Properties

A Dissertation submitted in partial satisfaction
of the requirements for the degree of

Doctor of Philosophy

in

Chemical and Environmental Engineering

by

Tingjun Wu

June 2016

Dissertation Committee:

Dr. Nosang V. Myung, Chairperson
Dr. Juchen Guo
Dr. David Jassby

The Dissertation of Tingjun Wu is approved:

Committee Chairperson

University of California, Riverside

Acknowledgements

In this long journey, there are a number of people whom I would like to acknowledge. Foremost, I would like to thank my advisor, Professor Nosang V. Myung, for his support, help, and the lessons he gave me both on my personal life and research. His enthusiasm and curiosity about science have always motivated me to move my project forward and I learned how to logically think under his valuable guidance.

I would like to express my gratitude to my committee, Professor Juchen Guo and Professor David Jassby, for the review of my dissertation as well as their insightful comments. I would like to acknowledge my previous and current group members: Miluo Zhang, Wayne Bosze, Hengchia Su, Jiwon Kim, Michael Nalbandian, Nicha Chartuprayoon, Hyunsung Jung, Saba Seyedmahmoudbaraghani, Navaneet Ramabadran and Sooyoun Yu; and those who gave me the possibility to complete this dissertation.

Finally, I would like to thank my family for their love, encouragement, and endless support during this journey.

ABSTRACT OF THE DISSERTATION

Electrochemical Synthesis of Tellurium & Lead Telluride from Alkaline Baths and Their Thermoelectric Properties

by

Tingjun Wu

Doctor of Philosophy, Graduate Program in Chemical and Environmental Engineering
University of California, Riverside, June 2016
Dr. Nosang V. Myung, Chairperson

Heat is the natural by-product of energy conversion processes. Of the 4.25×10^{20} J of energy the United States consumes every year, more than 60% is wasted in the form of heat. Therefore, waste heat recovery is a crucial step to improve the energy generation and utilization efficiency. Thermoelectric (TE) materials, which can directly convert rejected or waste heat into usable electric power, has been extensively developed for this issue. Thick-film-based devices have advantages over conventional TE module because of its compact size. By shrinking the size of thermoelectric devices, it not only allows the device to operate under smaller temperature gradients, but by so doing it expands its capability to handle a wider range of thermal and power management microelectronic systems. The combination of electrochemical deposition of compound semiconductors (metal tellurides) with standard integrated circuit technique makes fabrication of thermoelectric microdevices possible.

The overall objective of this work is to develop new baths to achieve high-rate electrodeposition of Te and PbTe thick films. The electrodeposition mechanisms of Te and PbTe were examined by electrochemical analysis method. Furthermore, the thermoelectric property of thick PbTe films were optimized by introducing energy barriers from crystal grain boundary and tellurium nanoinclusion, which was achieved by tailoring composition and crystal structures of the thick PbTe films. Additionally, control over the composition and crystal structures was realized by tuning the electrodeposition conditions, as well as post-annealing process.

TABLE OF CONTENTS

FIGURE LIST

1 Introduction: Electrochemical Synthesis Methods and Thermoelectrics

1.1 World Energy Challenges

The world energy consumption rate in 2012 is 17.7 TW, and it will keep increasing because of population and economic growth. In 2050, the world energy consumption rate is projected to be 40.8 TW.[1] More than 80 percent of this energy will be obtained from fossil fuels, including natural gas, oil and coal.[2] Consumption of fossil fuels, which produce large amount of CO_2, at such a high rate will produce a potentially significant global climate issue. A few scientific research studies, which are used to estimate the extent of global warming, indicate that a temperature rise of 0.6 ^oC has already occurred in the past century. Furthermore, the estimated temperature increase in the 21th century is 1.8 – 4.0 ^oC, which is likely to result in irreversible climate damage to Earth. [2]

To prevent or slow down the climate damage caused by CO_2 and CH_4 in the atmosphere, clean and renewable energy, such as solar energy, biomass, hydroelectric energy and so on, was developed. However, because of technological problems, the expenses of renewable energy are still higher than fossil fuels. This leads to the conclusion that renewable energy cannot become the primary energy source in the near future.

Heat is the natural by-product of energy conversion processes. According to Carnot's theorem, more than 60 percent of energy is wasted in the form of heat.[2] Therefore, waste heat recovery is a crucial step to improve the energy generation and

utilization efficiency. Thermoelectric (TE) materials, which can directly convert rejected or waste heat into usable electric power, has been extensively developed for this issue.

1.2 Thermoelectrics

1.2.1 An Overview of Thermoelectrics

The potential applications of thermoelectric generators, from niche devices to large scale waste heat recovery systems (e.g., human body heat, vehicle waste heat, industry waste heat, etc.), are illustrated in figure 1.1. The first real world application of thermoelectric device was to power spacecraft. NASA used the radioisotope thermoelectric generator (RTG), which was also named as atomic battery, in the Apollo missions, the Viking 2 mission to Mars, and Voyager missions. [3] Additionally, thermoelectric generators have been successfully utilized to power miniaturized autarkic sensor systems, wrist watches, and diagnostic medical equipment.[4] Furthermore, by integrating a thermoelectric generator onto exhaust pipes, it may be possible to convert up to one-fifth of the waste heat into electricity to power the car's air conditioner and other electrical accessories. This would improve the cars' fuel economy by approx. 7 miles per gallon. Scaling such a method nationwide could save 2.5 million barrels of oil per day. This application of automotive waste heat recovery is being investigated by research institutions such as the national renewable energy lab and corporations such as General Motors.[5]

The thermoelectric phenomena include Seebeck effect and the Peltier effect. (1) The Seebeck effect is the conversion of temperature differences directly into electricity. When a temperature gradient is established at the two ends of the material, charger carriers

(electrons in n-type conductor and holes in p-type conductor) would diffuse from hot side to cold side, creating a potential difference (Figure 1.2). The generated voltage, ΔV, is given by $\Delta V = S\,\Delta T$, where S is the Seebeck coefficient and ΔT is the temperature difference. [2] On the other hand, the Peltier effect is the generation of temperature gradient directly by electric energy. When the material is supported by an external electric power supply, charge carriers will flow to one end of the thermoelectric couple. The charge carriers also carry energy, resulting in a temperature difference between the two ends.

1.2.2 Thermoelectric figure of merit and efficiency

In thermoelectric devices, the dimensionless thermoelectric figure of merit (ZT) is defined by

$$ZT = \frac{S^2\sigma}{\kappa}T \qquad (1.1)$$

where S (V/K) is Seebeck coefficient, σ (S/m) is electrical conductivity, κ (W/mK) is thermal conductivity and T (K) is absolute temperature.[6] $S^2\sigma$ is referred to as the thermoelectric power factor. The thermoelectric energy conversion efficiency and the maximum cooling temperature for Peltier devices are dependent on ZT.

The maximum efficiency (η) of a thermoelectric device is defined as the energy provided to the load (W) divided by the heat energy consumed at the hot junction (Q). It is a function of ZT as well as the temperature of the hot and cold side (T_H, T_C).[6-9]

$$\eta = \frac{W}{Q} = \frac{T_H - T_C}{T_H}\frac{\sqrt{1+ZT}-1}{\sqrt{1+ZT}+\frac{T_H}{T_C}} \qquad (1.2)$$

Thus, η is proportional to the Carnot efficiency (η_c), which is defined as

$$\eta_c = \frac{T_H - T_C}{T_H} \qquad (1.3)$$

Figure 1.3 [10] [11] shows that various commercially available power generating technology, including existing practical mechanical systems, display an average ZT>4 over the entire temperature range shown. Compared to these mechanical systems, even the best reported thermoelectrics (ZT = 3.5, for n-type only) achieved so far show less efficiency.[11] Consequently, despite the advantages and various applications of thermoelectric devices, overcoming their low efficiency (ZT ~ 1) is the single greatest obstacle preventing thermoelectrics from being widely deployed.

1.2.2.1 Interdependence of Thermoelectric Parameters

Seebeck coefficient S, electrical conductivity σ, and thermal conductivity κ are key thermoelectric parameters. According to the definition of ZT, it requires a high Seebeck coefficient, high electrical conductivity, and a low thermal conductivity to maximize ZT. However, the interdependence of these material properties pose a stumbling block (Figure 1.4).[12]

1.2.2.1.1 S and σ

Typically, for metals and highly degenerated semiconductors, the Seebeck coefficient, S, can be illustrated as:

$$S = \frac{8\pi^2 k_B^2}{3eh^2} m^* T \left(\frac{\pi}{3n}\right)^{\frac{2}{3}} \qquad (1.4)$$

Where k_B is Boltzmann constant, e is the carrier charge, h is Planck's constant, m* is the effective mass of the charge carrier, and n is the carrier concentration.

Electrical conductivity is proportional to the product of how many (n) and how fast charge carriers can drift through the lattice. Additionally, semiconductors have both electron (n_e) and hole (n_h) charge carriers, so the electrical conductivity is expressed as:

$$\sigma = e(n_e\mu_e + n_h\mu_h) \qquad (1.5)$$

where e is the elementary charge; n_e and n_h are the carrier concentrations of electrons and holes, respectively; μ_e and μ_h are the carrier mobility of electrons and holes, respectively.

According to equations 1.4 and 1.5, increasing the carrier concentration increase the electrical conductivity, but decreases the Seebeck coefficient leading to the improvement in the power factor ($S^2\sigma$) difficult.

1.2.2.1.2 σ and κ

Electrical conductivity and thermal conductivity and also have an interdependent relationship. The thermal conductivity κ is composed of both electron and phonon transport:

$$\kappa = \kappa_e + \kappa_l \qquad (1.6)$$

where κ_e is the electrical thermal conductivity and κ_l is the lattice thermal conductivity. Based on Wiedemann-Franz law,[12] the electrical thermal conductivity can be expressed by the following equation:

$$\kappa_e = \sigma LT \qquad (1.7)$$

where L is the Lorentz number, taken as 2.4×10^{-8} J^2/k^2C^2 for a highly degenerated semiconductor. The equation shows that the thermal conductivity is coupled with the electrical conductivity. [12]

The lattice thermal conductivity describes the ability of phonons to transport thermal energy from a hot side to a cold side and can be approximated by

$$\kappa_L = C_L \nu l \qquad (1.8)$$

where C_L is the heat capacity, ν is the phonon velocity and l is the phonon mean free path. Semiconductors that have low sound velocity and a short phonon mean free path are expected to have a low thermal conductivity, therefore a greater ZT. The interdependency of the Seebeck coefficient, the electrical conductivity and the thermal conductivity is depicted in Figure 1.4.[12, 13]

1.2.3 Thermoelectric materials

Figure 1.5 shows the ZT of the state-of-art commercial thermoelectric materials as a function of temperature.[13] The maximum ZT's were achieved at different temperatures for different materials. Bi_2Te_3 and Sb_2Te_3 have been proven to be the most promising thermoelectric materials for near-room-temperature applications, with a ZT value close to one. For middle-high temperature range of 400 ^oC to 600 ^oC, PbTe based materials and other alloys (e.g., AgGeSbTe or TAGS) show a great potential with the ZT of 0.8 ~ 1.2. The skutterudites and clathrates also (e.g., $CoSb_3$) have a high ZT value around one in the similar temperature range. SiGe based materials were usually utilized in a high temperature range (i.e., over 900 ^oC), with remarkable reliability and stability.

1.2.4 Micro-thermoelectric (μTEG) device based on thick films and 3D-printing

The TE module is shown in figure 1.6. The performance of thermoelectric devices are maximized by connecting the thermoelectric legs electrically in series and thermally in

parallel.[3, 13] Although efficiency of thermoelectrics is relatively low compared to other power generation technologies, the thermoelectric devices have unique advantages. Thermoelectric devices are solid-state devices with no moving parts. They can be operated with no noise or vibration while maintaining high reliability.

μTEG devices have advantages over conventional macro TE module because of its compact size. By shrinking the size of thermoelectric devices, it not only allows the device to operate under smaller temperature gradients, but by so doing it expands its capability to handle a wider range of thermal and power management. The combination of electrochemical deposition of compound semiconductors (metal tellurides) with standard integrated circuit technique makes the fabrication of thermoelectric microdevices possible.

The common way to fabricate μTEG is by using photolithography. However, it has relatively high capital cost. Additionally, the maximum thickness of photoresist that can be achieved is about a few ten's micron. Herein, 3D-printing technology is used to fabricate thermoelectric devices combined with electrodeposition. The definition of 3D printing is conceptually straightforward: an object is created by starting with nothing and adding material a layer at a time until finished. [14] Because of this characteristic, 3D-printing will produce less waste. 3D printing is particularly useful for creating complex objects, making unique or custom items, or generating prototypes during the design phase of a project. [15] Additionally, 3D-printing has several other advantages, including cheap manufacturing and quick production.

In this research, 3D-printing technology was utilized to print a pattern, which was used as a template to electrodeposit a thermoelectric leg. This fabrication procedure is showed in figure 1.7. Figure 1.7A shows two prefabricated electrodes. Then, a template was produced by 3D printing and attached to the electrode (figure 1.7B). The first set of n-type (or p-type) thermoelectric legs were electrodeposited into the template using one of the electrodes (figure 1.7C). Then, the second set of p-type (or n-type) thermoelectric legs were electrodeposited into the template using the other electrode (figure 1.7D). Finally, the 3D printed template was removed and a top connection was made between the thermoelectric legs (figure 1.7E).

1.3 Electrochemical synthesis

Electrochemical synthesis methods, which includes electrodeposition and electroless deposition, are one of the most cost-effective techniques for synthesis of materials with different dimensions. There are various advantages of electrodeposition, including (1) it's a room temperature operation-yielding low thermal stress under low energy consumption, (2) low capital equipment cost by eliminating vacuum requirements, (3) high deposition rates, (4) good scalability, (5) and efficient material utilization because of spatial selectivity. Additionally, the combination of electrochemical deposition of semiconductors (tellurium and metal tellurides) with standard integrated circuit technique makes the fabrication of microdevices possible, which have advantages over conventional TE module because of its compact size.

1.3.1 Electrochemistry of Te

To synthesis tellurium and metal tellurides with different dimensions (1D, 2D and 3D) and morphology, it is essential to understand the electrochemistry of Te. In acidic solution Te(IV) is presented as $HTeO_2^+$ ions and can be reduced to Te(0) (reaction 1.1), then further reduced to H_2Te (reaction 1.2) (or HTe^- depend on different pH) (Figure 1.8). [16] The disadvantage of acidic solution is low solubility of Te(IV). The solubility of TeO_3^{2-} in acidic solution is low (e.g., 1.6 g/L or 10 mM at pH of zero)[16]. In alkaline solution, Te(IV) is presented as TeO_3^{2-} ions and their solubility is significantly higher (e.g., 87.8 g/L or 550 mM at pH of 10.5).[16] The higher solubility of TeO_3^{2-} in alkaline solution may allow to achieve high electrodeposition rates and provide a wider window to synthesize Te with different dimensions and morphology.

$HTeO_2^+(aq) + 3H^+(aq) + 4e^- \rightarrow Te(s) + 2H_2O(l)$ (E0 = 0.41 V vs. Ag/AgCl)

Reaction 1.1

$2Te(s) + 2H^+ + 2e^- \rightarrow H_2Te(aq)$ (E_0 = -0.91 V vs. Ag/AgCl)

Reaction 1.2

In acidic and neutral solution, Te (0) is directly reduced to Te^{2-} (-II) in one step (reaction 1.7). [17, 18] However, in alkaline solution an intermediate species such as Te_2^{2-} (-I) is formed prior to further reduction to Te^{2-} (-II). According to the Pourbaix diagram of Te, in alkaline solution TeO_3^{2-} (+IV) is reduced to Te(0) (reaction 1.3), then to Te_2^{2-} (-I) (reaction 1.5) confirmed by the observation of purple color.[19, 20] Furthermore, the Te_2^{2-} (-I) is reduced to Te^{2-} (-II) (reaction 1.8),[16, 21] confirmed by the observation that the purple solution became colorless. [19, 22] The electrochemical reactions of Te in alkaline

solution were reported by several groups. For example, Lingane *et al.* reported that two cathodic waves at mild alkaline solutions (i.e., pH of 9.4) where the first wave represented the reduction of TeO_3^{2-} (+IV) to Te (0), which was confirmed by coulometer reading that 3.95 - 4.07 electrons per TeO_3^{2-} (+IV) reduced. The meaning of the second cathodic wave was explained by further reduction of Te (0) to Te_2^{2-}. At strong alkaline solution (i.e., 1M NaOH (pH of 14)), only one cathodic wave was observed. Lingane reported that the overall reaction was written as reaction 1.6, but the reactions took place in three steps. The TeO_3^{2-} (+IV) was reduced to Te (0) confirmed by the phenomenon that black deposit was observed on the dropping mercury electrode, then Te (0) was further reduced Te_2^{2-} (-I) confirmed by the phenomenon that deep violet solution was formed. Finally the deep violet solution became colorless which meant that Te_2^{2-} (-I) was reduced to Te^{2-} (-II).[19] Schmidt *et al.* cited the Te reaction mechanism from Lingane's publication, however Schmidt did not reported the formation of Te_2^{2-}(-I). [23] Shinagawa *et al.* reported that TeO_3^{2-}(+IV) was reduced to Te (0), then further reduced to Te_2^{2-}(-I), finally Te_2^{2-}(-I) was reduced to Te^{2-} (-II) based on the observation that the deep violet solution became colorless. [24] Mishra *et al.* detected the presence of intermediate species Te_2^{2-} (-I) by rotating ring-disk electrode as Te^{2-} (-II) was oxidized to Te (0). [25] Pourbaix claimed that the direct transition from TeO_3^{2-} (+IV) to Te_2^{2-} (-I) (reaction 1.4) is possible, however, there is no evidence reported to prove this five-electron transition. [16] According to the Pourbaix diagram, the redox potential for Te_2^{2-}/Te^{2-} (reaction 1.8) is -1.47V vs. Ag/AgCl. [16] However, Panson *et al.* experimentally proved that Te_2^{2-} (-I) was reduced Te^{2-} (-II) at potential of -1.16V vs. sat. Ag/AgCl. [21] As a consequence, in alkaline solution TeO_3^{2-} (+IV) is reduced to Te (0)

(reaction 1.3), then Te (0) is reduced to Te_2^{2-} (-I) (reaction 1.5), finally further reduced to Te^{2-} (-II) (reaction 1.8).

Simultaneously with electrochemical reaction, the chemical reactions (reaction 1.9 – 1.11) may occur in the solution. Blanc *et al.* proposed the decomposition of Te_2^{2-} (-I) (reverse reaction of reaction 1.9) based on the observation that the electrolytic reduction of Te produced a deep violet solution of Te_2^{2-} (-I) and elementary Te (0) in the form of grey dust. [26] However, no further evidence was reported to support reaction 1.9 and the calculated Gibbs free energy of reverse reaction is G^O of -58.6 kJ/mol. The formed Te_2^{2-} (-I) and Te^{2-} (-II) interacts with TeO_3^{2-} (+IV) to chemically deposit solid Te in the solution as shown in reactions 1.10 and 1.11, respectively.

$TeO_3^{2-}(aq) + 3H_2O(l) + 4e^- \rightarrow Te(s) + 6OH^-(aq)$ (E_0 = - 0.45 V vs. Ag/AgCl)

(Reaction 1.3)

$2TeO_3^{2-}(aq) + 6H_2O(l) + 10e^- \rightarrow Te_2^{2-}(aq) + 12OH^-(aq)$($E_0$= -0.65 V vs.Ag/AgCl)

(Reaction 1.4)

$2Te(s) + 2e^- \rightarrow Te_2^{2-}(aq)$ (E_0 = -0.91 V vs. Ag/AgCl)

(Reaction 1.5)

$TeO_3^{2-}(aq) + 3H_2O(l) + 6e^- \rightarrow Te^{2-}(aq) + 6OH^-(aq)$($E_0$ = - 1.00 V vs. Ag/AgCl)

(Reaction 1.6)

$Te(s) + 2e^- \rightarrow Te^{2-}(aq)$ (E_0 = -1.34 V vs. Ag/AgCl)

(Reaction 1.7)

$Te_2^{2-}(aq) + 2e^- \rightarrow 2Te^{2-}(aq)$ (E_0 = -1.47 V vs. Ag/AgCl)

(Reaction 1.8)

$Te(s) + Te^{2-}(aq) \rightarrow Te_2^{2-}(aq)$ (ΔG^O = - 58.6 kJ/mol)

(Reaction 1.9)

$TeO_3^{2-}(aq) + 2Te_2^{2-}(aq) + 3H_2O(l) \rightarrow 5Te(s) + 6OH^-(aq)$($\Delta G^O$ = -164.1 kJ/mol)

(Reaction 1.10)

$TeO_3^{2-}(aq) + 2Te^{2-}(aq) + 3H_2O(l) \rightarrow 3Te(s) + 6OH^-(aq)$ (ΔG^O = -279.3 kJ/mol)

(Reaction 1.11)

The reaction kinetics of Te reduction reaction (*i.e.,* Te(IV) to Te(0) and Te(0) to Te (-I)) was investigated by several groups. A possible reaction mechanism was proposed and rate limiting steps were discuss at different conditions.

In alkaline solution, Te(+IV) exists in the form of anions (*e.g.*, TeO_3^{2-} [27] or $Te(OH)_6^{2-}$[28]). The direct reduction of Te(+IV) to Te(0) is highly unlikely on a negatively charged cathodic electrode surface. Instead, a 4 elemental reactions are proposed (Reaction 1.13 – 1.15) [27-29]

$Te(OH)_6^{2-}(aq) \leftrightarrow Te(OH)_3^+(aq) + 3OH^-(aq)$ (Reaction 1.12)

$Te(OH)_3^+(aq) + e^- \rightarrow Te(OH)_3(ads)$ (Reaction 1.13)

$Te(OH)_3(ads) + e^- \rightarrow Te(OH)_3^-(ads)$ (Reaction 1.14)

$Te(OH)_3^-(ads) + e^- \rightarrow Te(OH)_3^{2-}(ads)$ (Reaction 1.15)

$Te(OH)_3^{2-}(ads) + e^- \rightarrow Te(s) + 3OH^-(aq)$ (Reaction 1.16)

Reaction 1.12 shows that the anions $Te(OH)_6^{2-}$ are in equilibrium with cations $Te(OH)_3^+$. But once $Te(OH)_3^+$ is absorbed on the cathodic electrode surface, it obtains an electron from the electrode and is then discharged as $Te(OH)_3$. This cyclic mechanism of picking up an electron from the electrode is repeated in reactions 1.14 and 1.15 yielding

$Te(OH)_3^{2-}$. $Te(OH)_3^{2-}$ obtains a fourth and last electron in reaction 1.16 and in turn releases all three hydroxide ions to form Te element. According to the Tafel equation, by assuming a charge transfer coefficient of 0.5, the Tafel slopes are 118, 59, 39 and 30 mV/decade.A, when reactions 1.13, 1.14, 1.15 and 1.16 are the rate limiting steps, respectively.[30]

Komandenko *et al.* reproduced the Awad's results [30] and claimed that reaction 1.15 was the rate limiting step. The Tafel slopes ranged from 40 to 45 mV/decade.A.[29] Furthermore, Komandenko *et al*. also claimed that at low alkali concentration $Te(OH)_3^+$ would directly obtain two electrons and become $Te(OH)_3^-$. Thus, they replace reactions 1.13 and 1.14 with one reaction.[28].

The reaction mechanism of Te(0) to Te_2^{2-} was first reported by Awad *et al*. [31] Their results showed that at low NaOH concentrations, only one linear region was shown in the Tafel plot with a slope about 100 mV/decade.A. However at high NaOH concentrations, two linear regions were observed with Tafel slopes about 40 and 100 mV/decade.A. He proposed the two step reaction mechanism which involved Na^+ ions (reaction 1.17, 1.18). However, the calculated number of electrons transferred for each elementary reaction was surprising. At the first step (Reaction 1.17), two electrons were transferred; at the second step (Reaction 1.18) 4 electrons were transferred. The number of electrons could not be explained by this two-step reaction mechanism.

$$Te(s) + Na^+(aq) + e^- \rightarrow NaTe(ads) \qquad \text{(Reaction 1.17)}$$

$$NaTe(ads) + Te(s) + e^- \rightarrow Te_2^{2-}(aq) + Na^+ \qquad \text{(Reaction 1.18)}$$

Therefore, Awad *et al*. proposed a four-step reaction mechanism (reaction 1.19 – 1.22) and introduced the diatomic tellurium.

$$Te_2(s) + M^+(aq) + e^- \rightarrow MTe_2(ads) \qquad \text{(Reaction 1.19)}$$

$$MTe_2(ads) + M^+(aq) + e^- \rightarrow M_2Te_2(ads) \qquad \text{(Reaction 1.20)}$$

$$Te_2(s) + M_2Te_2(ads) + e^- \rightarrow M_2Te_4^-(aq) \qquad \text{(Reaction 1.21)}$$

$$M_2Te_4^-(aq) + e^- \rightarrow 2Te_2^{2-}(aq) + 2M^+(aq) \qquad \text{(Reaction 1.22)}$$

In the reactions, M^+ represented the monovalent cations (*e.g.*, Na^+ or Ba^{2+}) in the alkaline solution. Reaction 1.19 and 1.20 are discharge reactions, reactions 1.21 and 1.22 are electrochemical reactions. In the two discharge reactions, the reaction rate of the second step reaction (reaction 1.18) is relatively slower than the first step, which can be the rate limiting step. On the other hand, in the two electrochemical reactions, the reaction rate of the second step reaction was relatively slower than the first step, which can be the rate limiting step. Awad *et al.* used the energy barrier diagram of these four reactions to prove their assumptions. According to the energy barrier diagram, the first discharge (reaction 1.19) and electrochemical (reaction 1.21) steps have very low energy barriers compared to the second discharge (reaction 1.20) and electrochemical (reaction 1.22) steps. When reaction 1.20 was the rate limiting step, the Tafel slope was about 100 mV/decade.A, which is consistent with the theoretically calculated value 120 mV/decade.A taking into account the mechanism and the differences due to small changes in the charge transfer coefficient. When reaction 1.22 was the rate limiting step, the Tafel slope was about 40 mV/decade.A at low current density and 100 mV/decade.A at high current density. As a consequence, in mild alkaline solutions, the second discharge reaction (reaction 1.20) was the rate limiting

step throughout the whole current density range with a Tafel slope of 100 mV/decade.A. However in strong alkaline solutions, the second electrochemical reaction (reaction 1.22) was the rate limiting step with a Tafel slope of 40 mV/decade.A at low current density and a Tafel slope of 100 mV/decade.A at high current density. [32]

Another mechanism was suggested by Komandenko *et al*. together with Tafel slopes for reduction of Te(0) to Te_2^{2-} at mild alkaline solutions. Their data showed that the Tafel slope was about 40 mV/decade.A. Additionally, they proposed a different mechanism which involved OH^- ions shown in reaction 1.23 – 1.26 where reaction 1.24 was the rate limiting step. [33]

$$Te(s) + OH^-(aq) + e^- \rightarrow TeOH^{2-}(ads) \quad \text{(Reaction 1.23)}$$

$$TeOH^{2-}(ads) + Te(s) + e^- \rightarrow Te_2OH^{3-}(ads) \quad \text{(Reaction 1.24)}$$

$$Te_2OH^{3-}(ads) + Te(s) + e^- \rightarrow Te_3OH^{4-}(ads) \quad \text{(Reaction 1.25)}$$

$$Te_3OH^{4-}(ads) + Te(s) + e^- \rightarrow 2Te_2^{2-}(aq) + OH^-(aq) \quad \text{(Reaction 1.26)}$$

1.3.2 Electrochemical synthesis of tellurium

Significant efforts have been recently devoted to synthesize materials with different dimensions (1D, 2D and 3D) with controlled morphology to tune their unique size and shape-dependent properties.[34] The ability to adjust the morphology, dimension and crystal structure of these nanomaterials is essential to optimize their electrical, thermal, and mechanical behavior and thereby the overall device's performance.[35, 36] For examples, the piezoelectric effect can be enhanced by nano-engineering due to flexoelectric effect by reducing the diameter of one-dimensional (1-D) nanowires.[37-39] Additionally, a

refractive index gradient can be established by growing three-dimensional (3-D) nanostructures which significantly enhance light absorption.[40-42] Furthermore, enhanced photon-to-current conversion efficiency can also be achieved by using 3-D branched nanorod structures compared to thin film counterparts.[43] The greater sensitivity of a surface plasmon resonance nanosensor can best be achieved by "rice-like" nanostructures than by any other nanostructure. [44, 45] Specifically, its performance depends on the length and aspect ratio of the nanorice. [44, 46]

Trigonal-Tellurium (t-Te) is a p-type semiconductor with a narrow band-gap energy of 0.35 eV at room temperature. Its hexagonal crystal structure contains six spiral chains at each corner and one in the center, which are bound together via van der Waals forces[47]. Because of its anisotropic crystalline structure[47], Te has a strong tendency to grow along the c-axis to form 1-D structures without any additional physical templates or a film. Owing to its unique crystal structure, it exhibits many unique physical properties including high photoconductivity, piezoelectric effect, and catalytic activity.[18, 37, 48-50] Additionally, tellurium based alloys, such as Bi_2Te_3, PbTe, and Sb_2Te_3, have wide application in thermoelectrics[3].

1.3.2.1 Galvanic displacement reaction of Te

1-D Te nanostructures including nanowires, nanoribbons, nanobelts, and nanotubes have been synthesized by various methods including vapor deposition[51-59]; hydrothermal[60-73], solvothermal[74-77], and polyol processes[78-80]; ultrasonic[81], microwave[82], photothermal[83], surfactant[84-86] and biomolecule-assisted methods[64]; as well as amino acids[87] and gluconate[88] controlled methods. However,

several works have been reported on the synthesis of 3-D Te nanostructures including the Ostwald ripening process[76] [89], rapid crystallization[72], secondary nucleation[86], and solution-based approaches.[90] These reported methods generally require high operating temperature and pressure which limit its scalability and manufacturability.

Galvanic displacement reaction (GDR) is an electrochemical process driven by the difference in redox potentials between the solid substrate and the ions of the source materials, leading to deposition of the more noble material at the expense of the dissolution of the less noble material. Due to the ease of fabrication, GDR is an intriguing method to create various nanostructures with controllable morphology and dimensions. So far, synthesis of Te nanostructures by GDR have been reported with various nanostructures such as nanotubes[91], nanofibers[92], and nanowires.[93] Because of the low solubility of Te(IV) in a natural solution (1.6×10^{-4} g/L (0.001 mM) at pH of 7.0)[16], most syntheses were conducted in very acidic baths (pH close to zero)[18, 91-96], in which the Te(IV) is present as $HTeO_2^+$ ion where the concentration can be increased (1.6 g/L (10 mM) at pH of zero).[16] However, low solution pH may accelerate the dissolution rate of synthesized materials and promote secondary reactions (*e.g.*, hydrogen gas evolution reaction (HER)) to lower the reaction efficiency. In contrast, Te(IV) dissolves readily in an alkaline bath with a solubility of 87.8 g/L (550 mM) at pH of 10.5 which is 55 fold greater than that at pH of zero. The higher solubility of Te(IV) in alkaline baths augments the deposition range providing greater flexibility to control the deposit's morphology.

1.3.2.1.1 Galvanic displacement reaction of Te in acidic baths

Galvanic displacement reaction of Te in acidic baths was reported by the previous publications from our group.

Chang et al. reported the synthesis of Te thin films by galvanic displacement from acidic nitric baths (10 mM $HTeO_2^+$ + 1 M HNO_3) at room temperature using nickel, cobalt, and iron as sacrificial materials. The surface morphologies and crystal structure of galvanically displaced Te thin films strongly depended on the sacrificial materials and the thickness of sacrificial material films because of different chemical dissolution rates of the sacrificial films and mixed potential. Thicker sacrificial Fe films led to the formation of thicker and more compact of Te. [97]

Rheem et al. reported that tellurium nanotubes were synthesized by galvanic displacement of cobalt nanowires in acidic solution (10 mM $HTeO_2^+$ + 1 M HNO_3). The diameter and wall thickness (15 to 30 nm) of tellurium nanotubes were controlled by adjusting the diameter of cobalt nanowires, where the diameter and wall thickness of nanotube increased with increases in the diameter of cobalt nanowires. Furthermore, the length of tellurium nanotubes can be controlled by adjusting the length of sacrificial nanowire. The synthesized Te nanotubes show nanocrystalline with an average grain size below 10 nm. The mobility of Te nanotubes measured by field effect transistor was 0.01 $cm^2\ V^{-1}\ s^{-1}$. [98]

One-dimensional Te nanostructures with controlled dimensions and morphologies were synthesized by the galvanic displacement of electrodeposited nickel thin films nitric acid baths (XmM $HTeO_2^+$ + 1 M HNO_3). The preferred crystal orientation of sacrificial Ni

thin films was varied to synthesize Te nanostructures with various levels of distinctivenesss. The template-free GDR of the Ni thin film electrodeposited at 40 ºC with the current density of 150 mA cm-2 in the Watts' bath demonstrated vertically aligned hexagonal 1-D Te nanostructures with well-developed facets. The dimensions of the vertically aligned Te nanostructures were controlled by varying the concentration of $HTeO_2^+$ ions in the GDR electrolyte, when $HTeO_2^+$ concentration varied from 1 to 10 mM, the diameter and length of Te nanostructure changed from 70 to 900 nm and from 1 to 3.6 μm, respectively. [99]

Jeong et al. synthesized high-quality tetragonal tellurium (t-Te) nanowires by the galvanic displacement reaction of Si on a 4-in. Si wafer in the solution with 1 M $CdCl_2$, 1 mM $HTeO_2^+$, and 4.5 M HF. Furthermore, because seed nucleation and growth are both instantaneous, the synthesized nanowires had uniform lengths across the substrate. The average diameter and length of the nanowires were approximately 87 nm and 2.3 μm, respectively. [100]

Park et al. combined electrospinning and galvanic displacement reaction to synthesize ultra-long hollow Te nanofibers with controlled dimensions, morphology and crystallinity by simply tailoring the electrolyte concentration applied. Electrospun Ni nanofibers were used as sacrificial materials. Branched Te hollow nanofibers were synthesized from low HTeO2+ concentration baths (i.e.,0.5 and 1 mM) whereas smooth Te hollow nanofibers were synthesized from a higher $HTeO_2^+$ concentration bath (i.e., 10 mM) by galvanic displacement of smooth electrospun Ni nanofibers with an average diameter of 163 ± 11 nm.The branch diameter were also strongly influenced by solution

composition. When the $HTeO_2^+$ concentration was increased from 0.5 to 10 mM, the wall thickness of the nanofibers increased from 17 ± 5 to 27 ± 4 nm, while the average branch diameter changed from 10 ± 2 to 19 ± 3 nm. [92]

Suh, et al. reported that bamboo-like Te nanotubes were synthesized via the galvanic displacement reaction of NiFe nanowires with Ni-rich and Fe-rich segments in the solution with 10 mM $HTeO_2^+$ and 1 M HNO_3. The thick and thin components of the synthesized Te nanotubes were converted from the Ni-rich and Fe-rich segments in the NiFe nanowires respectively. The dimensions of the Te nanotubes were controlled by employing sacrificial NiFe nanowires with tailored dimensions as the template for the galvanic displacement reaction. The segment lengths of the Te nanotubes were found to be dependent on those of the sacrificial NiFe nanowires. [101]

1.3.2.1.2 Galvanic displacement reaction of Te in alkaline baths

Two sacrificial materials (i.e., zinc and aluminum) were used to synthesize Te nanostructures. Zinc was selected as a sacrificial material for three reasons, the low redox potential of the Zn/ZnO_2^{2-} , its ability to form soluble products (*i.e.*, ZnO_2^-) in alkaline baths, and low rare material cost. Tellurium (Te) nanostructures, including nanowires and branched nanorods, were synthesized by galvanic displacement reaction (GDR) of zinc foils in alkaline baths containing TeO_3^{2-} ions. The dimension, morphology, and crystal structure of the Te nanostructures were controlled by varying the electrolyte composition, pH, and the reaction temperature. For examples, single crystalline Te nanowires were synthesized at low TeO_3^{2-} concentrations (*e.g.,* 2 mM), whereas 3-D branched nanorods were obtained at higher TeO_3^{2-} concentrations (*e.g.,* >10 mM) at a fixed pH of 13.1. The

diameter of the branches was increased by increasing TeO_3^{2-} concentration. Solution pH also effected the morphology of Te heterostructures where the pH range from 12.8 to 13.1 yielded branched nanorods whereas higher pH (*i.e.,* 14.7) yielded nanowires at a fixed TeO_3^{2-} concentration (*i.e.,* 10 mM). Reaction temperature predominately effected on the dimension where the average diameter increased from 49 nm to 200 nm with increasing temperature from 4 ºC to 50 ºC. Various electrochemical analytical methods including open circuit potential (OCP), linear sweep voltammograms (LSVs) as well as linear potentiodynamic polarizations (LPs) were carried out to understand the underlying reaction mechanism. Based on these analysis, the formation of branched nanorods was attributed to secondary nucleation at the crystal imperfections. [20]

Aluminum was selected for the similar three reasons as Zn foil; namely, the low redox potential of the Al/AlO_2^- , its ability to form water soluble products (*i.e.,* AlO_2^-) in alkaline baths, and low material cost. However, the redox potential of Al/AlO_2^- (E^o = -2.50 V vs. sat. Ag/AgCl), which is 1.20 V more negative than the Zn/ZnO_2^{2-} (E^o = -1.30 vs. Ag/AgCl). Therefore, Al/AlO_2^- provides a much greater thermodynamic driving force to further reduce the Te (0) to Te_2^{2-} (-I) or further reduce Te_2^{2-} (-I) to Te^{2-} (-II) where both Te_2^{2-} (-I) to Te^{2-} (-II) are water soluble species. Under this circumstance, the dominant synthesis of Te nanostructures in the solution via chemical reaction between Te_2^{2-} or Te^{2-} and TeO_3^{2-} is expected, which is a different deposition mechanism compared to Zn foil as sacrificial materials leading to the formation of different Te nanostructures on the surface of sacrificial materials. Te “rice-like” nanostructures with controlled dimensions were synthesized by galvanic displacement reactions of aluminum in alkaline baths. The Te

"rice-like" nanostructures were deposited in the solution via chemical reaction between Te_2^{2-} (-I) or Te^{2-} (-II) and TeO_3^{2-} (IV). The formation of sharp tips may be attributed to the high density of surface charges at the tips. The morphology of the Te evolved from branched nanostructures together with some "rice-like" nanostructures to only "rice-like" nanostructures as the reaction time (10 to 90 min) and temperature (4 to 50 ^oC) increased. The nanostructures peaked in dimensions after 30 min. At pH < 11.9 the deposited Te film was amorphous. The amorphous to crystalline transformation at pH ≥ 11.9 was associated with a sharp increase in the average current density jumping from 0.03 mA/cm^2 in the amorphous state at pH=10.9 to 1.0 mA/cm^2 in the crystalline state at pH=11.9 to 10 mA/cm^2 at pH=15.0. Although the nanorice diameter increased from 125 nm to 175 nm (with no distinctive trendline) over this pH range ([TeO_3^{2-}] = 10 mM at 23^oC), the length of the nanostructures increased linearly from 0.4 µm to 1.2 µm. However, the diameter and length of the nanostructures depended most strongly on [TeO_3^{2-}]. The diameter increased from 125 nm at 10 mM to 573 nm at 550 mM (pH=13.1 @23 ^oC for 30 min), while the length increased from 0.7 to 5.7 µm. [102]

1.3.2.2 Electrodeposition of Te

1.3.2.2.1 Electrodeposition of Te in Acidic Baths

Te has been synthesized by electrodeposition in acidic media.[103-111] However, the acidic baths have its drawbacks as mentioned above. The solubility of $HTeO_2^+$ ion in acidic solution is relatively low (1.6 g/L (10 mM) at pH of zero)[16], which limited the deposition rate to about 20 µm/h. Unlike acidic baths, the solubility of TeO_3^{2-} is high in alkaline solution (87.8 g/L (550 mM) at pH of 10.5).[16] The higher solubility of TeO_3^{2-}

in alkaline solution makes it possible to achieve a high electrodeposition rate. There are a few publications that report the electrodeposition of Te in alkaline solution.

Qiu et al. electrodeposited Te thin films with a thickness up to 4 μm on monocrystalline tellurium substrate from a TeO_2-saturated aqueous solution. The thickness was relatively uniform. The needle-like defects with random orientation was observed when deposit on $(10\bar{1}0)$ surfaces. At high current densities, polycrystalline films consisting of 1 μm blades with random orientation were produced. [104]

Suggs et al. reported that well-ordered atomic layers of Te were formed electrochemically in aqueous solutions (0.4 mM TeO_3^{2-} in H_2SO_4 solution) on the low-index planes of Au. Formation of the first monolayer of Te proceeded through a sequence of structures. Initially, structures consisting of isolated Te atoms were formed at low coverages. Subsequent deposition did not occur for another 300 mV. At that stage, increased coverages resulted in compression of the Te atoms to form structures composed of Te dimers. Multiple dimer structures were observed on the Au(100) surface. Evidently, the potentials for deposition of Te atomic layers are less dependent on substrate structure than on chemical change. [105]

Ikemiya et al. investigated the atomic structures as well as the growth morphologies of electrodeposited Te films on Au(100) and Au(111) with large lattice misfits from sulfuric acid solutions (0.1 mM $HTeO_2^+$ + 0.05 M H_2SO_4) using in situ atomic force microscopy. On Au(100) and Au(111) the bulk deposited Te films are formed by a Stranski-Krastanov mechanism even at a slow deposition rate. This suggests that the surface diffusion process of Te adatoms on the monolayer-Te-coated Au is extremely slow.

Adlattice structures of Te films changed in a manner that is dependent on their thickness. [106]

Yagi et al. investigated the electrodeposition of Te in the solution with 0.5 mM TeO_2 and 0.1 M $HClO_4$ on polycrystalline gold electrodes using in situ optical second harmonic (SH) generation at two different excitation wavelengths. On 1064 nm excitation, the SH signal changed with the surface coverage of Te. It was also found that the first underpotential deposition layer of Te strongly perturbed the substrate surface. However, on 585 nm excitation, the SH signal changed in a complicated fashion during the desorption process of the Te monolayer from Au. These results were interpreted in terms of the existence of an optical resonance and the gradual structural change which accompanies energetic perturbation on Te-covered Au surfaces.[107]

Sorenson et al. reported the electrochemical formation of tellurium atomic layers on Au(110) and the phase transitions associated with those layers in the acidic bath (0.25 mM TeO_2 + 20 mM H_2SO_4). The voltammetry indicates two submonolayer deposition features and on one for bulk. The result of the slow deposition kinetics is that surfaces composed of a single atomic layer structure are not observed. [108]

Sorenson et al. also studied the electrodeposition of atomic layers of Te on Au(111) surfaces from aqueous solutions using in situ scanning tunneling microscopy in acidic bath (0.25 mM TeO_2 + 20 mM H_2SO_4). Te atomic layers were formed on Au(111) surfaces by underpotential deposition. Te atoms were place in a the Te atoms were placed in a variety of sites, indicating that some of the atoms would probably sit higher, in less energetically favorable sites.[109]

Jiang et al. electrodeposited Te film on polyaniline-coated macroporous phenolic foam in the solution with 10 mM $HTeO_2^+$ and 1 M HNO_3. The deposited film was composed of columnar crystals structures with preferred orientation along c-axis direction.[110]

Abad et al. reported the electrodeposition of Te films in the solution with 10 mM $HTeO_2^+$ and 1 M HNO_3, and the effect of sodium lignosulfonate was investigated. The present of sodium lignosulfonate implies a strong reduction in the grain size of Te. [111]

1.3.2.2.2 Electrodeposition of Te in alkaline baths

Ha *et al.* reported the electrochemical behavior of tellurium in 2.5 M NaOH solution with TeO_3^{2-} concentration of 10 mM. The morphology of Te electrodeposited in alkaline solution had a very porous nature and needle-like radial growth. The potential range for stable electrodeposition was between -0.8 V and -0.95 V vs. Hg/HgO. [112]

Sadeghi *et al.* investigated electrodeposition of Te on a nickel-coated copper substrate in alkali plating baths. The influence of current density, temperature, and pH were studied. Application of a very low current density results in a rather poor-quality deposit. Alternatively, a very high current density reduces the overvoltage of hydrogen, which decreases the quality of the deposit as well as the current efficiency. The higher temperature resulted in lower current efficiency. The higher current efficiency and better electrodeposited layers are obtained available in higher pH bath than in comparison to electrodeposited layers in lower pH bath. The optimum condition for electrodeposition of Te was: 6g/L (37.6 mM) TeO_2, pH of 10, and DC current density of 8.55 mA/cm^{-2} at room temperature. [113]

Electrodeposition of thick Te films in alkaline solutions was studied in this dissertation. Synthesis of thick dense Te films were demonstrated by electrodeposition in alkaline solution. To achieve dense morphology, the applied potential should be more positive than -1.0 V to avoid further reduction of Te to Te_2^{2-} or keep the reduction of Te to Te_2^{2-} at a low reaction rate, which would deteriorate the film morphology significantly. The XRD data showed that when the applied potential changed from -0.9 V to -1.0 V, the preferred orientation of thick Te film varied from (001) to (101), due to the dissolution of Te by reaction 1.5. The proper pH range to deposit a dense thick film is 11.3 to 12.5. Sufficient agitation (2000 rpm) is necessary to electrodeposit a dense film. Grain size of the thick Te films was from 66 to 135 nm, which is controlled by the applied potential, TeO_3^{2-} concentration and pH. The larger grain size resulted in lower carrier concentration due to less crystal defects. The lowest carrier concentration was 7.1×10^{18} cm^{-3}, where the thick Te film had a grain size of 135 nm. The Highest deposition rate was 130 μm/h achieved by high TeO_3^{2-} concentration (550 mM) and more negative applied potential (-1.0 V). Current efficiency for electrodeposition of Te thick films was higher than 85% in alkaline solution.

1.3.3 Electrochemistry of lead telluride (PbTe)

PbTe is a semiconductor with narrow band-gap energy of 0.31 eV at room temperature and a rock-salt crystal structure. PbTe can be n- or p-type as a result of departures from stoichiometry (Pb-rich PbTe is n-type, while Te-rich PbTe is p-type).[114] The state-of-the-art commercially available PbTe-based thermoelectric devices have the highest ZT of ~ 0.8 at ~ 600 K, which makes the materials a good candidate for

thermoelectric application in the middle-high temperature range. Furthermore, microdevices for thermoelectric application which based on thick film have drawn significant attention.[115] Thick-film-based devices have advantages over conventional TE module because of its compact size. By shrinking the size of thermoelectric devices, it not only allows the device to operate under smaller temperature gradients, but by so doing it expands its capability to handle a wider range of thermal and power management microelectronic systems.[115-119]

PbTe films have been synthesized by electrodeposition in acidic media.[120-127] However, the acidic baths have their drawbacks, which is low solubility of TeO_3^{2-} in acidic solution as mentioned above. Unlike acidic baths, the solubility of TeO_3^{2-} is high in alkaline solution (87.8 g/L (550 mM) at pH of 10.5).[16] Additionally, in both acidic [127] and alkaline [128, 129] solution, the electrodeposition mechanism reported that can electrodeposit dense PbTe films is the underpotential deposition mechanism, in which Te was electrodeposited first followed by the deposition of Pb on top of Te driven by the Gibbs free energy for PbTe crystal formation (-69.5 kJ/mol) [130]. Therefore, the deposition rate of PbTe depends on the Te deposition rate. The higher solubility of TeO_3^{2-} in alkaline solution makes it possible to achieve high electrodeposition rates.

According to the Pourbaix diagram (figure 1.9),[16] the electrochemical reaction of Pb is relatively simple compared with tellurium. It is an one-step reduction reaction from Pb(II) to Pb(0). Electrodeposition of PbTe in alkaline solution was investigated by several groups.

Saloniemi *et al.* reported electrodeposition of Te-rich thin PbTe films in alkaline solution of $Pb(CH_3COO)_2$, disodium salt of ethylendiaminetetraacetic acid (EDTA) and TeO_2. Electrochemical reactions were investigated by cyclic voltammetry, which showed that the formation of PbTe may occur via underpotential deposition of Pb on Te. Potential ranges to achieve constant composition were -0.70 to -0.90 V vs. SCE on SnO_2 substrate and -0.80 to -0.95 V vs. SCE on Cu substrates when the concentration of $PbEDTA^{2-}$ was 0.1 M and concentration of TeO_3^{2-} was 0.001 M. The corresponding potential ranges were -0.75 to -0.95 and -0.85 to -0.95 V vs. SCE when the $PbEDTA^{2-}$ concentration was 0.05 M.[128]

Additionally, Saloniemi *et al.* further investigated the electrochemical behavior of the related precursors TeO_3^{2-} and $PbEDTA^{2-}$ by an electrochemical quartz crystal microbalance (EQCM) combined with cyclic voltammetry (CV). The electrodeposition mechanism of PbTe was an induced codeposition mechanism (*i.e.*, underpotential deposition mechanism) via six electron reduction. The reduction of the $PbEDTA^{2-}$ complex to Pb(0) was a simple two electron reaction. On the other hand, the reduction mechanism of Te was complicated. Te deposits via a four-electron reaction. As the potential becomes more negative, the film becomes powdery and at most negative potentials the Te film is stripped off by further reaction of Te.[129]

Miranda *et al.* electrodeposited polycrystalline PbTe thin films on porous silicon layers from alkaline solution of 0.1 M $Pb(CH_3COO)_2$, 0.13 M disodium salt of ethylendiaminetetraacetic acid (EDTA) and 1 mM TeO_3^{2-} by galvanostatic and potentiostatic methods. For potentiostatic process the film growth was carried out at

potentials of -0.85 and -0.98 V vs. sat. Ag/AgCl. The grain size of PbTe thin films was approx. 100 nm.[131]

Qiu *et al*. synthesized PbTe nanorods with a diameter in the sub-10-nm regime that are highly uniform, single-crystalline, and pure through sonoelectrochemical method under ambient conditions. In the experiment, the concentration of Pb^{2+} and TeO_3^{2-} ions were fixed at 10 mM, and the solution pH was kept at approximately 8. Nitrilotriacetic acid (NTA) was used as complex reagent. The ratio of metal ion/ligand was used to control the composition of PbTe. When the $[Pb^{2+}]$/[NTA] changed from 0.20:1 to 0.10:1 to 0.05:1, the electrodeposited materials changed from pure PbTe to mixture of PbTe and Te to pure Te.[132]

Yang et al. synthesized PbTe nanowire arrays using lithographically patterned nanowire electrodeposition in the solution with 0.83 mM TeO_3^{2-}, 83 mM Pb^{2+} at pH of 10. The electrodeposited PbTe nanowires had a rectangular cross-section with adjustable width and height ranging between 60 to 400 nm and 20 to 100 nm, respectively. A cyclic electrodeposition-stripping technique was used to produce polycrystalline, stoichiometric, face-centered cubic PbTe with a mean grain diameter of 10 to 20 nm. The length of the nanowires were more than 1 mm. [133]

Erdogan et al. reported the synthesis of PbTe thin films on Au (111) substrates using electrodeposition by underpotential deposition mechanism in the solution containing EDTA, Pb^{2+}, and TeO_3^{2-} at a constant potential. The growth of PbTe thin film follows the nucleation and two dimensional growth mechanism, resulting in high crystalline films of

PbTe (200) in cubic structure. The atomic ratio of Pb and Te of PbTe film was approximately 1:1. [134]

1.4 References

1. Lewis, N.S. and D.G. Nocera, *Powering the planet: Chemical challenges in solar energy utilization.* Proceedings of the National Academy of Sciences, 2006. **103**(43): p. 15729-15735.
2. Arunachalam, V.S. and E.L. Fleischer, *The Global Energy Landscape and Materials Innovation.* MRS Bulletin, 2008. **33**.
3. LaLonde, A.D., et al., *Lead telluride alloy thermoelectrics.* Materials Today, 2011. **14**(11): p. 526-532.
4. Nielsch, K., et al., *Thermoelectric Nanostructures: From Physical Model Systems towards Nanograined Composites.* Advanced Energy Materials, 2011. **1**(5): p. 713-731.
5. Jihui, Y. and T. Caillat, *Thermoelectric materials for space and automotive power generation.* MRS Bulletin, 2006. **31**(3): p. 224-229.
6. Zebarjadi, M., et al., *Perspectives on thermoelectrics: from fundamentals to device applications.* Energy & Environmental Science, 2012. **5**(1): p. 5147-5162.
7. Nolas, G.S., J. Sharp, and H.J. Goldsmid, *Thermoelectrics : basic principles and new materials developments*2001, New York: Springer.
8. Sootsman, J.R., D.Y. Chung, and M.G. Kanatzidis, *New and Old Concepts in Thermoelectric Materials.* Angewandte Chemie-International Edition, 2009. **48**(46): p. 8616-8639.
9. Snyder, G.J. and T.S. Ursell, *Thermoelectric Efficiency and Compatibility.* Physical Review Letters, 2003. **91**(14): p. 148301.
10. Shakouri, A., *Recent Developments in Semiconductor Thermoelectric Physics and Materials.* Annual Review of Materials Research, 2011. **41**(1): p. 399-431.
11. Vining, C.B., *An inconvenient truth about thermoelectrics.* Nat Mater, 2009. **8**(2): p. 83-85.
12. Szczech, J.R., J.M. Higgins, and S. Jin, *Enhancement of the thermoelectric properties in nanoscale and nanostructured materials.* Journal of Materials Chemistry, 2011. **21**(12): p. 4037-4055.
13. Snyder, G.J. and E.S. Toberer, *Complex thermoelectric materials.* Nat Mater, 2008. **7**(2): p. 105-114.

14. Horvath, J., *Mastering 3D printing*2014, New York: Heinz Weinheimer.

15. Horvath, J. and R. Cameron, *3D Printing with MatterControl*2015, New York: Springer.

16. Pourbaix, M., *Atlas of electrochemical equilibria in aqueous solutions*1966, Long Island City, N.Y.: Pergamon Press Inc.

17. Gregory, B.W., M.L. Norton, and J.L. Stickney, *Thin-layer electrochemical studies of the underpotential deposition of cadmium and tellurium on polycrystalline gold, platinum and copper electrodes.* Journal of Electroanalytical Chemistry and Interfacial Electrochemistry, 1990. **293**(1–2): p. 85-101.

18. Zhang, M., et al., *A Rapid Room-Temperature NO2 Sensor Based on Tellurium–SWNT Hybrid Nanostructures.* The Journal of Physical Chemistry C, 2012. **116**(37): p. 20067-20074.

19. Lingane, J.J. and L.W. Niedrach, *Polarography of Selenium and Tellurium. II. The + 4 States.* Journal of the American Chemical Society, 1949. **71**(1): p. 196-204.

20. Wu, T., et al., *Synthesis of Tellurium Heterostructures by Galvanic Displacement Reaction of Zinc in Alkaline Baths.* Electrochimica Acta, 2014. **150**(0): p. 298-307.

21. Panson, A.J., *POLAROGRAPHY OF THE DITELLURIDE ION.* The Journal of Physical Chemistry, 1963. **67**(10): p. 2177-2180.

22. Shinagawa, M., N. Yano, and T. Kurosu, *Mechanism and analytical aspects of the polarographic maximum wave of tellurium.* Talanta, 1972. **19**(4): p. 439-450.

23. Schmidt, H., *Te - reduction in alkaline bath - Polarographic behavior of tellurites and tellurates.* Journal of the Polarographic society, 1962. **8**: p. 49-57.

24. Shinagawa, M., N. Yano, and T. Kurosu, *Te reudction - alkaline bath - Mechanism and analytical aspects of the polarographic maximum wave of tellurium.* Talanta, 1972. **19**(4): p. 439-450.

25. Mishra, K.K., D. Ham, and K. Rajeshwar, *Anodic Oxidation of Te Ions - alkaline - Te22- detected - RDE.* Journal of The Electrochemical Society, 1990. **137**(11): p. 3438-3441.

26. Blanc, M.L., *Can an element form both positive and negative ions.* Zeitschrift fuer Elektrochemie und Angewandte Physikalische Chemie, 1905. **11**: p. 813-18.

27. Bard, A.J., *Encyclopedia of electrochemistry of the elements*. Vol. IV. 1975, New York: MARCEL DEKKER, INC.

28. Komandenko, V.M. and A.L. Rotinyan, *Electrochemical behavior of a tellurium electrode in sodium tellurite solutions containing small excesses of free alkali.* Èlektrohimiâ, 1967. **3**(6): p. 723-728.

29. Komandenko, V.M. and A.L. Rotinyan, *Electrochemical behavior of tellurium in sodium tellurite solutions.* Zhurnal Prikladnoi Khimii 1966. **39**(1): p. 123-31.

30. Bard, A.J. and L.R. Faulkner, *Electrochemical methods fundamentals and applications*2001: John Wiley&Sons, Inc.

31. Awad, S.A., *Overpotential on tellurium cathodes in NaOH solutions.* Journal of the Electrochemical Society, 1961. **108**: p. 468-72.

32. Awad, S.A., *Electrochemical evidence for diatomicity of tellurium.* Journal of the Electrochemical Society, 1962. **109**: p. 865-70.

33. Komandenko, V.M. and A.L. Rotinyan, *Cathodic dissolution of tellurium in alkaline solutions.* Elektrokhimiya, 1967. **3**(5): p. 552-557.

34. Bang, J.H. and K.S. Suslick, *Applications of Ultrasound to the Synthesis of Nanostructured Materials.* Advanced Materials, 2010. **22**(10): p. 1039-1059.

35. Xia, Y., et al., *One-Dimensional Nanostructures: Synthesis, Characterization, and Applications.* Advanced Materials, 2003. **15**(5): p. 353-389.

36. Zečević, J., K.P. de Jong, and P.E. de Jongh, *Progress in electron tomography to assess the 3D nanostructure of catalysts.* Current Opinion in Solid State and Materials Science, 2013. **17**(3): p. 115-125.

37. Lee, T.I., et al., *High-Power Density Piezoelectric Energy Harvesting Using Radially Strained Ultrathin Trigonal Tellurium Nanowire Assembly.* Advanced Materials, 2013. **25**(21): p. 2920-2925.

38. Liu, J.-W., et al., *Rapid Microwave-Assisted Synthesis of Uniform Ultralong Te Nanowires, Optical Property, and Chemical Stability.* Langmuir, 2010. **26**(13): p. 11372-11377.

39. Wang, X., *Piezoelectric nanogenerators—Harvesting ambient mechanical energy at the nanometer scale.* Nano Energy, 2012. **1**(1): p. 13-24.

40. Diedenhofen, S.L., et al., *Broad-band and Omnidirectional Antireflection Coatings Based on Semiconductor Nanorods.* Advanced Materials, 2009. **21**(9): p. 973-978.

41. Chao, Y.-C., et al., *Light scattering by nanostructured anti-reflection coatings.* Energy & Environmental Science, 2011. **4**(9): p. 3436-3441.

42. Yan, C., C.M. Raghavan, and D.J. Kang, *Photocatalytic properties of shape-controlled ultra-long elemental Te nanowires synthesized via a facile hydrothermal method.* Materials Letters, 2014. **116**(0): p. 341-344.

43. Cho, I.S., et al., *Branched TiO2 Nanorods for Photoelectrochemical Hydrogen Production.* Nano Letters, 2011. **11**(11): p. 4978-4984.

44. Wang, H., et al., *Nanorice: A Hybrid Plasmonic Nanostructure.* Nano Letters, 2006. **6**(4): p. 827-832.

45. Sealy, C., *Nanorice combines best of both worlds: Nanoparticles.* Nano Today, 2006. **1**(2): p. 13.

46. Wei, H., et al., *Multipolar Plasmon Resonances in Individual Ag Nanorice.* ACS Nano, 2010. **4**(5): p. 2649-2654.

47. Hippel, A.v., *Structure and Conductivity in the VIb Group of the Periodic System* Journal of Chemical Physics, 1948. **16**: p. 372-380.

48. Arlt, G. and P. Quadflieg, *Electronic Displacement in Tellurium by Mechanical Strain.* physica status solidi (b), 1969. **32**(2): p. 687-689.

49. Liu, J.-W., et al., *Mesostructured Assemblies of Ultrathin Superlong Tellurium Nanowires and Their Photoconductivity.* Journal of the American Chemical Society, 2010. **132**(26): p. 8945-8952.

50. Wang, Y., et al., *Mirror-Like Photoconductive Layer-by-Layer Thin Films of Te Nanowires: The Fusion of Semiconductor, Metal, and Insulator Properties.* Advanced Materials, 2006. **18**(4): p. 518-522.

51. Li, X.-L., et al., *Synthesis and magnetoresistance measurement of tellurium microtubes.* Journal of Materials Chemistry, 2003. **14**(2): p. 244-247.

52. Mohanty, P., et al., *Synthesis of Single Crystalline Tellurium Nanotubes with Triangular and Hexagonal Cross Sections.* The Journal of Physical Chemistry B, 2006. **110**(2): p. 791-795.

53. Chen, H., et al., *The fabrication of Te nanowires with different orientations by vacuum vapor deposition.* Physics Letters A, 2007. **362**(1): p. 61-65.

54. Wang, Q., et al., *Fabrication and Growth Mechanism of Selenium and Tellurium Nanobelts through a Vacuum Vapor Deposition Route.* The Journal of Physical Chemistry C, 2007. **111**(35): p. 12926-12932.

55. Sen, S., et al., *Synthesis of Tellurium Nanostructures by Physical Vapor Deposition and Their Growth Mechanism.* Crystal Growth & Design, 2008. **8**(1): p. 238-242.

56. Siciliano, T., et al., *Tellurium microtubes synthesized by thermal evaporation method.* Crystal Research and Technology, 2011. **46**(8): p. 765-768.

57. Parsafar, N. and A. Ebrahimzad, *The effect of substrate temperature on fabrication of one-dimensional nanostructures of tellurium.* Int.J.Nano Dim., 2012. **2**(3): p. 177-183.

58. Hawley, C.J., et al., *Shape-Controlled Vapor-Transport Growth of Tellurium Nanowires.* Crystal Growth & Design, 2012. **12**(6): p. 2789-2793.

59. Geng, B., et al., *Large-scale synthesis of single-crystalline Te nanobelts by a low-temperature chemical vapour deposition route.* Nanotechnology, 2003. **14**(9): p. 983.

60. Mo, M., et al., *Controlled Hydrothermal Synthesis of Thin Single-Crystal Tellurium Nanobelts and Nanotubes.* Advanced Materials, 2002. **14**(22): p. 1658-1662.

61. Liu, Z., et al., *Shape-controlled synthesis and growth mechanism of one-dimensional nanostructures of trigonal tellurium.* New Journal of Chemistry, 2003. **27**(12): p. 1748-1752.

62. Xu, L., et al., *Large-scale Synthesis of Crystalline Tellurium Nanowires with Controlled-Diameters via a Hydrothermal-reduction Process.* Chemistry Letters, 2004. **33**(5): p. 592-593.

63. Liu, Z., et al., *Size-Controlled Synthesis and Growth Mechanism of Monodisperse Tellurium Nanorods by a Surfactant-Assisted Method.* Langmuir, 2004. **20**(1): p. 214-218.

64. Lu, Q., F. Gao, and S. Komarneni, *Biomolecule-Assisted Reduction in the Synthesis of Single-Crystalline Tellurium Nanowires.* Advanced Materials, 2004. **16**(18): p. 1629-1632.

65. Lu, Q., F. Gao, and S. Komarneni, *A Green Chemical Approach to the Synthesis of Tellurium Nanowires.* Langmuir, 2005. **21**(13): p. 6002-6005.

66. Zhu, Y.-J., H. Xian-Luo, and W. Wei-Wei, *Poly(vinylpyrrolidone): a new reductant for preparation of tellurium nanorods, nanowires, and tubes from TeO 2.* Nanotechnology, 2006. **17**(3): p. 645.

67. Qian, H.-S., et al., *Synthesis of Uniform Te@Carbon-Rich Composite Nanocables with Photoluminescence Properties and Carbonaceous Nanofibers by the Hydrothermal Carbonization of Glucose.* Chemistry of Materials, 2006. **18**(8): p. 2102-2108.

68. Qian, H.-S., et al., *High-Quality Luminescent Tellurium Nanowires of Several Nanometers in Diameter and High Aspect Ratio Synthesized by a Poly (Vinyl Pyrrolidone)-Assisted Hydrothermal Process.* Langmuir, 2006. **22**(8): p. 3830-3835.

69. Xu, W., et al., *Structural, Electrical, and Photoconductive Properties of Individual Single-Crystalline Tellurium Nanotubes Synthesized by a Chemical Route: Doping Effects on Electrical Structure.* Small, 2008. **4**(7): p. 888-893.

70. Liang, F. and H. Qian, *Synthesis of tellurium nanowires and their transport property.* Materials Chemistry and Physics, 2009. **113**(2): p. 523-526.

71. Wang, Z., et al., *Formation of single-crystal tellurium nanowires and nanotubes via hydrothermal recrystallization and their gas sensing properties at room temperature.* Journal of Materials Chemistry, 2010. **20**(12): p. 2457-2463.

72. Zhu, H., et al., *Controlled Synthesis of Tellurium Nanostructures from Nanotubes to Nanorods and Nanowires and Their Template Applications.* The Journal of Physical Chemistry C, 2011. **115**(14): p. 6375-6380.

73. Zhu, H., et al., *Controlled hydrothermal synthesis of tri-wing tellurium nanoribbons and their template reaction.* CrystEngComm, 2012. **14**(1): p. 251-255.

74. Wei, G., et al., *Solvothermal synthesis of porous tellurium nanotubes.* Chemical Physics Letters, 2003. **372**(3): p. 590-594.

75. Song, J.-M., et al., *Superlong High-Quality Tellurium Nanotubes: Synthesis, Characterization, and Optical Property.* Crystal Growth & Design, 2008. **8**(6): p. 1902-1908.

76. Wang, S., et al., *Synthesis, characterization and optical properties of flower-like tellurium.* CrystEngComm, 2010. **12**(1): p. 166-171.

77. Wu, X., et al., *Controlled synthesis of multi-morphology Te crystals by a convenient Lewis acid/base-assisted solvothermal method.* Journal of Nanoparticle Research, 2012. **14**(8): p. 1-10.

78. Mayers, B. and Y. Xia, *Formation of Tellurium Nanotubes Through Concentration Depletion at the Surfaces of Seeds.* Advanced Materials, 2002. **14**(4): p. 279-282.

79. Zhu, Y. and X. Hu, *tellurium nanorods and nanowires prepared by the microwave-polyol method.* Chemistry Letters, 2004. **33**.

80. Zhu, W., et al., *Controllable, Surfactant-Free Growth of 2D, Scroll-Like Tellurium Nanocrystals via a Modified Polyol Process.* Crystal Growth & Design, 2006. **6**(12): p. 2804-2808.

81. Zhou, B., et al., *A novel ultrasonic-assisted solution-phase approach for the fabrication of tellurium bundles of nanowhiskers.* Ultrasonics Sonochemistry, 2006. **13**(4): p. 352-358.

82. Zhu, Y.-J., et al., *Microwave-Assisted Synthesis of Single-Crystalline Tellurium Nanorods and Nanowires in Ionic Liquids.* Angewandte Chemie International Edition, 2004. **43**(11): p. 1410-1414.

83. Zhang, B., et al., *1D Tellurium Nanostructures: Photothermally Assisted Morphology-Controlled Synthesis and Applications in Preparing Functional Nanoscale Materials.* Advanced Functional Materials, 2007. **17**(3): p. 486-492.

84. Liu, Z., et al., *Surfactant-assisted growth of uniform nanorods of crystalline tellurium.* Journal of Materials Chemistry, 2003. **13**(1): p. 159-162.

85. Zheng, R., et al., *Synthesis of tellurium nanorods via spontaneous oxidation of NaHTe at room temperature.* Chemical Physics Letters, 2004. **395**: p. 302-305.

86. Gautam, U.K. and C.N.R. Rao, *Controlled synthesis of crystalline tellurium nanorods, nanowires, nanobelts and related structures by a self-seeding solution process.* Journal of Materials Chemistry, 2004. **14**(16): p. 2530-2535.

87. He, Z., S.-H. Yu, and J. Zhu, *Amino Acids Controlled Growth of Shuttle-Like Scrolled Tellurium Nanotubes and Nanowires with Sharp Tips.* Chemistry of Materials, 2005. **17**(11): p. 2785-2788.

88. F.Gao, Q. Lu, and S. Komarneni, *Gluconate controls one-dimensional growth of tellurium nanostructures.* Journal of Materials Research, 2006. **21**(02): p. 343-348.

89. Wang, S., et al., *Large-scale synthesis of feather-like single-crystal Te via a biphasic interfacial reaction route.* CrystEngComm, 2010. **12**(11): p. 3852-3857.

90. Shen, J.-M., et al., *Construction of Unconventional Hexapod-like Tellurium Nanostructure with Morphology-Dependent Photoluminescence Property.* The Journal of Physical Chemistry C, 2009. **113**(22): p. 9502-9508.

91. Rheem, Y., et al., *Synthesis of tellurium nanotubes by galvanic displacement.* Electrochimica Acta, 2010. **55**(7): p. 2472-2476.

92. Park, H., et al., *Branched tellurium hollow nanofibers by galvanic displacement reaction and their sensing performance toward nitrogen dioxide.* Nanoscale, 2013. **5**(7): p. 3058-3062.

93. Elazem, D., et al., *Morphology change of galvanically displaced one-dimensional tellurium nanostructures via controlling the microstructure of sacrificial Ni thin films.* Electrochimica Acta, 2013. **106**(0): p. 447-452.

94. Zhao, A.W., et al., *Tellurium nanowire arrays synthesized by electrochemical and electrophoretic deposition.* Journal of Materials Research, 2003. **18**: p. 2318-2322.

95. She, G., et al., *Template-Free Electrodeposition of One-Dimensional Nanostructures of Tellurium.* Crystal Growth & Design, 2009. **9**(2): p. 663-666.

96. Wang, X. and Y. Ni, *A facile electrochemical route for fast deposition of featherlike tellurium microstructures.* RSC Advances, 2011. **2**: p. 2340-2345.

97. Chang, C.H., et al., *Bi and Te thin films synthesized by galvanic displacement from acidic nitric baths.* Electrochimica Acta, 2010. **55**(3): p. 743-752.

98. Rheem, Y., et al., *Synthesis of tellurium nanotubes by galvanic displacement.* Electrochimica Acta, 2010. **55**(7): p. 2472-2476.

99. Elazem, D., et al., *Morphology change of galvanically displaced one-dimensional tellurium nanostructures via controlling the microstructure of sacrificial Ni thin films.* Electrochimica Acta, 2013. **106**: p. 447-452.

100. Jeong, D.-B., et al., *Template-free synthesis of vertically oriented tellurium nanowires via a galvanic displacement reaction.* Electrochimica Acta, 2013. **111**: p. 200-205.

101. Suh, H., et al., *Bamboo-like Te Nanotubes with Tailored Dimensions Synthesized from Segmental NiFe Nanowires as Sacrificial Templates.* Bulletin of the Korean Chemical Society, 2014. **35**(11): p. 3227-3231.

102. Wu, T., et al., *Size Controlled Synthesis of Tellurium Nanorices by Galvanic Displacement Reaction of Aluminum.* Electrochimica Acta, 2015. **176**: p. 1382-1392.

103. van Ngać, N., O. Vittori, and G. Quarin, *Voltammetric and chronoamperometric studies of tellurium electrodeposition of glassy carbon and gold electrodes.* Journal of Electroanalytical Chemistry and Interfacial Electrochemistry, 1984. **167**(1–2): p. 227-235.

104. Qiu, C.X. and I. Shih, *Epitaxial growth of tellurium by electrodeposition.* Materials Letters, 1989. **8**(8): p. 309-312.

105. Suggs, D.W. and J.L. Stickney, *Characterization of atomic layers of tellurium electrodeposited on the low-index planes of gold.* The Journal of Physical Chemistry, 1991. **95**(24): p. 10056-10064.

106. Ikemiya, N., et al., *Atomic structures and growth morphologies of electrodeposited Te film on Au(100) and Au(111) observed by in situ atomic force microscopy.* Surface Science, 1996. **369**(1–3): p. 199-208.

107. Yagi, I., et al., *In situ optical second harmonic generation studies of electrochemical deposition of tellurium on polycrystalline gold electrodes.* Journal of Electroanalytical Chemistry, 1996. **401**(1–2): p. 95-101.

108. Sorenson, T.A., et al., *Phase transitions in the electrodeposition of tellurium atomic layers on Au(100).* Journal of Electroanalytical Chemistry, 1999. **467**(1–2): p. 270-281.

109. Sorenson, T.A., et al., *Formation of and phase transitions in electrodeposited tellurium atomic layers on Au(1 1 1).* Surface Science, 2001. **470**(3): p. 197-214.

110. Jiang, C.H., et al., *Electrodeposition of tellurium film on polyaniline-coated macroporous phenolic foam and its thermopower.* Journal of Porous Materials, 2011. **19**(5): p. 819-823.

111. Abad, B., et al., *Thermoelectric properties of electrodeposited tellurium films and the sodium lignosulfonate effect.* Electrochimica Acta, 2015. **169**: p. 37-45.

112. Ha, Y.-C., et al., *Electrowinning of tellurium from alkaline leach liquor of cemented Te.* Journal of Applied Electrochemistry. **30**(3): p. 315-322.

113. Sadeghi, M., et al., *Thick tellurium electrodeposition on nickel-coated copper substrate for 124I production.* Applied Radiation and Isotopes, 2008. **66**(10): p. 1281-1286.

114. Dughaish, Z.H., *Lead telluride as a thermoelectric material for thermoelectric power generation.* Physica B: Condensed Matter, 2002. **322**(1–2): p. 205-223.

115. Fleurial, J.P., et al. *Power density-length of leg _ Thick-film thermoelectric microdevices*. in *Thermoelectrics, 1999. Eighteenth International Conference on*. 1999.

116. Semeniouk, V. and J.-P. Fleurial. *Temperature diff - thickness _ Modeling and Minimization of Intercascade Thermal Resistance in Multi-Stage Thermoelectric Cooler*. in *XVI Int. Conf. Thermoelectrics*. 1997. Dresden, Germany: IEEE.

117. Anatychuk, L.I., O.J. Luste, and L.N. Vikhor. *Optimal functions as an effective method for thermoelectric devices design*. in *Thermoelectrics, 1996., Fifteenth International Conference on*. 1996.

118. Anatychuk, L.I. and O.J. Luste. *Thickness limitation- lower limit_ Physical principles of microminiaturization in thermoelectricity*. in *Thermoelectrics, 1996., Fifteenth International Conference on*. 1996.

119. Snyder, G.J., et al., *Thermoelectric microdevice fabricated by a MEMS-like electrochemical process.* Nat Mater, 2003. **2**(8): p. 528-531.

120. Xiao, F., et al., *Recent progress in electrodeposition of thermoelectric thin films and nanostructures.* Electrochimica Acta, 2008. **53**(28): p. 8103-8117.

121. Beaunier, L., et al., *PbTe - acid _ Cd ion effect on morphology _ current limit because of Te ion mass transfer.* Journal of Electroanalytical Chemistry, 2002. **532**(1–2): p. 215-218.

122. Li, G.-R., et al., *Facile and Efficient Electrochemical Synthesis of PbTe Dendritic Structures.* Chemistry of Materials, 2008. **20**(10): p. 3306-3314.

123. Ni, Y., Y. Zhang, and J. Hong, *Potentiostatic Electrodeposition Route for Quick Synthesis of Featherlike PbTe Dendrites: Influencing Factors and Shape Evolution.* Crystal Growth & Design, 2011. **11**(6): p. 2142-2148.

124. Mondal, A., et al., *PbTe -acidic- electrodeposition - temperature effect&morphology - thickness saturation&time.* Thin Solid Films, 2006. **515**(4): p. 1255-1259.

125. Li, X. and I.S. Nandhakumar, *Direct electrodeposition of PbTe thin films on n-type silicon.* Electrochemistry Communications, 2008. **10**(3): p. 363-366.

126. Ivanova, Y.A., D.K. Ivanou, and E.A. Streltsov, *Electrochemical deposition of PbTe onto n-Si(1 0 0) wafers.* Electrochemistry Communications, 2007. **9**(4): p. 599-604.

127. Xiao, F., et al., *Electrodeposition of PbTe thin films from acidic nitrate baths.* Electrochimica Acta, 2006. **52**(3): p. 1101-1107.

128. Saloniemi, H., et al., *PbTe alkaline _ underpotential deposition _ potential&composition.* Thin Solid Films, 1998. **326**(1–2): p. 78-82.

129. Saloniemi, H., et al., *PbTe alkaline bath _ underpotential deposition.* Journal of Electroanalytical Chemistry, 2000. **482**(2): p. 139-148.

130. *CRC Handbook of Chemistry and Physics*2002, Cleveland: CRC Press.

131. Renata, C., B. Mirandaa, and P.G. Abramof, *PbTe _ alkaline _ stress increase because of smaller crystallites.* Materials Research, 2004. **7**: p. 619-623.

132. Qiu, X., et al., *PbTe Nanorods by Sonoelectrochemistry.* Angewandte Chemie International Edition, 2005. **44**(36): p. 5855-5857.

133. Yang, Y., et al., *Synthesis of PbTe Nanowire Arrays using Lithographically Patterned Nanowire Electrodeposition.* Nano Letters, 2008. **8**(8): p. 2447-2451.

134. Erdoğan, İ.Y., et al., *PbTe alkaline _ co-deposition.* Thin Solid Films, 2009. **517**(18): p. 5419-5424.

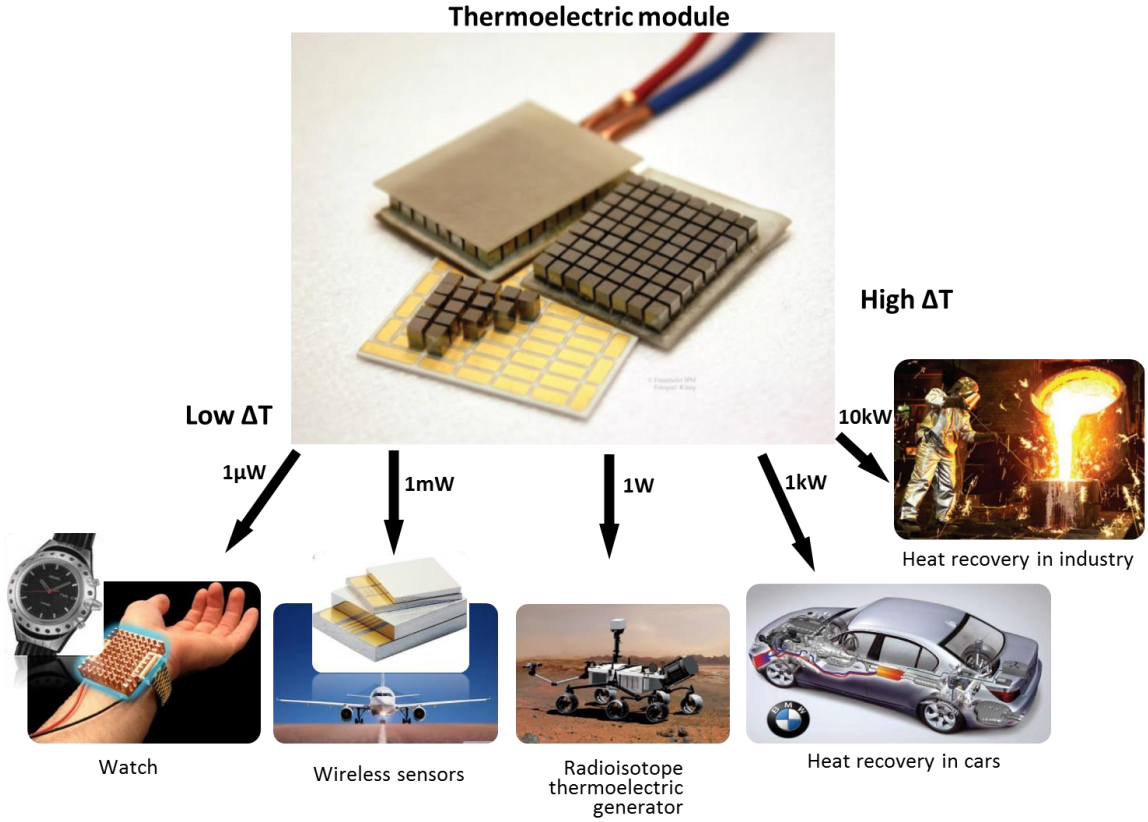

Figure 1.1 Application of thermoelectric devices

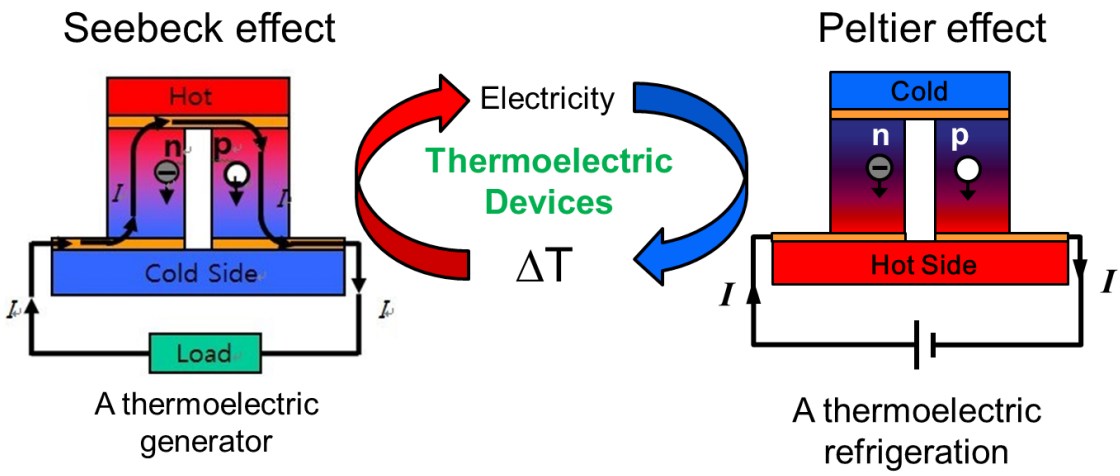

Figure 1.2 Schematic illustration of thermoelectric effect including the Seebeck effect and Peltier effect.

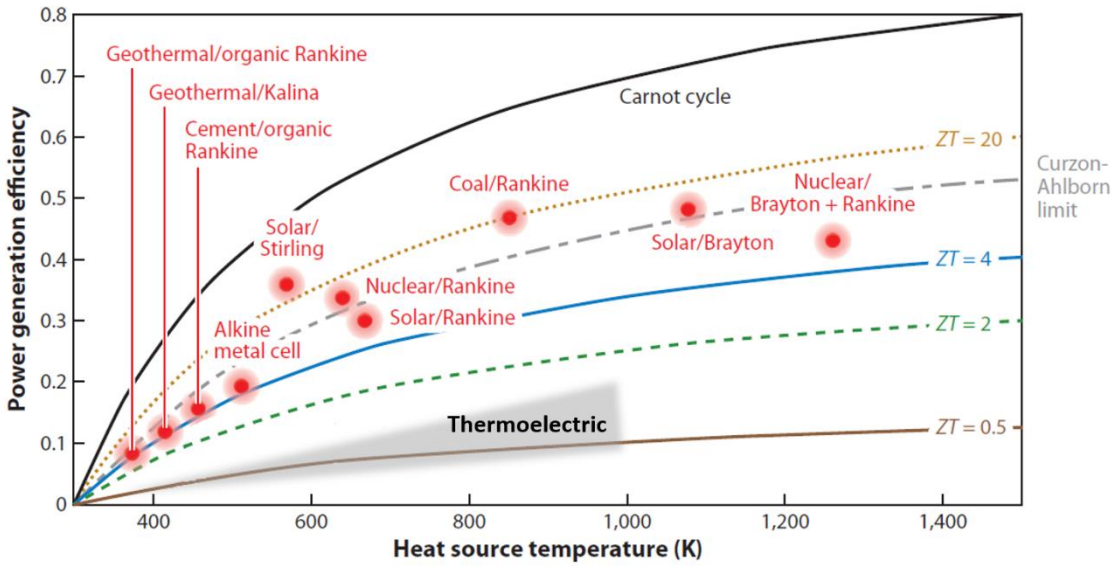

Figure 1.3 Thermoelectric power generation efficiency versus T_H. Efficiency for conventional mechanical engines as well as the Carnot limit are presented. [1, 2]

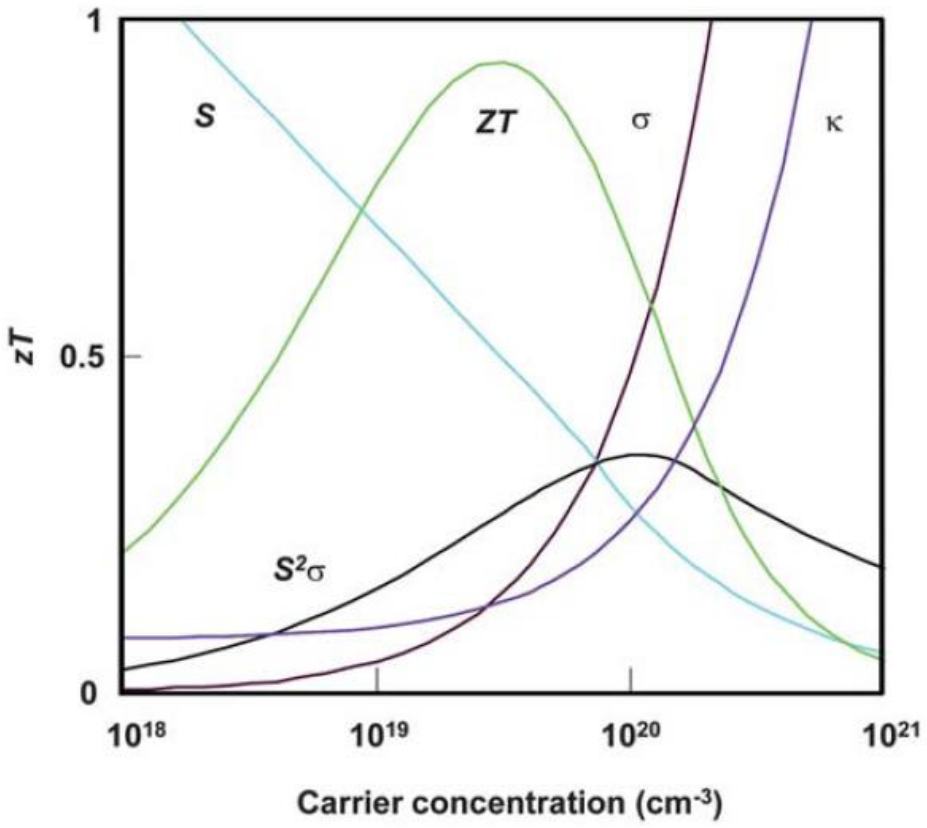

Figure 1.4 Interdependence of the Seebeck coefficient (S), electrical conductivity (σ), and thermal conductivity (κ). [3, 4]

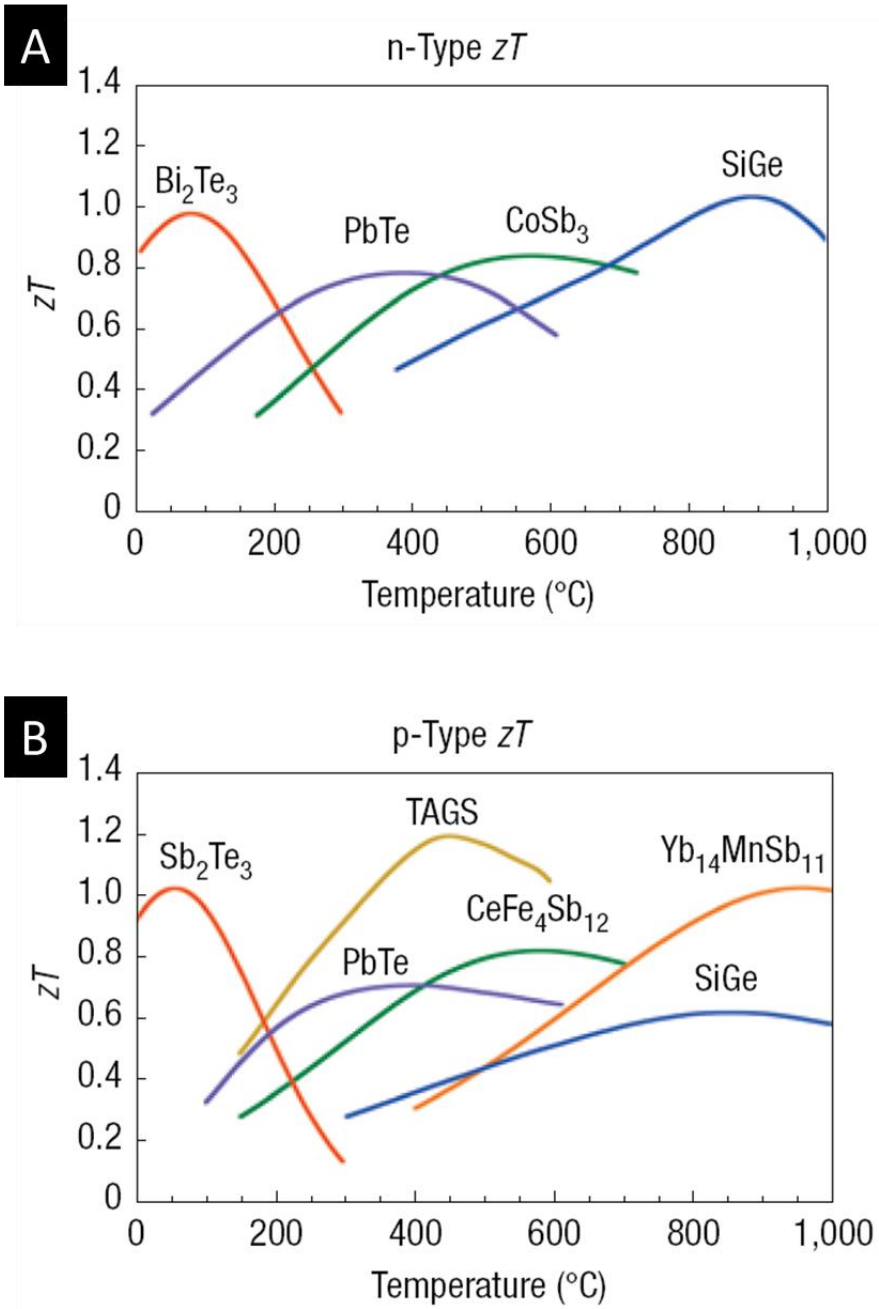

Figure 1.5 Thermoelectric performance (ZT) of the state-of-art commercial thermoelectric materials: (A) n-type and (B) p-type, as function of temperature. [3]

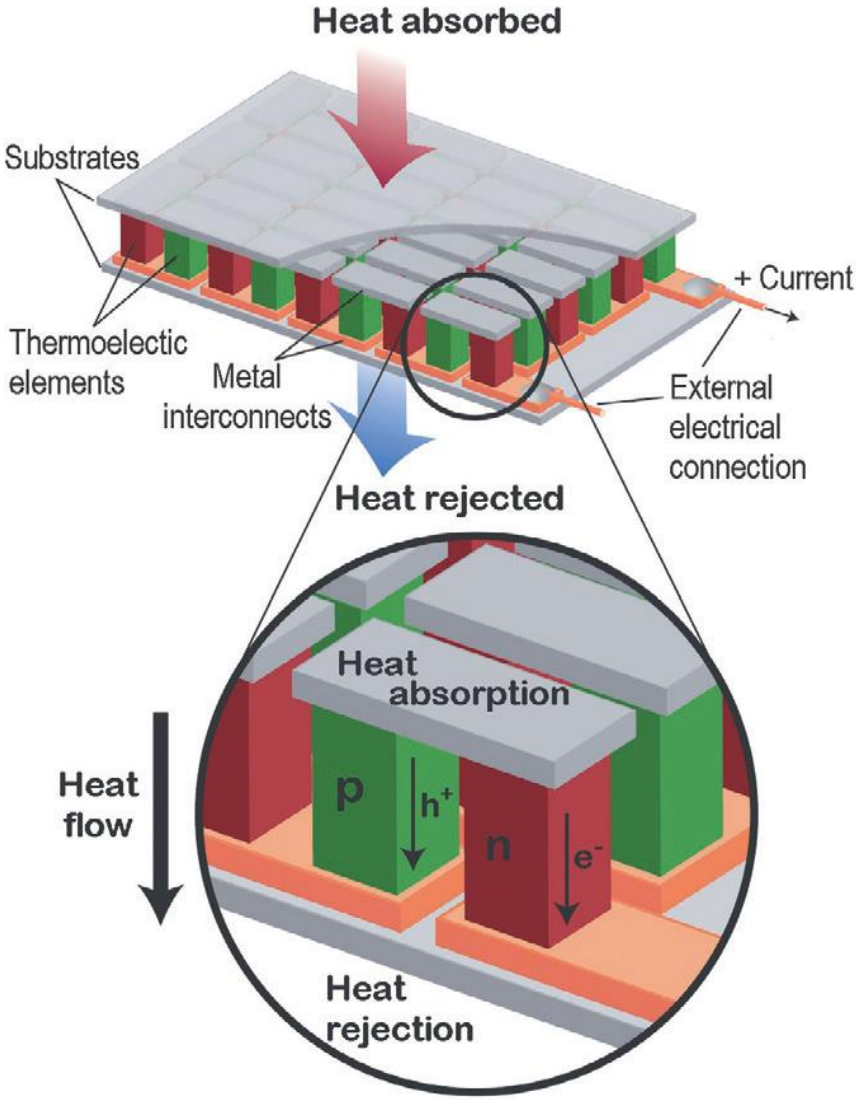

Figure 1.6 Thermoelectric module showing the direction of charge flow on both cooling and power generation. [3, 5]

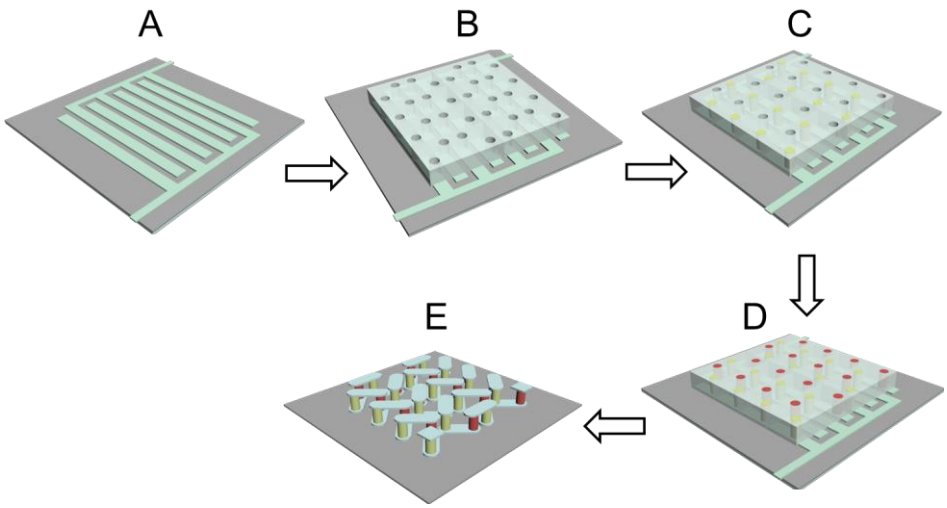

Figure 1.7 Electrochemical fabrication steps for thermoelectric microdevice using 3D printing.

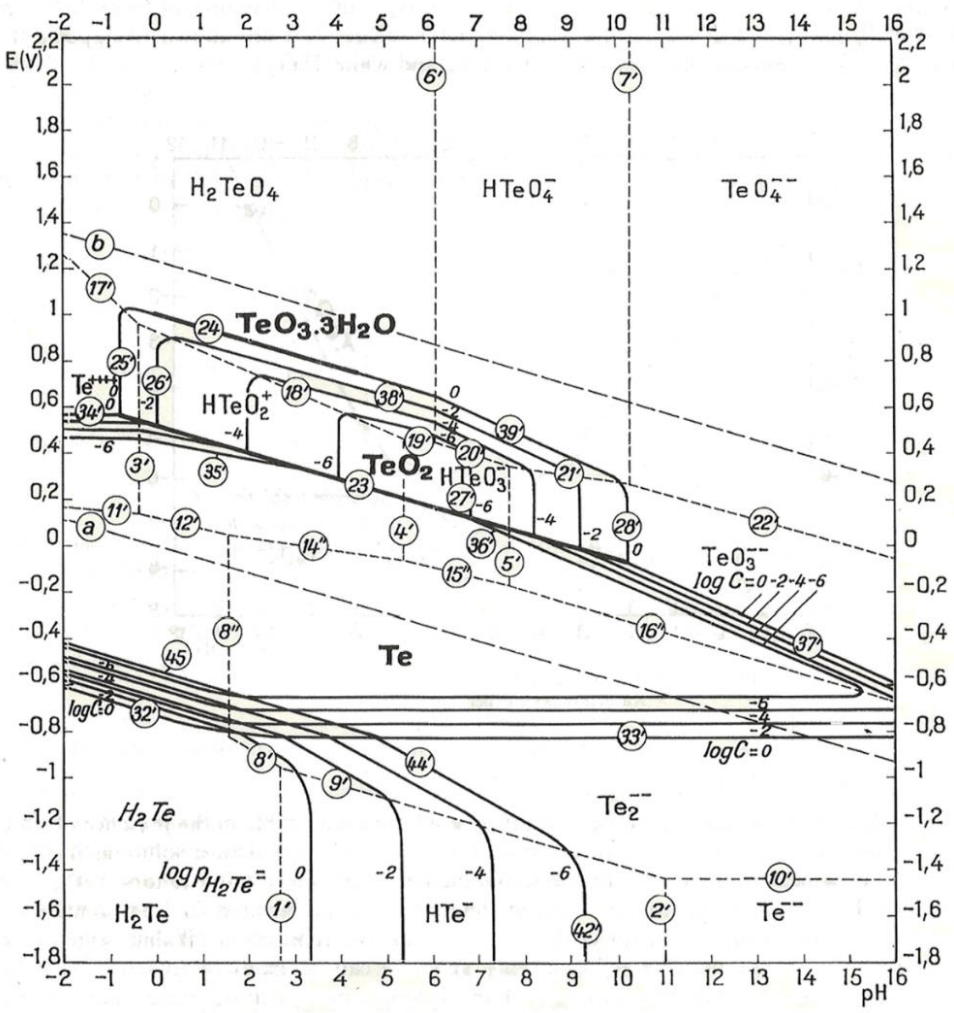

Figure 1.8 Pourbaix diagram of tellurium [6]

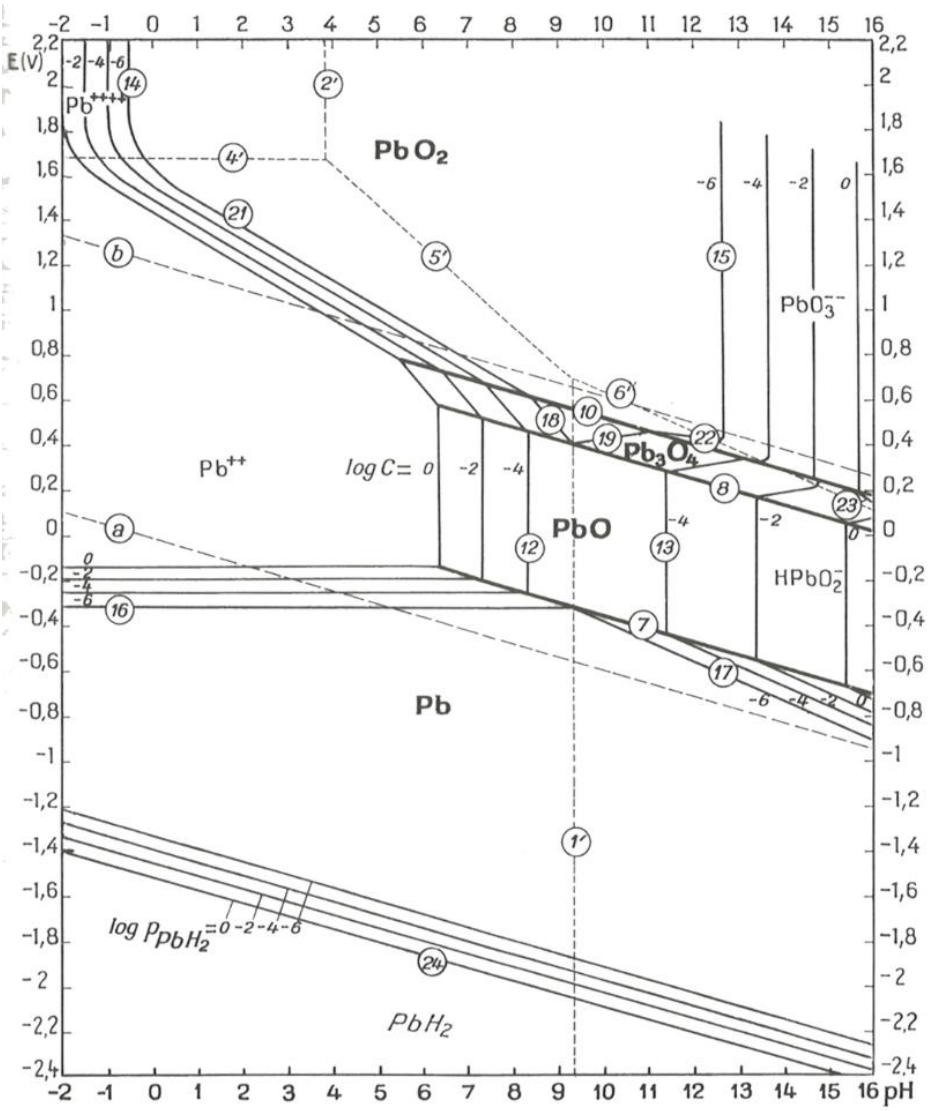

Figure 1.9 Pourbaix diagram of lead [6]

2 Synthesis of Tellurium Hetero-structures by Galvanic Displacement Reaction using Zinc as A Sacrificial Material

2.1 Abstract

Tellurium (Te) hetero-structures, including nanowires and branched structures, were synthesized by galvanic displacement reaction (GDR) in an alkaline bath using zinc foil as the sacrificial material. The Dimensions and morphology of the Te hetero-structures were well controlled by varying the electrolyte composition, pH, and reaction temperature. High aspect ratio single crystalline Te nanowires were synthesized at low TeO_3^{2-} concentrations (e.g. 2mM), while the branched Te nanostructures were obtained by varying TeO_3^{2-} concentration to 10 mM. The average diameter of the branches were controlled from 89 to 406 nm by increasing the TeO_3^{2-} concentration up to 550 mM in the alkaline bath. The branches had the same growth direction as the trunk, which was [001] direction. The average diameter of Te nanowires was tubed from 200 to 49 nm via varying the reaction temperature from 50 ^oC to 4 ^oC. Rising in the pH from 12.01 to 13.12 decreased the number of branches while increased the length of branches. When pH rose up to 14.70, nanowires were formed instead of branched structure. The reaction mechanism was investigated via electrochemical analysis methods, including linear sweep voltammetry (LSV), open-circuit potential (OCP), and linear potentiodynamic polarization (LP), which revealed that the transition from nanowires to branched structure was probably induced by the secondary nucleation from the crystal imperfection.

2.2 Introduction

In the last two decades, significant efforts have been devoted to synthesize different materials at nanoscales. Materials in the nanoscale regime often exhibit properties distinct from their bulk counterparts [1]. The morphology and dimension control of one-dimensional (1D) and three-dimensional (3D) nanostructures were intensively studied, since the morphology and dimension are of great importance in determining the properties of materials [2, 3]. For example, piezoelectric effect can be enhanced by reducing the diameter of nanowires [4, 5]; the 3D nanostructure can act as an antireflection coating which can enhance the light absorption by establish a refractive index gradient [6-8]; enhanced photon-to-current conversion efficiency was achieved by using 3D branched nanorod structure [9].

Tellurium (Te), a valuable p-type semiconductor with a narrow bandgap of 0.35eV, is a great candidate to form 1D or 3D nanostructures, since Te has an anisotropic crystal structure. Te atoms bond covalently to form helical chains, and the chains are bound together via van der Waals forces in hexagonal lattices [10]. Because of its anisotropic crystalline structure [10], Te has a strong tendency to grow along the c-axis into one dimension structures without any additional physical templates. Owing to its unique structure, Te exhibits many desirable properties which make it a promising candidate for the application of optoelectronic devices, sensors, piezoelectric devices, etc.

Synthesis of Te one-dimensional structure have been well studied. Various 1D nanostructured Te including nanowires, nanobults, and nanotubes, have been successfully

realized through Vapor deposition methods [11-19]; hydrothermal [20-33], solvothermal [34-37], and polyol process [38-40]; ultrasonic [41], microwave [42], photothermal [43], surfactant [44-46]; and biomolecule-assisted methods [24], as well as amino acids [47] and, gluconate [48] controlled methods. However, only several papers reported the formation of 3D Te nanostructure. Flower-like Te nanostructure were synthesized via Ostwald ripening process [36]. Feather-like Te nanostructure were formed by rapid crystallization at large supersaturation [32], secondary nucleation from crystal defects [46], and Ostwald ripening process [49]. Hexapod-like Te nanostructures were synthesized through a high temperature solution-based approaches [50]. In this studies, the synthesized 3D Te nanostructures were suspended in the solutions which required further processing to fabricate nano-devices. Consequently, it is important to develop a method to synthesize 3D Te nanostructure which is easy for device fabrication.

The GDR is a spontaneous electrochemical process driven by the redox potential difference between materials. It is a high-yielding, cost-effective and versatile process that operates near room temperature with low energy requirements, and is capable of handling complex geometries at a variety of scales. The synthesis of Te based on acidic bath has been reported [51-55]. In an acid bath the solubility of TeO_2 is very low, even at pH levels near zero. However, in an alkaline bath, TeO_2 has a rather high solubility where a wider range of TeO_2 concentration can function as electrolytes for GDR, which benefits the formation of 3D Te nanostructures. Zn foil is used as sacrificial materials in alkaline bath. The reasons why Zn is chosen as a sacrificial material are as follows: firstly, the reduction potential of Zn is more negative than Te, indicating the feasibility of GDR in

thermodynamics. Secondly, when Zn is oxidized in alkaline solution, it becomes a solvable specie – ZnO_2^{2-}, which is very important. Otherwise, if the Zn ion precipitates during GDR, it will cover the active spot of Zn foil leading to the termination of the GDR.

In this work, we demonstrated universal, cost-effective, and highly scalable process to synthesize 1D and 3D Te nanostructures by GDR in an alkaline bath using zinc foil as a sacrificial material. The morphology and dimensions of Te nanostructures were readily controlled by varying TeO_3^{2-} concentration, pH, and reaction temperature. The 3D nanostructures were well attached to the sacrificial materials which can be easily fabricated into device. Electrochemical analysis methods LSV, OCP, and LP were utilized to reveal the underlying reaction mechanism of Te branched structures. The probable mechanism for the formation of branched Te nanostructure was proposed.

2.3 Experimental

The electrolytes were prepared by dissolving tellurium dioxide (TeO_2, 99+%, Acros Organics) in a sodium hydroxide solution (NaOH, Fisher Chemical). Once the TeO_2, which has a stable form of TeO_3^{2-} in alkaline bath, was completely dissolved, the pH of the solution was adjusted by adding 10 M NaOH. Commercially available Zinc foil (Zn, 0.25 mm thick, 99.98%, Alfa Aesar, Inc.) was used as the sacrificial material and was cut into a size of 0.8 cm × 0.8 cm before use. The foil was first brushed in a soap solution, then rinsed by nanopure water and acetone (C_3H_6O, Fisher Chemical) sequentially for three times, and finally air dry.

A Teflon cell with a gasket and an open area of 0.272 cm^2 was applied as a reactor for all the GDR. The Zn foil was sandwiched between the gasket and Teflon sides. The Teflon sides were held together with screws to prevent any leakage. The GDR was carried out by adding 0.5 mL of electrolyte into the open area of the cell in contact with the Zn foil. The reaction was conducted for 30 min without disturbance. Once the reaction was completed, the electrolyte was carefully removed by pipette and the Te nanostructure was cleaned by nanopure water three times, then well-dispersed in isopropanol.

The morphology and dimension of the Te nanostructures were controlled by varying the concentration of TeO_3^{2-}, pH of the solutions, and the temperature of the reaction. The effect of TeO_3^{2-} concentration was investigated by varying the TeO_3^{2-} concentration from 2 to 550 mM, while fixing the pH at 13.12 at room temperature (23^{o}C). The pH effect was investigated by varying the pH from 12.61 to 14.70, while fixing the TeO_3^{2-} concentration at 10 mM. Additionally, the temperature effect was investigated by varying the temperature from 4 to 50 ^{o}C, while fixing the TeO_3^{2-} concentration at 2 mM and the pH at 13.12.

The underlying reaction mechanism was investigated by electrochemical analysis methods, including LSV, OCP, and LP. Transient OCP and LP were carried out in a three-electrode Teflon cell, with a Zn foil, a Ag/AgCl wire, and a Pt wire as the working, reference, and counter electrodes, respectively. To measure the LP, voltage was not controlled for the first 5 minutes, and OCP is measured. For 200 seconds following this period, the voltage was changed from OCP – 0.1 V to OCP +0.1 V with a scanning rate of 1 mV/s. This cycle was repeated three additional times. Characterization of LSV was

carried out in a 100 mL three-electrode cell with Ag/AgCl and a Pt-coated Ti strip as reference and counter electrodes. The working electrode was an E-beam-deposited Pt film with a thickness of 100 nm on a Si substrate.

The morphology, crystal orientation of Te hetero-structures were studied by emission-scanning electron microscopy (SEM, FEG-Philips XL30), X-ray diffraction (XRD, PANalytical Empyrean), and transmission electron microscopy (TEM, JEOL JEM-2100F). The Zn ion concentration in the solution after GDR was analyzed by atomic adsorption spectroscopy (AAS, PerkinElmer AAnalyst 800).

2.4 Results and discussion

LSV (figure 2.1) of Te deposition was studied at TeO_3^{2-} concentrations of 100 mM and pH of 13.12 using Pt substrate, Ag/AgCl, and Pt coated Ti strip as working, reference, and counter electrodes, respectively. The LSV curve is separated into 4 regions (i.e. A. B, C, and D) for Te reduction reaction. Region A, from -0.82V to -1.00V, is the deposition of Te from TeO_3^{2-} (reaction 2.1) [56-58]. It is also confirmed by the observation that Pt substrate is gradually covered by a gray Te film. Region B, from -1.00V to -1.14V, is the dissolution of deposited Te. In this region, the current increased significantly and then decrease dramatically. The increase in current is caused by the fast dissolution of Te to Te_2^{2-} (reaction 2.2) [56, 59]. From observation, a few shiny dots (i.e. Pt surface) appeared on the working electrode, which is the evidence of the dissolution of Te. Furthermore, at the maximum current, the Te thin film detached from Pt substrate. A minimum current appeared right after the maximum current. This is caused by the screening effect of the

Te_2^{2-}, which remained in the vicinity of the Pt substrate, on TeO_3^{2-} diffusion toward the electrode. Te_2^{2-} remained near the electrode and reacted reductively with the TeO_3^{2-} ions to cause the temporal decrease of the current [60, 61]. In region C from -1.14V to -1.30V, reactions (reaction 2.1, 2.2) happened simultaneously. Powder-like Te was deposited, Te tended to deposit on the Te surface instead of Pt substrate. Most of the Pt substrate was exposed to the electrolyte, on the Pt substrate hydrogen gas (reaction 2.3) evolution was observe. In region D from -1.30V to -1.50V, the increase in current was caused by an enhancement of hydrogen gas evolution and the deposition of powder Te.

$TeO_3^{2-}(aq) + 3H_2O(l) + 4e^- \rightarrow Te(s) + 6OH^-(aq)$ (E_0 = -0.59 V versus Ag/AgCl)

Reaction 2.1

$2Te(s) + 2e^- \rightarrow Te_2^{2-}(aq)$ (E_0 = -0.68V versus Ag/AgCl)

Reaction 2.2

$TeO_3^{2-}(aq) + 2Te_2^{2-}(aq) + 3H_2O(l) \rightarrow 5Te(s) + 6OH^-(aq)$ (ΔG = -164.05 KJ/mol)

Reaction 2.3

$2H_2O(l) + 2e^- \rightarrow H_2(g) + 2OH^-(aq)$ (E_0 = -0.98V versus Ag/AgCl)

Reaction 2.4

$Zn(s) + 4OH^-(aq) \rightarrow ZnO_2^{2-}(aq) + 2H_2O(aq) + 2e^-$ (E_0 = -1.30V versus Ag/AgCl)

Reaction 2.5

After understanding the reduction of Te in an alkaline bath, GDR was carried out and TeO_3^{2-} concentration effect was investigated. The morphology of the Te nanostructures can be varied by controlling the concentration of TeO_3^{2-}. Figure 2.2 (A-F) shows SEM images of six samples obtained at different TeO_3^{2-} concentrations, while the pH was fixed

at 13.12, the reaction temperature was 23 ^{o}C, and the reaction time was 30 min. These SEM images clearly indicate that when the TeO_3^{2-} concentrations were set at 2 mM and 3 mM, Te nanowires were formed. When TeO_3^{2-} concentration was increased to 10 mM, branched Te structures were produced. Further increasing the TeO_3^{2-} concentration to 50 mM or higher resulted in the formation of thicker branches. Although there was a varying distribution for the diameters of the nanostructures (figure 2.2 G-L), the average diameters increased consistently: 89±34 nm, 155±62 nm, 248±115 nm, 260±93 nm, 302±120 nm and 406±126 nm when TeO_3^{2-} concentrations were 2 mM, 3 mM, 10 mM, 50 mM, 100 mM and 550 mM, respectively. The morphology change phenomenon will be discussed with the OCP and LP results.

As well as the TeO_3^{2-} concentration, pH of the solution is another important factor used to control the morphology and dimensions of Te nanostructures. Figure 2.3 shows SEM images of Te nanostructures synthesized at different pH levels. When the pH level was at 14.70 (calculated), Te nanowires were formed. However, when the pH decreased to 13.12, branched structures were obtained. Further reducing the pH leads to a decline of the average diameter, as well as the length and aspect ratio of the branches. When the pH level was at 13.12, 12.94 and 12.61, the average diameter of the branches were 248 ± 115 nm, 158 ± 50 nm and 103 ± 30 nm; the length of branches were 2797 ± 476 nm, 1647 ± 201 nm and 780 ± 199 nm; and the aspect ratio of branches were 10.1 ± 4.2, 9.3 ± 2.4, and 6.3 ± 2.4, respectively. Additionally, the number of branches increased with decreasing pH. The morphology change at high pH will be discussed with the OCP and LP results.

Since temperature is one of the most important factors in reaction kinetics, we varied the reaction temperature during the GDR to get better control over the morphology and dimensions of the Te nanostructures. Figure 2.4 shows SEM images of the Te nanostructures synthesized at different temperatures while the TeO_3^{2-} concentration was fixed at 2 mM with a pH of 13.12. The morphology of the Te nanostructures did not change; i.e. they retained the nanowire structure. However, the diameter of the nanowires had a wider distribution and the average diameter increased significantly as reaction temperature increased from 4 to 50 ^oC. At 4 ^oC, thin Te nanowires with an average diameter of 49 ± 23 nm were synthesized. Increasing the reaction temperature to 23 and 50 ^oC increased the average diameter of Te nanowires to 89 ± 34 and 200 ± 94 nm, respectively. At 50 ^oC, the Zn ion concentration, tested by AAS (figure 2.10) in electrolytes after GDR, was higher, which means that the Zn foil dissolution rate was faster. At higher reaction temperature the grow rate in the direct perpendicular to [001] increase significantly, which was the reason for increase in diameter of the nanowires.

The XRD spectrum (figure 2.5) of the nanostructures synthesized at TeO_3^{2-} concentration of 550mM shows a typical XRD pattern of the as-synthesized tellurium products. All the strong and sharp reflection peaks of the XRD pattern can be indexed to trigonal Te. The Te lattice constants calculated from the XRD data of the nanostructure are a = 4.4531 Å and c = 5.9265 Å, which are consistent with the standard literature values of a = 4.4579 Å and c = 5.9270 Å (JCPDS-International Center for Diffraction Data, No. 36-1452).

Figure 2.6 shows typical high (a) and low (b) magnification transmission electron microscope (TEM) images, a high-resolution transmission electron microscopy (HRTEM) image, and selected area electron diffraction (SAED) pattern of the sample obtained at 4 ^{o}C with TeO_3^{2-} concentration of 2 mM and pH of 13.12. HRTEM images shown in figure 2.6C demonstrates lattice spacing of ca. 0.4 nm and 0.6 nm, respectively, corresponding to the lattice spacing of the (100) planes and (001) planes for trigonal Te. This demonstrates that the growth direction of Te the nanowire is [001]. On the other hand, the HRTEM image (figure 2.6C) shows that the Te nanowires is single crystalline.

Figure 2.7A displays a TEM image of Te branched structures. The HRTEM images of different positions of the given Te branched structure is shown in figure 2.7 B-D. The lattice spacing of the trunk is 0.6 nm (figure 2.7B), indicating the growth direction of the trunk is [001]. The lattice spacing of a branch (figure 2.7C) is 0.6 nm, which means the branches had the same growth direction of [001] as the trunk. HRTEM images of the intersection (figure 2.7D) clearly show the boundary between the trunk and the branch, and the angle between the growth direction of trunk and branches is 46^{o}. According to the hexagonal crystal structure of Te, the angle between plane (112) and [001] direction is 44.2^{o}, therefore the complementary angle based on the normal vector of plane (112) and [001] direction is 45.8^{o}, which is comparable to the observed angle (46^{o}) from figure 2.7D.

The OCPs, at TeO_3^{2-} concentrations from 2 to 550 mM with a fixed pH of 13.12, were measured to keep track of the reactions between the metal ions (TeO_3^{2-}) in the electrolyte and the sacrificial Zn foil (figure 2.8A). The sacrificial Zn foil was galvanically displaced to form Te nanostructures because of the difference in redox potentials between

the Te and the sacrificial Zn foil. Galvanic displacement occurred spontaneously because the redox potential of Te metal is more positive than the redox potential of Zn, which means that Te is more noble than Zn. Figure 2.8A shows that OCP decreased rapidly at the beginning of the reaction and approaches a constant value after about 10 minutes, which means the GDR reached steady state and continued during the experiments. The stable values of OCP increased with increasing TeO_3^{2-} concentration, which is expected according to the reaction 2.6: where $E^0_{sacrificial\ materials}$ is the standard redox potential of the sacrificial material, k is the Boltzmann constant, T is the absolute temperature, q is the elementary charge, and j_{oC} and j_{oA} are the cathodic and anodic exchange current densities, respectively. The increment of TeO_3^{2-} concentration resulted in large cathodic exchange current density (j_{oc}), which leaded to increase of OCP. The range of stable values was between -1.41V and -1.45V vs. Ag/AgCl.

$$E_{(OCP)} = \frac{1}{2}E^0_{sacrificial\ material} + \frac{kT}{q}ln\left(\frac{j_{oC}}{j_{oA}}\right)$$

Equation 2.1

According to the OCP, the GDR happened in region D of figure 6.1, so all reactions (reaction 2.1-2.5) can happen during GDR. However, no significant hydrogen gas evolution reaction was observed, which was different from the observation during LSV. This may be caused by the high overpotential of hydrogen gas evolution reaction on Zn surface [62].

Figure 2.8B displays the Tafel plot at different TeO_3^{2-} concentrations. The curve can be separated into two parts: cathodic and anodic. During the GDR, the cathodic part includes Te reduction reaction; while the anodic part is Zn dissolution reaction. Since we

varied the TeO_3^{2-} concentrations and fixed the pH, the cathodic part shifted as TeO_3^{2-} concentrations increased, while the anodic parts of the curve overlapped. When fitting linearly for both cathodic and anodic curves, there was an interception. From the interception, corrosion potential and current can be obtained. Figure 2.8(C, D) shows the corrosion potential and corrosion current of GDR at different TeO_3^{2-} concentrations as a function of time. Raising the TeO_3^{2-} concentration led to a more positive corrosion potential, which is consistent with the OCP data. This is also in accordance with the Nernst equation. Increasing the concentration of TeO_3^{2-} results in the increase of the reduction potential of the Te reduction reaction (reaction 2.1), which enlarged the reduction potential difference between Zn and Te, leading to the increment of driving force. Corrosion current increased when the TeO_3^{2-} concentration increased (figure 2.8D). This was expected because a high TeO_3^{2-} concentration can increase the cathodic reaction rate significantly.

The Te nanostructures changed from nanowire to branched structure as TeO_3^{2-} concentration increased from 2 to 10 mM. The average corrosion currents of GDR at TeO_3^{2-} concentration of 2 and 10 mM were 0.95 and 1.30 mA/cm^2, respectively, which means that the reaction rate increased about 40% when TeO_3^{2-} concentration rose from 2 to 10 mM. The fast deposition rate can result in an increase in crystal defects [46], which can act as a secondary nucleation spot. Additionally, the chemical deposition of Te from the interactions of TeO_3^{2-} and Te_2^{2-} [56, 60], near the Te surface, which was caused by high TeO_3^{2-} concentration, also contributed to the formation of crystal defects [46]. Furthermore, in the case of high TeO_3^{2-} concentration (10 mM), Te has a larger possibility to nucleate and grow on the imperfections of the deposited Te, because of the high mass transfer rate

[60]. However, in diluted solutions (2 mM), a long diffusion length (exhausted TeO_3^{2-} area) was formed, so charge transfer occurred only at the growing tip of Te. As a result, the sufficient Te source at TeO_3^{2-} concentration of 10 mM made the secondary nucleation to happen, which was responsible for the formation branched structures [46, 63].

OCP as a function of reaction time during GDR at different pH levels was also measured, as presented in Figure 2.9A, showing that the OCP shifts to the positive side with decreasing pH owing to the increment of anodic current (j_{oA}), which was expected according to equation 2.1. There was a sudden change in OCP (about 0.3 V) when the pH varied from 12.61 to 12.60. The difference between these two pH levels was very small and probably due to the limitations of the pH-meter, while NaOH concentrations for the pH values of 12.60 and 12.61 were 0.2 M and 0.3 M, respectively. These two pH values were the two boundary conditions. When pH $\leq$ 12.60, no Te nanostructures were formed. However, when pH $\geq$ 12.61, Te nanostructure were synthesized by GDR. Figure 2.9B shows a Tafel plot of GDR at different pH levels, and during these experiments TeO_3^{2-} concentration was fixed at 10 mM. When pH varied from 12.61 to 13.12, the cathodic part curve overlapped and the anodic curve shifted, indicating that anodic reaction (i.e. Zn dissolution reaction) was effect by pH. However, when pH was as high as 14.70, the cathodic part also shifted, which meant the cathodic reaction was also effected (equation 2.1). When the pH was 12.60 and 12.44, the Tafel plot shifted to positive side significantly.

Corrosion potential and current were obtained from the Tafel plot. Corrosion potential of GDR tested at different pH levels (figure 2.9C) by a linear polarization curve was consistent with OCP. When the pH decreased, the corrosion potential became more

positive, which illustrated the decline of the GDR driving force. When pH varied from 12.61 to 12.60, the corrosion potential moved to the positive side significantly. This was also confirmed by OCP data (figure 2.9A). According to the reaction observation of GDR, when the electrolyte pH was below 12.60, there was no formation of Te nanostructure. In this case, after Zn was oxidized, it formed zinc hydroxide precipitate [56], which passivated the Zn surface, resulting in the increase in corrosion potential and OCP. Additionally, the corrosion current of GDR shown in figure 2.9D was about 0.018 mA/cm^2 when pH is 12.60. Compared to 0.202 mA/cm^2 at pH of 12.61, 0.018 mA/cm^2 was more than 11 times lower, revealing the reaction barely happened and confirmed by the observation that no Te nanostructures were formed. Consequently, to obtain Te nanostructures using GDR in alkaline bath using Zn as sacrificial materials, the pH value should be no lower than 12.61 to prevent the passivation of Zn surface. At pH of 14.70, the corrosion current was higher compare to lower pH, while nanostructure change from branched structure to nanowire. In this case, the corrosion potential was -1.52 ± 0.02 V (figure 2.9C) leading to the fast reduction of Te to Te_2^{2-} [56, 59], and the factor that Te_2^{2-} ion is stable at such a high pH [64, 65] prevented the chemical deposition of Te from Te_2^{2-} and TeO_3^{2-} , then Te_2^{2-} accumulated near Te, which was confirmed by the color of solution change from no color to purple – the color of Te_2^{2-} [64]. Consequently, the secondary nucleation was inhibited leading to the formation nanowire at pH of 14.70.

2.5 Conclusions

In summary, this work demonstrated Te hetero-structures, including 1D and 3D nanostructures, were synthesized by galvanic displacement reaction in an alkaline bath

using zinc foil as sacrificial material. Single crystal Te nanowires were synthesized at TeO_3^{2-} concentration of 2 mM, as shown in HRTEM results. The diameter of Te nanowires were controlled from 200 ± 94 nm to 49 ± 23 nm by reducing temperature from 50 ^oC to 4 ^oC, revealed by SEM results. The morphology of the Te nanostructures were successfully modulated from nanowire to branched structures through varying the TeO_3^{2-} concentration from 2 to 10 mM, while fixing pH at 13.12. The diameter of the branches were thickened as TeO_3^{2-} concentration increasing up to 550 mM. The HRTEM images of branched structure showed that the branches and the trunk had the same growth direction (i.e. [001]). The morphology were tuned from nanowires to branched structures as pH reduced from 14.70 to 13.12, while fixing the TeO_3^{2-} concentration at 10 mM. The diameter of branches decreased from 248 ± 115 nm to 103 ± 30 nm, the length of branches decreased from 2797 ± 476 nm to 780 ± 199 nm, and aspect ratio of branches decreased from 10.1 ± 4.2 to 6.3 ± 2.4 by controlling the pH from 13.12 to 12.01, according to SEM images. The electrochemical analysis together with the SEM and TEM results indicated that the transition from nanowires to branched structure was attributed to secondary nucleation at high Te reduction rate and sufficient Te source.

2.6 References

1. Bang, J.H. and K.S. Suslick, *Applications of Ultrasound to the Synthesis of Nanostructured Materials.* Advanced Materials, 2010. **22**(10): p. 1039-1059.
2. Xia, Y., et al., *One-Dimensional Nanostructures: Synthesis, Characterization, and Applications.* Advanced Materials, 2003. **15**(5): p. 353-389.
3. Zečević, J., K.P. de Jong, and P.E. de Jongh, *Progress in electron tomography to assess the 3D nanostructure of catalysts.* Current Opinion in Solid State and Materials Science, 2013. **17**(3): p. 115-125.

4. Lee, T.I., et al., *High-Power Density Piezoelectric Energy Harvesting Using Radially Strained Ultrathin Trigonal Tellurium Nanowire Assembly.* Advanced Materials, 2013. **25**(21): p. 2920-2925.

5. Liu, J.-W., et al., *Rapid Microwave-Assisted Synthesis of Uniform Ultralong Te Nanowires, Optical Property, and Chemical Stability.* Langmuir, 2010. **26**(13): p. 11372-11377.

6. Diedenhofen, S.L., et al., *Broad-band and Omnidirectional Antireflection Coatings Based on Semiconductor Nanorods.* Advanced Materials, 2009. **21**(9): p. 973-978.

7. Chao, Y.-C., et al., *Light scattering by nanostructured anti-reflection coatings.* Energy & Environmental Science, 2011. **4**(9): p. 3436-3441.

8. Yan, C., C.M. Raghavan, and D.J. Kang, *Photocatalytic properties of shape-controlled ultra-long elemental Te nanowires synthesized via a facile hydrothermal method.* Materials Letters, 2014. **116**(0): p. 341-344.

9. Cho, I.S., et al., *Branched TiO2 Nanorods for Photoelectrochemical Hydrogen Production.* Nano Letters, 2011. **11**(11): p. 4978-4984.

10. Hippel, A.v., *Structure and Conductivity in the VIb Group of the Periodic System* Journal of Chemical Physics, 1948. **16**: p. 372-380.

11. Li, X.-L., et al., *Synthesis and magnetoresistance measurement of tellurium microtubes.* Journal of Materials Chemistry, 2003. **14**(2): p. 244-247.

12. Mohanty, P., et al., *Synthesis of Single Crystalline Tellurium Nanotubes with Triangular and Hexagonal Cross Sections.* The Journal of Physical Chemistry B, 2006. **110**(2): p. 791-795.

13. Chen, H., et al., *The fabrication of Te nanowires with different orientations by vacuum vapor deposition.* Physics Letters A, 2007. **362**(1): p. 61-65.

14. Wang, Q., et al., *Fabrication and Growth Mechanism of Selenium and Tellurium Nanobelts through a Vacuum Vapor Deposition Route.* The Journal of Physical Chemistry C, 2007. **111**(35): p. 12926-12932.

15. Sen, S., et al., *Synthesis of Tellurium Nanostructures by Physical Vapor Deposition and Their Growth Mechanism.* Crystal Growth & Design, 2008. **8**(1): p. 238-242.

16. Siciliano, T., et al., *Tellurium microtubes synthesized by thermal evaporation method.* Crystal Research and Technology, 2011. **46**(8): p. 765-768.

17. Parsafar, N. and A. Ebrahimzad, *The effect of substrate temperature on fabrication of one-dimensional nanostructures of tellurium.* Int.J.Nano Dim., 2012. **2**(3): p. 177-183.

18. Hawley, C.J., et al., *Shape-Controlled Vapor-Transport Growth of Tellurium Nanowires.* Crystal Growth & Design, 2012. **12**(6): p. 2789-2793.

19. Geng, B., et al., *Large-scale synthesis of single-crystalline Te nanobelts by a low-temperature chemical vapour deposition route.* Nanotechnology, 2003. **14**(9): p. 983.

20. Mo, M., et al., *Controlled Hydrothermal Synthesis of Thin Single-Crystal Tellurium Nanobelts and Nanotubes.* Advanced Materials, 2002. **14**(22): p. 1658-1662.

21. Liu, Z., et al., *Shape-controlled synthesis and growth mechanism of one-dimensional nanostructures of trigonal tellurium.* New Journal of Chemistry, 2003. **27**(12): p. 1748-1752.

22. Xu, L., et al., *Large-scale Synthesis of Crystalline Tellurium Nanowires with Controlled-Diameters via a Hydrothermal-reduction Process.* Chemistry Letters, 2004. **33**(5): p. 592-593.

23. Liu, Z., et al., *Size-Controlled Synthesis and Growth Mechanism of Monodisperse Tellurium Nanorods by a Surfactant-Assisted Method.* Langmuir, 2004. **20**(1): p. 214-218.

24. Lu, Q., F. Gao, and S. Komarneni, *Biomolecule-Assisted Reduction in the Synthesis of Single-Crystalline Tellurium Nanowires.* Advanced Materials, 2004. **16**(18): p. 1629-1632.

25. Lu, Q., F. Gao, and S. Komarneni, *A Green Chemical Approach to the Synthesis of Tellurium Nanowires.* Langmuir, 2005. **21**(13): p. 6002-6005.

26. Zhu, Y.-J., H. Xian-Luo, and W. Wei-Wei, *Poly(vinylpyrrolidone): a new reductant for preparation of tellurium nanorods, nanowires, and tubes from TeO 2.* Nanotechnology, 2006. **17**(3): p. 645.

27. Qian, H.-S., et al., *Synthesis of Uniform Te@Carbon-Rich Composite Nanocables with Photoluminescence Properties and Carbonaceous Nanofibers by the Hydrothermal Carbonization of Glucose.* Chemistry of Materials, 2006. **18**(8): p. 2102-2108.

28. Qian, H.-S., et al., *High-Quality Luminescent Tellurium Nanowires of Several Nanometers in Diameter and High Aspect Ratio Synthesized by a Poly (Vinyl Pyrrolidone)-Assisted Hydrothermal Process.* Langmuir, 2006. **22**(8): p. 3830-3835.

29. Xu, W., et al., *Structural, Electrical, and Photoconductive Properties of Individual Single-Crystalline Tellurium Nanotubes Synthesized by a Chemical Route: Doping Effects on Electrical Structure.* Small, 2008. **4**(7): p. 888-893.

30. Liang, F. and H. Qian, *Synthesis of tellurium nanowires and their transport property.* Materials Chemistry and Physics, 2009. **113**(2): p. 523-526.

31. Wang, Z., et al., *Formation of single-crystal tellurium nanowires and nanotubes via hydrothermal recrystallization and their gas sensing properties at room temperature.* Journal of Materials Chemistry, 2010. **20**(12): p. 2457-2463.

32. Zhu, H., et al., *Controlled Synthesis of Tellurium Nanostructures from Nanotubes to Nanorods and Nanowires and Their Template Applications.* The Journal of Physical Chemistry C, 2011. **115**(14): p. 6375-6380.

33. Zhu, H., et al., *Controlled hydrothermal synthesis of tri-wing tellurium nanoribbons and their template reaction.* CrystEngComm, 2012. **14**(1): p. 251-255.

34. Wei, G., et al., *Solvothermal synthesis of porous tellurium nanotubes.* Chemical Physics Letters, 2003. **372**(3): p. 590-594.

35. Song, J.-M., et al., *Superlong High-Quality Tellurium Nanotubes: Synthesis, Characterization, and Optical Property.* Crystal Growth & Design, 2008. **8**(6): p. 1902-1908.

36. Wang, S., et al., *Synthesis, characterization and optical properties of flower-like tellurium.* CrystEngComm, 2010. **12**(1): p. 166-171.

37. Wu, X., et al., *Controlled synthesis of multi-morphology Te crystals by a convenient Lewis acid/base-assisted solvothermal method.* Journal of Nanoparticle Research, 2012. **14**(8): p. 1-10.

38. Mayers, B. and Y. Xia, *Formation of Tellurium Nanotubes Through Concentration Depletion at the Surfaces of Seeds.* Advanced Materials, 2002. **14**(4): p. 279-282.

39. Zhu, Y. and X. Hu, *tellurium nanorods and nanowires prepared by the microwave-polyol method.* Chemistry Letters, 2004. **33**.

40. Zhu, W., et al., *Controllable, Surfactant-Free Growth of 2D, Scroll-Like Tellurium Nanocrystals via a Modified Polyol Process.* Crystal Growth & Design, 2006. **6**(12): p. 2804-2808.

41. Zhou, B., et al., *A novel ultrasonic-assisted solution-phase approach for the fabrication of tellurium bundles of nanowhiskers.* Ultrasonics Sonochemistry, 2006. **13**(4): p. 352-358.

42. Zhu, Y.-J., et al., *Microwave-Assisted Synthesis of Single-Crystalline Tellurium Nanorods and Nanowires in Ionic Liquids.* Angewandte Chemie International Edition, 2004. **43**(11): p. 1410-1414.

43. Zhang, B., et al., *1D Tellurium Nanostructures: Photothermally Assisted Morphology-Controlled Synthesis and Applications in Preparing Functional Nanoscale Materials.* Advanced Functional Materials, 2007. **17**(3): p. 486-492.

44. Liu, Z., et al., *Surfactant-assisted growth of uniform nanorods of crystalline tellurium.* Journal of Materials Chemistry, 2003. **13**(1): p. 159-162.

45. Zheng, R., et al., *Synthesis of tellurium nanorods via spontaneous oxidation of NaHTe at room temperature.* Chemical Physics Letters, 2004. **395**: p. 302-305.

46. Gautam, U.K. and C.N.R. Rao, *Controlled synthesis of crystalline tellurium nanorods, nanowires, nanobelts and related structures by a self-seeding solution process.* Journal of Materials Chemistry, 2004. **14**(16): p. 2530-2535.

47. He, Z., S.-H. Yu, and J. Zhu, *Amino Acids Controlled Growth of Shuttle-Like Scrolled Tellurium Nanotubes and Nanowires with Sharp Tips.* Chemistry of Materials, 2005. **17**(11): p. 2785-2788.

48. F.Gao, Q. Lu, and S. Komarneni, *Gluconate controls one-dimensional growth of tellurium nanostructures.* Journal of Materials Research, 2006. **21**(02): p. 343-348.

49. Wang, S., et al., *Large-scale synthesis of feather-like single-crystal Te via a biphasic interfacial reaction route.* CrystEngComm, 2010. **12**(11): p. 3852-3857.

50. Shen, J.-M., et al., *Construction of Unconventional Hexapod-like Tellurium Nanostructure with Morphology-Dependent Photoluminescence Property.* The Journal of Physical Chemistry C, 2009. **113**(22): p. 9502-9508.

51. Zhao, A.W., et al., *Tellurium nanowire arrays synthesized by electrochemical and electrophoretic deposition.* Journal of Materials Research, 2003. **18**: p. 2318-2322.

52. She, G., et al., *Template-Free Electrodeposition of One-Dimensional Nanostructures of Tellurium.* Crystal Growth & Design, 2009. **9**(2): p. 663-666.

53. Wang, X. and Y. Ni, *A facile electrochemical route for fast deposition of featherlike tellurium microstructures.* RSC Advances, 2011. **2**: p. 2340-2345.

54. Park, H., et al., *Branched tellurium hollow nanofibers by galvanic displacement reaction and their sensing performance toward nitrogen dioxide.* Nanoscale, 2013. **5**(7): p. 3058-3062.

55. Zhang, M., et al., *A Rapid Room-Temperature NO2 Sensor Based on Tellurium–SWNT Hybrid Nanostructures.* The Journal of Physical Chemistry C, 2012. **116**(37): p. 20067-20074.

56. Pourbaix, M., *Atlas of electrochemical equilibria in aqueous solutions*1966, Long Island City, N.Y.: Pergamon Press Inc.

57. Jamieson, R.A. and S.P. Perone, *Polarographic, coulometric, and stationary electrode studies of the electroreduction of Te(IV) in alkaline solution.* Journal of Electroanalytical Chemistry and Interfacial Electrochemistry, 1969. **23**(3): p. 441-455.

58. Sarala, Y. and S. Jayarama Reddy, *Electrochemical reduction of tellurium(IV).* Journal of Electroanalytical Chemistry and Interfacial Electrochemistry, 1986. **214**(1–2): p. 179-190.

59. Barbier, M.-J., A.-M. De Becdelievre, and J. De Becdelievre, *Electrochemical study of tellurium oxido-reduction in aqueous solutions.* Journal of Electroanalytical Chemistry and Interfacial Electrochemistry, 1978. **94**(1): p. 47-57.

60. Shinagawa, M., N. Yano, and T. Kurosu, *Mechanism and analytical aspects of the polarographic maximum wave of tellurium.* Talanta, 1972. **19**(4): p. 439-450.

61. Shinagawa, M., et al., *Studies on the prewave of tellurium and its photo-effect.* Journal of Electroanalytical Chemistry and Interfacial Electrochemistry, 1977. **75**(2): p. 809-817.

62. Bockris, J.O.M., *Recent Developments in the Study of Hydrogen Overpotential.* Chemical Reviews, 1948. **43**(3): p. 525-577.

63. Sounart, T.L., et al., *Secondary Nucleation and Growth of ZnO.* Journal of the American Chemical Society, 2007. **129**(51): p. 15786-15793.

64. Mishra, K.K., D. Ham, and K. Rajeshwar, *Anodic Oxidation of Telluride Ions in Aqueous Base: A Rotating Ring‐Disk Electrode Study.* Journal of The Electrochemical Society, 1990. **137**(11): p. 3438-3441.

65. Panson, A.J., *POLAROGRAPHY OF THE DITELLURIDE ION.* The Journal of Physical Chemistry, 1963. **67**(10): p. 2177-2180.

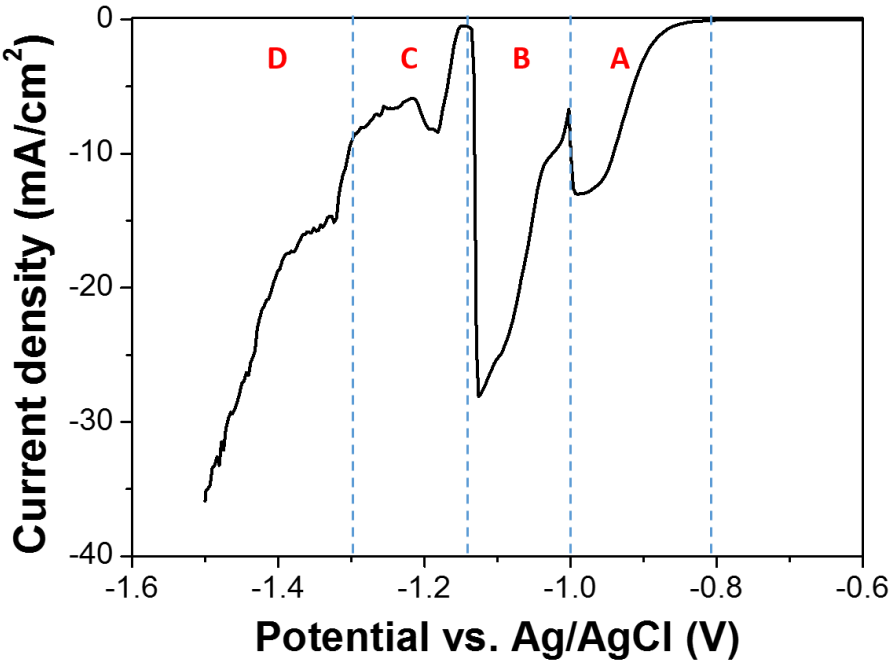

Figure 2.1 LSV of Te deposition on Pt substrate with TeO_3^{2-} concentrations of 100mM, pH of 13.12 at 23°C. The scan rate was 1mV/s. A, B, C, and D indicate different Te reduction regions.

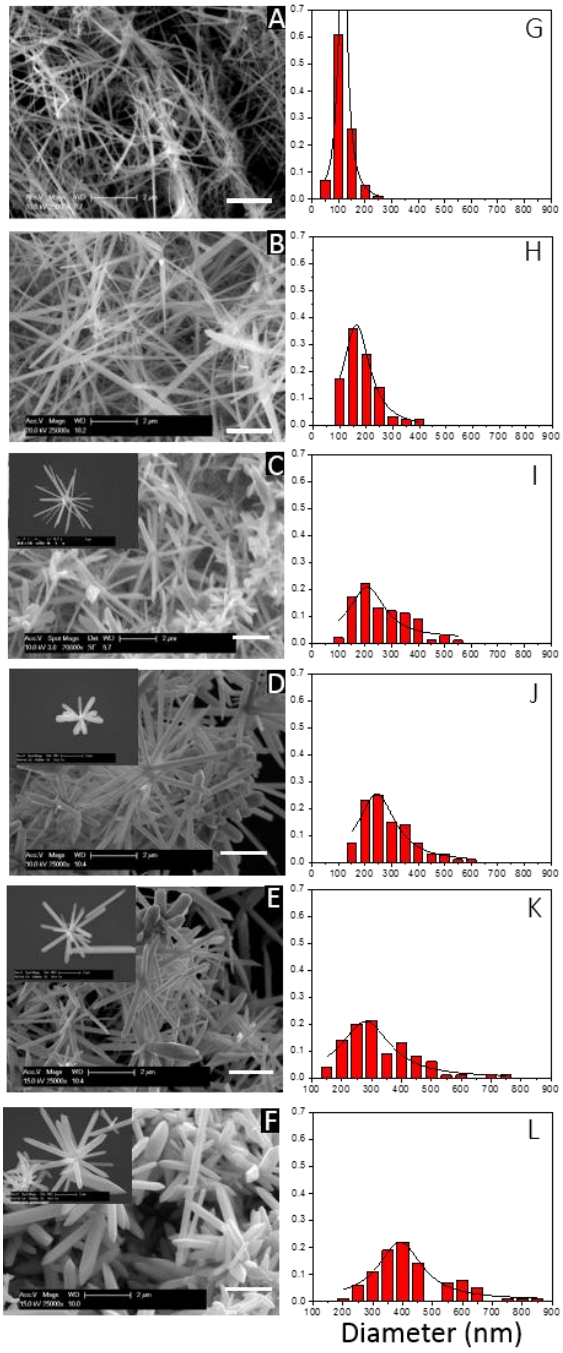

Figure 2.2 SEM image of Te nanostructures synthesized at different TeO_3^{2-} concentrations: (A)2, (B)3, (C)10, (D)50, (E)100, (F)550 mM, with pH of 13.12, reaction time of 30 min at 23 ^oC. Diameter distribution of Te nanostructures synthesized at different TeO_3^{2-} concentrations: (G)2, (H)3, (I)10, (J)50, (K)100, (L)550 mM, the black curves are Lorentz fit according to the diameter distribution. All scale bars in (A-F) are 2 μm. The inset images in (C-F) are the SEM images of the dispersed sample.

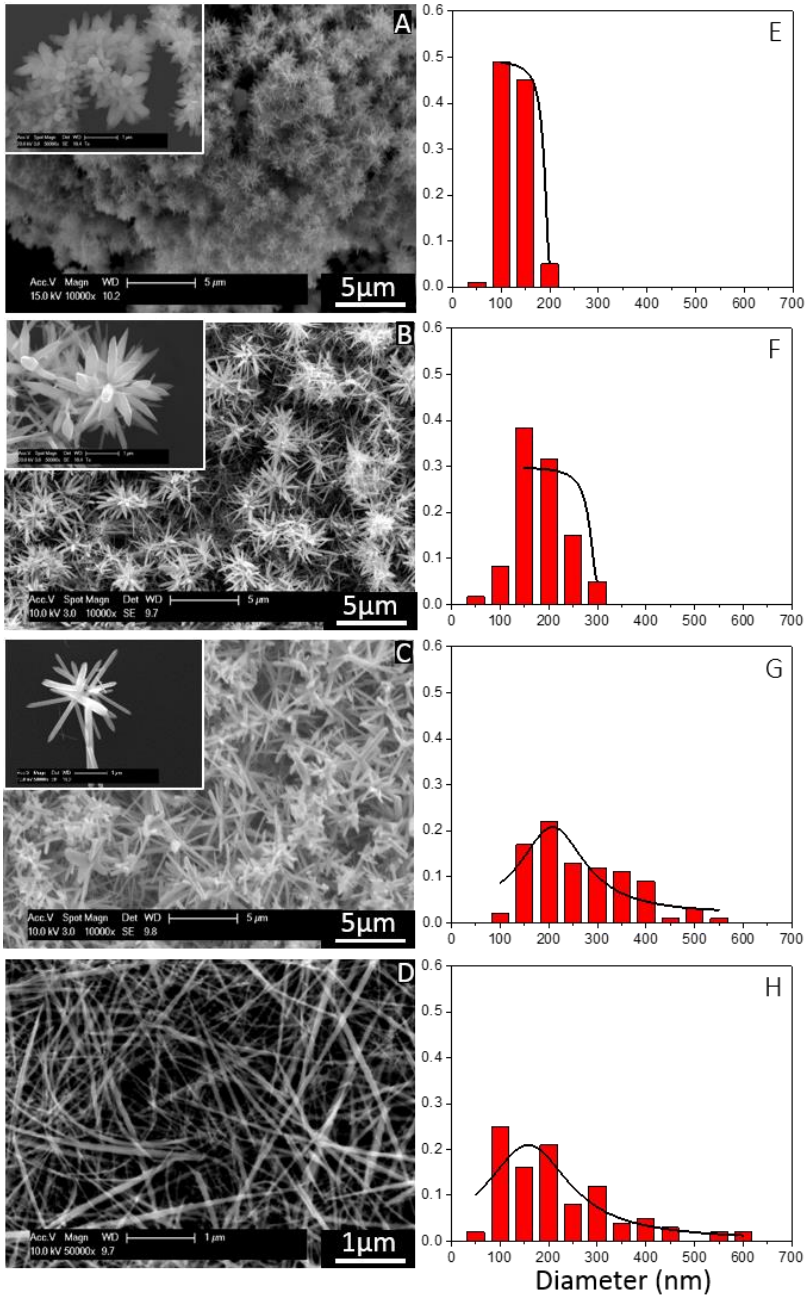

Figure 2.3 SEM image of Te nanostructure synthesized at different pH: (A)12.01, (B)12.21, (C)13.12, (D)14.70(Calculated value). Diameter distribution of Te nanostructure synthesized at different pH: (E)12.01, (F)12.21, (G)13.12, (H)14.70(Calculated value), the black curves are Lorentz fit according to the diameter distribution. TeO_3^{2-} concentration is fixed at 10 mM. Reaction time was 30 min, reaction temperature was room temperature (23 ^oC). The inset images in (A-C) are the SEM images of dispersed samples.

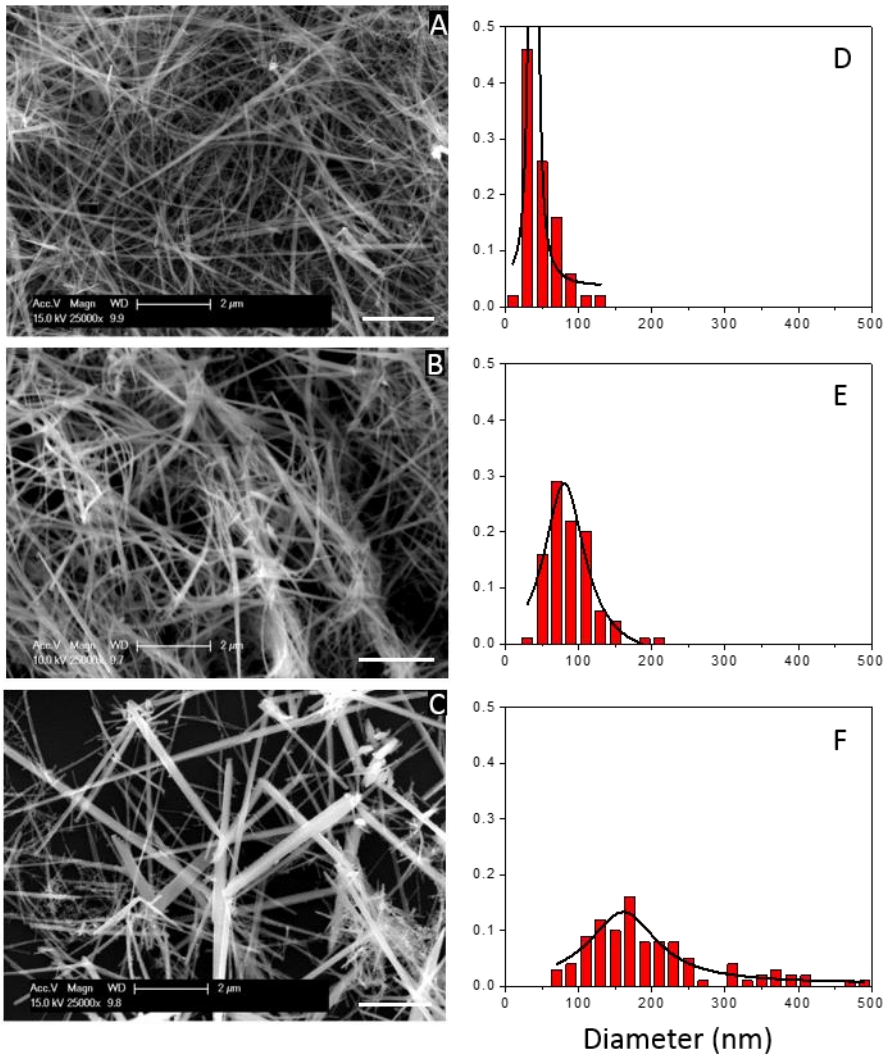

Figure 2.4 SEM images of Te nanostructure synthesized at different temperature: (A)4, (B)23, (C)50 ^{o}C. Diameter distribution of Te nanostructure synthesized at different temperature: (D)4, (E)23, (F)50 ^{o}C, the black curves are Lorentz fit according to the diameter distribution. TeO_3^{2-} concentration and pH were fixed at 2 mM and 13.12, respectively. Reaction time was 30 min.

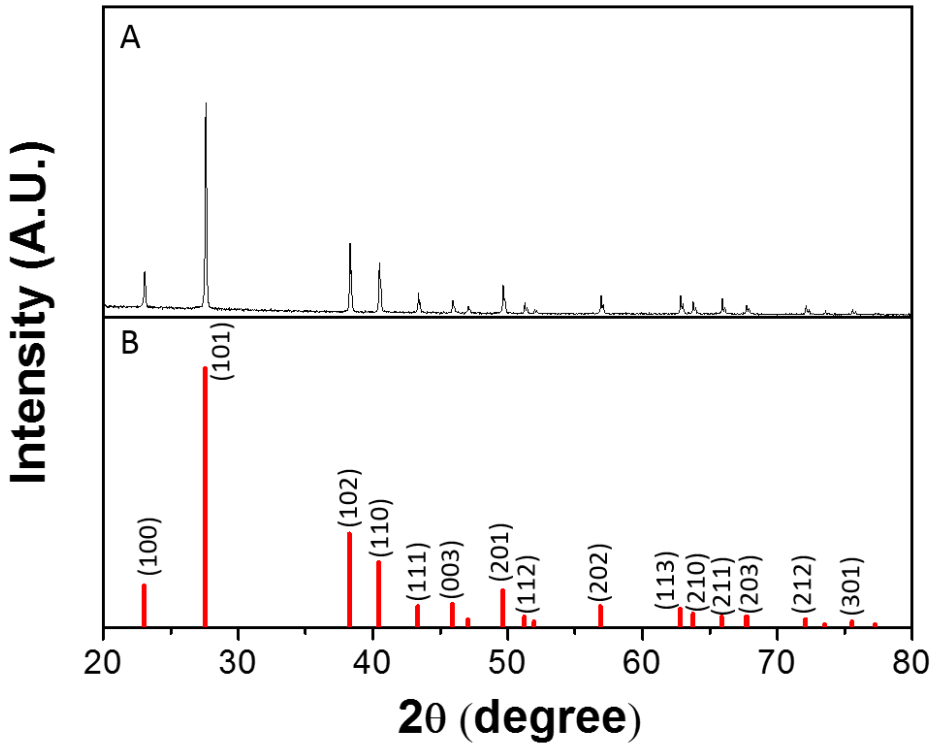

Figure 2.5 (A) The powder XRD pattern of Te nanostructure synthesized with TeO_3^{2-} concentration of 550mM TeO_3^{2-}, pH of 13.12. Reaction time was 30 min, reaction temperature was 23 ^{o}C. (B) Reference XRD pattern of Te (JCPDS, No. 36-1452).

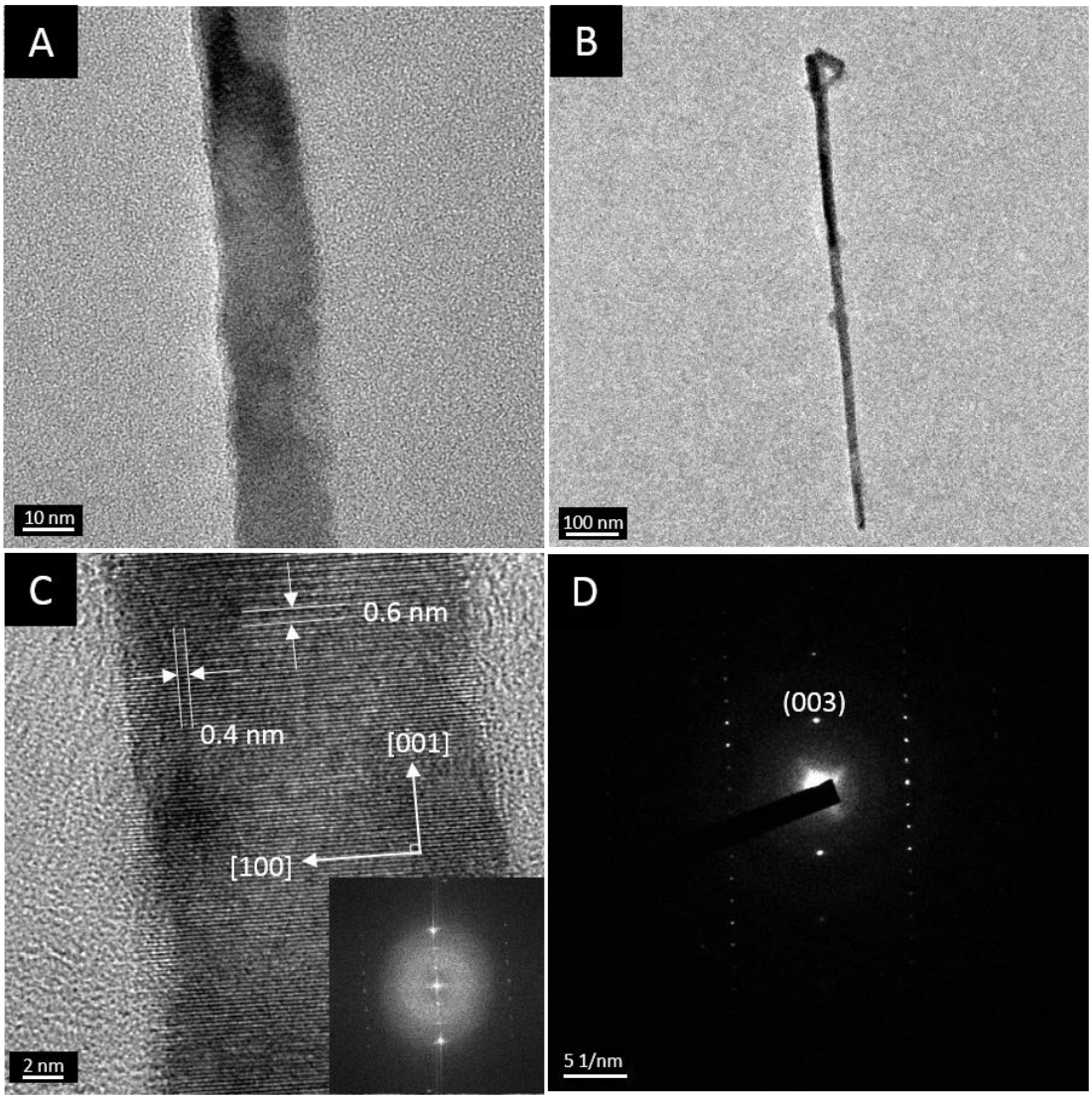

Figure 2.6 (A), (B) TEM images of the Te nanowire at high and low magnification. (C) HRTEM image and (D) SAED patterns of the Te nanowire, which was synthesized at 4ºC with TeO_3^{2-} concentration of 2 mM and pH of 13.12 as shown in figure 2.4(A).

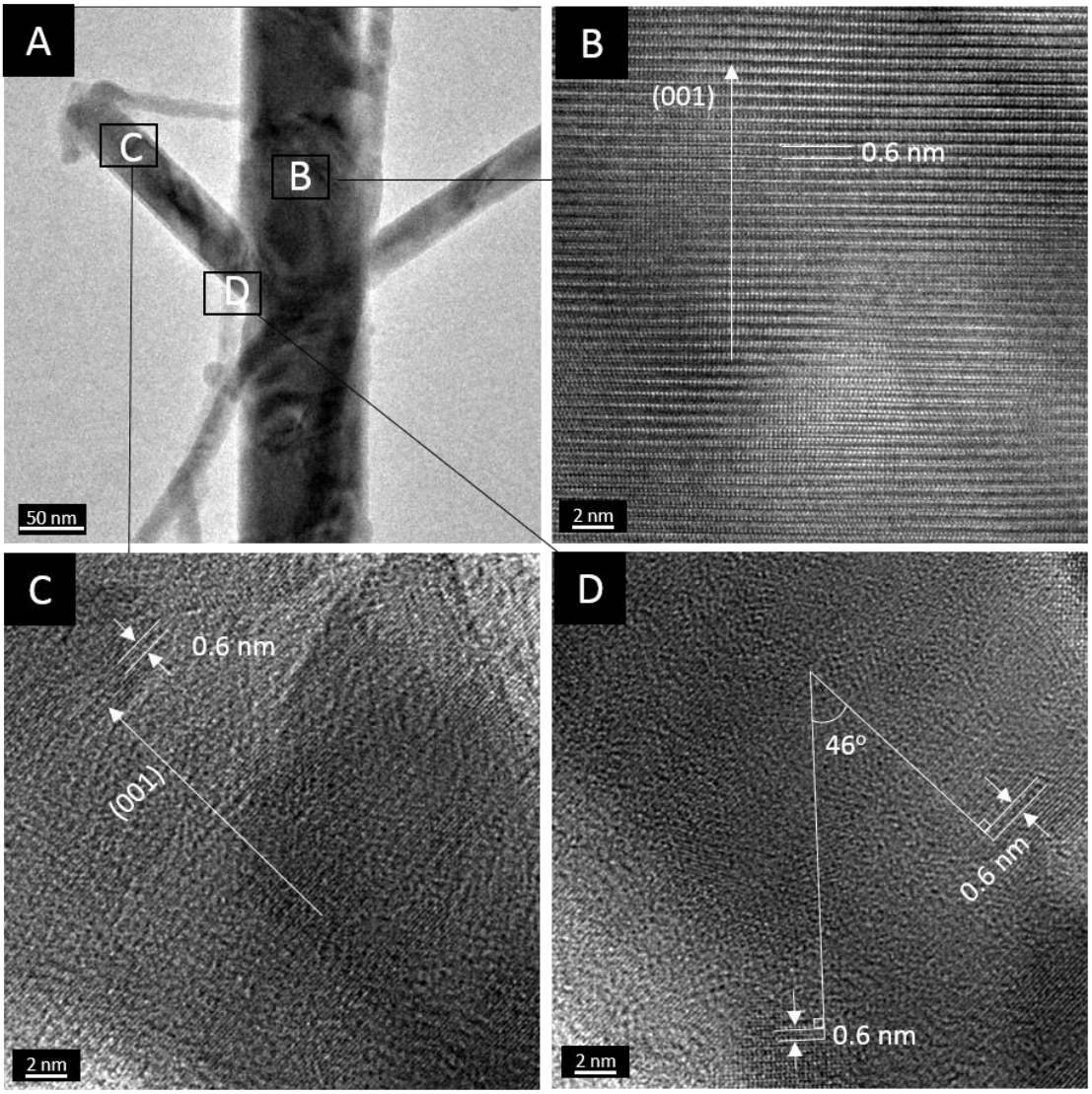

Figure 2.7 (A) TEM image of Te branched structure. (B,C,D) HRTEM images recorded from the marked area in (A). The sample is synthesized at 23°C with TeO_3^{2-} concentration of 10 mM and pH of 12.21 as shown in figure 2.3B.

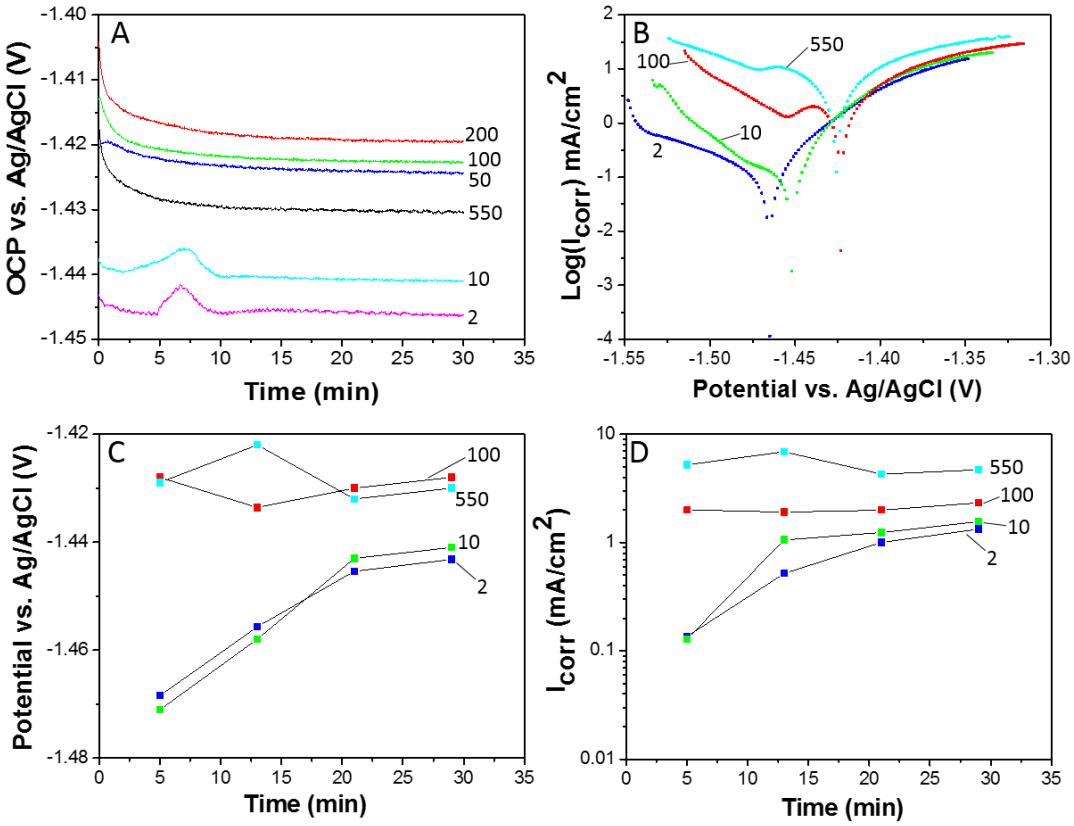

Figure 2.8 (A) Open-circuit potential of GDR at different TeO_3^{2-} concentrations: 2, 10, 50, 100, 200, and 550mM. (B) Tafel plot from the first cycle of LP at 5 minutes, (C) corrosion potential, and (D) corrosion current of GDR at different TeO_3^{2-} concentrations: 2, 10, 100, and 550 mM with pH of 13.12. Reaction temperature was 23ºC. TeO_3^{2-} concentration is marked in the figure with a unit of mM.

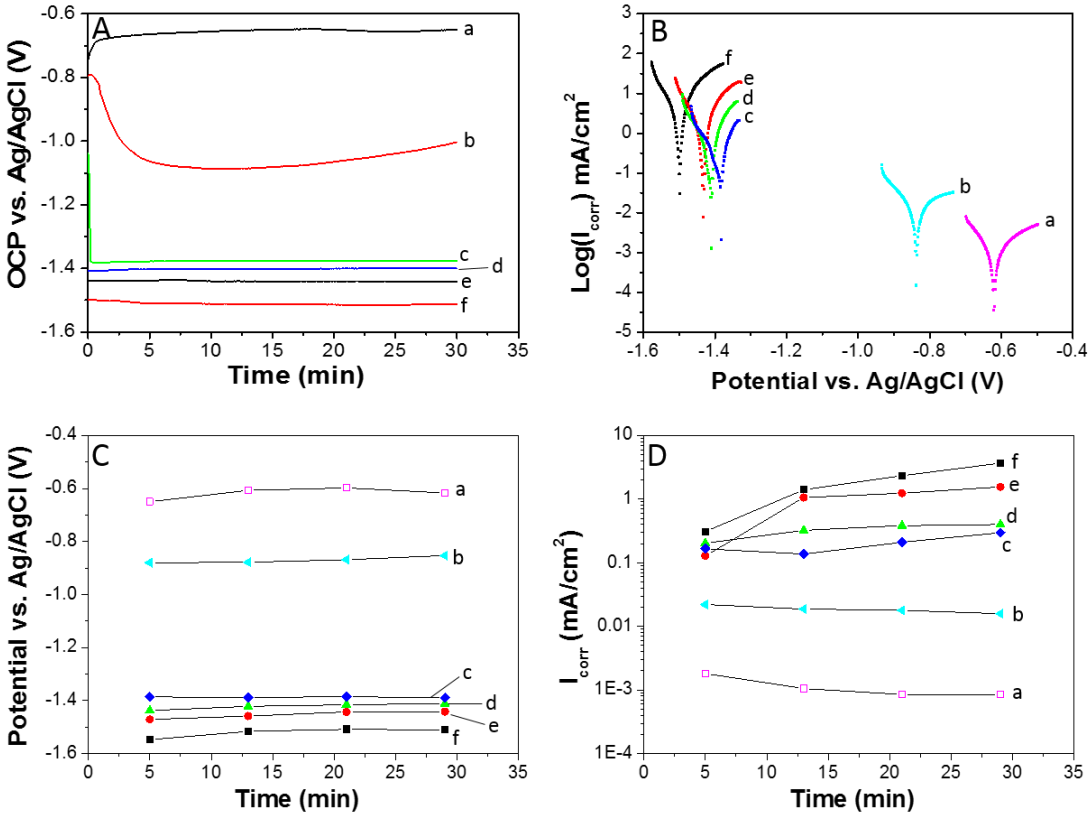

Figure 2.9 (A) Open-circuit potential, (B) Tafel plot from the first cycle of LP at 5 minutes, (C) corrosion potential, and (D) corrosion current of GDR at different pH: (a)12.44, (b)12.60, (c)12.61, (d)12.94, (e)13.12, (f)14.70(calculated value) as marked in the figure. TeO_3^{2-} concentration was fixed at 13.12. Reaction temperature was 23ºC.

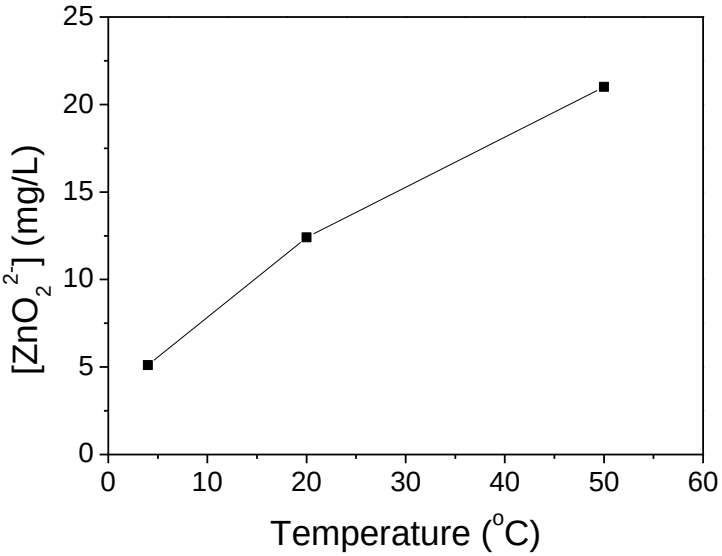

Figure 2.10 The concentration of dissolved Zn in the solution after the galvanic displacement reaction at different reaction temperature: 4, 23, 50 ^{o}C.

3 Size Controlled Synthesis of Tellurium Nanorices by Galvanic Displacement Reaction of Aluminum

3.1 Abstract

"Rice-like" tellurium nanostructures were synthesized by galvanic displacement reaction (GDR) of aluminum in an alkaline solution containing TeO_3^{2-} ions for the first time. Due to negative redox potential of Al/AlO_2^- (*i.e.*, -2.50 V vs. sat. Ag/AgCl), TeO_3^{2-} (+IV) can be reduced to Te_2^{2-} (-I) and Te^{2-} (-II), which resulted in the deposition of Te (0) nanostructures in the solution via chemical reaction between Te_2^{2-} or Te^{2-} and TeO_3^{2-}. The deposition mechanism led to the formation of unique "rice-like" nanostructures in the solution instead of branched structures on the substrate. The sharp tips of the "rice-like" nanostructures may be attributed to the high density of surface charges at the tips. The morphology, diameter and aspect ratio of Te "rice-like" nanostructures were altered by the TeO_3^{2-} concentration, solution pH, reaction time and the reaction temperature. Electrochemical analytical methods, including open circuit potential (OCP) and linear polarizations (LPs), were used to investigate the reaction mechanisms.

3.2 Introduction

Significant efforts have been recently devoted to synthesize various nanomaterials with precisely controlled morphology and dimensions to tune their unique size and shape-dependent properties.[1] To optimize their electrical, thermal, and mechanical behavior and thereby the device's overall performance, it is essential to adjust the morphology, size and crystal structure of these nanomaterials.[2, 3] For example, the greater sensitivity of a

surface plasmon resonance nanosensor can best be achieved by a "rice-like" nanostructures geometry than by any other nanostructure. [4, 5] Specifically, its performance depends on the length and aspect ratio of the nanorice. [4, 6]

Trigonal-Tellurium (t-Te) is a p-type semiconductor with a narrow band-gap energy of 0.35 eV at room temperature. Its unique crystal structure, helical conformation and lack of centro-symmetry[7], leads to many unique physical properties including high photoconductivity, piezoelectric effect, and catalytic activity. [8-12] Several reaction mechanisms have been utilized to synthesize Te nanostructures. For instance, Te powder was used as a precursor and was recrystallized via solution phase based method [13-18] and physical vapor deposition [19-26]. Te (+IV) was the most commonly used precursor to synthesize Te nanostructures via disproportionation [27, 28] or reduction. In the case of reduction, Te (+IV) was reduced by reductant such as hydrazine [26, 29-35], glucose [36], sodium sulfite [37, 38], polyvinylpyrrolidone [39], ethylene glycol [40-44], 2,2'-dithiodibenzoic acid [45], alginic acid [46, 47], ascorbic acid [47], sodium borohydride [48], and sodium hypophosphite [49, 50] to synthesize Te nanostructures with or without surfactant. Te(+VI) was also used as a precursor and reduced by reductant such as formamide [51], starch [52] ethylene glycol [53], and sodium gluconate [54] to form Te (0) nanostructures. Additionally, Te in the valence state of -II was also utilized to synthesize Te nanostructures via chemical vapor deposition [55] and amino acid controlled methods [56]. However, the reaction mechanism of Te (+IV) interacting with Te_2^{2-} (-I) or Te^{2-} (-II) to form Te (0) nanostructure so far was seldom reported.

GDR is an electrochemical process driven by the difference in redox potentials between the solid substrate and the ions of the source materials, leading to deposition of the more noble material at the expense of the less noble material. Due to the ease of fabrication, GDR is an ideal method to synthesize various nanostructures with controlled morphology and dimensions. Various tellurium and metal tellurides have been synthesized by GDR in acidic media by our group to demonstrate its feasibility of creating unique nanostructures. [57-65] Although, acidic bath is an excellent solution to perform the GDR reaction, the low solubility of TeO_3^{2-} limited reaction rate and morphology. Unlike acidic baths, Te (+IV) dissolves readily in an alkaline bath with a high solubility (*e.g*, 87.8 g/L at pH of 10.5). The higher solubility of Te (+IV) in alkaline baths augments the deposition range providing greater flexibility to control the deposit's morphology. In our previous work, we demonstrated the ability to synthesize Te nanowires and branched nanowires by utilizing zinc as sacrificial material. [66] The Zn provided negative redox potential, but the synthesized Te nanostructures were well attached to the surface of the Zn foil which indicated that the deposition of Te mainly took place on the electrode surface, and the dominant reaction was the reduction of TeO_3^{2-} (+IV) to Te (0).[66]

In this work, Te "rice-like" nanostructures with controlled sizes were synthesized by galvanic displacement reaction using aluminum foils as a sacrificial material in alkaline baths. Aluminum was selected for the similar three reasons as Zn foil; namely, the low redox potential of the Al/AlO_2^- , its ability to form water soluble products (*i.e.*, AlO_2^-) in alkaline baths, and low material cost. However, the redox potential of Al/AlO_2^- (E^o = -2.50 V vs. sat. Ag/AgCl), which is 1.20 V more negative than the Zn/ZnO_2^{2-} (E^o = -1.30 vs.

Ag/AgCl). Therefore, Al/AlO_2^- provides much greater thermodynamic driving force to further reduced the Te (0) to Te_2^{2-} (-I) or further reduced Te_2^{2-} (-I) to Te^{2-} (-II) where both Te_2^{2-} (-I) to Te^{2-} (-II) are water soluble species. Under this circumstance, the dominant synthesis of Te nanostructures in the solution via chemical reaction between Te_2^{2-} or Te^{2-} and TeO_3^{2-} is expected, which is a different deposition mechanism compared to Zn foil as sacrificial materials leading to the formation of different Te nanostructures on the surface of sacrificial materials. The physical dimensions of the resulting Te nanostructures were systematically studied as a function of TeO_3^{2-} concentration, pH, reaction time, and reaction temperature of the electrolyte. The reaction driving forces and reaction rates of the GDR were investigated by the electrochemical analysis methods including OCP and LPs. A probable mechanism for the formation of Te nanostructures was proposed.

3.3 Experimental

All GDR solutions were prepared by dissolving various amounts of tellurium dioxide (TeO_2, 99+%, Acros Organics) in sodium hydroxide solutions (NaOH, 10 N, Fisher Chemical). The sacrificial material was aluminum foils (Al, 0.015 mm thick, 99.3%, MTI, corp.), cut into squares 0.8 cm on edge. Before reaction, the foils were cleaned with detergents, rinsed three times by nanopure water and acetone (Fisher Chemical), then air dried. The reactor (Figure 3.10) for all GDRs was a two piece Teflon cell with a fitted O-ring around an open area of 0.272 cm^2 squeezed together and securely sealed by screws. The Al foils were sandwiched and sealed between the O-ring and the Teflon sides. The GDRs were started by adding 0.5 mL of naturally aerated solution into the open area of the Teflon cell in contact with the Al foil and terminated by removing the solutions after a

specified time. Once the reaction was terminated, the sample was carefully collected by pipette, rinsed three times with nanopure water, and then dispersed in isopropanol (Fisher Chemical).

The electrochemical analysis methods, including OCP and LP, were used to investigate the reaction mechanism. Transient OCPs were measured in the same three-electrode Teflon cell as GDR for 30 minutes, with an Al foil, a saturated Ag/AgCl, and a Pt wire as the working, reference, and counter electrodes, respectively. LP characterizations were carried out in the same Teflon cell by sweeping the voltage from -0.1 V to + 0.1 V vs. open circuit potential at a scan rate of 1 mV/s.

The crystal structure of the "rice-like" Te nanostructures was examined by powder X-ray diffraction (XRD, PANalytical Empyrean) patterns and transmission electron microscopy (TEM, JEOL JEM-2100F). The morphology and size of the "rice-like" nanostructures were investigated via the field emission-scanning electron microscope (FE-SEM, FEG-Philips XL30).

3.4 Results and discussion

3.4.1 Synthesis and material characterization of Te "rice-like" nanostructures

Figure 3.1 A-D shows the SEM images of synthesized Te nanostructures by varying the TeO_3^{2-} concentration from 10 to 550 mM while fixing the solution pH at 13.1 and reaction temperature at 23 ^oC for 30 min. Although, the morphology of Te nanostructure did not change significantly, these images clearly show that the dimensions of synthesized Te "rice-like" nanostructures strongly depend on the concentration of TeO_3^{2-}. Specifically,

Figure 3.1 E shows that the diameter (*i.e.*, ranging from 121 nm to 573 nm), length (*i.e.*, ranging from 0.7 μm to 8.3 μm), and the aspect ratio (*i.e.*, ranging from 4.7 ± 1 to 8.3 ± 2.7) increased monotonically over the concentration range, but showing a rather flat response between 10 mM to 50 mM. The reason for the change in its size as a function of [TeO_3^{2-}] will be discussed in a later section of this paper along with the OCP and LP results.

The solution pH is another important factor that affects the growth of Te nanostructure. Figure 3.2 A-E shows SEM images of synthesized Te and their size distributions at solution pH of 10.9, 11.9, 13.1, 14.7 and 15.0 with a fixed [TeO_3^{2-}] of 10 mM at 23ºC for 30 min. At pH of 10.9, Te is amorphous. As shown in Figure 3.2 F, the average diameter (*i.e.*, 123 nm) were independent of pH from 11.9 to 13.1 then increased to 165 nm at pH=15; whereas, the average length increased linearly with solution pH. Figure 3.2 H shows the corresponding increase in aspect ratios ranging from 3.5 ± 1.1 to 6.8 ± 1.9 across the pH range. The solid state phase transformation from amorphous to crystallized Te nanostructures and the control of their dimensions will be discussed together with the OCP and LP results.

Figure 3.3 A-C shows SEM images of the Te "rice-like" nanostructures synthesized at temperatures 4, 23, and 50 ºC, at a fixed [TeO_3^{2-}] of 10 mM and pH of 13.1 for 30 min. "Rice-like" nanostructures were synthesized throughout the entire temperature range. Figure 3.3 D shows that their average diameter remained flat at about 120 nm; whereas, Figure 3.3 F shows that average length increased exponentially from 0.5 ± 0.2 μm to 1.0 ± 0.4 μm. Figure 3.3 G shows that the corresponding aspect ratios of "rice-like" nanostructures increased from 4.3 ± 0.6 to 7.0 ± 1.9.

The effect of the reaction time on the morphology and dimensions of Te nanostructure was investigated in 100 mM TeO_3^{2-} solution with pH of 14.7 and temperature of 23 ^oC. At the earliest stage studied at 10 minutes, the Te branched structures together with the Te "rice-like" nanostructures were formed (Figure 3.4A). Additionally, small crystal defects were observed on the surface of the Te branched structures. When the reaction time increase to 30 minutes, the number of branched structures reduced while the number of "rice-like" nanostructures increased. The diameter, length and aspect ratio of Te nanostructures increased as reaction time increased from 10 minutes to 30 minutes. By 90 minutes, only Te "rice-like" nanostructures were present. When the reaction time increased from 10 minutes to 30 minutes, the synthesized branched structure dissolved in the alkaline solution which provide soluble Te_2^{2-} (-I) ions to chemically deposit Te "rice-like" nanostructures in the solution. This provides the reason why at 30 minutes the number of branched structures decreased.

At [TeO_3^{2-}] of 550 mM (Figure 3.11), the Te nanostructure morphology changed as temperature increased. At 4 ^oC, 3D Te branched structures were observed (Figure 3.11 A). However, when the temperature increased to 23 ^oC, 1D Te "rice-like" nanostructures with every small amount of branched structures were obtained (Figure 3.11 B). When the temperature further increased to 50 ^oC, only "rice-like" nanostructures were formed.

Sahoo reported that the formation of selenium nanorods was a result of the breaking of the branched structure. [67] If the "rice-like" nanostructures are results of the breaking of branched structure, there would be only one sharp end and the other end of "rice-like" nanostructures should show the breaking edge. However, in our work the synthesized "rice-

like" nanostructures have two sharp ends which means that the nanostructure grew in both directions. As a consequence, the formation of "rice-like" nanostructures probably came from the chemical deposition of Te in the solution, which was confirmed by the observation that the synthesized nanostructures were suspended in the solution instead of attaching to the Al foil surface. Ozaki *et al.* [68] and He *et al.* [56] also reported the solution phase based synthesis of hematite particles and Te nanowire with sharp tips, respectively.

Several reasons may cause the formation of sharp tips. Zhu *et al.* synthesized the tri-wing tellurium nanoribbons via hydrothermal synthesis method and proposed that the sharp tip is ascribed to the effect of the surfactant. [50] Chen *et al.* fabricated the sharp-tipped Te nanowires via vacuum vapor deposition and suggested that the crystal growth was favored along a sharp tip direction because a sharp tip can efficiently reduce the energy of adsorbed atoms. [21] However, in our system there were no surfactants and the Te precursor was not neutral Te atoms, therefore these mechanisms do not apply. In our system, the formation of sharp tips was probably triggered because the absorbed Te ions varies with the location on the nanorice. Since the distribution of surface charge density is strongly dependent on the curvature of the nanorice, the highest surface charge density resides at the tip. [69] Since Te is a p-type semiconductor, the holes density at the tip is larger than other location on the "rice-like" nanostructures. This results in the higher surface electrostatic adhesion, which attracts more TeO_3^{2-}, Te_2^{2-} and Te^{2-} ions to the Te surface than other areas thus leading to the growth of sharp tips. The same mechanism was reported by Li *et al.* to synthesize ZnO nanotip arrays. [70]

The effect of dissolved O_2 reduction reaction on the morphology and dimensions of Te is shown in Figure 3.12. The results indicated that the dissolved O_2 in the solution did not influence the morphology and dimensions of Te nanostructure significantly. The average diameters of "rice-like" nanostructures before and after dissolved O_2 suppression were 439 ± 159 nm and 513 ± 117 nm. The average length before and after dissolved O_2 suppression were 2.8 ± 1.1 μm and 2.4 ± 0.3 μm. The average aspect ratio before and after dissolved O_2 suppression were 5.6 ± 1.3 and 4.8 ± 0.9. However, the OCP and LP results were affected by the dissolved O_2 (Figure 3.13).

The Te "rice-like" nanostructures synthesized from the solution containing 100 mM TeO_3^{2-} with a pH of 13.1 at 23 ^oC were characterized by X-ray diffraction. Figure 3.5 shows that the Te "rice-like" nanostructures are well-crystallized trigonal Te. All the diffraction peaks can be indexed as a trigonal-Te phase with calculated lattice constant a = 4.4531 Å and c = 5.9265 Å, which are consistent with the standard literature values (JCPDS-International Center for Diffraction Data, No. 36-1452).

The HRTEM image in Figure 3.6C was taken of the "rice-like" nanostructures in Figure 3.3B. The image shows a lattice spacing of ca. 0.40 nm and 0.59 nm, corresponding to a lattice spacing of the (1 0 0) plane and (0 0 1) plane for trigonal Te, respectively. Figure 3.6D shows the SAED pattern of the "rice-like" nanostructures. The HRTEM image and the SAED pattern revealed that the Te "rice-like" nanostructures was single crystalline and grew along the [001] direction.

3.4.2 Electrochemical behavior of GDR

The possible electrochemical and chemical reaction of Te and Al in aqueous solution are listed below.

$TeO_3^{2-}(aq) + 3H_2O(l) + 4e^- \rightarrow Te(s) + 6OH^-(aq)$

(E_0 = - 0.45 V vs. Ag/AgCl) Reaction 3.1

$2TeO_3^{2-}(aq) + 6H_2O(l) + 10e^- \rightarrow Te_2^{2-}(aq) + 12OH^-(aq)$

(E_0 = - 0.65 V vs. Ag/AgCl) Reaction 3.2

$2Te(s) + 2e^- \rightarrow Te_2^{2-}(aq)$

(E_0 = -0.91 V vs. Ag/AgCl) Reaction 3.3

$TeO_3^{2-}(aq) + 3H_2O(l) + 6e^- \rightarrow Te^{2-}(aq) + 6OH^-(aq)$

(E_0 = - 1.00 V vs. Ag/AgCl) Reaction 3.4

$Te(s) + 2e^- \rightarrow Te^{2-}(aq)$

(E_0 = -1.34 V vs. Ag/AgCl) Reaction 3.5

$Te_2^{2-}(aq) + 2e^- \rightarrow 2Te^{2-}(aq)$

(E_0 = -1.47 V vs. Ag/AgCl) Reaction 3.6

$Te(s) + Te^{2-}(aq) \rightarrow Te_2^{2-}(aq)$

(ΔG^O = - 58.6 kJ/mol) Reaction 3.7

$TeO_3^{2-}(aq) + 2Te_2^{2-}(aq) + 3H_2O(l) \rightarrow 5Te(s) + 6OH^-(aq)$

(ΔG^O = - 164.1 kJ/mol) Reaction 3.8

$TeO_3^{2-}(aq) + 2Te^{2-}(aq) + 3H_2O(l) \rightarrow 3Te(s) + 6OH^-(aq)$

(ΔG^O = - 279.3 kJ/mol) Reaction 3.9

$2H_2O(l) + 2e^- \rightarrow H_2(g) + 2OH^-(aq)$

(E_0 = - 0.90 V vs. Ag/AgCl) Reaction 3.10

$$Al(s) + 4OH^-(aq) \rightarrow AlO_2^-(aq) + 2H_2O(l) + 3e^-$$

(E_0 = - 2.50 V vs. Ag/AgCl) Reaction 3.11

$$3TeO_3^{2-}(aq) + 4Al(s) + H_2O(l) \rightarrow 3Te(s) + 4AlO_2^-(aq) + 2OH^-(aq)$$

(ΔG^O = - 554.2 kJ/mol) Reaction 3.12

Sacrificial materials with appropriate redox potential is critical for a GDR. In our previous publication, Zinc were used as sacrificial material and the reduction of TeO_3^{2-} (+IV) in an alkaline solution has been studied, in which TeO_3^{2-} (+IV) was reduced to Te (0) (reaction 3.1), then to Te_2^{2-} (-I) (reaction 3.3) confirmed by the observation of deep violet color.[66] However, when Aluminum was used as sacrificial material, Te_2^{2-} (-I) can further reduced to Te^{2-} (-II) (reaction 3.6), since the redox potential of the Al/AlO_2^- pair is -2.5 V vs. sat. Ag/AgCl, which provides large driving force to reduce TeO_3^{2-} (+IV) all the way to Te^{2-} (-II).[71, 72] In acidic and neutral solution, Te (0) is directly reduced to Te^{2-} (-II) in one step (reaction 3.5). [12, 73] However, in alkaline solution an intermediate specie Te_2^{2-} (-I) is formed before Te (0) is further reduced to Te^{2-} (-II) as reported by several groups. For example, Lingane *et al.* reported that at pH of 9.4 two cathodic waves were observed, the first wave represented the reduction of TeO_3^{2-} (+IV) to Te (0), which was confirmed by coulometer reading that 3.95 - 4.07 electrons per TeO_3^{2-} (+IV) reduced. The meaning of the second cathodic wave was explained by further reduction of Te (0). At pH of 14 (i.e., 1M NaOH), only one cathodic wave was observed. Lingane reported that the overall reaction was written as reaction 3.4, but the reactions took place in three steps. The TeO_3^{2-} (+IV) was reduced to Te (0) confirmed by the phenomenon that black deposit was observed

on the dropping mercury electrode, then Te (0) was further reduced Te_2^{2-} (-I) confirmed by the phenomenon that deep violet solution was formed, finally the deep violet solution became colorless which meant that Te_2^{2-} (-I) was reduced to Te^{2-} (-II).[74] Schmidt *et al.* cited the Te reaction mechanism from Lingane's publication, however Schmidt did not mention the formation of Te_2^{2-}(-I). [75] Shinagawa *et al.* reported that TeO_3^{2-}(+IV) was reduced to Te (0), then further reduced to Te_2^{2-}(-I), finally Te_2^{2-}(-I) was reduced to Te^{2-} (-II) based on the observation that deep violet solution became colorless. [71] Mishra detected the presence of intermediate species Te_2^{2-} (-I) by rotating ring-disk electrode as Te^{2-} (-II) was oxidized to Te (0). [76] Pourbaix claimed that the direct transition from TeO_3^{2-} (+IV) to Te_2^{2-} (-I) (reaction 3.2) is possible, but there was no evidence reported to prove this five-electron transition. [77] According to the Pourbaix diagram, the redox potential for Te_2^{2-}/Te^{2-} (reaction 3.6) is -1.47V vs. Ag/AgCl. [77] However, Panson *et al.* experimentally proved that Te_2^{2-} (-I) was reduced Te^{2-} (-II) at potential of -1.16V vs. sat. Ag/AgCl. [78] As a consequence, in alkaline solution TeO_3^{2-} (+IV) is reduced to Te (0) (reaction 3.1), then Te (0) is reduced to Te_2^{2-} (-I) (reaction 3.3), finally further reduced to Te^{2-} (-II) (reaction 3.6). All the Te reactions that may happen in the alkaline solution were summarized in the schematic (figure 3.7), in which the numbers in the diamond represent the number of the reaction. The black arrows with solid lines represent the electrochemical reactions and the red arrows with dotted lines represent the chemical reactions.

Simultaneously with electrochemical reaction, the chemical reactions (reaction 3.7 – 3.9) occurred in the solution. Blanc *et al.* proposed the decomposition of Te_2^{2-} (-I) (reverse reaction of reaction 3.7) based on the observation that the electrolytic reduction of

Te produced a deep violet solution of Te_2^{2-} (-I) and elementary Te (0) in the form of grey dust. [79] However, no further evidence was reported to support reaction 3.7 and the calculated Gibbs free energy of reverse reaction is 58.6 kJ/mol. The formed Te_2^{2-} (-I) and Te^{2-} (-II) interacts with TeO_3^{2-} (+IV) to chemically deposit solid Te in the solution as shown in reactions 8 and 9, respectively. This two reactions result in the formation of nanostructured Te in the solution. Since the redox potential of Al/AlO_2^- was significantly negative than TeO_3^{2-}/Te (reaction 3.1), Te/Te_2^{2-} (reaction 3.3) and Te_2^{2-}/Te^{2-} (reaction 3.6), the electrodeposited Te by reaction 3.1 can further reduce to soluble Te_2^{2-} (-I) or Te^{2-} (-II). The soluble Te_2^{2-} (-I) and Te^{2-} (-II) will chemical reaction with TeO_3^{2-} to form elemental Te (0) in solution. This was also confirmed by the observation that the solution became a black suspension after GDR started. The anodic part reaction was Al oxidation (reaction 3.11), which provides electrons for the reduction of Te. The cathodic reactions included Te reduction and hydrogen gas evolution (reaction 3.10). For Te reduction, TeO_3^{2-} (+IV) was reduced to Te (0) (reaction 3.1), then to Te_2^{2-} (-I) (reaction 3.3) and Te^{2-} (-II) (reaction 3.6) .The intermediate states (*i.e.*, Te_2^{2-} and Te^{2-}) were water soluble but not stable in the solution - it spontaneously interacted with TeO_3^{2-} (+IV) to chemically deposit Te (0) according to reaction 3.8 and reaction 3.9 [71]. In addition, hydrogen gas evolution (reaction 3.10) simultaneously occurred with Te reduction, which was verified by the observation of gas bubbling. The overall reaction of GDR is represented by reaction 3.12 with a large, negative Gibbs free energy (ΔG^o) of -554.2 kJ/mol, which indicates the GDR was most thermodynamically favorable. It was also confirmed by the observation that the solution became a black suspension as soon as the TeO_3^{2-} electrolyte was added onto the

surface of aluminum foil. The black particles were found to be “rice-like” nanostructures by SEM.

Transient OCPs were measured at TeO_3^{2-} concentrations ranging from 10 to 550 mM with a fixed pH of 13.1 at 23 ºC to monitor the reaction (Figure 3.8A). For the GDRs containing low concentrations of TeO_3^{2-} (*i.e.*, ≤ 50 mM), the potentials first increased rapidly, then stabilized at a constant value signaling the onsets of steady-state reactions. At high TeO_3^{2-} concentrations (*i.e.*, 100 and 550 mM), the OCP fluctuated significantly. This may be attributed by changing working electrode surface area between Aluminum and GDR deposited Te due to the two step reduction reactions of Te (reaction 3.1 and 3.3). [71, 72, 80, 81] First the Aluminum is covered with Te (0) when TeO_3^{2-} (+IV) was reduced to Te (0) followed by exposure to the electrolyte again when Te (0) was reduced to water soluble Te_2^{2-} (-I) Furthermore, the OCP increased up to -1.2 V at TeO_3^{2-} concentration of 550 mM after 18 minutes because the Al foil was completely dissolved. With a same sacrificial material at a certain temperature, the OCP of the reaction mainly depends on the cathodic exchange current density, which is directly related to the concentration of the electrolytes.[66, 82, 83] An increase in the electrolytes’ concentration will augment the cathodic exchange current density, thus increasing the OCP. As shown in the Figure 3.8A, OCPs increased with [TeO_3^{2-}], which was likely a result of an increased cathodic exchange current density. [66, 82, 83]

Linear polarization curves (Figure 3.8B) of Al foils in naturally aerated electrolytes with various concentrations of TeO_3^{2-} were examined by the same method used for the OCP measurements. In certain solutions, the Tafel curve can be divided into two sides (*i.e.*,

cathodic and anodic sides), with two Te reduction reactions (reaction 3.1 and 3.3) and hydrogen gas evolution (reaction 3.10) in the cathodic side and Al oxidation reaction (reaction 3.11) in the anodic side. By fitting linearly both the cathodic and anodic sides of the Tafel plot, an intercept can be obtained from which the corrosion potential and current density are calculated.

Figures 8C and 8D show the corrosion potential and corrosion current at different TeO_3^{2-} concentrations as functions of the reaction time in naturally aerated solution. A more positive corrosion potential was observed at a higher TeO_3^{2-} concentration, which was in agreement with the OCP data. This indicates that the driving forces of the GDR at low TeO_3^{2-} concentrations (*i.e.*, 10 and 50 mM) is slightly greater than that at higher concentrations (*i.e.*, 100 and 550 mM). The corrosion current increased substantially with the TeO_3^{2-} concentration (Figure 3.8D). After 13 min at TeO_3^{2-} concentration of 550 mM, no corrosion current data were obtained since the Al foil was fully dissolved at that time. At TeO_3^{2-} concentration of 50 mM and 100 mM after 21 minutes, the corrosion current decreased significantly because the Al foil was almost completely dissolved. As mentioned in the previous publication, the difference in the reaction rates of different TeO_3^{2-} concentrations may lead to the size change of nanostructures. Higher TeO_3^{2-} concentrations result in higher reaction and mass transfer rates, which may lead to larger diameters, longer lengths and higher aspect ratios of Te "rice-like" nanostructures.

Transient OCPs in naturally aerated solution at different pH values ranging 10.9 to 15.0 are shown in Figure 3.9A. The OCPs shift to the more negative direction and the increase in pH was attributed to the decrease of the anodic current [82, 83]. Crystallized

Te was deposited at pH ≥ 11.9 while amorphous Te was formed at pH = 10.9, indicating that 11.9 was the onset pH for crystalline depositions.

Linear polarization curves of GDRs at various pH values was conducted using the same conditions applied for the OCP measurements. Quantified assessments of the corrosion potential and current density as functions of reaction time are shown in Figure 3.9C and D. The corrosion potential becoming more negative when the pH increased from 10.9 to 15.0 is consistent with the OCP data. This indicated that a greater driving force was provided to the GDR at a higher pH in an alkaline bath.

At pH of 10.9, aluminum hydroxide [77] was anticipated to coat the Al foil surface acting as a passivation layer increasing the corrosion potential thus decreasing the corrosion current density. As shown in Figure 3.9D, the average corrosion current density at a pH of 10.9 is approximately 0.03 mA/cm^2, which is 30 times lower than when at a pH of 11.9. The diminutive current density shows that the reaction could barely happen at pH of 10.9, and this includes the Te deposition reaction. At 11.9 ≤ pH ≤ 15.0, the average current density increased with respect to pH indicating a faster reaction rate in a more alkaline bath, which led to longer lengths and larger aspect ratios.

Transient OCPs were measured in naturally aerated and deaerated solution at TeO_3^{2-} concentrations of 100 mM, pH of 13.1, and temperature of 23 ^oC (Figure 4.13 A). Both of the two OCP curves fluctuated. The value of OCP became more positive after deaeration, which agreed with the corrosion potential (Figure 4.13 C). The LP curves (Figure 4.13 B) indicate that the dissolved O_2 effected both cathodic and anodic reactions.

Figure 4.13 D shows that naturally aerated solution, the corrosion current remained relatively stable for 21 minutes but declined rapidly at 29 minutes because the Al foil was totally dissolved. However, the corrosion current decreased gradually in deaerated solution.

3.5 Conclusions

In summary, Te "rice-like" nanostructures with controlled dimensions were synthesized by galvanic displacement reactions of aluminum in alkaline baths. The Te "rice-like" nanostructures were deposited in the solution via chemical reaction between Te_2^{2-} (-I) or Te^{2-} (-II) and TeO_3^{2-} (IV). The formation of sharp tips may be attributed to the high density of surface charges at the tips. The morphology of the Te evolved from branched nanostructures together with some "rice-like" nanostructures to only "rice-like" nanostructures as the reaction time (10 to 90 min) and temperature (4 to 50 ^oC) increased. The nanostructures peaked in dimensions after 30 min. At pH < 11.9 the deposited Te film was amorphous. The amorphous to crystalline transformation at pH ≥ 11.9 was associated with a sharp increase in the average current density jumping from 0.03 mA/cm^2 in the amorphous state at pH=10.9 to 1.0 mA/cm^2 in the crystalline state at pH=11.9 to 10 mA/cm^2 at pH=15.0. Although the nanorice diameter increased from 125 nm to 175 nm (with no distinctive trendline) over this pH range ($[TeO_3^{2-}]$ = 10 mM at 23^oC), the length of the nanostructures increased linearly from 0.4 µm to 1.2 µm. However, the diameter and length of the nanostructures depended most strongly on $[TeO_3^{2-}]$. The diameter increased from 125 nm at 10 mM to 573 nm at 550 mM (pH=13.1 @23 ^oC for 30 min), while the length increased from 0.7 to 5.7 µm.

3.6 References

1. Bang, J.H. and K.S. Suslick, *Applications of Ultrasound to the Synthesis of Nanostructured Materials.* Advanced Materials, 2010. **22**(10): p. 1039-1059.
2. Xia, Y., et al., *One-Dimensional Nanostructures: Synthesis, Characterization, and Applications.* Advanced Materials, 2003. **15**(5): p. 353-389.
3. Zečević, J., K.P. de Jong, and P.E. de Jongh, *Progress in electron tomography to assess the 3D nanostructure of catalysts.* Current Opinion in Solid State and Materials Science, 2013. **17**(3): p. 115-125.
4. Wang, H., et al., *Nanorice: A Hybrid Plasmonic Nanostructure.* Nano Letters, 2006. **6**(4): p. 827-832.
5. Sealy, C., *Nanorice combines best of both worlds: Nanoparticles.* Nano Today, 2006. **1**(2): p. 13.
6. Wei, H., et al., *Multipolar Plasmon Resonances in Individual Ag Nanorice.* ACS Nano, 2010. **4**(5): p. 2649-2654.
7. Hippel, A.v., *Structure and Conductivity in the VIb Group of the Periodic System* Journal of Chemical Physics, 1948. **16**: p. 372-380.
8. Lee, T.I., et al., *High-Power Density Piezoelectric Energy Harvesting Using Radially Strained Ultrathin Trigonal Tellurium Nanowire Assembly.* Advanced Materials, 2013. **25**(21): p. 2920-2925.
9. Arlt, G. and P. Quadflieg, *Electronic Displacement in Tellurium by Mechanical Strain.* physica status solidi (b), 1969. **32**(2): p. 687-689.
10. Liu, J.-W., et al., *Mesostructured Assemblies of Ultrathin Superlong Tellurium Nanowires and Their Photoconductivity.* Journal of the American Chemical Society, 2010. **132**(26): p. 8945-8952.
11. Wang, Y., et al., *Mirror-Like Photoconductive Layer-by-Layer Thin Films of Te Nanowires: The Fusion of Semiconductor, Metal, and Insulator Properties.* Advanced Materials, 2006. **18**(4): p. 518-522.
12. Zhang, M., et al., *A Rapid Room-Temperature NO2 Sensor Based on Tellurium–SWNT Hybrid Nanostructures.* The Journal of Physical Chemistry C, 2012. **116**(37): p. 20067-20074.
13. Wei, G., et al., *Solvothermal synthesis of porous tellurium nanotubes.* Chemical Physics Letters, 2003. **372**(3): p. 590-594.
14. Gautam, U.K. and C.N.R. Rao, *Controlled synthesis of crystalline tellurium nanorods, nanowires, nanobelts and related structures by a self-seeding solution process.* Journal of Materials Chemistry, 2004. **14**(16): p. 2530-2535.

15. Liu, Z., et al., *Size-Controlled Synthesis and Growth Mechanism of Monodisperse Tellurium Nanorods by a Surfactant-Assisted Method.* Langmuir, 2004. **20**(1): p. 214-218.

16. Zhou, B., et al., *A novel ultrasonic-assisted solution-phase approach for the fabrication of tellurium bundles of nanowhiskers.* Ultrasonics Sonochemistry, 2006. **13**(4): p. 352-358.

17. Shen, J.-M., et al., *Construction of Unconventional Hexapod-like Tellurium Nanostructure with Morphology-Dependent Photoluminescence Property*. The Journal of Physical Chemistry C, 2009. **113**(22): p. 9502-9508.

18. Wang, Z., et al., *Formation of single-crystal tellurium nanowires and nanotubes via hydrothermal recrystallization and their gas sensing properties at room temperature.* Journal of Materials Chemistry, 2010. **20**(12): p. 2457-2463.

19. Li, X.-L., et al., *Synthesis and magnetoresistance measurement of tellurium microtubes.* Journal of Materials Chemistry, 2003. **14**(2): p. 244-247.

20. Mohanty, P., et al., *Synthesis of Single Crystalline Tellurium Nanotubes with Triangular and Hexagonal Cross Sections.* The Journal of Physical Chemistry B, 2006. **110**(2): p. 791-795.

21. Chen, H., et al., *The fabrication of Te nanowires with different orientations by vacuum vapor deposition.* Physics Letters A, 2007. **362**(1): p. 61-65.

22. Wang, Q., et al., *Fabrication and Growth Mechanism of Selenium and Tellurium Nanobelts through a Vacuum Vapor Deposition Route.* The Journal of Physical Chemistry C, 2007. **111**(35): p. 12926-12932.

23. Sen, S., et al., *Synthesis of Tellurium Nanostructures by Physical Vapor Deposition and Their Growth Mechanism.* Crystal Growth & Design, 2008. **8**(1): p. 238-242.

24. Siciliano, T., et al., *Tellurium microtubes synthesized by thermal evaporation method.* Crystal Research and Technology, 2011. **46**(8): p. 765-768.

25. Parsafar, N. and A. Ebrahimzad, *The effect of substrate temperature on fabrication of one-dimensional nanostructures of tellurium.* Int.J.Nano Dim., 2012. **2**(3): p. 177-183.

26. Hawley, C.J., et al., *Shape-Controlled Vapor-Transport Growth of Tellurium Nanowires.* Crystal Growth & Design, 2012. **12**(6): p. 2789-2793.

27. Mo, M., et al., *Controlled Hydrothermal Synthesis of Thin Single-Crystal Tellurium Nanobelts and Nanotubes.* Advanced Materials, 2002. **14**(22): p. 1658-1662.

28. Yu, H., P.C. Gibbons, and W.E. Buhro, *Bismuth, tellurium, and bismuth telluride nanowires.* Journal of Materials Chemistry, 2004. **14**(4): p. 595-602.

29. Mayers, B. and Y. Xia, *One-dimensional nanostructures of trigonal tellurium with various morphologies can be synthesized using a solution-phase approach.* Journal of Materials Chemistry, 2002--. **12**(6): p. 1875-1881.

30. Liu, Z., et al., *Shape-controlled synthesis and growth mechanism of one-dimensional nanostructures of trigonal tellurium.* New Journal of Chemistry, 2003. **27**(12): p. 1748-1752.

31. Qian, H.-S., et al., *Synthesis of Uniform Te@Carbon-Rich Composite Nanocables with Photoluminescence Properties and Carbonaceous Nanofibers by the Hydrothermal Carbonization of Glucose.* Chemistry of Materials, 2006. **18**(8): p. 2102-2108.

32. Qian, H.-S., et al., *High-Quality Luminescent Tellurium Nanowires of Several Nanometers in Diameter and High Aspect Ratio Synthesized by a Poly (Vinyl Pyrrolidone)-Assisted Hydrothermal Process.* Langmuir, 2006. **22**(8): p. 3830-3835.

33. Zhang, B., et al., *1D Tellurium Nanostructures: Photothermally Assisted Morphology-Controlled Synthesis and Applications in Preparing Functional Nanoscale Materials.* Advanced Functional Materials, 2007. **17**(3): p. 486-492.

34. Lin, Z.-H., Z. Yang, and H.-T. Chang, *Preparation of Fluorescent Tellurium Nanowires at Room Temperature.* Crystal Growth & Design, 2008. **8**(1): p. 351-357.

35. Lin, Z.-H., et al., *Selective growth of gold nanoparticles onto tellurium nanowires via a green chemical route.* Journal of Materials Chemistry, 2008. **18**(22): p. 2569-2572.

36. Xu, L., et al., *Large-scale Synthesis of Crystalline Tellurium Nanowires with Controlled-Diameters via a Hydrothermal-reduction Process.* Chemistry Letters, 2004. **33**(5): p. 592-593.

37. Liu, Z., et al., *Surfactant-assisted growth of uniform nanorods of crystalline tellurium.* Journal of Materials Chemistry, 2003. **13**(1): p. 159-162.

38. Liang, F. and H. Qian, *Synthesis of tellurium nanowires and their transport property.* Materials Chemistry and Physics, 2009. **113**(2): p. 523-526.

39. Zhu, Y.-J., H. Xian-Luo, and W. Wei-Wei, *Poly(vinylpyrrolidone): a new reductant for preparation of tellurium nanorods, nanowires, and tubes from TeO 2.* Nanotechnology, 2006. **17**(3): p. 645.

40. Zhu, Y. and X. Hu, *tellurium nanorods and nanowires prepared by the microwave-polyol method.* Chemistry Letters, 2004. **33**.

41. Song, J.-M., et al., *Superlong High-Quality Tellurium Nanotubes: Synthesis, Characterization, and Optical Property.* Crystal Growth & Design, 2008. **8**(6): p. 1902-1908.

42. Xu, W., et al., *Structural, Electrical, and Photoconductive Properties of Individual Single-Crystalline Tellurium Nanotubes Synthesized by a Chemical Route: Doping Effects on Electrical Structure.* Small, 2008. **4**(7): p. 888-893.

43. Wu, X., et al., *Controlled synthesis of multi-morphology Te crystals by a convenient Lewis acid/base-assisted solvothermal method.* Journal of Nanoparticle Research, 2012. **14**(8): p. 1-10.

44. Zhu, W., et al., *Controllable, Surfactant-Free Growth of 2D, Scroll-Like Tellurium Nanocrystals via a Modified Polyol Process.* Crystal Growth & Design, 2006. **6**(12): p. 2804-2808.

45. Wang, S., et al., *Synthesis, characterization and optical properties of flower-like tellurium.* CrystEngComm, 2010. **12**(1): p. 166-171.

46. Lu, Q., F. Gao, and S. Komarneni, *Biomolecule-Assisted Reduction in the Synthesis of Single-Crystalline Tellurium Nanowires.* Advanced Materials, 2004. **16**(18): p. 1629-1632.

47. Xi, G., et al., *Large-Scale Synthesis, Growth Mechanism, and Photoluminescence of Ultrathin Te Nanowires.* Crystal Growth & Design, 2006. **6**(11): p. 2567-2570.

48. Zhu, Y.-J., et al., *Microwave-Assisted Synthesis of Single-Crystalline Tellurium Nanorods and Nanowires in Ionic Liquids.* Angewandte Chemie International Edition, 2004. **43**(11): p. 1410-1414.

49. Zhu, H., et al., *Controlled Synthesis of Tellurium Nanostructures from Nanotubes to Nanorods and Nanowires and Their Template Applications.* The Journal of Physical Chemistry C, 2011. **115**(14): p. 6375-6380.

50. Zhu, H., et al., *Controlled hydrothermal synthesis of tri-wing tellurium nanoribbons and their template reaction.* CrystEngComm, 2012. **14**(1): p. 251-255.

51. Xi, G., et al., *Synthesis, Characterization, and Growth Mechanism of Tellurium Nanotubes.* Crystal Growth & Design, 2005. **5**(1): p. 325-328.

52. Lu, Q., F. Gao, and S. Komarneni, *A Green Chemical Approach to the Synthesis of Tellurium Nanowires.* Langmuir, 2005. **21**(13): p. 6002-6005.

53. Mayers, B. and Y. Xia, *Formation of Tellurium Nanotubes Through Concentration Depletion at the Surfaces of Seeds.* Advanced Materials, 2002. **14**(4): p. 279-282.

54. F.Gao, Q. Lu, and S. Komarneni, *Gluconate controls one-dimensional growth of tellurium nanostructures.* Journal of Materials Research, 2006. **21**(02): p. 343-348.

55. Geng, B., et al., *Large-scale synthesis of single-crystalline Te nanobelts by a low-temperature chemical vapour deposition route.* Nanotechnology, 2003. **14**(9): p. 983.

56. He, Z., S.-H. Yu, and J. Zhu, *Amino Acids Controlled Growth of Shuttle-Like Scrolled Tellurium Nanotubes and Nanowires with Sharp Tips.* Chemistry of Materials, 2005. **17**(11): p. 2785-2788.

57. Chang, C.H., et al., *Galvanic displacement of BixTey thin films from sacrificial iron group thin films.* Electrochimica Acta, 2010. **55**(3): p. 1072-1080.

58. Chang, C.H., et al., *Bi and Te thin films synthesized by galvanic displacement from acidic nitric baths.* Electrochimica Acta, 2010. **55**(3): p. 743-752.

59. Rheem, Y., et al., *Synthesis of tellurium nanotubes by galvanic displacement.* Electrochimica Acta, 2010. **55**(7): p. 2472-2476.

60. Yoo, B.Y., et al., *Electrochemically deposited thermoelectric n-type Bi2Te3 thin films.* Electrochimica Acta, 2005. **50**(22): p. 4371-4377.

61. Jung, H., et al., *Electrodeposited Single Crystalline PbTe Nanowires and Their Transport Properties.* Journal of Physical Chemistry C, 2011. **115**(7): p. 2993-2998.

62. Xiao, F., et al., *Electrodeposition of PbTe thin films from acidic nitrate baths.* Electrochimica Acta, 2006. **52**(3): p. 1101-1107.

63. Lim, J.H., et al., *Electrodeposition of p-Type SbxTey Thermoelectric Films.* Journal of Electronic Materials, 2011. **40**(5): p. 1321-1325.

64. Park, K., et al., *Electrochemical deposition of thermoelectric SbxTey thin films and nanowires.* Journal of Alloys and Compounds, 2009. **485**(1-2): p. 362-366.

65. Xiao, F., et al., *Electro-transport studies of electrodeposited (Bi(1-x)Sbx)(2)Te-3 nanowires.* Nanotechnology, 2007. **18**(33).

66. Wu, T., et al., *Synthesis of Tellurium Heterostructures by Galvanic Displacement Reaction of Zinc in Alkaline Baths.* Electrochimica Acta, 2014. **150**(0): p. 298-307.

67. Sahoo, A.K. and S.K. Srivastava, *Morpholine-4-Carbodithioate Se and Te Complex as Single Source Precursor for Synthesis of Se and Te with Diverse Morphologies.* Crystal Growth & Design, 2011. **11**(5): p. 1597-1606.

68. Ozaki, M., S. Kratohvil, and E. Matijević, *Formation of monodispersed spindle-type hematite particles.* Journal of Colloid and Interface Science, 1984. **102**(1): p. 146-151.

69. Santore, M.M. and N. Kozlova, *Micrometer scale adhesion on nanometer-scale patchy surfaces: adhesion rates, adhesion thresholds, and curvature-based selectivity.* Langmuir, 2007. **23**(9): p. 4782-4791.

70. Li, G. and H. Wang. *In situ chemical etching synthesis of ZnO nanotips array*. in *Proceedings of the 2nd WSEAS international conference on Nanotechnology*. 2010. World Scientific and Engineering Academy and Society (WSEAS).

71. Shinagawa, M., N. Yano, and T. Kurosu, *Te reudction - alkaline bath - Mechanism and analytical aspects of the polarographic maximum wave of tellurium.* Talanta, 1972. **19**(4): p. 439-450.

72. Shinagawa, M., et al., *Te alkaline&acidic baths - reduction reactions - Studies on the prewave of tellurium and its photo-effect.* Journal of Electroanalytical Chemistry and Interfacial Electrochemistry, 1977. **75**(2): p. 809-817.

73. Gregory, B.W., M.L. Norton, and J.L. Stickney, *Thin-layer electrochemical studies of the underpotential deposition of cadmium and tellurium on polycrystalline gold, platinum and copper electrodes.* Journal of Electroanalytical Chemistry and Interfacial Electrochemistry, 1990. **293**(1–2): p. 85-101.

74. Lingane, J.J. and L.W. Niedrach, *Polarography of Selenium and Tellurium. II. The + 4 States.* Journal of the American Chemical Society, 1949. **71**(1): p. 196-204.

75. Schmidt, H., *Te - reduction in alkaline bath - Polarographic behavior of tellurites and tellurates.* Journal of the Polarographic society, 1962. **8**: p. 49-57.

76. Mishra, K.K., D. Ham, and K. Rajeshwar, *Anodic Oxidation of Te Ions - alkaline - Te22- detected - RDE.* Journal of The Electrochemical Society, 1990. **137**(11): p. 3438-3441.

77. Pourbaix, M., *Atlas of electrochemical equilibria in aqueous solutions*1966, Long Island City, N.Y.: Pergamon Press Inc.

78. Panson, A.J., *POLAROGRAPHY OF THE DITELLURIDE ION.* The Journal of Physical Chemistry, 1963. **67**(10): p. 2177-2180.

79. Blanc, M.L., *Can an element form both positive and negative ions.* Zeitschrift fuer Elektrochemie und Angewandte Physikalische Chemie, 1905. **11**: p. 813-18.

80. Vittori, O., *Polarographlc study of adsorbed tellurium at the hanging and dropping mercury electrodes in 1 m hydrochloric or perchloric acid solutions.* Analytica Chimica Acta, 1980. **121**(0): p. 315-319.

81. Sarala, Y. and S. Jayarama Reddy, *Electrochemical reduction of tellurium(IV).* Journal of Electroanalytical Chemistry and Interfacial Electrochemistry, 1986. **214**(1–2): p. 179-190.

82. Zhang, M., et al., *Galvanically Displaced Ultralong PbxSeyNiz Hollow Nanofibers with High Thermopower.* Chemistry of Materials, 2014. **26**(8): p. 2557-2566.

83. Wu, T., et al., *Synthesis of Tellurium Heterostructures by Galvanic Displacement Reaction of Zinc in Alkaline Baths.* electrochimica acta, 2014.

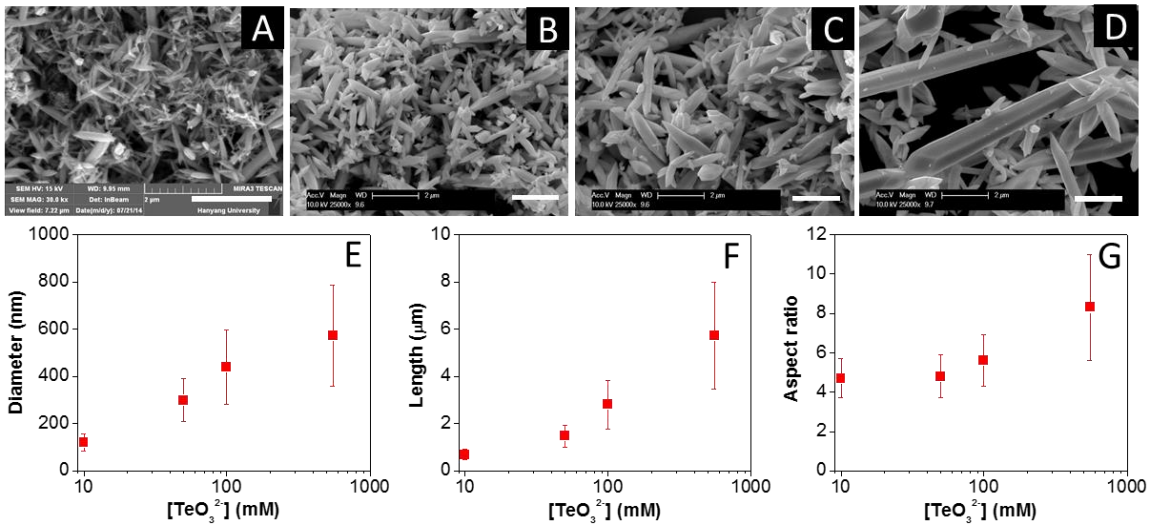

Figure 3.1 SEM images of the synthesized Te nanostructures synthesized at (A) 10 mM, (B) 50 mM, (C) 100 mM, (D) 550 mM TeO_3^{2-}, with a fixed pH of 13.1 and at 23 ºC for 30 min. Average diameter (E), length (F), and aspect ratio (G) as function of TeO_3^{2-} concentration. All scale bars in A-D are 2 µm.

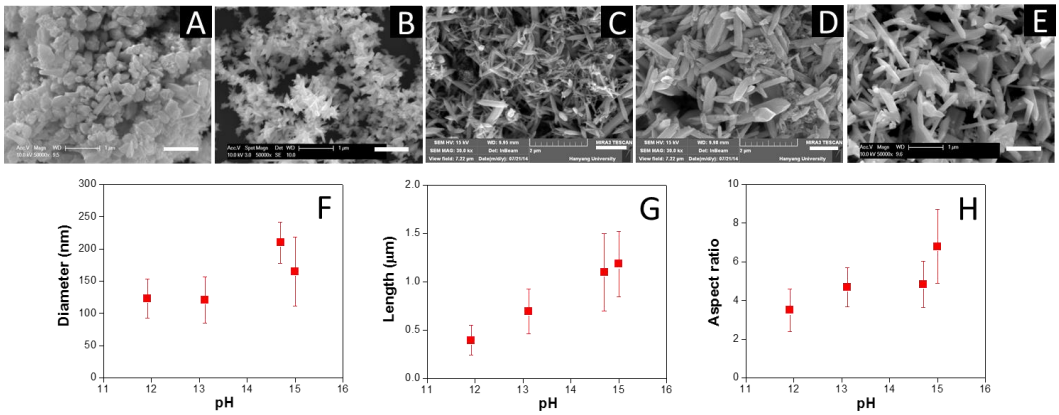

Figure 3.2 SEM images of Te nanostructures synthesized at different pH: (A) 10.9, (B) 11.9, (C) 13.1, (D) 14.7 (Calculated value), (E) 15.0 (Calculated value) with 10 mM TeO_3^{2-} at 23 ºC for 30 min. Average diameter (F), length (G), and aspect ratio (H) as function of solution pH. All scale bars in A-E are 1 μm.

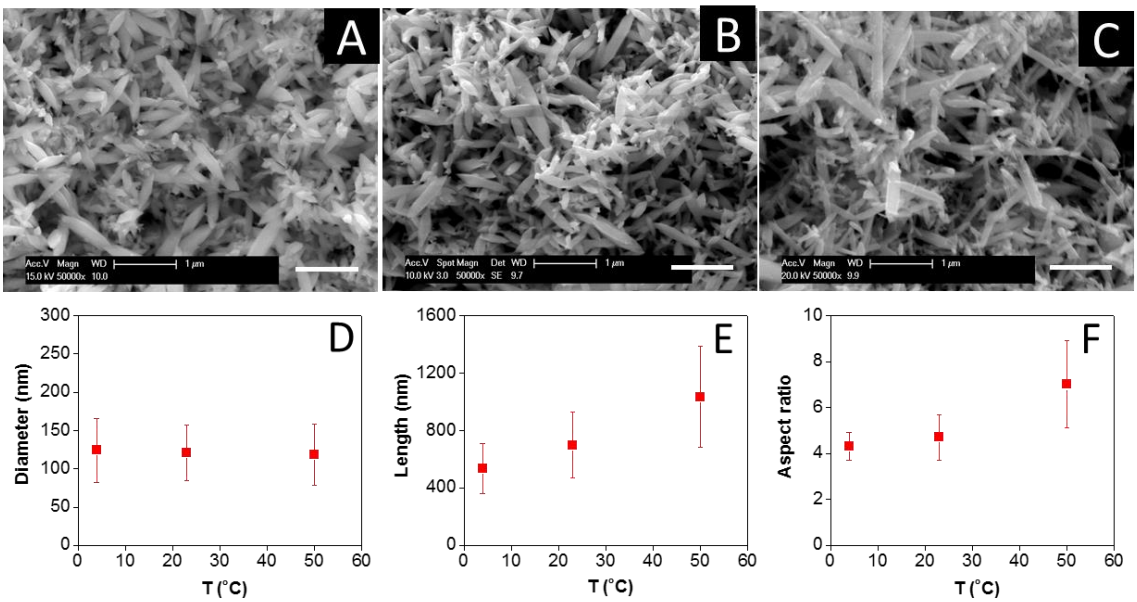

Figure 3.3 SEM images of Te nanostructures synthesized at various temperatures: (A) 4 ^{o}C, (B) 23 ^{o}C, (C) 50 ^{o}C. Average diameter (D), length (E), and aspect ratio (F) as function of temperature. The GDRs were conducted with 10 mM TeO_3^{2-} at pH of 13.1 for 30 min. All scale bars in A-C are 1 µm.

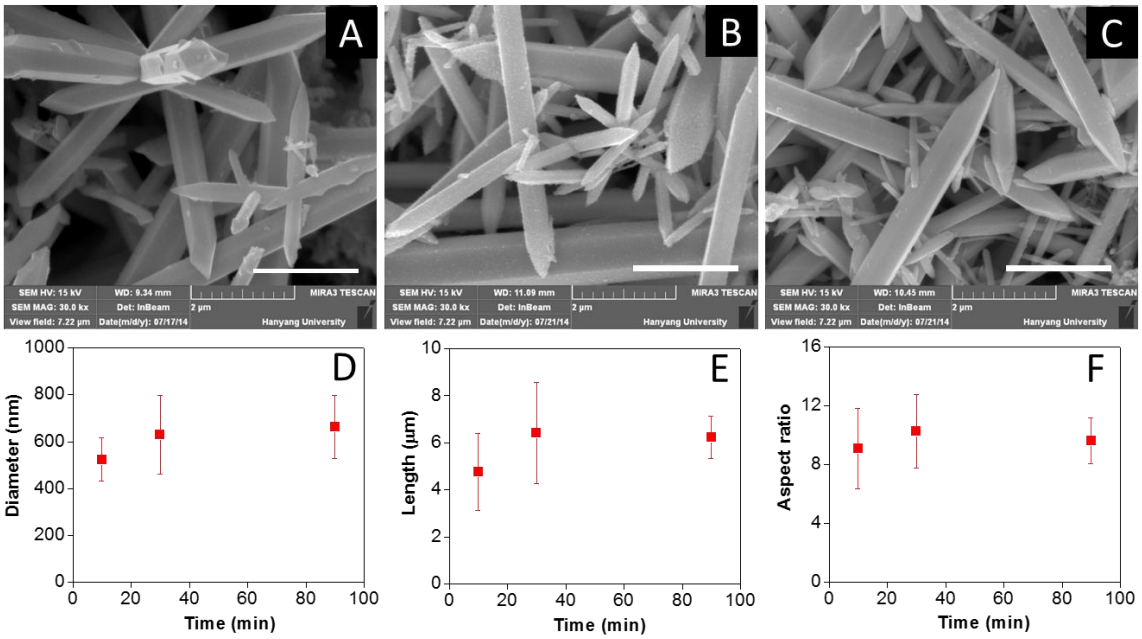

Figure 3.4 SEM images of Te nanostructures synthesized at different reaction time: (A) 10 min, (B) 30 min, (C) 90 min. Average diameter (D), length (E), and aspect ratio (F) as function of reaction time. The GDRs were conducted with 100 mM TeO_3^{2-} at pH of 14.7 and temperature of 23 ºC. All scale bars in A-C are 2 μm.

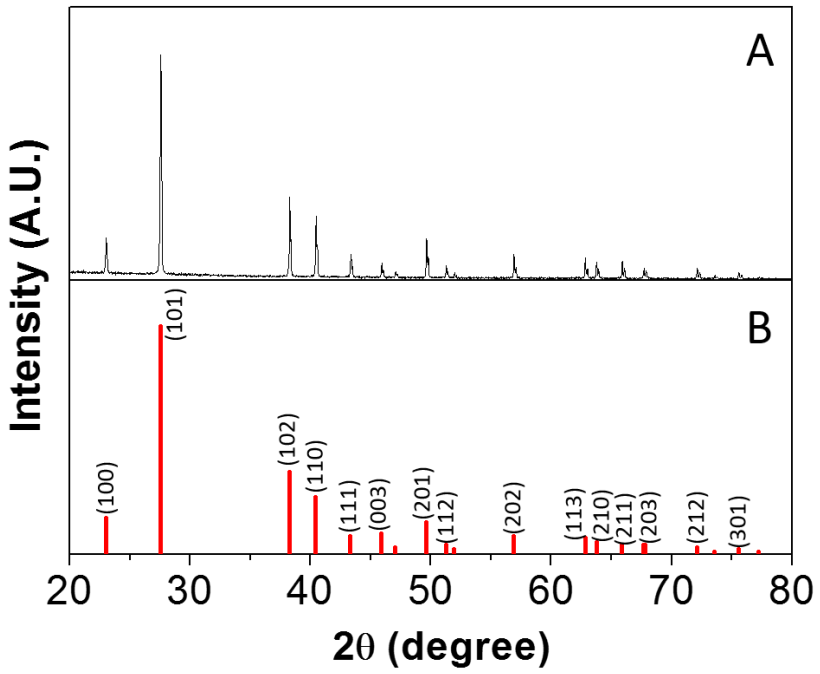

Figure 3.5 (A) The XRD pattern of Te "rice-like" nanostructures synthesized in the electrolyte containing 100 mM TeO_3^{2-} with pH of 13.1 at 23 ºC for 30 min. (B) Reference XRD pattern of trigonal-Te (JCPDS, No. 36-1452).

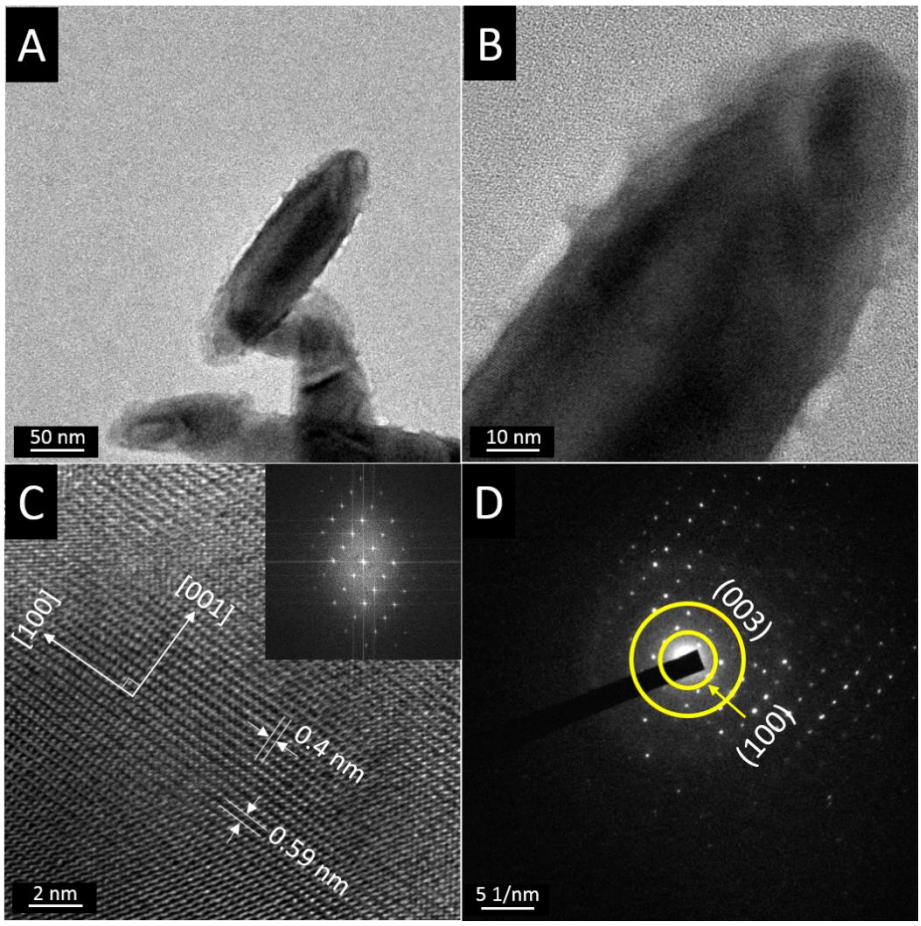

Figure 3.6 (A) High and (B) low magnification TEM images, (C) HRTEM image, and (D) SAED pattern of a Te "rice-like" nanostructures. The "rice-like" nanostructures was synthesized in 10 mM TeO_3^{2-} solution with pH of 13.1 at 23ºC for 30 min.

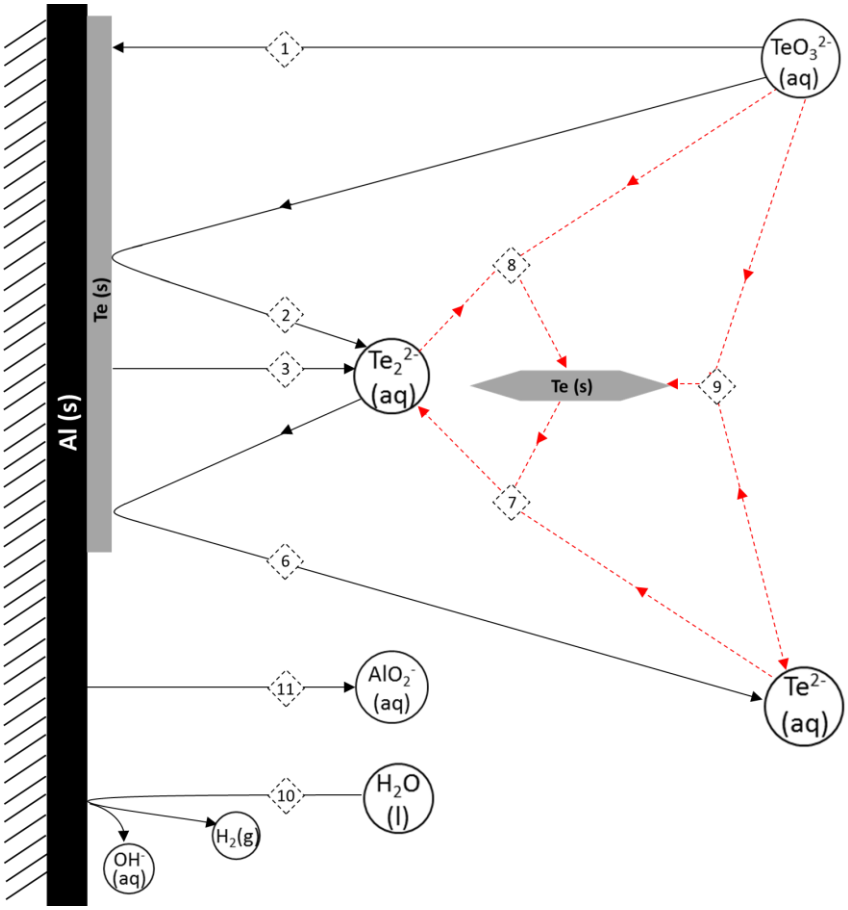

Figure 3.7 Schematic representation of Te electrochemical and chemical reaction in alkaline baths. The numbers in the diamond represent the number of the reaction. The black arrows with solid lines represent the electrochemical reactions and the red arrows with dotted lines represent the chemical reactions.

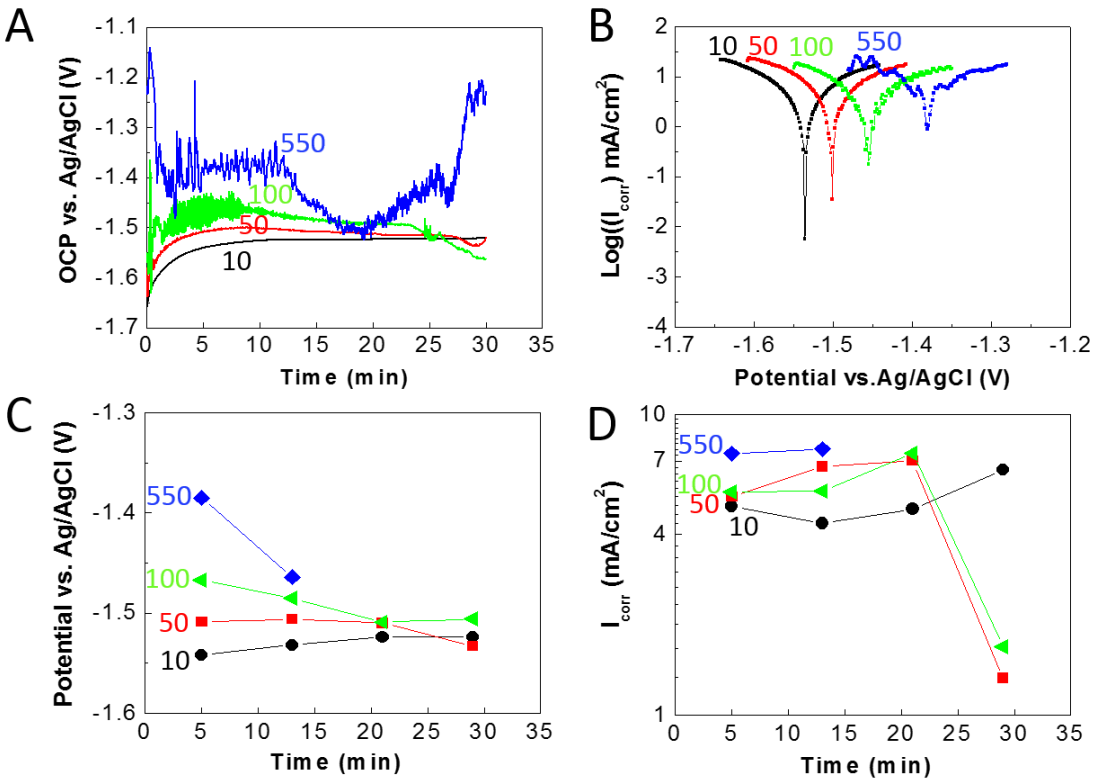

Figure 3.8 (A) Transient open-circuit potentials (OCP), (B) linear polarization curves, (C) calculated corrosion potential, and (D) corrosion current with TeO_3^{2-} concentrations of 10, 50, 100, and 550 mM. The pH of the solution was fixed at 13.1. The TeO_3^{2-} concentrations are marked in the figure with a unit of mM.

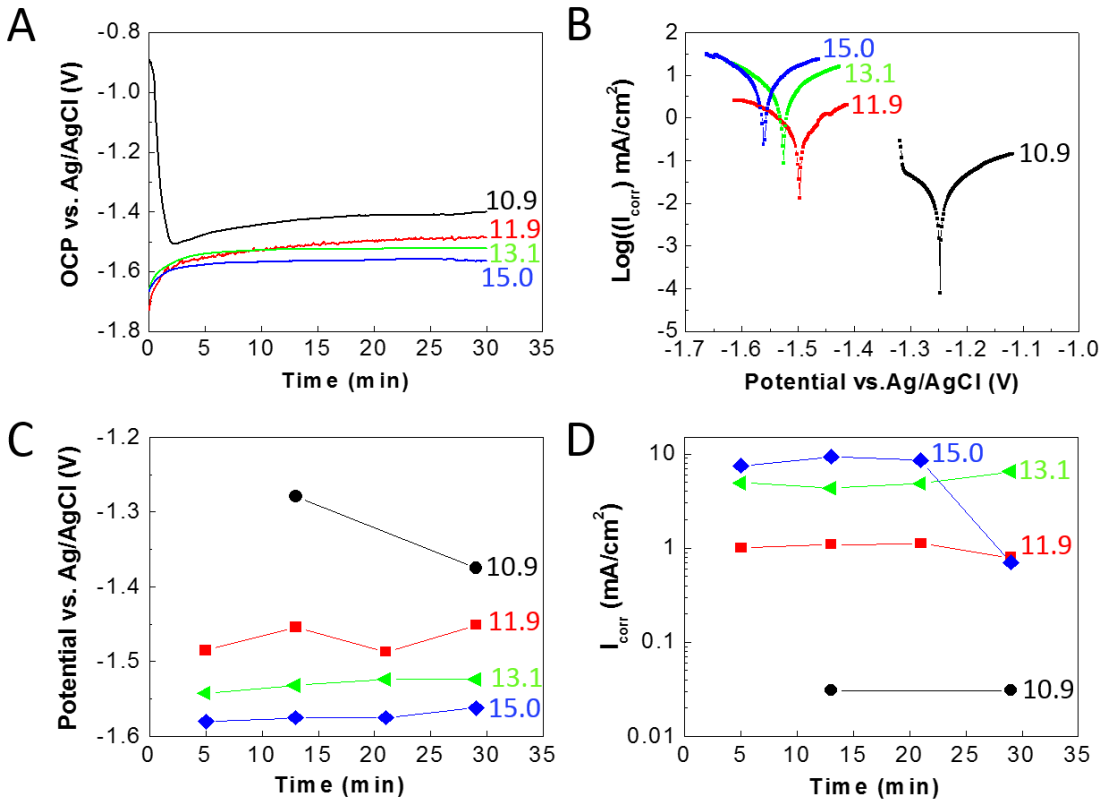

Figure 3.9 (A) Transient open-circuit potential (OCP), (B) linear polarization curves, (C) calculated corrosion potential, and (D) corrosion current with various pH of (a) 10.9, (b) 11.9, (c) 13.1, and (d) 15.0 (calculated value) and a fixed TeO_3^{2-} concentration of 10 mM. The reaction temperature was 23°C.

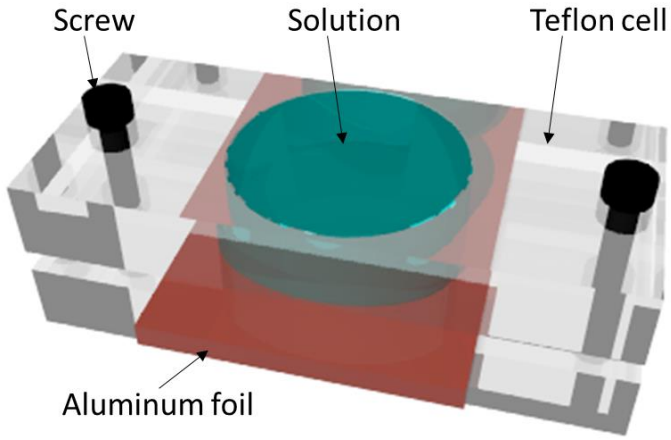

Figure 3.10 Schematic representation of reactor for galvanic displacement reaction.

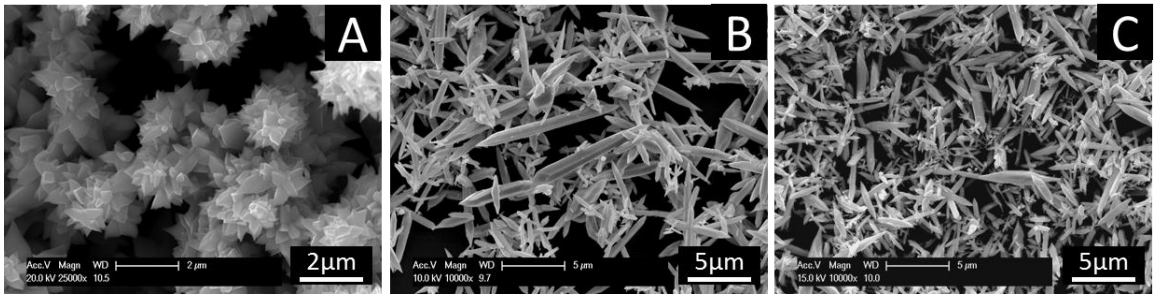

Figure 3.11 SEM images of Te nanostructures synthesized at various temperatures: (A) 4 ºC, (B) 23 ºC, (C) 50 ºC. The GDRs were conducted with 550 mM TeO_3^{2-} at pH of 13.1 for 30 min.

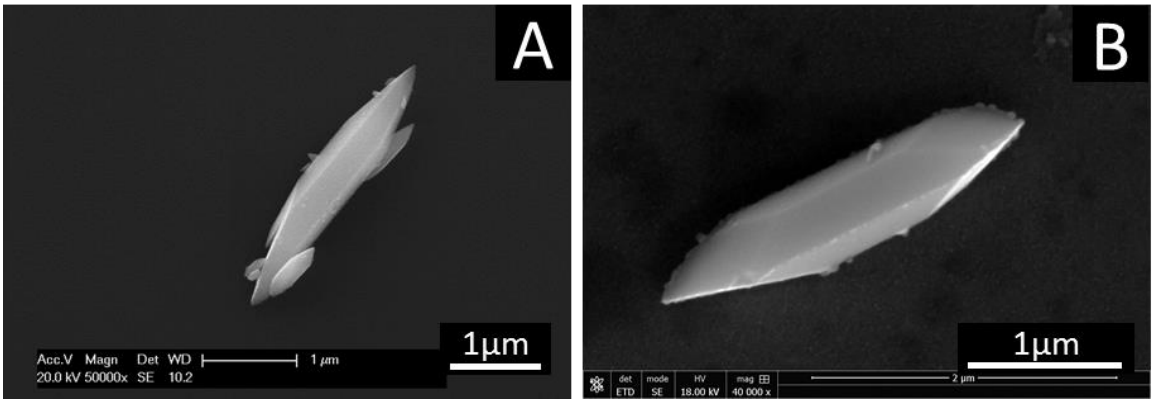

Figure 3.12 SEM images of Te nanostructures synthesized before (A) and after (B) O_2 was suppressed. The GDRs were conducted with 100 mM TeO_3^{2-} and pH of 13.1 at 23 ºC for 30 min.

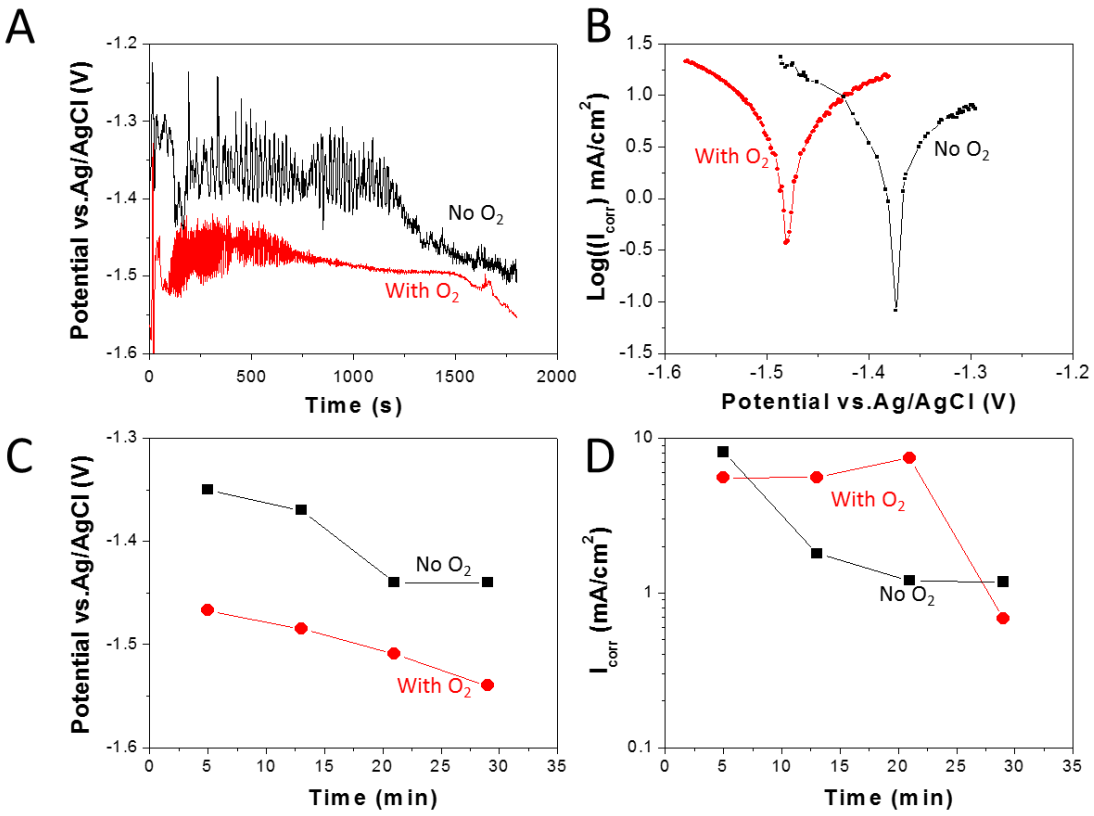

Figure 3.13 (A) Transient open-circuit potentials (OCP), (B) linear polarization curves, (C) calculated corrosion potential, and (D) corrosion current of Al foils in the electrolytes before (with O_2) and after (No O_2) O_2 suppression. The [TeO_3^{2-}] of the solution was 100 mM and the pH was fixed at 13.1. The reaction temperature was 23°C.

4 Electrodeposition of Tellurium Thick Films from Alkaline Baths

4.1 Abstract

Thick dense Te films were electrodeposited with current efficiency higher than 85% in alkaline solution. To deposit a dense Te film, the pH needs to be controlled from 11.3 to 12.5 with solution agitation set at 2000 rpm. In order to avoid further reduction of Te to Te_2^{2-} or keep the reduction of Te to Te_2^{2-} at a low enough reaction rate, the applied potential needs to be more positive than -1.0 V. XRD data showed a thick film orientation of (001) at applied potentials -0.8 and -0.9 V, and an orientation of (101) at applied potential -1.0 V. Grain size of the thick Te films ranged from 66 to 135 nm and was controlled by applied potential, TeO_3^{2-} concentration, and pH. Carrier concentration of the thick Te films ranged from 7.0×10^{18} to 3.1×10^{19} cm^{-3}. The larger grain size resulted in a lower carrier concentration because of less structural defects. High deposition rates were achieved by high TeO_3^{2-} concentrations and a more negative applied potential.

4.2 Introduction

Tellurium is a p-type semiconductor with a narrow band-gap energy of 0.35 eV at room temperature. Owing to its unique crystal structure, tellurium exhibits many unique physical properties including photoconductivity [1, 2], piezoelectric effect [3], gas sensing [4, 5], and catalytic activity [6-8]. Additionally, tellurium based alloys, such as Bi_2Te_3, PbTe, and Sb_2Te_3, have wide application in thermoelectric devices[9].

Film-based micro thermoelectric devices (TEG) have drawn significant attention.[10] By shrinking the size of thermoelectric devices, it not only allows the device

to operate under smaller temperature gradients, but by so doing it expands its capability to handle a wider range of thermal and power management microelectronic systems.[10-14]

Various methods can be utilized to synthesis films including sputtering, evaporation, and electrodeposition [15]. Electrodeposition is a cost-effective approach to fabricate micro-thermoelectric devices because it combines simple equipment and processing conditions with high deposition rates and well controlled materials properties. [16] Most of Tellurium and its alloy films have been synthesized by electrodeposition in acidic media.[17-25] However, the acidic bath has its drawbacks when depositing thick films with high deposition rate due to low solubility of TeO_3^{2-} (e.g., 10 mM at pH of zero)[26]. The solubility of TeO_3^{2-} can be significantly enhanced in alkaline solution (e.g., 550 mM at pH of 10.5).[26] which allows to achieve greater electrodeposition rates. Although few works investigated the electrodeposition of Te in alkaline baths, these works were focused on the electrochemical kinetic studies where they investigated the reduction of TeO_3^{2-} (IV) to Te(0), then to Te_2^{2-} (-I).[27, 28] The presence of Te_2^{2-} (-I) was also detected by Mishra *et al.* who observed the oxidation of Te^{2-} (-II) to Te(0) using a rotating ring-disk electrode. [29] Shinagawa *et al.* investigated the reduction of Te_2^{2-} (-I) to Te^{2-} (-II),[26, 30]. [27, 31]

In this study, systematic studies were performed to deposit dense Te thick films with high current efficiency and deposition rate. Electrolyte compositions including TeO_3^{2-} concentration and pH were optimized to achieve the goals. Applied potentials were also systematically varied to understand their effects on the deposition rate and morphology of

Te films. The carrier concentration of as-deposited Te films was examined by Mott-Schottky, and the effect of grain size on carrier concentration was discussed.

4.3 Experimental

All solutions were prepared by dissolving various amounts of tellurium dioxide (TeO_2, 99+%, Acros Organics) in alkaline solutions, and pH of the solutions were adjusted by sodium hydroxide (NaOH, 10 N, Fisher Chemical). All the electrodeposition experiments were performed in a conventional three-electrode cell using a rotating disk electrodes (RDE) (gold or tellurium/gold coated copper embedded in a cylindrical Teflon holder (6.4 mm in diameter)) as the working electrodes, platinum coated titanium stripe as the counter electrode, and saturated Ag/AgCl as the reference electrode. The Te electrode was fabricated by electrodeposition 50 micron thick Te on an Au electrode. The reaction temperature was kept constant at 23 ^{o}C. For most of experiments, the agitation rate was also fixed at 2000 rpm to minimize the mass transfer effect. All the solutions are deaerated by bubbling high purity N_2. [32]

Linear sweep voltammograms (LSVs) and potentiostatic electrodeposition were conducted to investigate electrodeposition mechanism of Te and their effect on the deposition rate, current efficiency, morphology and crystallinity. The effect of TeO_3^{2-} concentration was investigated by varying the TeO_3^{2-} concentration from 50 to 550 mM with a fixed solution pH of 12.0. The pH effect was investigated by varying the solution pH from 10.2 to 14.7 (calculated value), while fixing the TeO_3^{2-} concentration of 550 mM. To investigate the electrochemical reduction sequence of Te (Te(IV) to Te(0), Te(0) to Te(-I)), Te electrodes were used as the working electrodes where TeO_3^{2-} concentration and

solution pH were varied from 0 and 300 mM and 12.5 and 14.7, respectively. The agitation effect was investigated by varying the rotation rate from 0 to 2000 rpm at the fixed TeO_3^{2-} concentration of 300 mM and pH of 12.5. For most of potentiostatic deposition of Te films, the applied potential was fixed at -0.9V vs. sat. Ag/AgCl. The applied potential effect on the Te morphology was investigated by varying the applied potential from -0.8 to -1.9 V vs. sat. Ag/AgCl at fixed TeO_3^{2-} concentration of 300 mM.

The morphology and crystal orientation of the thick Te films were studied by scanning electron microscopy (TESCAN VEGA) and X-ray diffraction (XRD, PANalytical Empyrean). The current efficiency during electrodeposition of thick Te films was calculated using the action measured mass of electrodeposited thick Te films divided by the mass calculated from charge based on chronoamperograms. The Mott-Schottky analysis was conducted using the same electrochemical cell as electrodeposition at frequency of 10K Hz to determine the carrier concentration of the Te films. The solution used for Mott-Schottky analysis was 0.2 M $NaClO_4$ aqueous solution and the voltage range is from -0.1 to -0.5 V.

4.4 Results and discussion

The Te reactions and hydrogen gas evolution in alkaline solutions was investigated by LSV (figure 4.1). According to the Pourbaix diagram, in alkaline solution TeO_3^{2-} can be reduced to $Te_{(0)}$ (reaction 4.1), then to Te_2^{2-} (reaction 4.2). Furthermore, Te_2^{2-} can be reduced to Te^{2-} (reaction 4.4). [26] The three solid LSV curved shown the reduction of TeO_3^{2-} to $Te_{(0)}$ (solid black), reduction of $Te_{(0)}$ to Te_2^{2-} (solid red), and hydrogen gas evolution reaction (solid blue) at pH of 12.5. In the solid black curve, the increase in current

density at applied potential of -0.74 V vs sat. Ag/AgCl is caused by the reduction of TeO_3^{2-} to $Te_{(0)}$. In the solid red curve, the reduction of TeO_3^{2-} to $Te_{(0)}$ cannot occur because absence of TeO_3^{2-}, so the onset potential (-0.98 V) of the LSV curve indicate the reduction of $Te_{(0)}$ to Te_2^{2-}, which was confirmed by the observation that the Te electrode was dissolving and the solution became purple in color. [26] Gray particles were also observed during the LSV, which was probably caused by the disproportionation of Te_2^{2-} to $Te_{(0)}$ and Te^{2-}. This disproportionation reaction was previously reported by Blanc et al.[33] After the dip point (-1.72 V), the current density started to decrease because the Te electrode is almost completed dissolved, and the Au was exposed in the solution. The further increase in current density at more negative applied potential was caused by the reduction of Te_2^{2-} to Te^{2-} and hydrogen gas evolution. According to the solid blue curve hydrogen gas evolution reaction at pH of 12.5 was triggered at -1.72 V vs sat. Ag/AgCl. However, the hydrogen gas evolution was difficult to observe because of the agitated solution. At pH of 12.5 (solid curve), the difference in onset potentials between reaction TeO_3^{2-} to Te (reaction 4.1) and Te to Te_2^{2-} (reaction 4.3) is 0.24 V. However, at pH of 14.7 (dashed curve), the difference is 0.08 V, in which the onset potential for reaction 4.1 and 4.3 were -0.84 V and -0.92 V, respectively. Because Te_2^{2-} is a solvable species, the reduction reaction of $Te_{(0)}$ to Te_2^{2-} deteriorate the morphology of thick Te film significantly. To electrodeposit dense Te films, the applied potential should be negative enough to reduce TeO_3^{2-} to Te, but not negative enough to trigger the dissolution of $Te_{(0)}$ to Te_2^{2-}. As a consequence, at pH of 12.5 the applied potential window to deposit thick Te films with dense morphology is larger than that at pH of 14.7. Furthermore, at pH of 14.7 (dashed red curve), the Te dissolution rate

was faster than that at pH of 12.5 (red solid curve). For example, when the applied potential was -1.05 V, the current density at pH of 12.5 was -4.7 mA/cm^2, but the current density at pH of 14.7 was 162.1 mA/cm^2, which is about 34 times higher.

The LSV investigation of reduction reactions of TeO_3^{2-} in alkaline solutions as a function of pH is shown in Figure 4.2. At pH of 10.2 and 12.5, the current density started to increase at -0.66 and -0.71 V vs sat. Ag/AgCl, respectively. The increase in current density was caused by the reduction of TeO_3^{2-} to $Te_{(0)}$ which was confirmed by the fact that at applied potential of -0.9 V vs sat. Ag/AgCl a thick Te film was electrodeposited. However, the LSV curves at pH of 10.2 and 12.5 did not show the second reduction wave or a maximum current density wave. [31] The current density increased monotonically as applied potential became more negative. The reported LSV studied about TeO_3^{2-} in alkaline solutions were conducted with low TeO_3^{2-} concentration (0.1 to 10 mM).[27, 31, 34-36] In this case, after the reduction of TeO_3^{2-} to Te happened, it showed the diffusion current because of mass transfer limitation.[27] Once the further reduction of $Te_{(0)}$ to Te_2^{2-} was triggered, another reduction wave appeared. After the second wave, there was a maximum current was because the generated Te_2^{2-} can react with the TeO_3^{2-} ions near the working electrode, resulting in a screening effect which hindered diffusion of TeO_3^{2-} toward the electrode surface.[31] In this study, the TeO_3^{2-} concentration was high (550 mM) and the solution was well agitated using a rotating disk electrode; therefore, the LSV curve did not show the diffusion current. Although the second reduction wave did not show, the reduction of $Te_{(0)}$ to Te_2^{2-} (reaction 4.3) was expected to occur. Additionally, Te_2^{2-} ions were not stable in the solution, which meant that it reacted with TeO_3^{2-} to chemically

deposit Te before it can diffuse into the bulk solution. Furthermore, the TeO_3^{2-} ions were replenished because of high TeO_3^{2-} concentration and agitation. As a result, the screening effect, which caused the maximum wave, was not apparent leading to the fact that the LSV curves at pH of 10.2 and 12.5 did not show the second reduction wave (Te to Te_2^{2-}).

At pH of 14.7, onset potential was -0.86 V vs sat. Ag/AgCl, the increase in current density was due to the reduction of TeO_3^{2-} to Te, confirmed by the fact that at applied potential of -0.9 V, Te film was electrodeposited. Compared with the LSV curves at pH of 10.2 and 12.5, the LSV have a maximum wave. The reason is that in high pH (14.7) solution, Te_2^{2-} is relatively stable [30] and its formation rate is high (figure 4.1 dashed red curve), so there is enough time for Te_2^{2-} to diffuse into the bulk solution to react with TeO_3^{2-} (reaction 4.5) caused the screening effect. This screening effect was confirmed by the observation that black particles were formed in the solution and gold substrate was re-exposed. The synthesis of Te particle through reaction 4.5 was discussed in our previous publications. [28, 31] The sharp spike in current density at -1.8 V may be caused by a hydrogen gas evolution reaction. [26] At the dip point (-1.25 V), the deposited Te on gold substrate was completely dissolved caused by the reduction of Te to Te_2^{2-} (reaction 4.3). The applied potential to trigger reaction 4.3 was more positive than dip point (-1.25 V), which was confirmed by the LSV curves in figure 4.1 (dashed red curve). Additionally, the mixed potentials were extracted from the Tafel plot (insert of figure 4.2). Figure 4.21 showed that the mixed potential decreased from -0.39 to -0.44 V vs. sat. Ag/AgCl when pH increased from 10.2 to 14.7.

$TeO_3^{2-}(aq) + 3H_2O(l) + 4e^- \rightarrow Te(s) + 6OH^-(aq)$($E_0$ = - 0.45 V vs. sat. Ag/AgCl)

Reaction 4.1

$2H_2O(l) + 2e^- \rightarrow H_2(g) + 2OH^-(aq)$ (E_0 = - 0.90 V vs. sat. Ag/AgCl)

Reaction 4.2

$2Te(s) + 2e^- \rightarrow Te_2^{2-}(aq)$ (E_0 = -0.91 V vs. sat. Ag/AgCl)

Reaction 4.3

$Te_2^{2-}(aq) + 2e^- \rightarrow 2Te^{2-}(aq)$ (E_0 = -1.47 V vs. sat. Ag/AgCl)

Reaction 4.4

$TeO_3^{2-}(aq) + 2Te_2^{2-}(aq) + 3H_2O(l) \rightarrow 5Te(s) + 6OH^-(aq)$($\Delta G^O$ = -164.1 kJ/mol)

Reaction 4.5

$TeO_3^{2-}(aq) + 2Te^{2-}(aq) + 3H_2O(l) \rightarrow 3Te(s) + 6OH^-(aq)$($\Delta G^O$ = -279.3 kJ/mol)

Reaction 4.6

LSV of TeO_3^{2-} in alkaline solutions at different agitation rates are shown in figure 4.3. The insert image is the full scale LSV curves. At the same applied potential, the current density increased as agitation rate increase from 0 to 2000 rpm. For example, at applied potential of -0.9 V vs. sat. Ag/AgCl, when the agitation rate increased from 0 to 1000 to 2000 rpm, the current density increased from 12.9 to 22.0 to 27.8 mA/cm^2. This is because the mass transfer rate was enhanced by convection. When the agitation rate increased from 1000 to 2000 rpm, the LSV curve essentially did not change except for the increase in current density. However, at agitation rate of 0 rpm, the sharp of LSV curve was significantly different. When the applied potential was more negative than -1.07 V, the current density started to fluctuate instead of increasing monotonically. Although the

TeO_3^{2-} concentration in the solution is relatively high (300 mM), the replenishment of TeO_3^{2-} ion was insufficient without agitation. Therefore, the screening effect may still occur, leading to the decline of current density. The fluctuation was probably attributed to the combination of Te electrodeposition (reaction 4.1), Te dissolution (reaction 4.3), Te chemical deposition (reaction 4.5 and 4.6) and insufficient TeO_3^{2-} mass transfer rate. Furthermore, the agitation also played a critical role to controlling the morphology of thick Te films, which will be discussed later.

The effect of applied potential on the morphology of Te thick films was investigated and the results are shown in figure 4.4. At applied potential of -0.8 and -0.9 V vs. sat. Ag/AgCl, based on LSV curve in figure 4.1 (solid black curve) the only Te reduction reaction that occurred was reaction 4.1. The electrodeposited Te film was dense and cluster growth (figure 4.4 A-B). The top view SEM images clearly show well-developed crystal facet. At -0.8 V vs. sat. Ag/AgCl, the SEM image (figure 4.4B) showed triangle and star sharped micro structure on top of Te films. When the applied potential increased to -0.9 V vs. sat. Ag/AgCl, the top view SEM image also showed the triangle and star shaped micro structure, but the star shaped micro structure growth was larger and became dominant. According to the XRD data (figure 4.7), the sharp diffraction peaks indicate that the electrodeposited Te films were well crystallized. The XRD patterns of the Te thick films match with the standard reference data (JCPDS-International Center for Diffraction Data, No. 36-1452). The un-indexed peak at 29.5 degree is attributed to the reflection of a frequency doubling radiation wave.[37]

The preferred orientation of electrodeposited Te films was (003), which is in the c-direction. This crystal growth direction for Te is typical, especially for the synthesis of Te nanostructures such as nanowires[38], nanotubes[39], nanobelts [37] and so on. Te crystals preference to grow along the c-direction is because of its anisotropic crystal structure [40]. At applied potential of -1.0 V, although the deposited Te film was still a dense morphology, the surface morphology showed nodule instead of facet according to the SEM image (figure 4.4C). Additionally, the crystal orientation with highest diffraction intensity was (101), which is consistent with the reference data (JCPDS, No. 36-1452). According to the LSV curves shown in figure 4.1 (solid red curve), the applied potential (-1.0 V) is high enough to trigger the dissolution of Te to Te_2^{2-} (reaction 4.3), although the reaction rate of reaction 4.3 is expected to be low because of the small overpotential. Te_2^{2-} is an intermediate state, which is not stable in the solution and interacts with TeO_3^{2-} to form Te (reaction 4.5). This reaction has been used to synthesize Te nanorices which is reported in our previous publication.[41] Te synthesized through reaction 4.5 should lead to suspended particles in the solution. However, this phenomenon was not observed during electrodeposition of thick Te films (i.e.: the solution was clear). The reason was that at high TeO_3^{2-} concentration, the formed Te_2^{2-} reacted with TeO_3^{2-} locally and had no time to diffuse from the electrode surface into the bulk solution, therefore the Te synthesized though reaction 4.5 redeposited onto the Te film. The dissolution (reaction 4.3) and redeposit (reaction 4.5) of Te disturbed the growth of the Te film along the c-direction and made it more randomly oriented.

When the applied potential was more negative than -1.1 V, the rate of reaction 4.3 increased significantly, leading to the deterioration of Te morphology. Figure 4.15 shows that porous Te films was electrodeposited at applied potential of -1.1 to -1.9 V. At applied potential of -1.1 and -1.2 V, although the morphology of Te film has a porous structure, it still shows crystallized facet. As the applied potential increased to -1.4, -1.75 and -1.9 V the crystal facets were not observed. The chronoamperograms of Te electrodeposition is shows in figure 4.14. The cathodic current density increased when the applied potential became more negative, which was expected. At applied potential of -0.8, -0.9 and -1.0 V, the current density was relatively stable, which meant that it did not change significantly as a function of time. However, when the applied potential is more negative than -1.1 V, the current density increase as reaction time increase, which was attributed to the increase of actual surface area of working electrode caused by porous morphology.

Another critical factor to control morphology of Te films is pH. If pH is not in the right range, even the applied potential is not negative enough to trigger the reduction of Te to Te_2^{2-} (reaction 4.3), the electrodeposited film would be porous. When pH is 10.5, Te film was dendritic (figure 4.5A). At pH of 11.3 to 12.5, the electrodeposited Te films had a dense morphology (figure 4.5B-C). However, when pH was further increased to 13.6 and 14.7 (figure 4.5D-E), the morphology became porous. The XRD data figure 4.17) showed that the dense thick Te films electrodeposited at pH of 11.3 and 12.5 have much higher intensity caused by the better developed Te crystal with preferred orientation of (003). The change of morphology was probably caused by change of the rate limited step of reduction reaction (TeO_3^{2-} to Te), which will be reported in next paper with kinetic data.

Agitation also plays an important role to electrodeposit a dense Te film. Without agitation, the electrodeposited Te film was porous (figure 4.6A), which meant that even at high TeO_3^{2-} concentration (300 mM), convection was necessary to enhance the mass transfer rate to make the reaction in kinetic control instead of mass-transfer control. When the agitation rate increase to 1000 rpm, the deposited film became denser, but it was nodular growth (figure 4.6B). At agitation rate of 2000 rpm, the Te films had a dense morphology (figure 4.6C), and the top view image shows that top morphology of Te films had well-developed facets. According to the XRD (figure 4.16), at 2000 rpm the electrodeposited thick Te film had preferred orientation of (003).

Variation of TeO_3^{2-} concentration will not change the morphology of the Te film significantly (figure 4.13). At the TeO_3^{2-} range (50 to 550 mM), dense thick Te films were electrodeposited. The top view SEM image showed that the films have crystal facets. Additionally, the TeO_3^{2-} concentration has a significant effect on the deposition rate. Higher TeO_3^{2-} concentrations resulted in higher deposition rates (figure 4.10). Additionally, the mixed potentials at different TeO_3^{2-} concentration were extracted from the Tafel plot (insert of figure 4.10). Figure 4.22 showed that the mixed potential decreased from -0.46 to -0.70 V vs sat. Ag/AgCl when TeO_3^{2-} concentration increased from 50 to 550 mM.

To investigate the effect of electrodeposition conditions on grain sizes, twelve thick dense Te films were synthesized at TeO_3^{2-} concentration of 300 and 500 mM, pH of 11.3 and 12.5, and applied potential of -0.8, -0.9 and -1.0 V. The grain size (figure 4.9) of the films was calculated from XRD data based on the Scherrer equation. The grain size ranged from 66 to 135 nm, the largest grain size was achieved at TeO_3^{2-} concentration of 300 mM,

pH of 12.5, and applied potential of -0.9 V. Film growth rate (figure 4.18) was calculated using the thickness of the films measured from SEM image divided by the electrodeposition time. According to figure 4.18, the TeO_3^{2-} concentration and the applied potential have a significant effect on deposition rate, in which high TeO_3^{2-} concentration and more negative applied potential lead to higher deposition rates. This can be explained by Butler-Volmer equation. Compared with TeO_3^{2-} concentration and applied potential, solution pH has only a minor effect on the deposition rate. The highest deposition rate (130 μm/h) was achieved at TeO_3^{2-} concentration of 550 mM, pH of 12.5, and applied potential of -1.0 V. According to figure 4.19, the current efficiency during electrodeposition is higher than 85%. The condition to deposit dense thick Te films with highest deposition rate had a current efficiency of 96%.

Tellurium is an elemental chalcogen semiconductor, which belongs to the so called lone-pair semiconductors. In tellurium, the lone-pair orbitals ($5p^4$) form the upper part of the valence band. If the crystalline network contains defects with unsaturated chemical bonds (dangling bonds), the interaction between these defects and the lone-pair electrons occurs. The dangling bond interacts with the neighboring lone-pair, bonding with it by distorting its environment. Such interaction results in the release of holes which makes extrinsic tellurium always a p-type semiconductor.[42, 43] Carrier concentration of Te film was reported by several research groups. Champness calculated the intrinsic carrier concentration in tellurium at room temperature using measured values of electrical conductivity, Hall coefficient, and transverse magnetoresistance. The result showed that the intrinsic carrier concentration in tellurium was 3.7 to 5.0 × 10^{15} cm^{-3}. [44] Alexis De

vos et al. investigated the carrier concentration of thin evaporated tellurium films (13 nm thickness) using resistivity and Hall voltage which were made by Van der Pauw's method. The carrier concentration of tellurium was 4.0 to 12.0 × 10^{18} cm^{-3}. [45] Okuyama reported the carrier concentration of tellurium films with various grain size and the data showed the same trend that a small grain Te film had higher carrier concentration. The grain sizes of Te films were 1500, 400 and 100 nm with the carrier concentration of 1.0 × 10^{17}, 1.0 × 10^{19} and 4.0 × 10^{19} cm^{-3}, respectively. [46]

To determine carrier concentration, thick dense Te films were characterized by Mott-Schottky analysis [47] in this work. The raw data were presented in figure 5.8. Figure 5.9 showed that texture coefficient had no effect on the carrier concentration. However, grain size had an essential effect on carrier concentration. Smaller grain size resulted in higher defect density, leading to higher carrier concentration. This trend was probably caused by the reason that Te films with smaller grain size have larger number of structural defects, resulting in a higher carrier concentration. [45, 48] The lowest carrier concentration was 7.1 × 10^{18} cm^{-3}, where the thick Te film had a grain size of 135 nm and was electrodeposited in the solution with 550 mM TeO_3^{2-} at pH of 12.5 and applied potential of -0.9 V. The highest carrier concentration was 3.0 × 10^{19} cm^{-3}, where the thick Te film had a grain size of 69 nm and was electrodeposited in the solution with 300 mM TeO_3^{2-} at pH of 11.3 and applied potential of -0.8 V.

4.5 Conclusion

In summary, the synthesis of thick, dense Te films were demonstrated by electrodeposition in alkaline solution. To achieve dense morphology, applied potential should be more positive than -1.0 V to avoid further reduction of Te to Te_2^{2-} or keep the reduction of Te to Te_2^{2-} at a low reaction rate, because this reduction reaction would deteriorate the film morphology significantly. The XRD data showed that when applied potential changed from -0.9 V to -1.0 V, the preferred orientation of thick Te film varied from (001) to (101), due to the dissolution of Te by reaction 4.3. The proper pH range to deposit dense thick film is 11.3 to 12.5. Sufficient agitation (2000 rpm) is necessary to electrodeposit a dense film. Grain size of the thick Te films was from 66 to 135 nm, which is controlled by applied potential, TeO_3^{2-} concentration and pH. The larger grain size resulted in lower carrier concentration due to less crystal defects. The lowest carrier concentration was 7.1×10^{18} cm^{-3}, where the thick Te film had a grain size of 135 nm. The Highest deposition rate was 130 μm/h achieved by high TeO_3^{2-} concentration (550 mM) and more negative applied potential (-1.0 V). The Current efficiency for electrodeposition of Te thick films was higher than 85% in alkaline solution.

4.6 Reference

1. Liu, J.-W., et al., *Mesostructured Assemblies of Ultrathin Superlong Tellurium Nanowires and Their Photoconductivity.* Journal of the American Chemical Society, 2010. **132**(26): p. 8945-8952.
2. Wang, Y., et al., *Mirror-Like Photoconductive Layer-by-Layer Thin Films of Te Nanowires: The Fusion of Semiconductor, Metal, and Insulator Properties.* Advanced Materials, 2006. **18**(4): p. 518-522.

3. Lee, T.I., et al., *High-Power Density Piezoelectric Energy Harvesting Using Radially Strained Ultrathin Trigonal Tellurium Nanowire Assembly.* Advanced Materials, 2013. **25**(21): p. 2920-2925.

4. Zhang, M., et al., *A Rapid Room-Temperature NO2 Sensor Based on Tellurium–SWNT Hybrid Nanostructures.* The Journal of Physical Chemistry C, 2012. **116**(37): p. 20067-20074.

5. Park, H., et al., *Branched tellurium hollow nanofibers by galvanic displacement reaction and their sensing performance toward nitrogen dioxide.* Nanoscale, 2013.

6. Fujiwara, S.-i., et al., *A marvelous catalysis of tellurium in the formation of isothiocyanates from isocyanides and sulfur.* Tetrahedron Letters, 1992. **33**(46): p. 7021-7024.

7. Kambe, N., et al., *Tellurium-catalyzed Carbonylation of Amines with Carbon Monoxide.* Bulletin of the Chemical Society of Japan, 1981. **54**(5): p. 1460-1464.

8. Bradstreet, R.B., *Comparison of Tellurium and Selenium as Catalysts for Kjeldahl Digestion.* Analytical Chemistry, 1949. **21**(8): p. 1012-1013.

9. LaLonde, A.D., et al., *Lead telluride alloy thermoelectrics.* Materials Today, 2011. **14**(11): p. 526-532.

10. Fleurial, J.P., et al. *Power density-length of leg _ Thick-film thermoelectric microdevices*. in *Thermoelectrics, 1999. Eighteenth International Conference on*. 1999.

11. Semeniouk, V. and J.-P. Fleurial. *Temperature diff - thickness _ Modeling and Minimization of Intercascade Thermal Resistance in Multi-Stage Thermoelectric Cooler*. in *XVI Int. Conf. Thermoelectrics*. 1997. Dresden, Germany: IEEE.

12. Anatychuk, L.I., O.J. Luste, and L.N. Vikhor. *Optimal functions as an effective method for thermoelectric devices design*. in *Thermoelectrics, 1996., Fifteenth International Conference on*. 1996.

13. Anatychuk, L.I. and O.J. Luste. *Thickness limitation- lower limit_ Physical principles of microminiaturization in thermoelectricity*. in *Thermoelectrics, 1996., Fifteenth International Conference on*. 1996.

14. Snyder, G.J., et al., *Thermoelectric microdevice fabricated by a MEMS-like electrochemical process.* Nat Mater, 2003. **2**(8): p. 528-531.

15. Mattox, D.M., *Handbook of Physical Vapor Deposition (PVD) Processing (Second Edition)*2010, Boston: William Andrew Publishing. 1-24.

16. Dini, J.W., *Electrodeposition - the materials science of coating and substrates*1993, Westwood, New jersey: Noyes Publications.

17. van Ngać, N., O. Vittori, and G. Quarin, *Voltammetric and chronoamperometric studies of tellurium electrodeposition of glassy carbon and gold electrodes.* Journal of Electroanalytical Chemistry and Interfacial Electrochemistry, 1984. **167**(1–2): p. 227-235.

18. Qiu, C.X. and I. Shih, *Epitaxial growth of tellurium by electrodeposition.* Materials Letters, 1989. **8**(8): p. 309-312.

19. Suggs, D.W. and J.L. Stickney, *Characterization of atomic layers of tellurium electrodeposited on the low-index planes of gold.* The Journal of Physical Chemistry, 1991. **95**(24): p. 10056-10064.

20. Ikemiya, N., et al., *Atomic structures and growth morphologies of electrodeposited Te film on Au(100) and Au(111) observed by in situ atomic force microscopy.* Surface Science, 1996. **369**(1–3): p. 199-208.

21. Yagi, I., et al., *In situ optical second harmonic generation studies of electrochemical deposition of tellurium on polycrystalline gold electrodes.* Journal of Electroanalytical Chemistry, 1996. **401**(1–2): p. 95-101.

22. Sorenson, T.A., et al., *Phase transitions in the electrodeposition of tellurium atomic layers on Au(100).* Journal of Electroanalytical Chemistry, 1999. **467**(1–2): p. 270-281.

23. Sorenson, T.A., et al., *Formation of and phase transitions in electrodeposited tellurium atomic layers on Au(1 1 1).* Surface Science, 2001. **470**(3): p. 197-214.

24. Jiang, C.H., et al., *Electrodeposition of tellurium film on polyaniline-coated macroporous phenolic foam and its thermopower.* Journal of Porous Materials, 2011. **19**(5): p. 819-823.

25. Abad, B., et al., *Thermoelectric properties of electrodeposited tellurium films and the sodium lignosulfonate effect.* Electrochimica Acta, 2015. **169**: p. 37-45.

26. Pourbaix, M., *Atlas of electrochemical equilibria in aqueous solutions*1966, Long Island City, N.Y.: Pergamon Press Inc.

27. Lingane, J.J. and L.W. Niedrach, *Polarography of Selenium and Tellurium. II. The + 4 States.* Journal of the American Chemical Society, 1949. **71**(1): p. 196-204.

28. Wu, T., et al., *Synthesis of Tellurium Heterostructures by Galvanic Displacement Reaction of Zinc in Alkaline Baths.* Electrochimica Acta, 2014. **150**(0): p. 298-307.

29. Mishra, K.K., D. Ham, and K. Rajeshwar, *Anodic Oxidation of Te Ions - alkaline - Te22- detected - RDE.* Journal of The Electrochemical Society, 1990. **137**(11): p. 3438-3441.

30. Panson, A.J., *POLAROGRAPHY OF THE DITELLURIDE ION.* The Journal of Physical Chemistry, 1963. **67**(10): p. 2177-2180.

31. Shinagawa, M., N. Yano, and T. Kurosu, *Mechanism and analytical aspects of the polarographic maximum wave of tellurium.* Talanta, 1972. **19**(4): p. 439-450.

32. Butler, I.B., M.A.A. Schoonen, and D.T. Rickard, *Removal of dissolved oxygen from water: A comparison of four common techniques.* Talanta, 1994. **41**(2): p. 211-215.

33. Blanc, M.L., *Can an element form both positive and negative ions.* Zeitschrift fuer Elektrochemie und Angewandte Physikalische Chemie, 1905. **11**: p. 813-18.

34. Schmidt, H., *Te - reduction in alkaline bath - Polarographic behavior of tellurites and tellurates.* Journal of the Polarographic society, 1962. **8**: p. 49-57.

35. Shinagawa, M., et al., *Te alkaline&acidic baths - reduction reactions - Studies on the prewave of tellurium and its photo-effect.* Journal of Electroanalytical Chemistry and Interfacial Electrochemistry, 1977. **75**(2): p. 809-817.

36. Dergacheva, M.B., V.N. Statsyuk, and L.A. Fogel, *TeO32- reduction - pH 5-10 - limiting current@TeO32- concentration.* Russian Journal of Electrochemistry, 2001. **37**(6): p. 626-628.

37. Mo, M., et al., *Controlled Hydrothermal Synthesis of Thin Single-Crystal Tellurium Nanobelts and Nanotubes.* Advanced Materials, 2002. **14**(22): p. 1658-1662.

38. Gautam, U.K. and C.N.R. Rao, *Controlled synthesis of crystalline tellurium nanorods, nanowires, nanobelts and related structures by a self-seeding solution process.* Journal of Materials Chemistry, 2004. **14**(16): p. 2530-2535.

39. Xi, G., et al., *Synthesis, Characterization, and Growth Mechanism of Tellurium Nanotubes.* Crystal Growth & Design, 2005. **5**(1): p. 325-328.

40. Hippel, A.v., *Structure and Conductivity in the VIb Group of the Periodic System* Journal of Chemical Physics, 1948. **16**: p. 372-380.

41. Wu, T., et al., *Size Controlled Synthesis of Tellurium Nanorices by Galvanic Displacement Reaction of Aluminum.* Electrochimica Acta, 2015. **176**: p. 1382-1392.

42. Kastner, M. and H. Fritzsche, *Defect chemistry of lone-pair semiconductors.* Philosophical Magazine Part B, 1978. **37**(2): p. 199-215.

43. Tsiulyanu, D., et al., *Characterization of tellurium-based films for NO2 detection.* Thin Solid Films, 2005. **485**(1–2): p. 252-256.

44. Champness, C.H., *Calculation of intrinsic carrier concentration in tellurium taking anisotropy into account.* Canadian Journal of Physics, 1976. **54**(9): p. 967-969.

45. Vos, A.D., *The influence of deposition rate on the electrical properties of thin Te films.* Thin Solid Films, 1977. **46**: p. 223-228.

46. Okuyama, K., *Mobility studies of evaporated tellurium films.* Thin Solid Films, 1976. **33**(2): p. 165-171.

47. Windisch, C.F. and G.J. Exarhos, *Mott–Schottky analysis of thin ZnO films.* Journal of Vacuum Science & Technology A, 2000. **18**(4): p. 1677-1680.

48. Capers, M.J. and M. White, *The electrical properties of vacuum deposited tellurium films.* Thin Solid Films, 1973. **15**(1): p. 5-14.

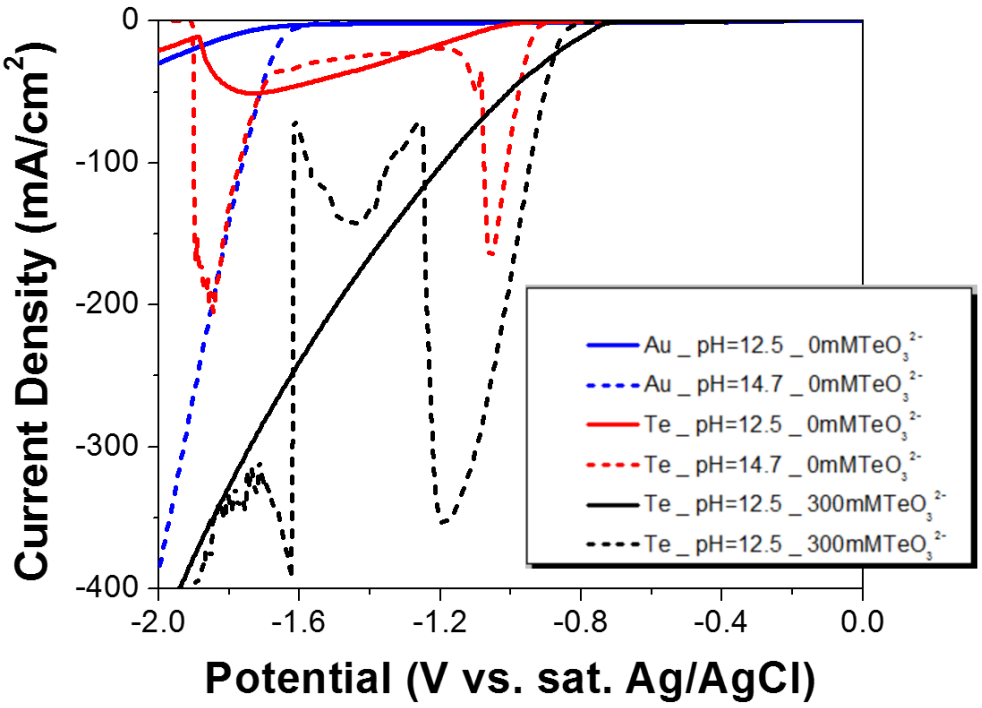

Figure 4.1 LSV curve of Te reactions and hydrogen gas evolution in alkaline solutions. The reduction reaction of TeO_3^{2-} to $Te_{(0)}$ was investigated in the solution with 300 mM TeO_3^{2-} at pH of 12.5 and 14.7 using Te as working electrode. The reduction reaction of $Te_{(0)}$ to Te_2^{2-} was investigated in the solution with 0 mM TeO_3^{2-} at pH of 12.5 and 14.7 using Te as working electrode. Hydrogen gas evolution was studied in the solution with 0 mM TeO_3^{2-} at pH of 12.5 and 14.7 using Au as working electrode.

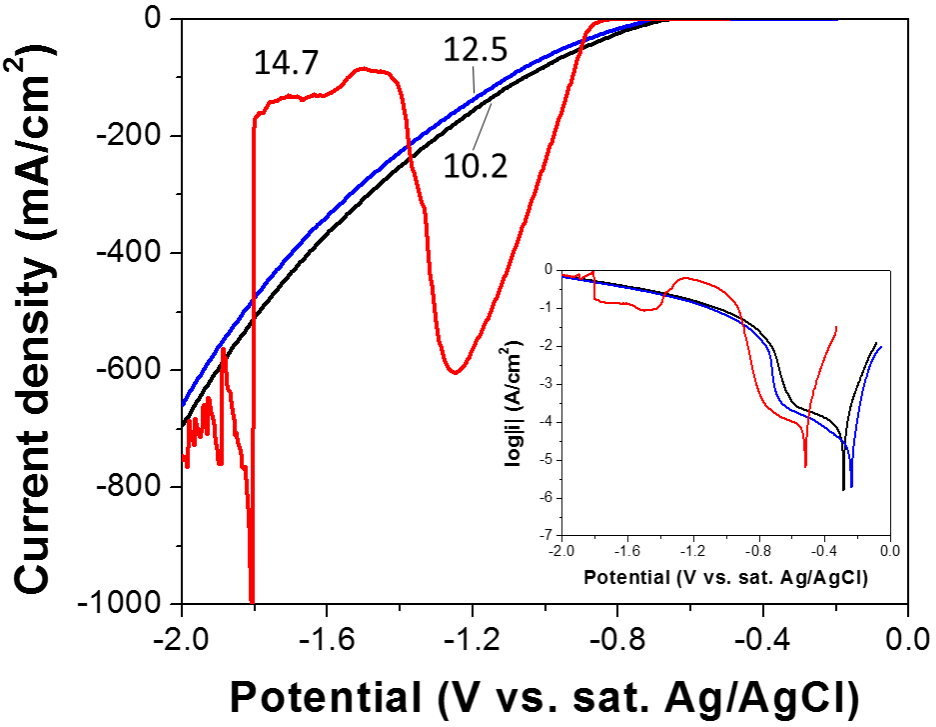

Figure 4.2 LSV curve of TeO_3^{2-} in alkaline solutions at different pH (10.2, 12.5, 14.7). TeO_3^{2-} concentration was fixed at 550 mM and temperature was fixed at 23 ^oC. The substrates were gold coated copper rods. The inserted plot at the bottom right corner is the Tafel plot based on the LSV data.

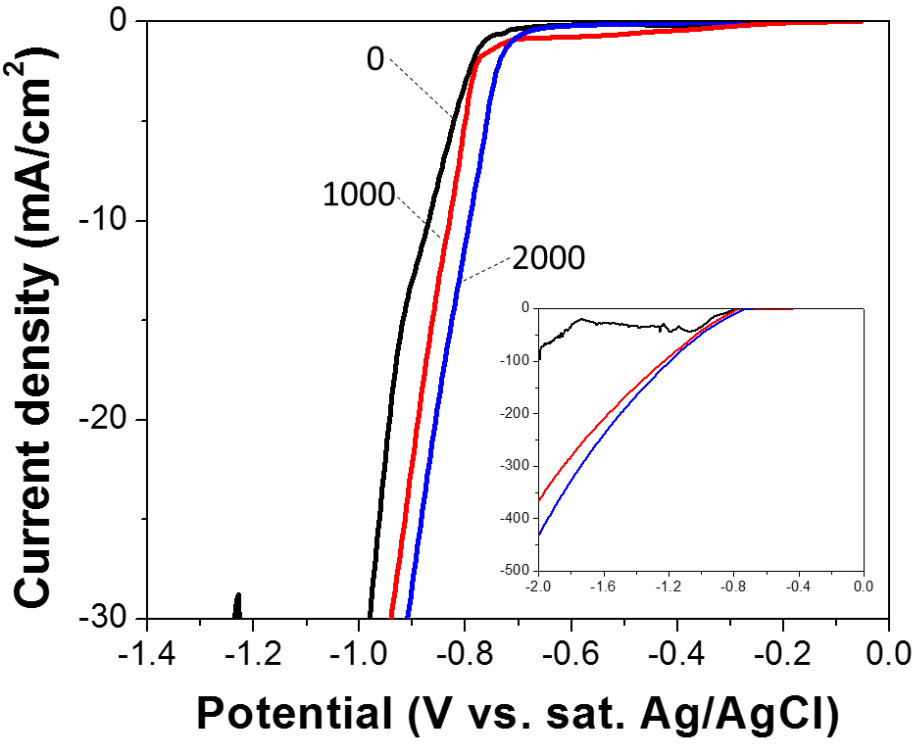

Figure 4.3 LSV curve of TeO_3^{2-} in alkaline solutions at different agitation rate (0, 1000, 2000 rpm). TeO_3^{2-} concentration was fixed at 300 mM, pH was 12.5 and temperature was fixed at 23 ^oC. The substrates were gold coated copper rods.

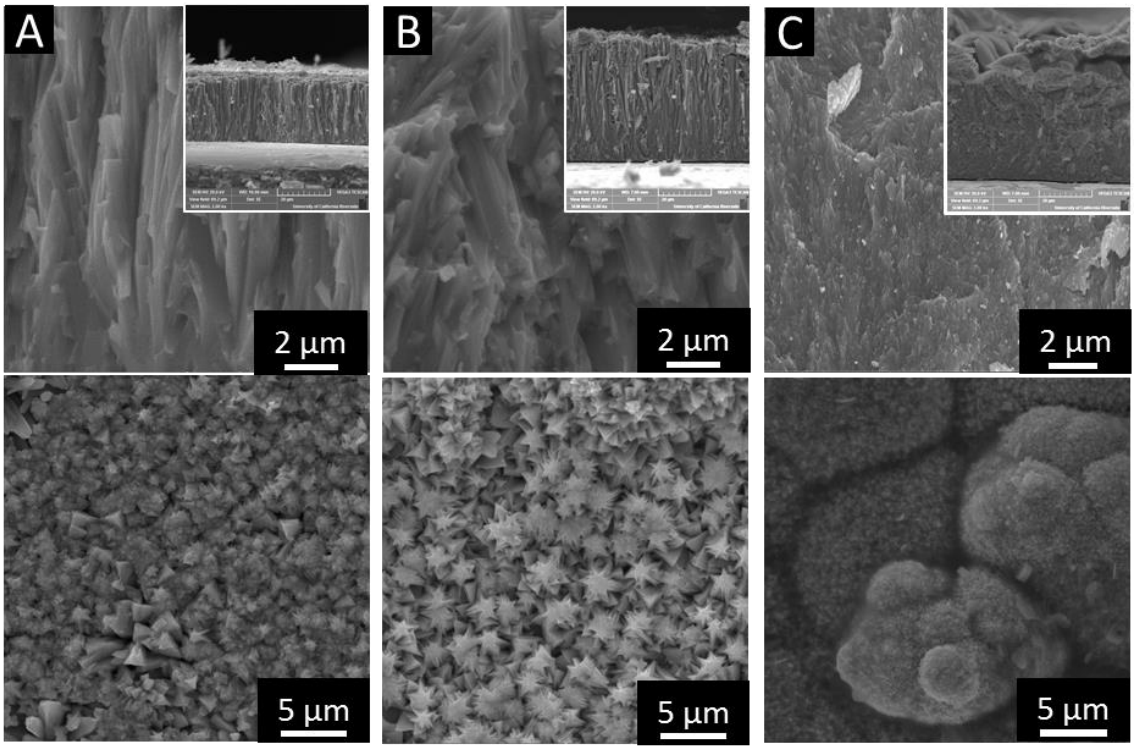

Figure 4.4 SEM images of Te electrodeposited at different applied potential: (A) -0.8, (B) -0.9, and (C) -1.0 V vs. sat. Ag/AgCl with 300 mM TeO_3^{2-} at pH of 12.5 and temperature of 23 ^oC. The top row images are cross-section view, and the bottom row images are top view. The small images at top right corner are the low magnification images.

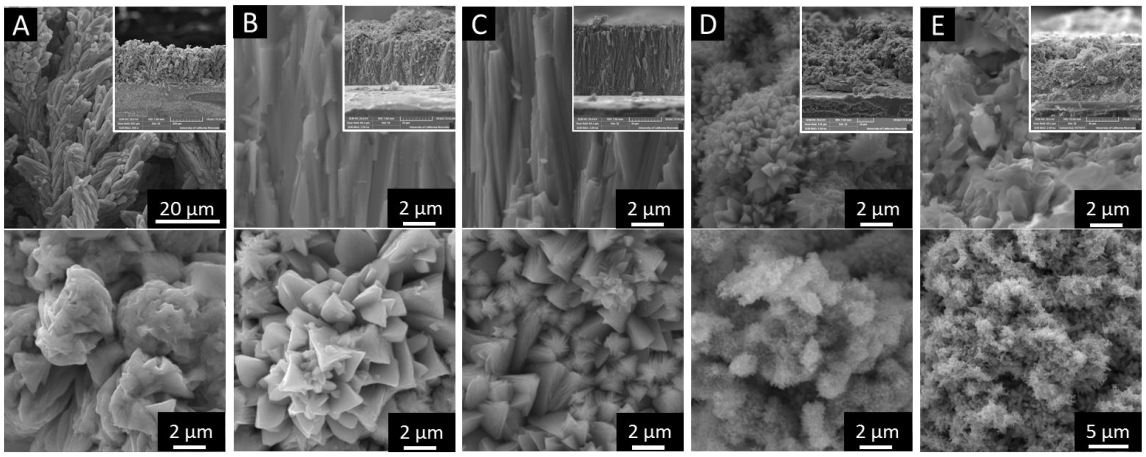

Figure 4.5 SEM images of Te electrodeposited at different pH: (A) 10.2, (B) 11.3, (C) 12.5, (D) 13.6, (E) 14.7, at TeO_3^{2-} of 550 mM, applied potential of -0.9 V vs. sat. Ag/AgCl and temperature of 23 ^{o}C. The top row images are cross-section view, and the bottom row images are top view. The small images at top right corner are the low magnification images.

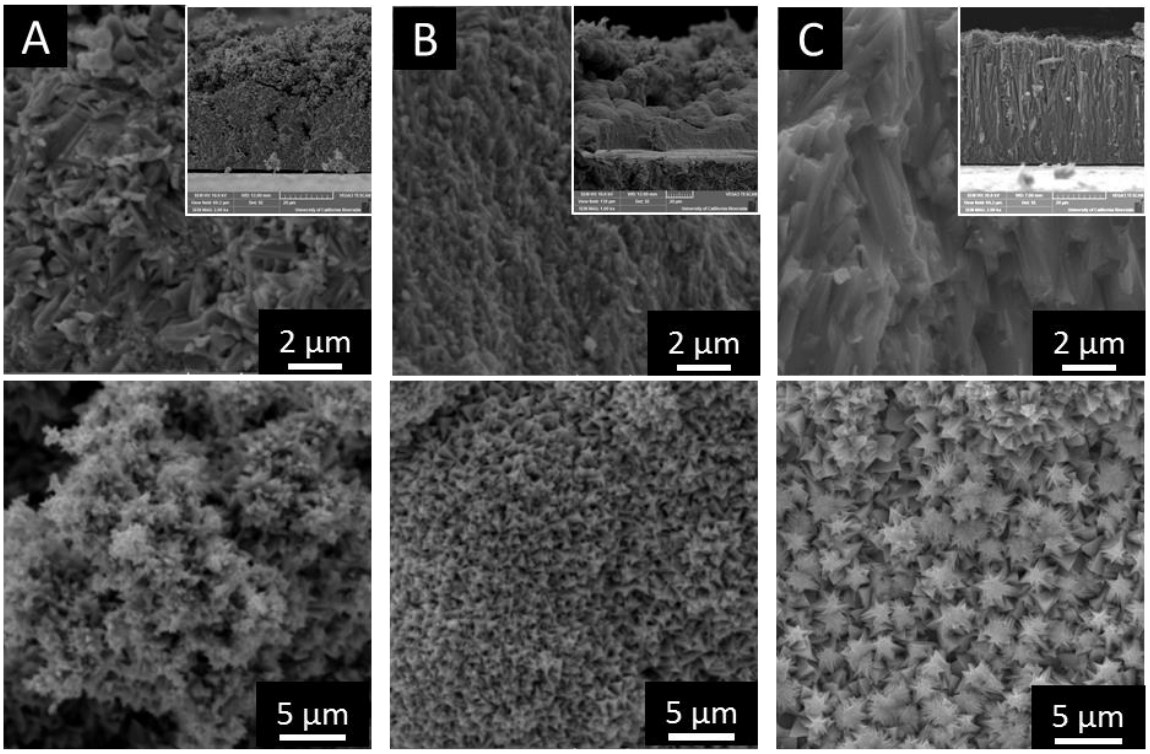

Figure 4.6 SEM images of Te electrodeposited at different agitation: (A) 0, (B) 1000, (C) 2000 rpm with 300 mM TeO_3^{2-} at pH of 12.5, applied potential of -0.9 V vs. sat. Ag/AgCl and temperature of 23 ^oC. The top row images are cross-section view, and the bottom row images are top view. The small images at top right corner are the low magnification images.

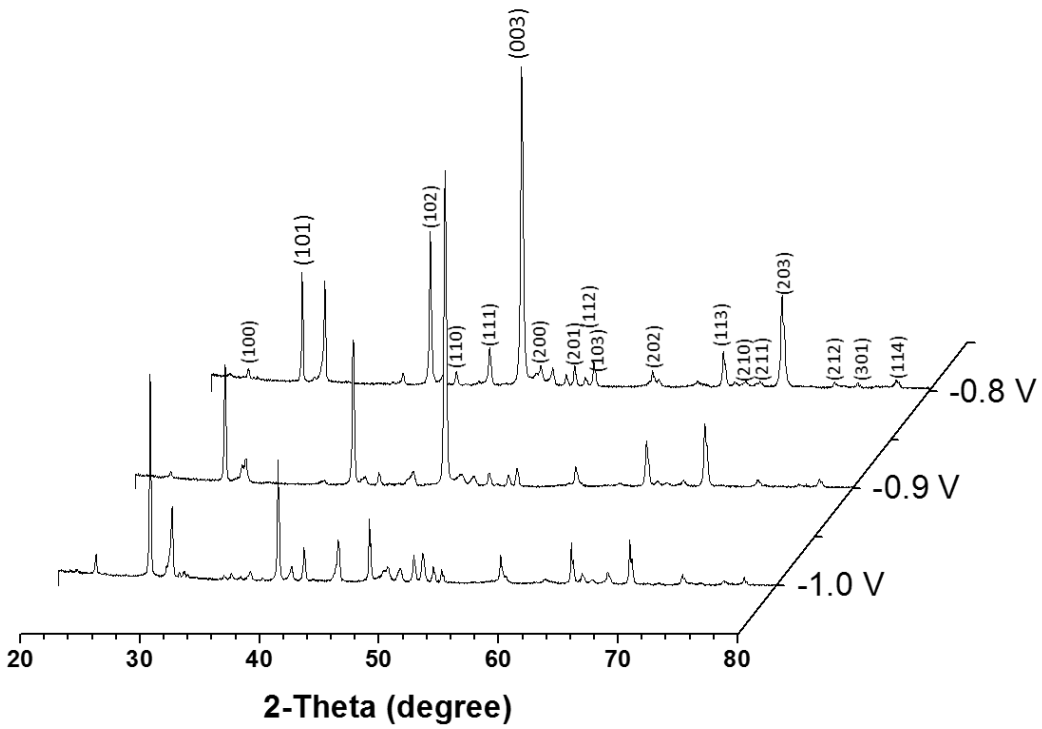

Figure 4.7 (A) The XRD pattern of thick Te films synthesized at different applied potential -0.8, -0.9, and -1.0 V in the electrolyte containing 300 mM TeO_3^{2-} with pH of 12.5 at 23 ^oC. The reference XRD pattern of Te is JCPDS, No. 36-1452.

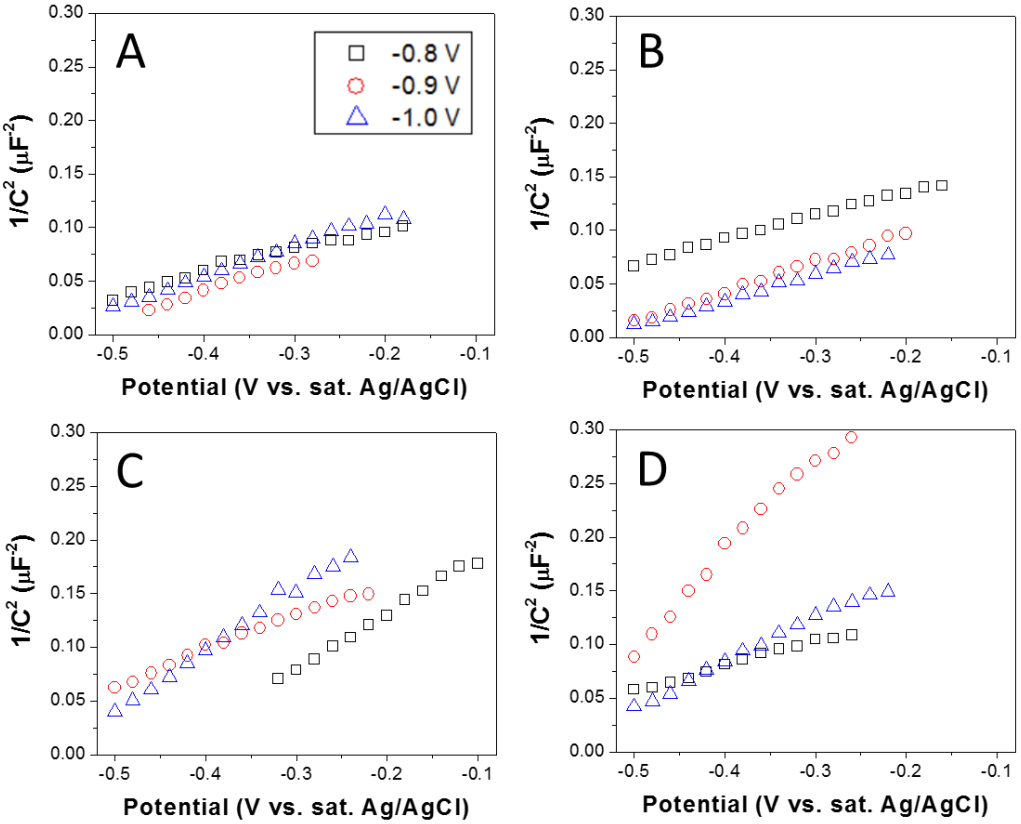

Figure 4.8 Mott-Schottky data of thick Te films synthesis by different applied potential (-0.8, -0.9 and -1.0 V vs. sat. Ag/AgCl), TeO_3^{2-} concentration (300 and 550 mM), and pH (11.3 and 12.5). (A) 300 mM at pH of 11.3, (B) 550 mM at pH of 11.3, (C) 300 mM at pH of 12.5, and (D) 550 mM at pH of 12.5. Mott-Schottky experiments were conducted at frequency of 10K Hz.

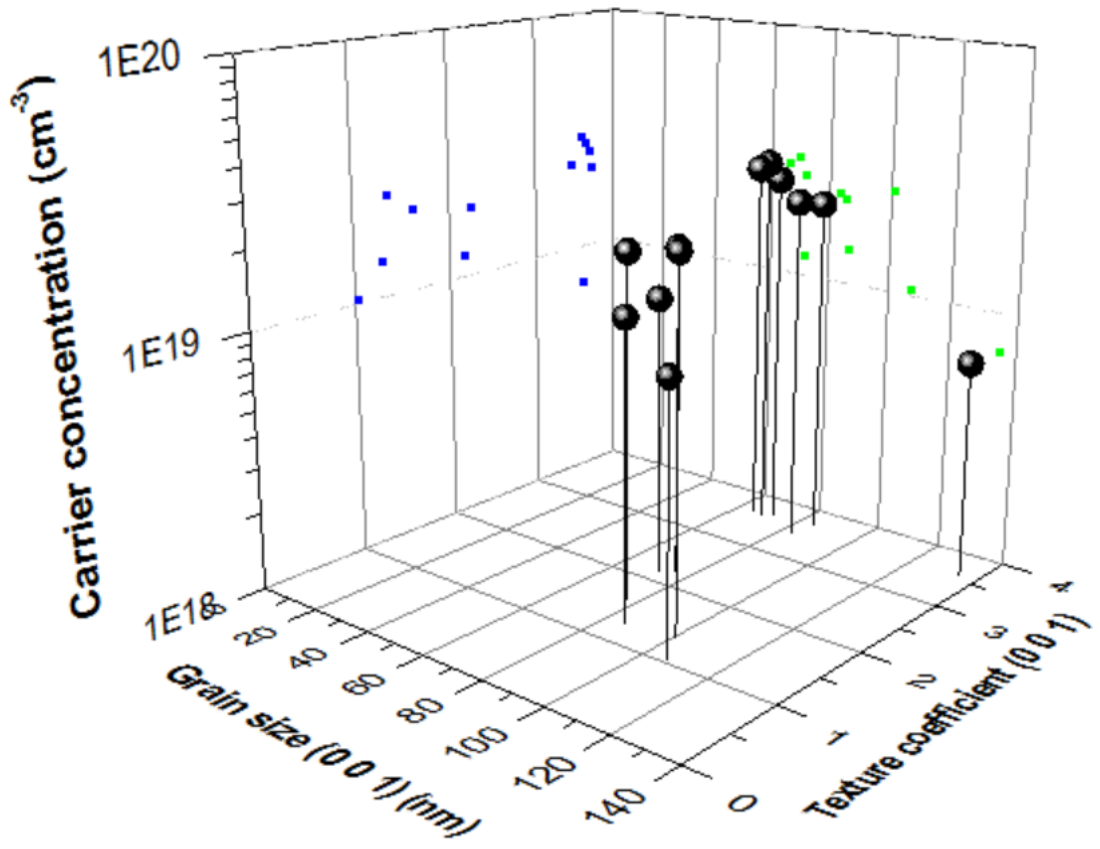

Figure 4.9 Carrier concentration of thick Te films as a function of Grain size and texture coefficient. The 3D spheres were projected on texture coefficient - carrier concentration Cartesian coordinate plane as blue squares and on grain size - carrier concentration Cartesian coordinate plane as green squares.

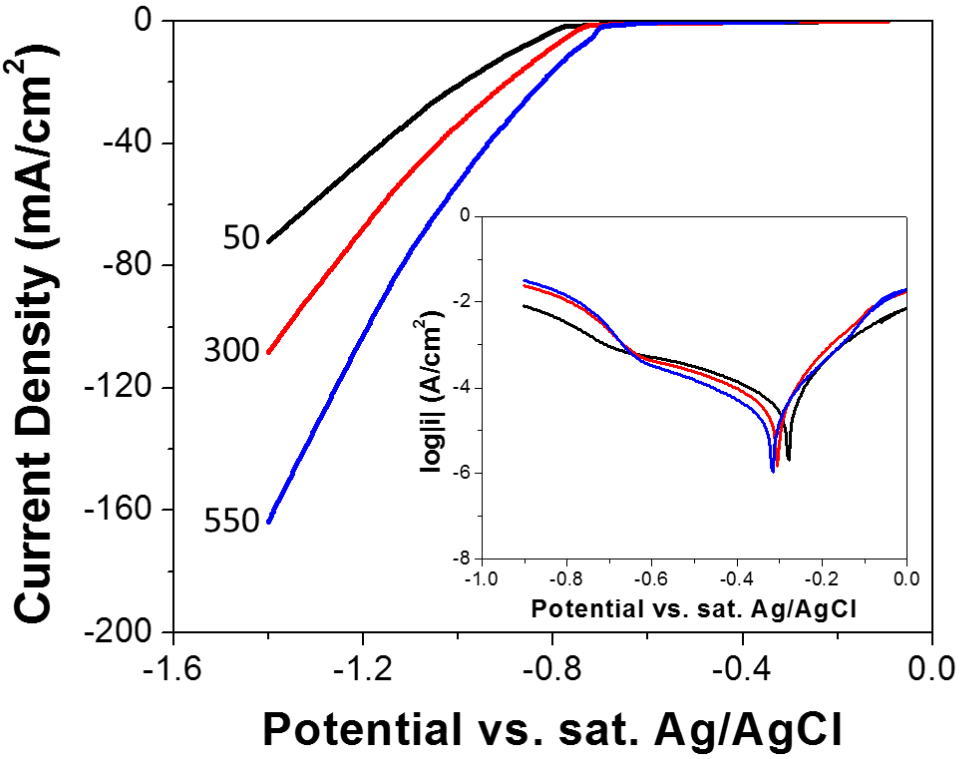

Figure 4.10 LSV curve of TeO_3^{2-} in alkaline solutions with different TeO_3^{2-} concentration (50, 100 and 550 mM) at pH of 12.0 and temperature of 23 ^oC. The substrates were gold coated copper rods. The inserted plot is Tafel plots at different TeO_3^{2-} concentration.

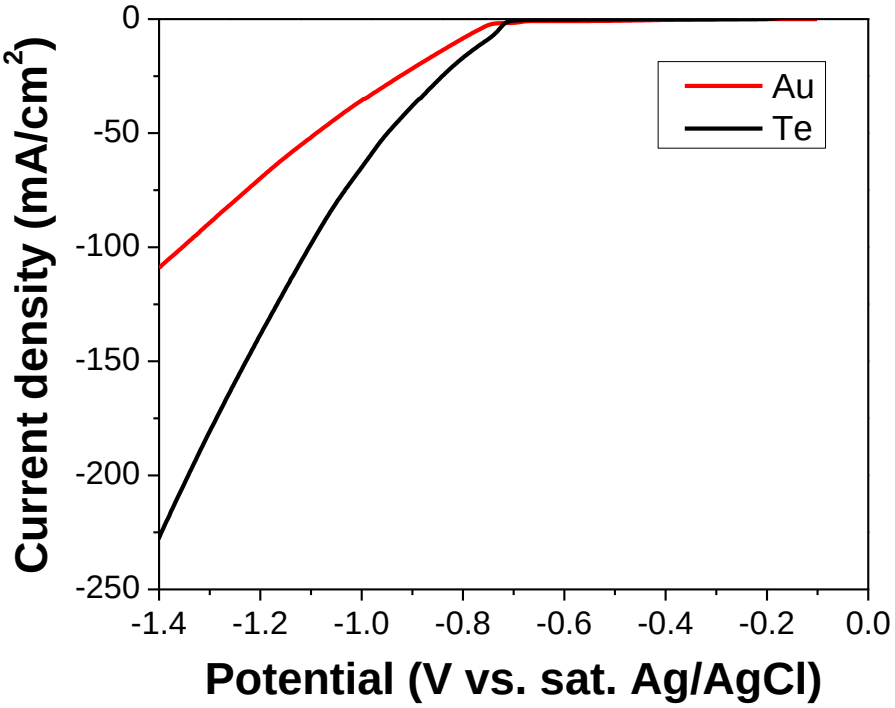

Figure 4.11 LSV curve of TeO_3^{2-} in alkaline solutions on different substrate: Au and Te. TeO_3^{2-} concentration was fixed at 300 mM and pH was fixed at 12.5 at temperature of 23 ^oC.

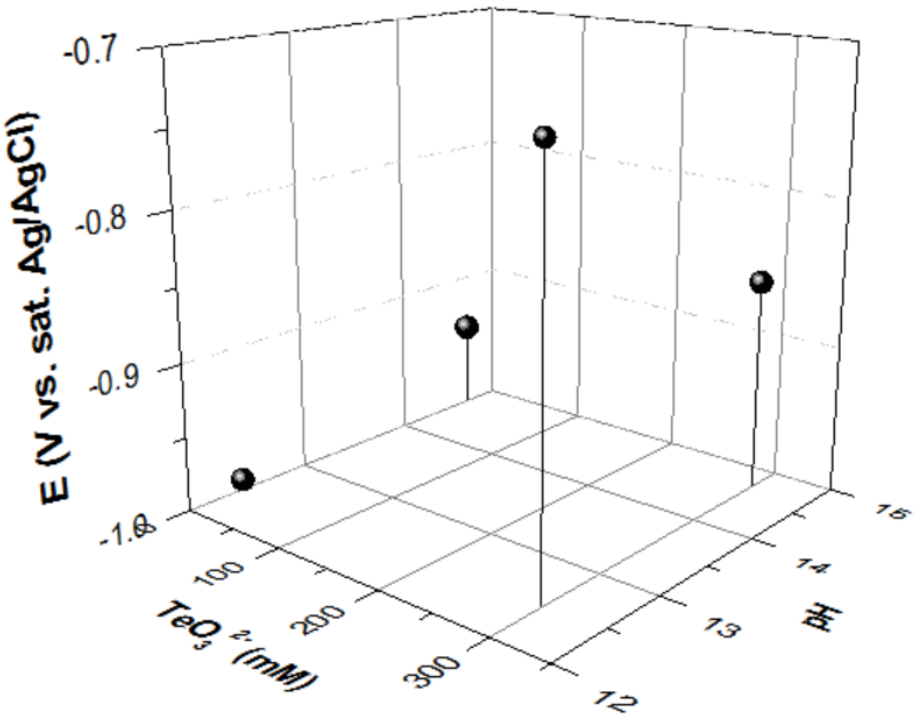

Figure 4.12 Onset potential of TeO_3^{2-} in alkaline solutions with 0 and 300 mM TeO_3^{2-} at pH of 12.5 and 14.7. Thick Te films were used as substrate.

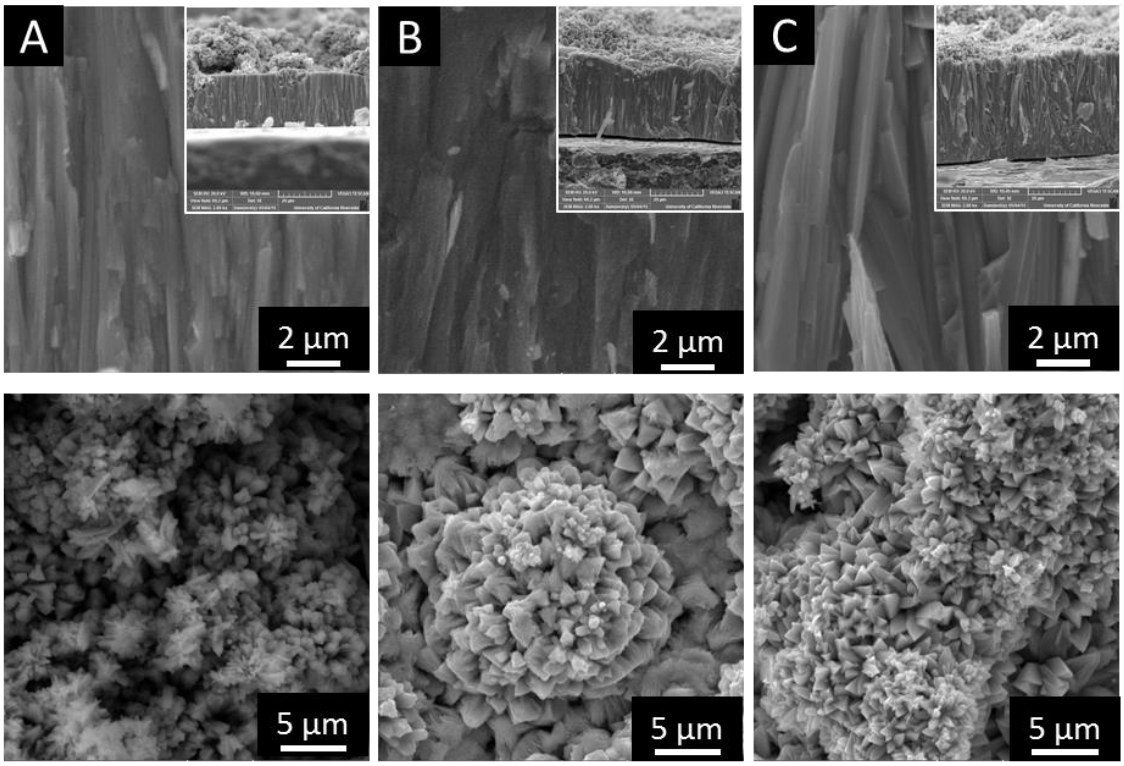

Figure 4.13 SEM images of Te electrodeposited at different TeO_3^{2-} concentration: (A) 50, (B) 100, (C) 550 mM at pH of 12.0, applied potential of -0.9 V vs. sat. Ag/AgCl and temperature of 23 ºC. The top row images are cross-section view, and the bottom row images are top view. The small images at top right corner are the low magnification images.

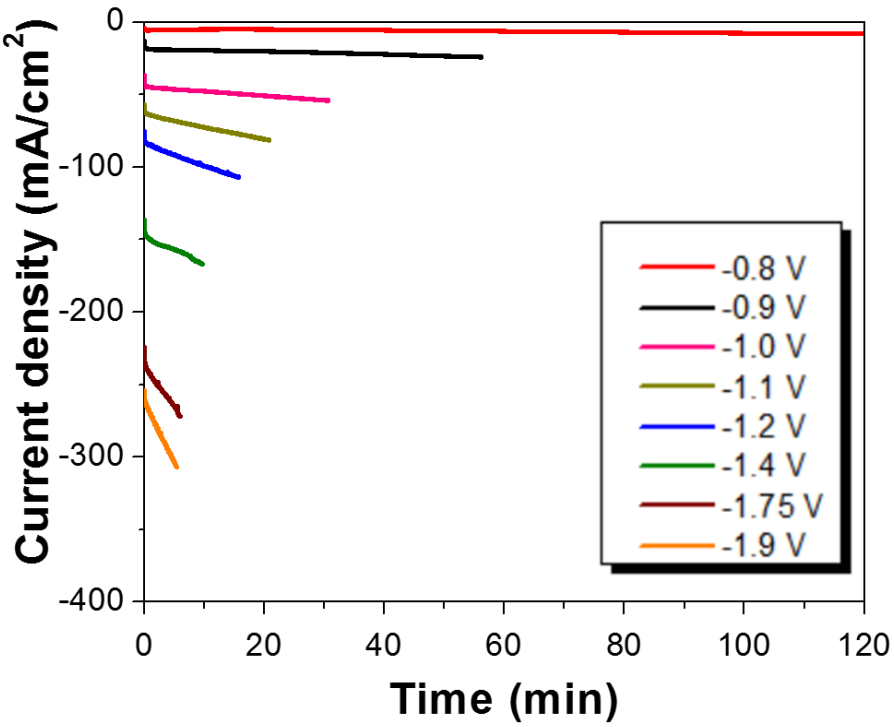

Figure 4.14 Chronoamperograms of Te electrodeposition in alkaline solutions at different applied potential with 300 mM [TeO_3^{2-}] at pH of 12.5 and agitation of 2000 rpm.

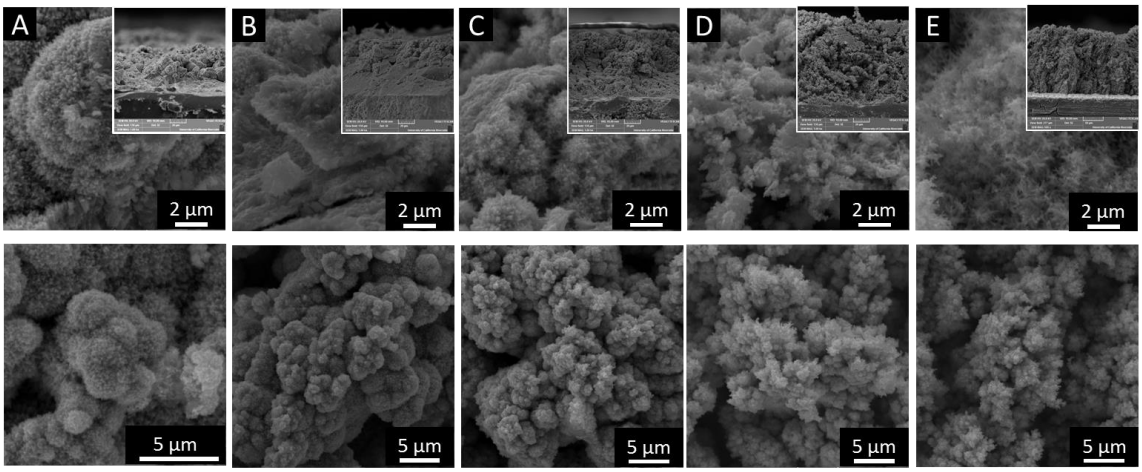

Figure 4.15 SEM images of Te electrodeposited at different applied potential: (A) -1.1, (B) -1.2, (C) -1.4, (D) -1.75, and (E) -1.9 V with 300 mM TeO_3^{2-} at pH of 12.5 and temperature of 23 ^oC. The top row images are cross-section view, and the bottom row images are top view. The small images at top right corner are the low magnification images.

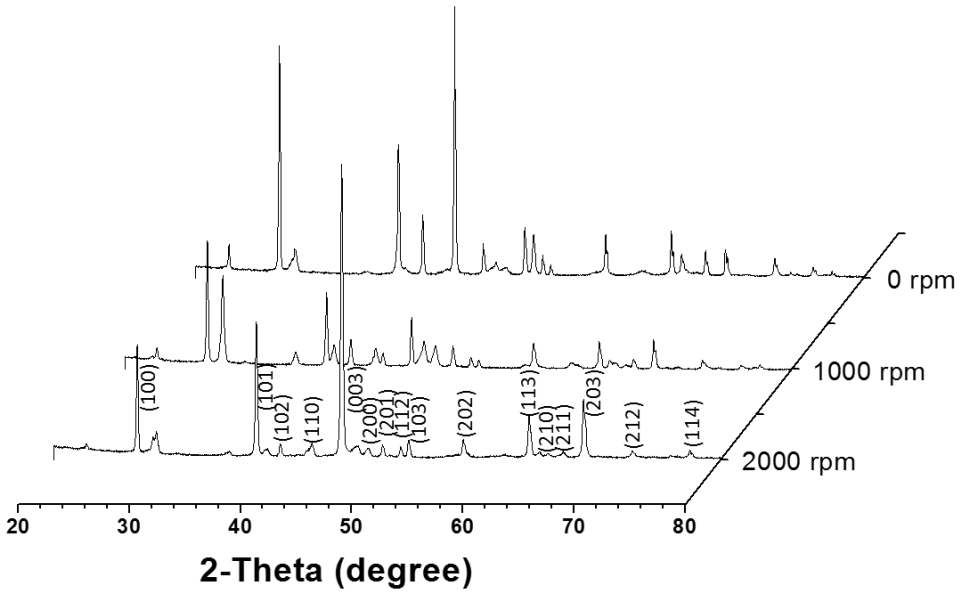

Figure 4.16 XRD of Te electrodeposited at different agitation: 0, 1000, 2000 rpm with 300 mM TeO_3^{2-} at pH of 12.5 and temperature of 23 ^oC.

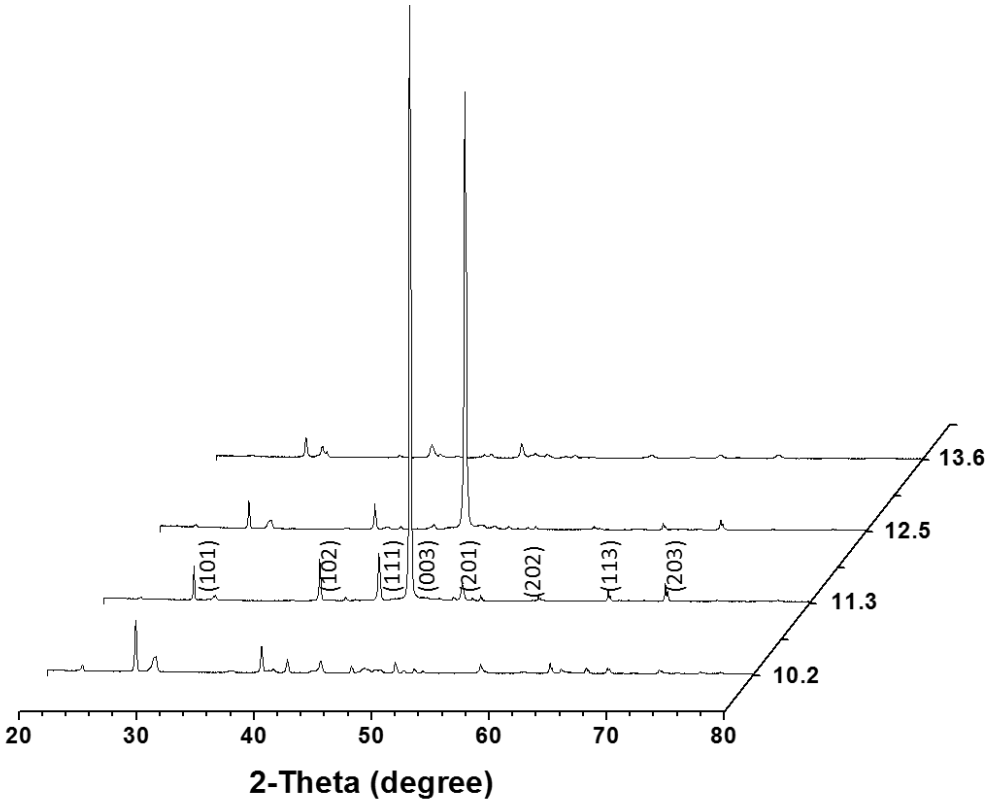

Figure 4.17 XRD images of Te electrodeposited at different pH: 10.2, 11.3, 12.5 and 13.6 with 550 mM TeO_3^{2-} at applied potential of -0.9 V vs. sat. Ag/AgCl, temperature of 23 ºC and agitation of 2000 rpm.

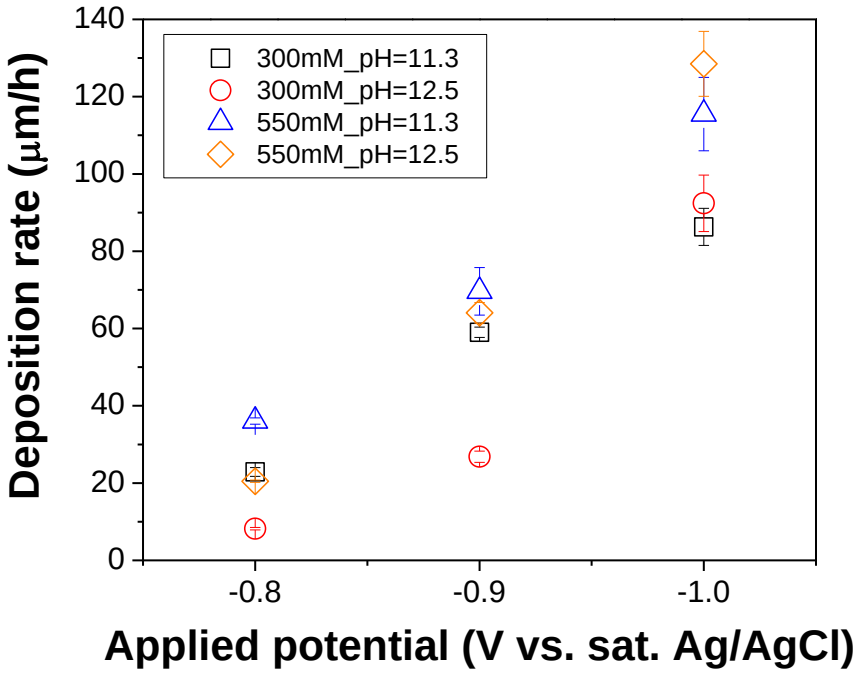

Figure 4.18 Deposition rate as a function of applied potential, TeO_3^{2-} concentration, and pH. Agitation was fixed at 2000 rpm and reaction temperature was fixed at 23 ^{o}C.

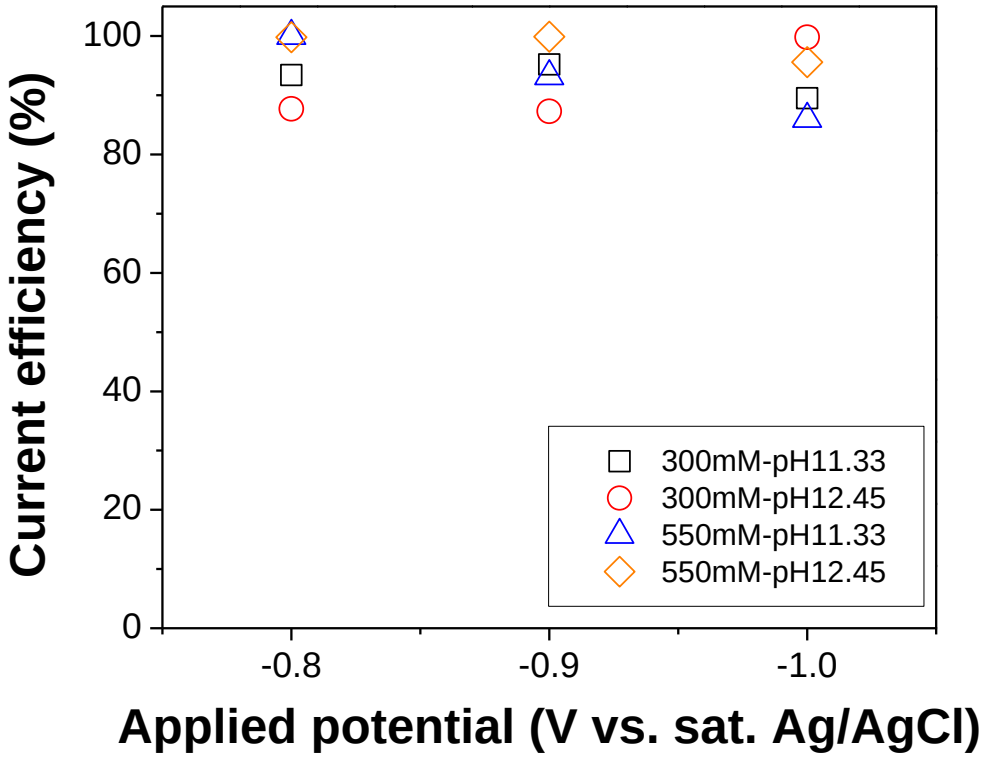

Figure 4.19 Current efficiency as a function of applied potential, TeO_3^{2-} concentration, and pH.

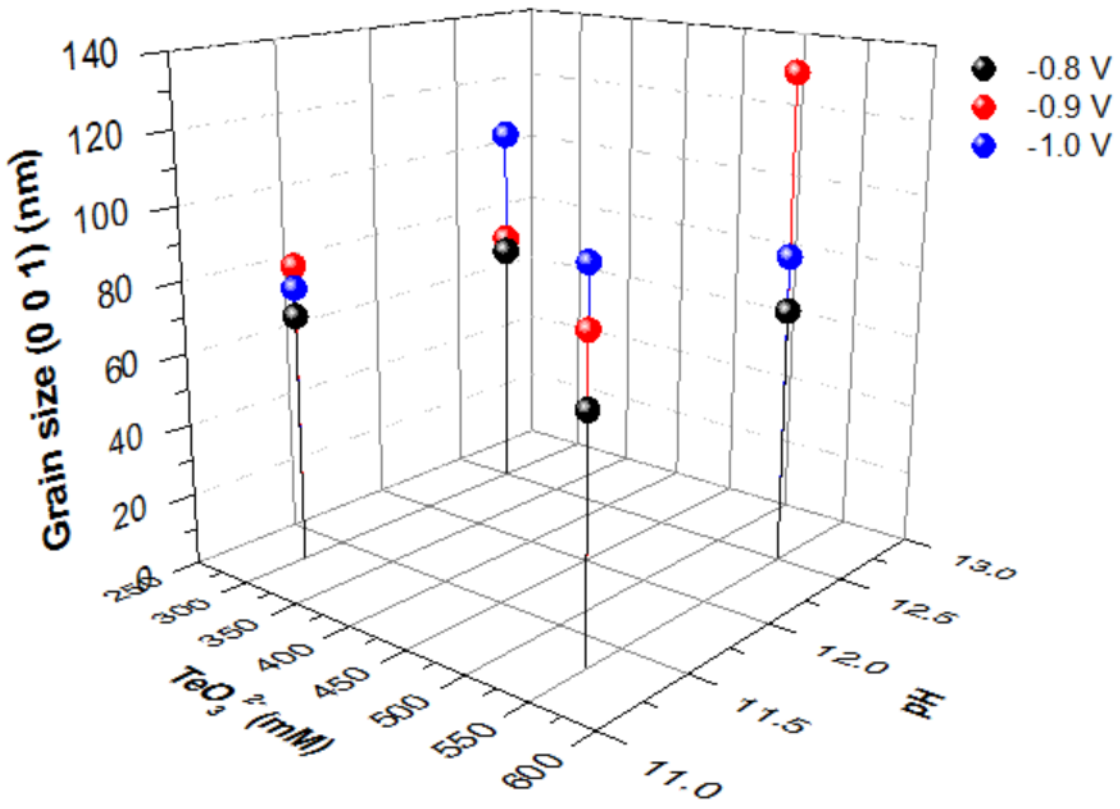

Figure 4.20 Grain size of thick Te films as a function of TeO_3^{2-} concentration, pH, and applied potential.

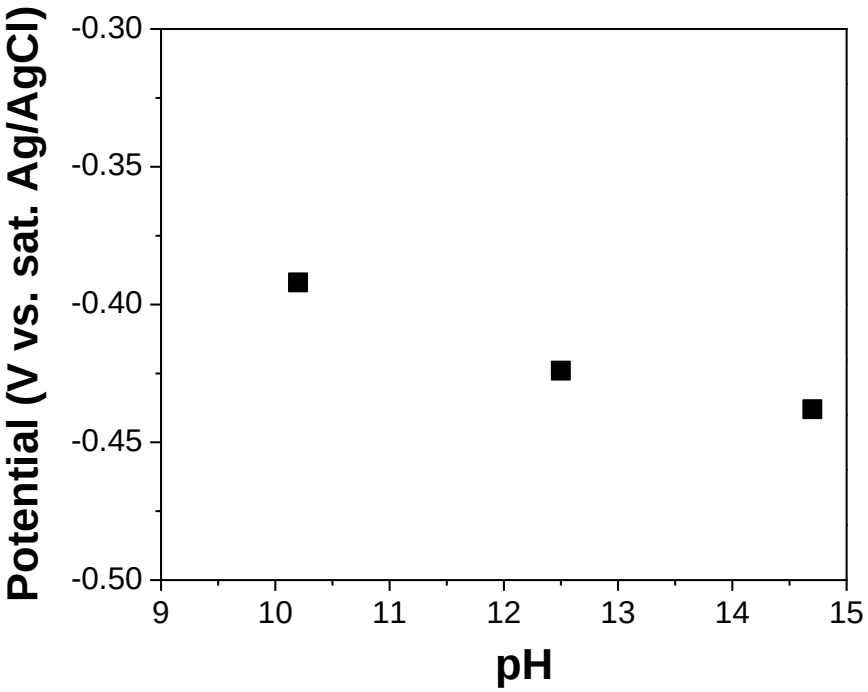

Figure 4.21 Mixed potential of TeO_3^{2-} in alkaline solutions at different pH (10.2, 12.5, 14.7). TeO_3^{2-} concentration was fixed at 550 mM and temperature was fixed at 23 ^oC. The substrates were gold coated copper rods.

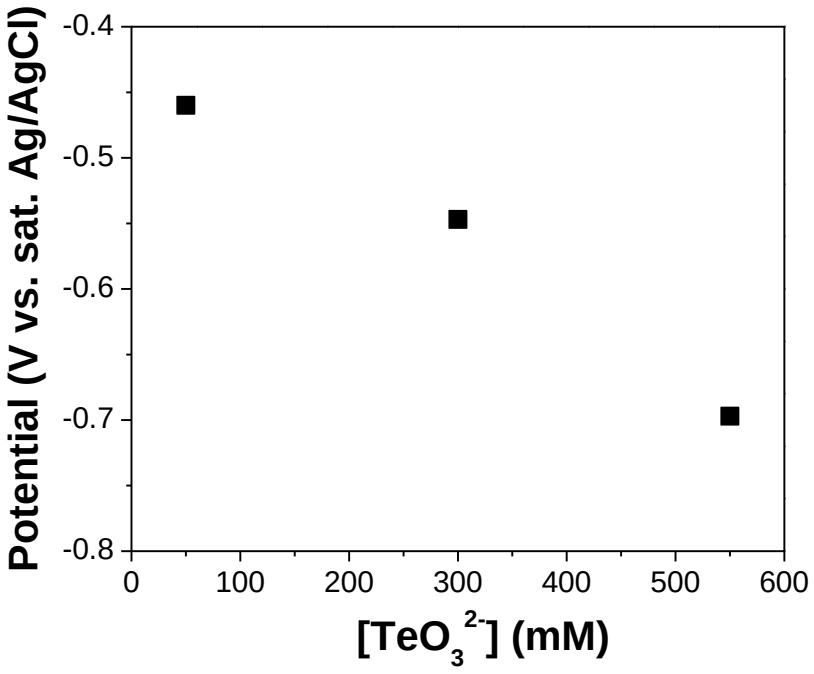

Figure 4.22 Mixed potential of TeO_3^{2-} in alkaline solutions with different TeO_3^{2-} concentration (50, 100 and 550 mM) at pH of 12.0 and temperature of 23 ^{o}C. The substrates were gold coated copper rods.

5 Reaction Kinetics of Reduction Reactions of Te(IV) to Te(0) to Te(-I) in Alkaline Solution

5.1 Abstract

TeO_3^{2-} concentration, solution pH influenced reaction mechanisms and reaction kinetics. The effects of these three parameters on reaction mechanisms and reaction kinetics were discussed in terms revealed by linear sweep voltammograms (LSVs) and Tafel plots. The rate limiting step at different reaction conditions was investigated by Tafel slopes. The EQCM data indicated that proper applied potential range was essential to deposit Te(0) on the surface of electrode. The formation of Te(0) in the solution would happen when applied potential was negative enough. Furthermore, increasing the pH accelerated the reduction rate of Te(0) to Te(-I).

5.2 Introduction

Tellurium is a p-type semiconductor with a narrow band-gap energy of 0.35 eV at room temperature. Owing to its unique crystal structure, it exhibits many unique physical properties including photoconductivity [1, 2], piezoelectric effect[3], gas sensing[4, 5], and catalytic activity[6-8]. Additionally, tellurium based alloys, such as Bi_2Te_3, PbTe, Ag-PbTe, Sb_2Te_3, and CdTe, have wide application in thermoelectrics [9], phase change memory[10], topological insulator[11], and solar cells[12], and controlling the material's morphology can result in remarkable enhancements in performance in the final device. For examples, the piezoelectric property of one-dimensional (1-D) nanowires can be enhanced by reducing the diameter of the nanowire due to flexoelectric effect.[3, 13, 14]

The enhancement of light absorption observed in 3-D nanostructures is attributed to the effect nanostructure has on the material's refractive index gradient.[15-17] Furthermore, the sensing performance of a gas sensor can be improved by Nano-engineering. [4]

Various methods have been used to synthesis Te, including vapor deposition[18-26]; hydrothermal[27-40], solvothermal[41-44], and polyol processes[45-47]; ultrasonic[48], microwave[49], photothermal[50], surfactant[51-53] and biomolecule-assisted methods[31]; as well as amino acids[54] and gluconate[55] controlled methods. A few works have been reported on the synthesis of 3-D Te nanostructures including the Ostwald ripening process[43] [56], rapid crystallization[39], secondary nucleation[53], and solution-based approaches.[57] However, these fabrication techniques generally require high operating temperature and pressure - making their manufacture difficult to scale-up.

Electrodeposition is a widely used electrochemical method to synthesize various materials due to the ease of fabrication. The synthesis of Te via electrodeposition has been reported by several groups. Zhao et al. synthesized Te nanowire arrays via template directed electrodeposition at pH of 2.[58] Wang et al. reported the electrodeposition of featherlike Te microstructures in acidic solutions.[59] She et al. used template-free electrodeposition to synthesize 1-D nanostructures of Te in an alkaline solution, but an electrochemical analysis detailing the reaction mechanism was not provided.[60] The advantage of alkaline solutions over acidic baths is the higher solubility of TeO_2, in alkaline solutions, which was emphasized in our previous publication using galvanic displacement reaction (GDR).[61, 62] GDR has the common advantage of the electrochemical synthesis method, but the drive force window is relatively small which is limited by the sacrificial

material. In contrast, the drive force window in electrodeposition can be controlled in a wide range via externally applied potential or current. Electrochemical analysis of Te(IV) reduction reactions in alkaline solution have been studied . To synthesis Te structures by electrochemical method, it is essential to understand the mechanism and kinetics of Te electrochemical reactions.

In this work, electrochemical reaction mechanisms were investigated via CV, Tafel plots and EQCM. Reaction parameters, including Te(IV) concentration, pH and applied potential, were utilized to control the reaction mechanism and kinetics.

5.3 Experimental

All solutions were prepared by dissolving various amounts of tellurium dioxide (TeO_2, 99+%, Acros Organics) in sodium hydroxide solutions (NaOH, 10 N, Fisher Chemical) and pH of the solutions were adjusted by NaOH. All the electrodeposition experiments were performed in a conventional three-electrode cell using a rotating disk electrode (RDE) (6.4 mm in diameter gold coated copper rods embedded in a cylindrical Teflon holder) as working electrodes, platinum coated titanium stripe as counter electrode, and saturated Ag/AgCl as reference electrode.

Linear sweep voltammograms (LSV) and Tafel plot experiments were conducted in the same three-electrode system as used in electrodeposition. However, the working electrodes were 50 μm thick Te films, which were electrodeposited on gold coated copper rods. All the solutions are deaerated by bubbling N_2 for 40 minutes. [63]

The effect of TeO_3^{2-} concentration on the Tafel slope for reduction reaction of Te(IV) to Te(0) was investigated by varying the TeO_3^{2-} concentration from 50 to 550 mM with a fixed solution pH of 12.0 at 23ºC. Additionally, the pH effect on the Te(IV) to Te(0) reaction was investigated by varying the pH from 10.2 to 14.7 (calculated value), while fixing the TeO_3^{2-} concentration at 550 mM at 23 ºC. The pH effect on reaction of Te(0) to Te(-I) was investigated by varying the solution pH from 10.2 to 14.7, while fixing the TeO_3^{2-} concentration and temperature at 0 mM and 23 ºC, respectively. A potentiostat (Bio Logic, SP-200) combined with an electrochemical quartz crystal microbalance (EQCM) (Stanford Research Systems, QCM200) was used for electrochemical investigation.

5.4 Results and discussion

Reduction of Te(IV) in alkaline solution goes through three steps; namely, (1) Te(IV) is reduced to Te(0), (2) Te(0) is reduced to Te(-I), and (3) Te(-I) is reduced to Te(-II).[62, 64] Based on curve (a) in Figure 5.1, the first reduction reaction, Te(IV) to Te(0), started at -0.77 V. The second reduction, Te(0) to Te(-I), started between -0.77 V and -1.25 V, where -1.25V marks the dip point. The rapid drop in current density at more negative potentials than the dip point is the result of the near completion of reducing Te(0) to Te(-I) or to Te(-II). These two products can then react with Te(IV) inhibiting its transport to the electrode surface and instead produce black particles in solution. The presence of such black particles was confirmed by observing their formation in the solution right after re-exposing the gold substrate. We discussed this latter reaction in our previous publications. [61, 65] The sharp spike in current density at -1.8 V may be caused by a hydrogen gas evolution reaction. [66]

The curve (b) in (figure 5.1) was obtained by cathodic reduction of the Te electrode in a NaOH solution. According to the red dashed curve, the reduction reaction, Te(0) to Te(-I), started at a potential of -0.92 V. As the applied potential became more negative, the Te(0) to Te(-I) reduction reaction increases resulting in a sharp increase in the cathodic current density verses applied potential. However, at applied potential of -1.06 V the Te substrate is almost completely dissolved, leading to the rapid decrease in current density just beyond this point. When the applied potential became more negative than -1.7 V, the current density increased again, but this time the increase was due to the H_2 gas evolution and the reduction of Te(-I) to Te(-II).[66]

$TeO_3^{2-}(aq) + 3H_2O(l) + 4e^- \rightarrow Te(s) + 6OH^-(aq)$ (E_0 = - 0.45 V vs. Ag/AgCl)

Reaction 5.1

$2H_2O(l) + 2e^- \rightarrow H_2(g) + 2OH^-(aq)$ (E_0 = - 0.90 V vs. Ag/AgCl)

Reaction 5.2

$2Te(s) + 2e^- \rightarrow Te_2^{2-}(aq)$ (E_0 = -0.91 V vs. Ag/AgCl)

Reaction 5.3

$Te_2^{2-}(aq) + 2e^- \rightarrow 2Te^{2-}(aq)$ (E_0 = -1.47 V vs. Ag/AgCl)

Reaction 5.4

$TeO_3^{2-}(aq) + 2Te_2^{2-}(aq) + 3H_2O(l) \rightarrow 5Te(s) + 6OH^-(aq)$ (ΔG^O = - 164.1 kJ/mol)

Reaction 5.5

$TeO_3^{2-}(aq) + 2Te^{2-}(aq) + 3H_2O(l) \rightarrow 3Te(s) + 6OH^-(aq)$ (ΔG^O = - 279.3 kJ/mol)

Reaction 5.6

To study the effect of reaction conditions on the reaction kinetics of Te reduction reaction (i.e., TeO_3^{2-} to Te and Te to Te_2^{2-}), LSV experiments at different reaction conditions was conducted shown in figure 5.2-5.4. The onset potential was extracted from the LSV curves. Figure 5.5 shows that the onset potential of TeO_3^{2-} to Te became more positive when [TeO_3^{2-}] increased. However, the onset potential of TeO_3^{2-} to Te(0) became more negative when pH increased (figure 5.6). Additionally, the onset potential of Te(0) to Te_2^{2-} became more negative when pH increased (figure 5.10).

The Tafel slopes of reduction reactions, TeO_3^{2-} to Te(0) and Te(0) to Te_2^{2-}, were extracted from the Tafel plots (figure 5.12-5.14). In alkaline solution, Te(IV) exists in the form of anion (e.g., TeO_3^{2-} [67], $Te(OH)_6^{2-}$[68]). The direct reduction of Te(IV) to Te(0) is highly unlikely on a negatively charged cathodic electrode surface. Instead, a 4-step process is proposed through the sequence of reactions 5.8 – 5.11 [67-69] Reaction 5.7 shows that the anions $Te(OH)_6^{2-}$ are in equilibrium with cations $Te(OH)_3^{+}$. But once $Te(OH)_3^{+}$ is absorbed on the cathodic electrode surface, it obtains an electron from the electrode and is then discharged as $Te(OH)_3$. This cyclic mechanism of picking up an electron from the electrode is repeated in reactions 5.9 and 5.10 yielding $Te(OH)_3^{2-}$. $Te(OH)_3^{2-}$ obtains a fourth and last electron in reaction 5.11 and in turn releases all three hydroxide ions to form Te element. According to the Tafel equation, by assuming a charge transfer coefficient of 0.5, the Tafel slopes are 118, 59, 39 and 30 mV/decade.A, when reaction 5.8, 5.9, 5.10 and 5.11 are the rate limiting steps, respectively.[70]

Komandenko et al. reported that under their experimental conditions reaction 1.10 was the rate limiting step. The Tafel slopes ranged from 40 to 45 mV/decade.A.[69]

Furthermore, Komandenko et al. also claimed that at low alkali concentration $Te(OH)_3^+$ would directly obtain two electrons and become $Te(OH)_3^-$. Thus, they replace reactions 8 and 9 with one reaction.[68].

Figure 5.9 shows that when the $Te(OH)_6^{2-}$ concentration increased from 50 to 550 mM at pH of 12.0, the Tafel slopes ranged from 90 to 117 mV/decade.A. The differences between Tafel slopes were attributed the change of charge transfer coefficient. This meant that the TeO_3^{2-} concentration did not influence the rate limiting step substantially. In the whole concentration range, the rate limiting step was reaction 5.8, which was the discharge of $Te(OH)_3^+$.

Figure 5.10 indicated that at low pH (i.e., 10.5), the Tafel slope was 61 mV/decade.A, which meant that reaction 5.9 was the rate limiting step. However, when the pH was varied between 11.0 and 12.5, the Tafel slopes of the reaction ranged from 92 to 103 mV/decade.A. This meant that reaction 5.8 was the rate limiting step. When pH increased to 13.1, the Tafel slope was 65 mV/decade.A and the rate limiting step was reaction 5.9. When pH further increased to 14.7, the Tafel slope was further reduced to 39 mV/decade.A, meaning that reaction 5.10 is the rate limiting step.

The reduction of Te(IV) to Te(0) involved four elementary steps (reaction 5.8 – 5.11).

$Te(OH)_6^{2-}(aq) \rightarrow Te(OH)_3^+(aq) + 3OH^-(aq)$ Reaction 5.7

$Te(OH)_3^+(aq) + e^- \rightarrow Te(OH)_3(ads)$ Reaction 5.8

$Te(OH)_3(ads) + e^- \rightarrow Te(OH)_3^-(ads)$ Reaction 5.9

$$Te(OH)_3^-(ads) + e^- \rightarrow Te(OH)_3^{2-}(ads)$$ Reaction 5.10

$$Te(OH)_3^{2-}(ads) + e^- \rightarrow Te(s) + 3OH^-(aq)$$ Reaction 5.11

The reaction mechanism of Te(0) to Te_2^{2-} was first reported by Awad et al. [71] Their results showed that at low NaOH concentrations, only one linear region was shown in the Tafel plot with a slope about 100 mV/decade.A. However at high NaOH concentrations, two linear regions were observed with Tafel slopes about 40 and 100 mV/decade.A. He proposed the two step reaction mechanism which involved Na^+ ions (reaction 5.12and 5.13). However, the calculated number of electrons transferred for each elementary reaction was surprising. At the first step (reaction 5.12), 2 electrons were transferred; at the second step (reaction 5.13) 4 electrons were transferred. The number of electrons could not be explained by this two-step reaction mechanism.

$$Te(s) + Na^+(aq) + e^- \rightarrow NaTe(ads)$$ Reaction 5.12

$$NaTe(ads) + Te(s) + e^- \rightarrow Te_2^{2-}(aq) + Na^+$$ Reaction 5.13

Therefore, Awad et al. proposed a four-step reaction mechanism (reaction 5.14 – 5.17) and introduced the diatomic tellurium. In the equations, M^+ represented the cations (e.g., Na^+ or Ba^{2+}) in the alkaline solution. Reaction 5.14 and 5.15 are discharge reactions, reaction 5.16 and 5.17 are electrochemical reactions. In the two discharge reactions, the reaction rate of the second step reaction (reaction 5.13) is relatively slower than the first step, which can be the rate limiting step. On the other hand, in the two electrochemical reactions, the reaction rate of the second step reaction was relatively slower than the first step, which can be the rate limiting step. Awad et al. used the energy barrier diagram of these four reactions to prove their assumptions. According to the energy barrier diagram,

the first discharge (reaction 5.14) and electrochemical step (reaction 5.16) steps have very low energy barriers compared to the second discharge (reaction 5.15) and electrochemical (reaction 5.17) steps. When reaction 5.15 was the rate limiting step, the Tafel slope was about 100 mV/decade.A, which is consistent with the theoretically calculated value 120 mV/decade.A taking into account the mechanism and the differences due to small changes in the charge transfer coefficient. When reaction 1.17 was the rate limiting step, the Tafel slope was about 40 mV/decade.A at low current density and 100 mV/decade.A at high current density. As a consequence, in weak alkaline solutions, the second discharge reaction (reaction 5.15) was the rate limiting step throughout the whole current density range with a Tafel slope of 100 mV/decade.A. However in strong alkaline solutions, the second electrochemical reaction (reaction 5.17) was the rate limiting step with a Tafel slope of 40 mV/decade.A at low current density and a Tafel slope of 100 mV/decade.A at high current density. [72]

$Te_2(s) + M^+(aq) + e^- \rightarrow MTe_2(ads)$ Reaction 5.14

$MTe_2(ads) + M^+(aq) + e^- \rightarrow M_2Te_2(ads)$ Reaction 5.15

$Te_2(s) + M_2Te_2(ads) + e^- \rightarrow M_2Te_4^-(aq)$ Reaction 5.16

$M_2Te_4^-(aq) + e^- \rightarrow 2Te_2^{2-}(aq) + 2M^+(aq)$ Reaction 5.17

Another mechanism was reported by Komandenko et al. together with Tafel slopes for reduction of Te(0) to Te_2^{2-} at moderate alkaline solutions. Their data showed that the Tafel slope was about 40 mV/decade.A. Additionally, they proposed a different mechanism which involved OH^- ions shown in reaction 5.18 – 5.21 where reaction 5.19 was the rate limiting step. [73]

$$Te(s) + OH^-(aq) + e^- \rightarrow TeOH^{2-}(ads)$$ Reaction 5.18

$$TeOH^{2-}(ads) + Te(s) + e^- \rightarrow Te_2OH^{3-}(ads)$$ Reaction 5.19

$$Te_2OH^{3-}(ads) + Te(s) + e^- \rightarrow Te_3OH^{4-}(ads)$$ Reaction 5.20

$$Te_3OH^{4-}(ads) + Te(s) + e^- \rightarrow 2Te_2^{2-}(aq) + OH^-(aq)$$ Reaction 5.21

Figure 5.11 shows that at relatively weak alkaline solutions (i.e., pH ≤ 12.5), the Tafel slope is about 120 mV/decade.A. The result can be explained by Awad's mechanism, in which the second discharge reaction (reaction 5.15) was the rate limiting step. [72] At strong alkaline solutions (i.e., pH = 14.7), the Tafel slope was 40 mV/decade.A. at low current density, which meant that the second electrochemical reaction (reaction 5.17) was the rate limiting step based on Awad's mechanism. However, at high current density the Tafel slope kept at 40 mV/decade.A instead of 100 mV/decade.A.

The reduction reaction of Te(IV) to Te(0) was further investigated by EQCM. Figure 5.15 showed the change of charge and mass as a function of applied potential at different pH, in which the curve (a) represented the charge and the curve (b) represented the mass. At pH of 10.2 (figure 5.15A), the mass increased when electrical charge increased monotonically. This meant that during the whole CV experiment, Te was deposited onto the working electrode. At pH of 12.5 (figure 5.15B) when applied potential was scanning forward (0 to -2.0 V), the mass kept increasing as increase of charge. However, when applied potential was scanning backward (-2.0 to 0 V), the mass decreased first, then increase. This meant that during the backward scan, the deposited Te on the electrode surface was further reduced to Te_2^{2-}, after the applied potential become more positive, the deposition of Te occurred again. At pH of 13.1 (figure 5.15C), the reduction reaction of

Te(IV) to Te(0) started at applied potential of -0.75 V. When applied potential increased to -1.50 V, the mass of Te(0) kept increasing as the increase of electrical charge. However, applied potential further increased from -1.50 to -1.68 V, the mass of Te(0) decreased from the maximum value to zero, which was caused by the reduction of Te(0) to Te(-I). This reduction reaction happened earlier than -1.50 V. The mass of Te(0) reached the maximum value at -1.50 V, because at this applied potential reduction reaction rate of Te(0) to Te(-I) surpassed the reduction reaction rate of Te(IV) to Te(0). According to the QCM data, at pH of 13.1, the applied potential should be controlled from -0.75 to -1.50 V to deposit Te on the surface of working electrode. When applied potential was from -1.50 to -2.0 V, Te(0) was formed in the solution as reported in our previous publications. At pH of 14.7 (figure 5.15D), the applied potential range to deposit Te(0) on electrode surface became even smaller (-0.92 to -1.31 V). When applied potential is more negative than -1.31 V, Te(0) was formed in the solution.

The mass change rate (dm/dt) and current density as a function of applied potential were presented in figure 5.16. At pH of 10.2 (figure 5.16A), the mass change rate was positive, which is consistent with the fact that the mass of Te(0) kept increasing during the CV. At pH of 12.5, 13.1 and 14.7 (figure 5.16 B-D), the mass change rate switched to negative when applied potential became negative enough, which meant that the dissolution rate of Te(0) surpassed the deposition rate of Te(0).

The reduction reaction of Te(0) to Te(-I) was also studied using EQCM at different pH. During the experiments Te thin films with mass of 70 ± 3.5 μg/cm^2 was pre-deposited on the top of working electrode. Furthermore, in the solution there was no TeO_3^{2-} ions. The

mass change was negative because the QCM was recording the mass change for the reduction of Te(0) to Te(-I), which was the dissolution of Te(0). At pH of 10.2 (figure 5.17A), the mass of Te(0) decreased during the forward scan, but the Te thin film was not completed dissolved. At pH of 12.5 (figure 5.17B), the mass started to decrease at -1.0 V. When applied potential was -1.54 V, the Te thin film was completely dissolved. At pH of 13.1 (figure 5.17C), the dissolution of Te thin film started at -1.0 V and Te thin film was dissolved completely dissolved at -1.49 V. At pH of 14.7 (figure 5.17D), Te thin film started to be dissolved at -0.95 V and was dissolved completely at -1.19 V. Additionally, figure 6.18 showed that dissolution rate of Te increased when pH increased.

5.5 Conclusion

The TeO_3^{2-} concentration affected the mass transfer and reaction rate, but it did not influence the reaction rate limiting step. Controlling pH, however, was essential to control the rate limiting step. When the solution pH was 11.0 and 12.5, in which the discharge of $Te(OH)_3^+$ (reaction 5.8) was the rate limiting step. For the reduction of Te(0) to Te_2^{2-} at relatively weak alkaline solutions (i.e., pH $\leq$ 12.5), the Tafel slope is about 120 mV/decade.A., which meant that the second discharge reaction was the rate limiting step. At strong alkaline solutions (i.e., pH = 14.7), the Tafel slope was 40 mV/decade.A. at low current density, which meant that the second electrochemical reaction was the rate limiting step. A proper applied potential range was essential to deposit Te(0) on the surface of electrode based on the EQCM data, the range can be different at different pH value. When applied potential was negative enough, Te was formed in the solution instead of electrode surface. Additionally, higher pH would accelerate the reduction rate of Te(0) to Te(-I).

5.6 Reference

1. Liu, J.-W., et al., *Mesostructured Assemblies of Ultrathin Superlong Tellurium Nanowires and Their Photoconductivity.* Journal of the American Chemical Society, 2010. **132**(26): p. 8945-8952.
2. Wang, Y., et al., *Mirror-Like Photoconductive Layer-by-Layer Thin Films of Te Nanowires: The Fusion of Semiconductor, Metal, and Insulator Properties.* Advanced Materials, 2006. **18**(4): p. 518-522.
3. Lee, T.I., et al., *High-Power Density Piezoelectric Energy Harvesting Using Radially Strained Ultrathin Trigonal Tellurium Nanowire Assembly.* Advanced Materials, 2013. **25**(21): p. 2920-2925.
4. Zhang, M., et al., *A Rapid Room-Temperature NO2 Sensor Based on Tellurium–SWNT Hybrid Nanostructures.* The Journal of Physical Chemistry C, 2012. **116**(37): p. 20067-20074.
5. Park, H., et al., *Branched tellurium hollow nanofibers by galvanic displacement reaction and their sensing performance toward nitrogen dioxide.* Nanoscale, 2013.
6. Fujiwara, S.-i., et al., *A marvelous catalysis of tellurium in the formation of isothiocyanates from isocyanides and sulfur.* Tetrahedron Letters, 1992. **33**(46): p. 7021-7024.
7. Kambe, N., et al., *Tellurium-catalyzed Carbonylation of Amines with Carbon Monoxide.* Bulletin of the Chemical Society of Japan, 1981. **54**(5): p. 1460-1464.
8. Bradstreet, R.B., *Comparison of Tellurium and Selenium as Catalysts for Kjeldahl Digestion.* Analytical Chemistry, 1949. **21**(8): p. 1012-1013.
9. LaLonde, A.D., et al., *Lead telluride alloy thermoelectrics.* Materials Today, 2011. **14**(11): p. 526-532.
10. Wuttig, M. and N. Yamada, *Phase-change materials for rewriteable data storage.* Nat Mater, 2007. **6**(11): p. 824-832.
11. Guo, Y., Z. Liu, and H. Peng, *A Roadmap for Controlled Production of Topological Insulator Nanostructures and Thin Films.* Small, 2015. **11**(27): p. 3290-3305.
12. Kumar, S.G. and K.S.R.K. Rao, *Physics and chemistry of CdTe/CdS thin film heterojunction photovoltaic devices: fundamental and critical aspects.* Energy & Environmental Science, 2014. **7**(1): p. 45-102.
13. Liu, J.-W., et al., *Rapid Microwave-Assisted Synthesis of Uniform Ultralong Te Nanowires, Optical Property, and Chemical Stability.* Langmuir, 2010. **26**(13): p. 11372-11377.

14. Wang, X., *Piezoelectric nanogenerators—Harvesting ambient mechanical energy at the nanometer scale.* Nano Energy, 2012. **1**(1): p. 13-24.

15. Diedenhofen, S.L., et al., *Broad-band and Omnidirectional Antireflection Coatings Based on Semiconductor Nanorods.* Advanced Materials, 2009. **21**(9): p. 973-978.

16. Chao, Y.-C., et al., *Light scattering by nanostructured anti-reflection coatings.* Energy & Environmental Science, 2011. **4**(9): p. 3436-3441.

17. Yan, C., C.M. Raghavan, and D.J. Kang, *Photocatalytic properties of shape-controlled ultra-long elemental Te nanowires synthesized via a facile hydrothermal method.* Materials Letters, 2014. **116**(0): p. 341-344.

18. Li, X.-L., et al., *Synthesis and magnetoresistance measurement of tellurium microtubes.* Journal of Materials Chemistry, 2003. **14**(2): p. 244-247.

19. Mohanty, P., et al., *Synthesis of Single Crystalline Tellurium Nanotubes with Triangular and Hexagonal Cross Sections.* The Journal of Physical Chemistry B, 2006. **110**(2): p. 791-795.

20. Chen, H., et al., *The fabrication of Te nanowires with different orientations by vacuum vapor deposition.* Physics Letters A, 2007. **362**(1): p. 61-65.

21. Wang, Q., et al., *Fabrication and Growth Mechanism of Selenium and Tellurium Nanobelts through a Vacuum Vapor Deposition Route.* The Journal of Physical Chemistry C, 2007. **111**(35): p. 12926-12932.

22. Sen, S., et al., *Synthesis of Tellurium Nanostructures by Physical Vapor Deposition and Their Growth Mechanism.* Crystal Growth & Design, 2008. **8**(1): p. 238-242.

23. Siciliano, T., et al., *Tellurium microtubes synthesized by thermal evaporation method.* Crystal Research and Technology, 2011. **46**(8): p. 765-768.

24. Parsafar, N. and A. Ebrahimzad, *The effect of substrate temperature on fabrication of one-dimensional nanostructures of tellurium.* Int.J.Nano Dim., 2012. **2**(3): p. 177-183.

25. Hawley, C.J., et al., *Shape-Controlled Vapor-Transport Growth of Tellurium Nanowires.* Crystal Growth & Design, 2012. **12**(6): p. 2789-2793.

26. Geng, B., et al., *Large-scale synthesis of single-crystalline Te nanobelts by a low-temperature chemical vapour deposition route.* Nanotechnology, 2003. **14**(9): p. 983.

27. Mo, M., et al., *Controlled Hydrothermal Synthesis of Thin Single-Crystal Tellurium Nanobelts and Nanotubes.* Advanced Materials, 2002. **14**(22): p. 1658-1662.

28. Liu, Z., et al., *Shape-controlled synthesis and growth mechanism of one-dimensional nanostructures of trigonal tellurium.* New Journal of Chemistry, 2003. **27**(12): p. 1748-1752.

29. Xu, L., et al., *Large-scale Synthesis of Crystalline Tellurium Nanowires with Controlled-Diameters via a Hydrothermal-reduction Process.* Chemistry Letters, 2004. **33**(5): p. 592-593.

30. Liu, Z., et al., *Size-Controlled Synthesis and Growth Mechanism of Monodisperse Tellurium Nanorods by a Surfactant-Assisted Method.* Langmuir, 2004. **20**(1): p. 214-218.

31. Lu, Q., F. Gao, and S. Komarneni, *Biomolecule-Assisted Reduction in the Synthesis of Single-Crystalline Tellurium Nanowires.* Advanced Materials, 2004. **16**(18): p. 1629-1632.

32. Lu, Q., F. Gao, and S. Komarneni, *A Green Chemical Approach to the Synthesis of Tellurium Nanowires.* Langmuir, 2005. **21**(13): p. 6002-6005.

33. Zhu, Y.-J., H. Xian-Luo, and W. Wei-Wei, *Poly(vinylpyrrolidone): a new reductant for preparation of tellurium nanorods, nanowires, and tubes from TeO 2.* Nanotechnology, 2006. **17**(3): p. 645.

34. Qian, H.-S., et al., *Synthesis of Uniform Te@Carbon-Rich Composite Nanocables with Photoluminescence Properties and Carbonaceous Nanofibers by the Hydrothermal Carbonization of Glucose.* Chemistry of Materials, 2006. **18**(8): p. 2102-2108.

35. Qian, H.-S., et al., *High-Quality Luminescent Tellurium Nanowires of Several Nanometers in Diameter and High Aspect Ratio Synthesized by a Poly (Vinyl Pyrrolidone)-Assisted Hydrothermal Process.* Langmuir, 2006. **22**(8): p. 3830-3835.

36. Xu, W., et al., *Structural, Electrical, and Photoconductive Properties of Individual Single-Crystalline Tellurium Nanotubes Synthesized by a Chemical Route: Doping Effects on Electrical Structure.* Small, 2008. **4**(7): p. 888-893.

37. Liang, F. and H. Qian, *Synthesis of tellurium nanowires and their transport property.* Materials Chemistry and Physics, 2009. **113**(2): p. 523-526.

38. Wang, Z., et al., *Formation of single-crystal tellurium nanowires and nanotubes via hydrothermal recrystallization and their gas sensing properties at room temperature.* Journal of Materials Chemistry, 2010. **20**(12): p. 2457-2463.

39. Zhu, H., et al., *Controlled Synthesis of Tellurium Nanostructures from Nanotubes to Nanorods and Nanowires and Their Template Applications.* The Journal of Physical Chemistry C, 2011. **115**(14): p. 6375-6380.

40. Zhu, H., et al., *Controlled hydrothermal synthesis of tri-wing tellurium nanoribbons and their template reaction.* CrystEngComm, 2012. **14**(1): p. 251-255.

41. Wei, G., et al., *Solvothermal synthesis of porous tellurium nanotubes.* Chemical Physics Letters, 2003. **372**(3): p. 590-594.

42. Song, J.-M., et al., *Superlong High-Quality Tellurium Nanotubes: Synthesis, Characterization, and Optical Property.* Crystal Growth & Design, 2008. **8**(6): p. 1902-1908.

43. Wang, S., et al., *Synthesis, characterization and optical properties of flower-like tellurium.* CrystEngComm, 2010. **12**(1): p. 166-171.

44. Wu, X., et al., *Controlled synthesis of multi-morphology Te crystals by a convenient Lewis acid/base-assisted solvothermal method.* Journal of Nanoparticle Research, 2012. **14**(8): p. 1-10.

45. Mayers, B. and Y. Xia, *Formation of Tellurium Nanotubes Through Concentration Depletion at the Surfaces of Seeds.* Advanced Materials, 2002. **14**(4): p. 279-282.

46. Zhu, Y. and X. Hu, *tellurium nanorods and nanowires prepared by the microwave-polyol method.* Chemistry Letters, 2004. **33**.

47. Zhu, W., et al., *Controllable, Surfactant-Free Growth of 2D, Scroll-Like Tellurium Nanocrystals via a Modified Polyol Process.* Crystal Growth & Design, 2006. **6**(12): p. 2804-2808.

48. Zhou, B., et al., *A novel ultrasonic-assisted solution-phase approach for the fabrication of tellurium bundles of nanowhiskers.* Ultrasonics Sonochemistry, 2006. **13**(4): p. 352-358.

49. Zhu, Y.-J., et al., *Microwave-Assisted Synthesis of Single-Crystalline Tellurium Nanorods and Nanowires in Ionic Liquids.* Angewandte Chemie International Edition, 2004. **43**(11): p. 1410-1414.

50. Zhang, B., et al., *1D Tellurium Nanostructures: Photothermally Assisted Morphology-Controlled Synthesis and Applications in Preparing Functional Nanoscale Materials.* Advanced Functional Materials, 2007. **17**(3): p. 486-492.

51. Liu, Z., et al., *Surfactant-assisted growth of uniform nanorods of crystalline tellurium.* Journal of Materials Chemistry, 2003. **13**(1): p. 159-162.

52. Zheng, R., et al., *Synthesis of tellurium nanorods via spontaneous oxidation of NaHTe at room temperature.* Chemical Physics Letters, 2004. **395**: p. 302-305.

53. Gautam, U.K. and C.N.R. Rao, *Controlled synthesis of crystalline tellurium nanorods, nanowires, nanobelts and related structures by a self-seeding solution process.* Journal of Materials Chemistry, 2004. **14**(16): p. 2530-2535.

54. He, Z., S.-H. Yu, and J. Zhu, *Amino Acids Controlled Growth of Shuttle-Like Scrolled Tellurium Nanotubes and Nanowires with Sharp Tips.* Chemistry of Materials, 2005. **17**(11): p. 2785-2788.

55. F.Gao, Q. Lu, and S. Komarneni, *Gluconate controls one-dimensional growth of tellurium nanostructures.* Journal of Materials Research, 2006. **21**(02): p. 343-348.

56. Wang, S., et al., *Large-scale synthesis of feather-like single-crystal Te via a biphasic interfacial reaction route.* CrystEngComm, 2010. **12**(11): p. 3852-3857.

57. Shen, J.-M., et al., *Construction of Unconventional Hexapod-like Tellurium Nanostructure with Morphology-Dependent Photoluminescence Property.* The Journal of Physical Chemistry C, 2009. **113**(22): p. 9502-9508.

58. Zhao, A.W., et al., *Tellurium nanowire arrays synthesized by electrochemical and electrophoretic deposition.* Journal of Materials Research, 2003. **18**: p. 2318-2322.

59. Wang, X. and Y. Ni, *A facile electrochemical route for fast deposition of featherlike tellurium microstructures.* RSC Advances, 2011. **2**: p. 2340-2345.

60. She, G., et al., *Template-Free Electrodeposition of One-Dimensional Nanostructures of Tellurium.* Crystal Growth & Design, 2009. **9**(2): p. 663-666.

61. Wu, T., et al., *Synthesis of Tellurium Heterostructures by Galvanic Displacement Reaction of Zinc in Alkaline Baths.* Electrochimica Acta, 2014. **150**(0): p. 298-307.

62. Wu, T., et al., *Size Controlled Synthesis of Tellurium Nanorices by Galvanic Displacement Reaction of Aluminum.* Electrochimica Acta, 2015. **176**: p. 1382-1392.

63. Butler, I.B., M.A.A. Schoonen, and D.T. Rickard, *Removal of dissolved oxygen from water: A comparison of four common techniques.* Talanta, 1994. **41**(2): p. 211-215.

64. Lingane, J.J. and L.W. Niedrach, *Polarography of Selenium and Tellurium. II. The + 4 States.* Journal of the American Chemical Society, 1949. **71**(1): p. 196-204.

65. Shinagawa, M., N. Yano, and T. Kurosu, *Mechanism and analytical aspects of the polarographic maximum wave of tellurium.* Talanta, 1972. **19**(4): p. 439-450.

66. Pourbaix, M., *Atlas of electrochemical equilibria in aqueous solutions*1966, Long Island City, N.Y.: Pergamon Press Inc.

67. Bard, A.J., *Encyclopedia of electrochemistry of the elements*. Vol. IV. 1975, New York: MARCEL DEKKER, INC.

68. Komandenko, V.M. and A.L. Rotinyan, *Electrochemical behavior of a tellurium electrode in sodium tellurite solutions containing small excesses of free alkali.* Èlektrohimiâ, 1967. **3**(6): p. 723-728.

69. Komandenko, V.M. and A.L. Rotinyan, *Electrochemical behavior of tellurium in sodium tellurite solutions.* Zhurnal Prikladnoi Khimii 1966. **39**(1): p. 123-31.

70. Bard, A.J. and L.R. Faulkner, *Electrochemical methods fundamentals and applications*2001: John Wiley&Sons, Inc.

71. Awad, S.A., *Overpotential on tellurium cathodes in NaOH solutions.* Journal of the Electrochemical Society, 1961. **108**: p. 468-72.

72. Awad, S.A., *Electrochemical evidence for diatomicity of tellurium.* Journal of the Electrochemical Society, 1962. **109**: p. 865-70.

73. Komandenko, V.M. and A.L. Rotinyan, *Cathodic dissolution of tellurium in alkaline solutions.* Elektrokhimiya, 1967. **3**(5): p. 552-557.

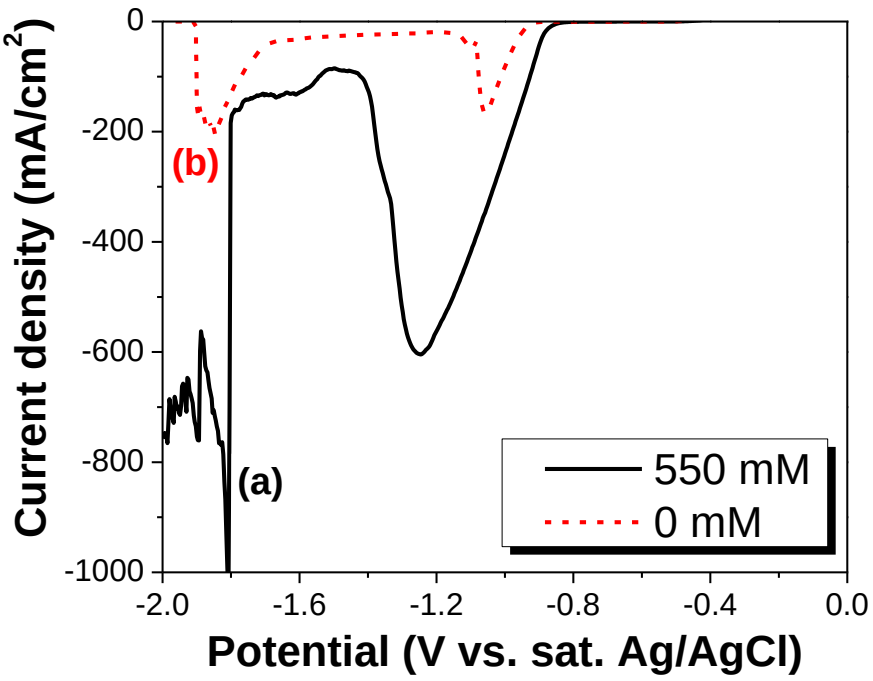

Figure 5.1 LSV curve of TeO_3^{2-} in alkaline solutions at pH of 14.7. The black solid curve is at TeO_3^{2-} concentration of 550 mM (a) and the red dashed curve is at TeO_3^{2-} concentration of 0 mM (b). In both of the experiments, thick Te films were used as substrate.

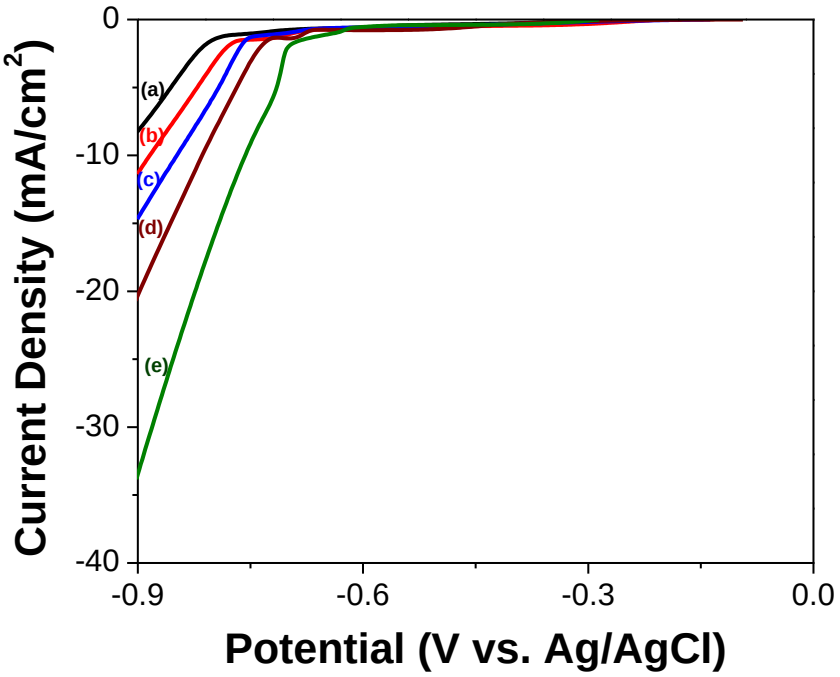

Figure 5.2 LSV curve of TeO_3^{2-} in alkaline solutions with different TeO_3^{2-} concentration: (a) 25, (b) 50, (c) 100, (d) 300 and (e) 550 mM at pH of 12.0 and temperature of 23 ºC. Thick Te films were used as substrate.

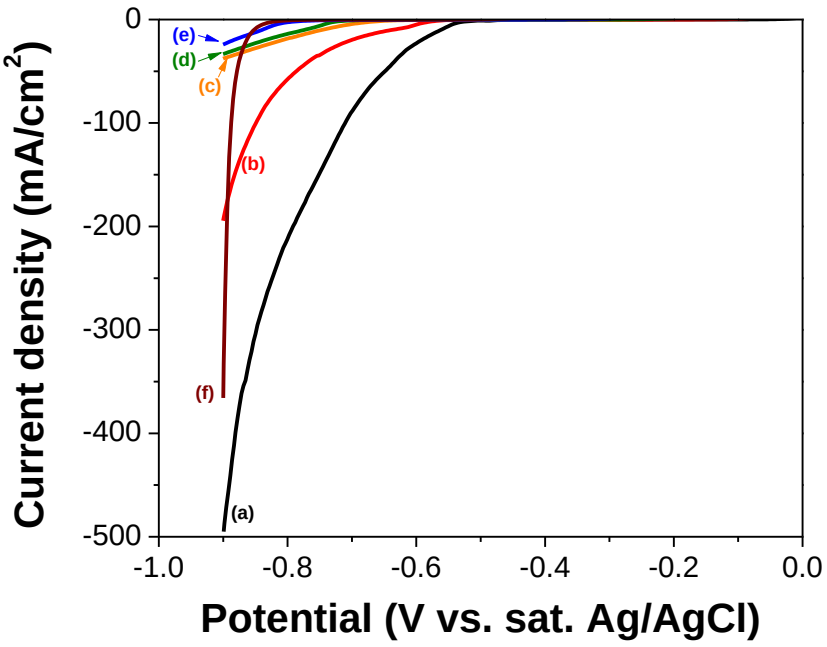

Figure 5.3 LSV curve of TeO_3^{2-} in alkaline solutions at different pH: (a) 10.2, (b) 11.0, (c) 12.2, (d) 12.5, (e) 13.1 and (f) 14.7. TeO_3^{2-} concentration was fixed at 550 mM and temperature was fixed at 23 ºC. Thick Te films were used as substrate.

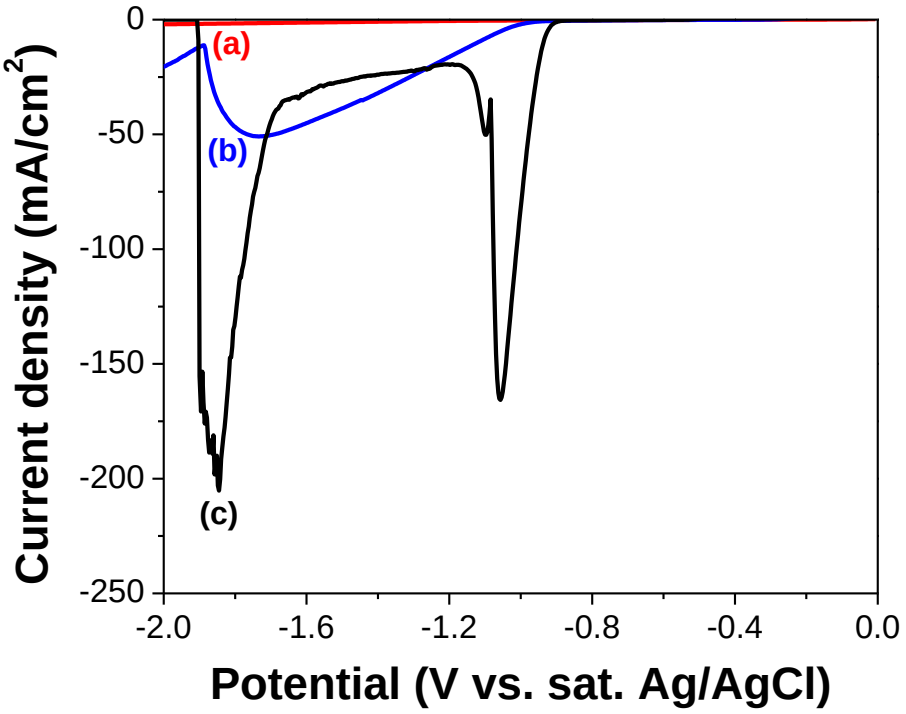

Figure 5.4 LSV curve of Te in alkaline solutions at different pH: (a) 10.2, (b) 12.5 and (c) 14.7. TeO_3^{2-} concentration was 0 mM and temperature was fixed at 23 ^oC. Thick Te films were used as substrate.

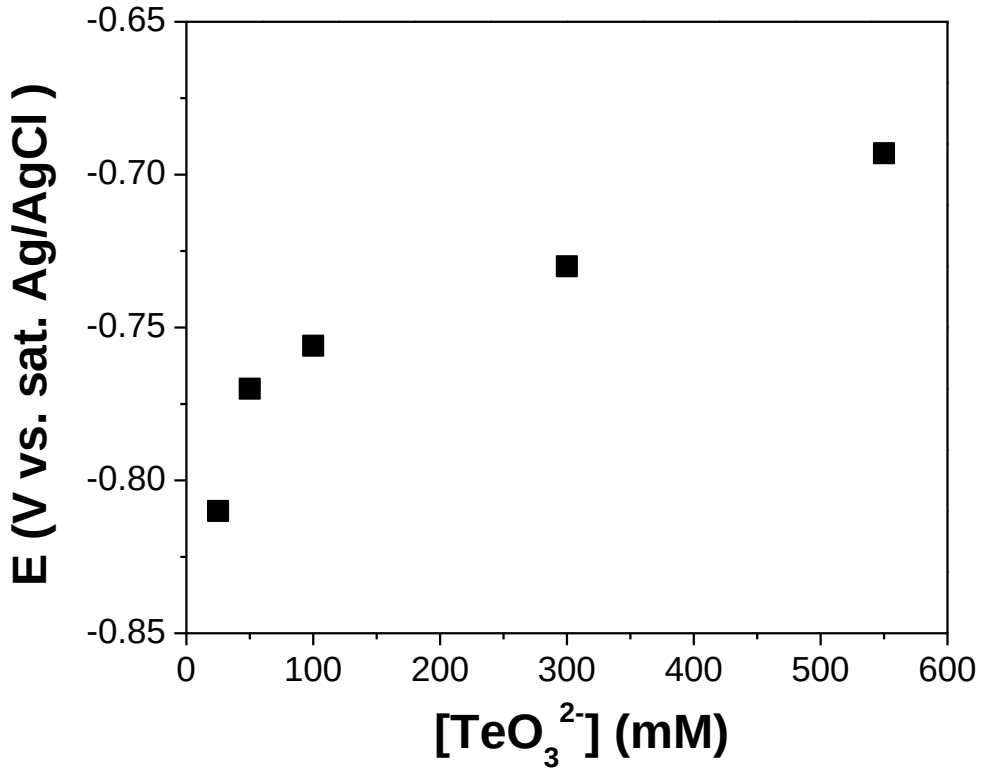

Figure 5.5 Onset potential of TeO_3^{2-} reduction reaction in alkaline solutions with different TeO_3^{2-} concentration (25, 50, 100, 300 and 550 mM) at pH of 12.0 and temperature of 23 ^{o}C. Thick Te films were used as substrate.

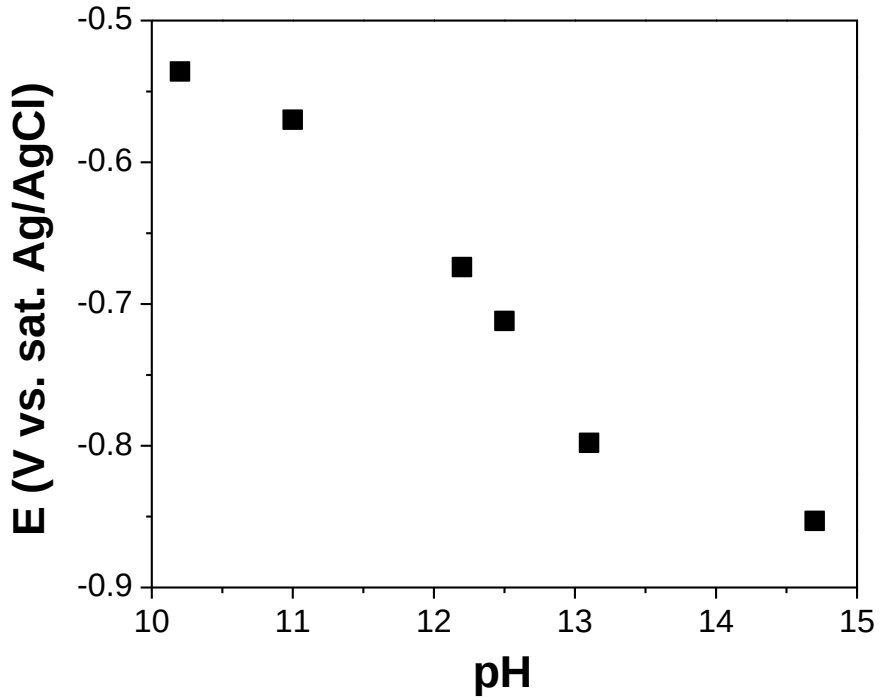

Figure 5.6 Onset potential of TeO_3^{2-} reduction reaction in alkaline solutions at different pH (10.2, 11.0, 12.2, 12.5, 13.1 and 14.7). TeO_3^{2-} concentration was fixed at 550 mM and temperature was fixed at 23 ºC. Thick Te films were used as substrate.

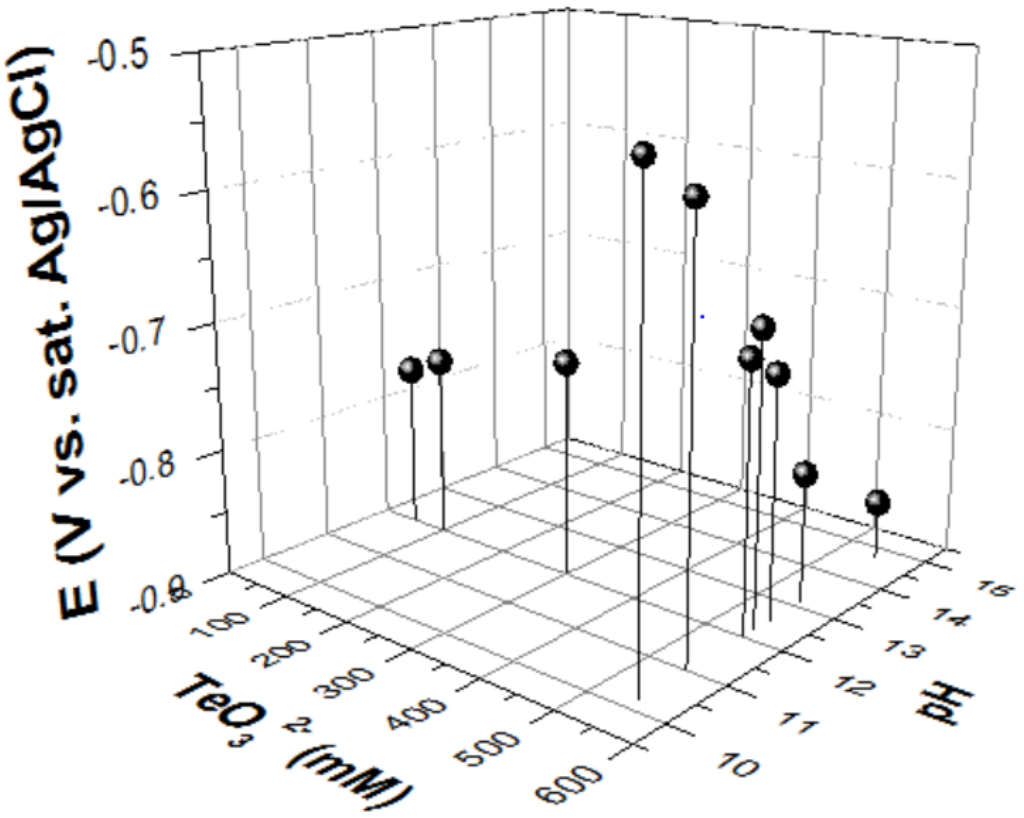

Figure 5.7 Onset potential of TeO_3^{2-} reduction reaction in alkaline solutions with different TeO_3^{2-} concentration (25, 50, 100, 300 and 550 mM) and pH (10.2, 11.0, 12.2, 12.5, 13.1 and 14.7) at temperature of 23 ºC. Thick Te films were used as substrate.

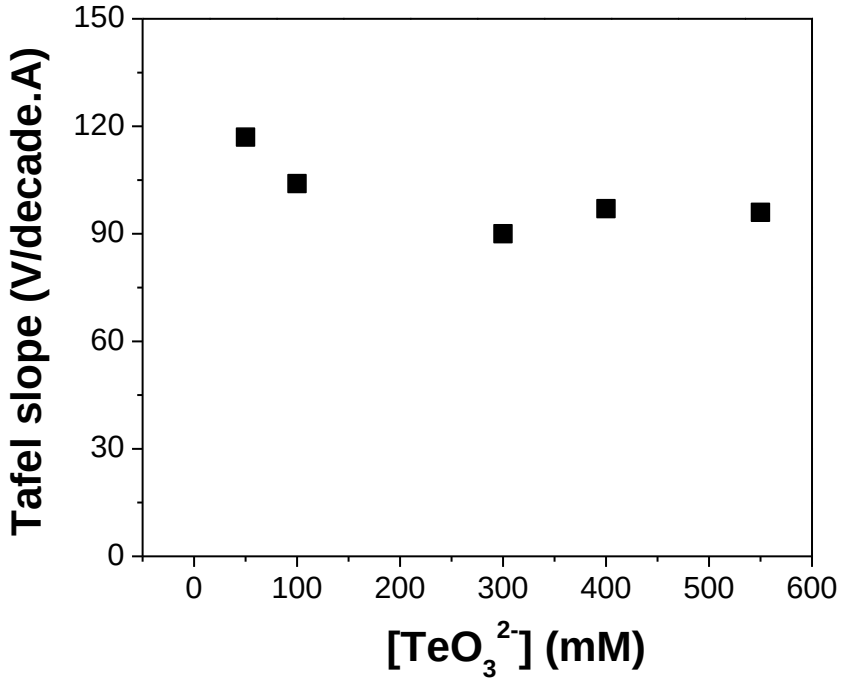

Figure 5.8 Tafel slope of TeO_3^{2-} reduction reaction in alkaline solutions with different $[TeO_3^{2-}]$: 50, 100, 300, 400, and 550 mM. The experiments were conducted using Te as a substrate at pH of 12.0 and temperature of 23 ^{o}C.

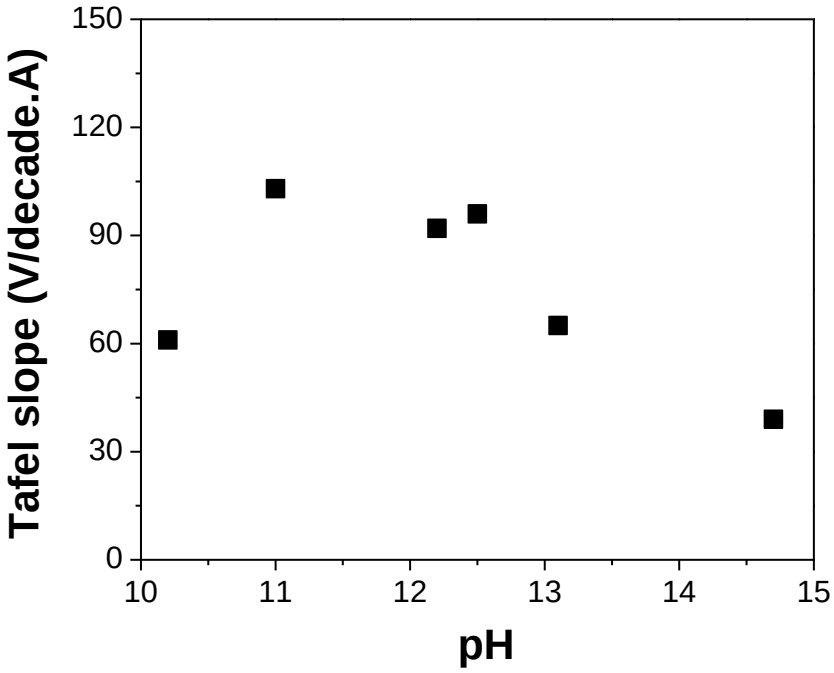

Figure 5.9 Tafel slope of TeO_3^{2-} reduction reaction in alkaline solutions with different pH: 10.2, 11.0, 12.2, 12.5, 13.1, and 14.7 (calculated value). The experiments were conducted using Te as a substrate at [TeO_3^{2-}] of 550 mM and temperature of 23 ^oC.

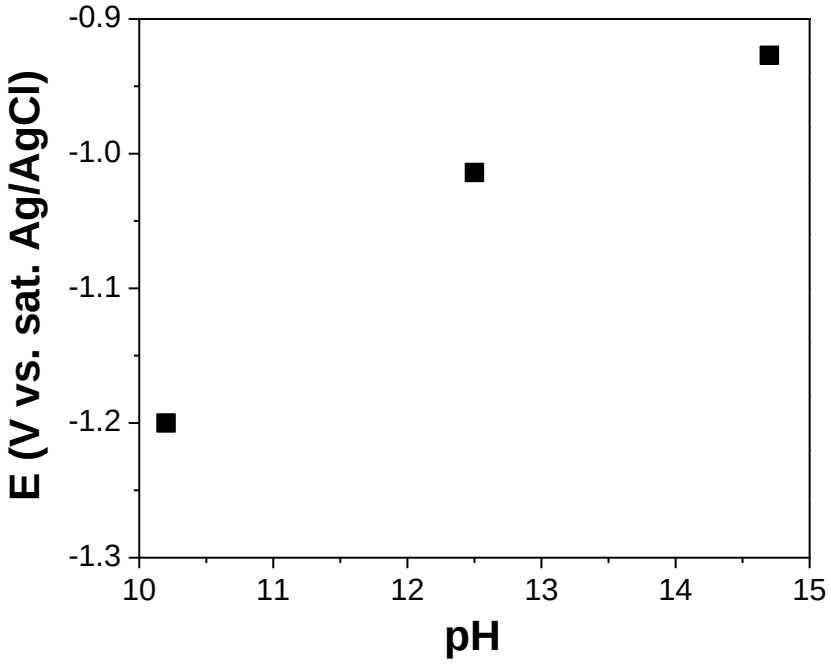

Figure 5.10 Onset potential of Te reduction reaction in alkaline solutions at different pH (10.2, 12.5 and 14.7). TeO_3^{2-} concentration was 0 mM and temperature was fixed at 23 ^{o}C. Thick Te films were used as substrate.

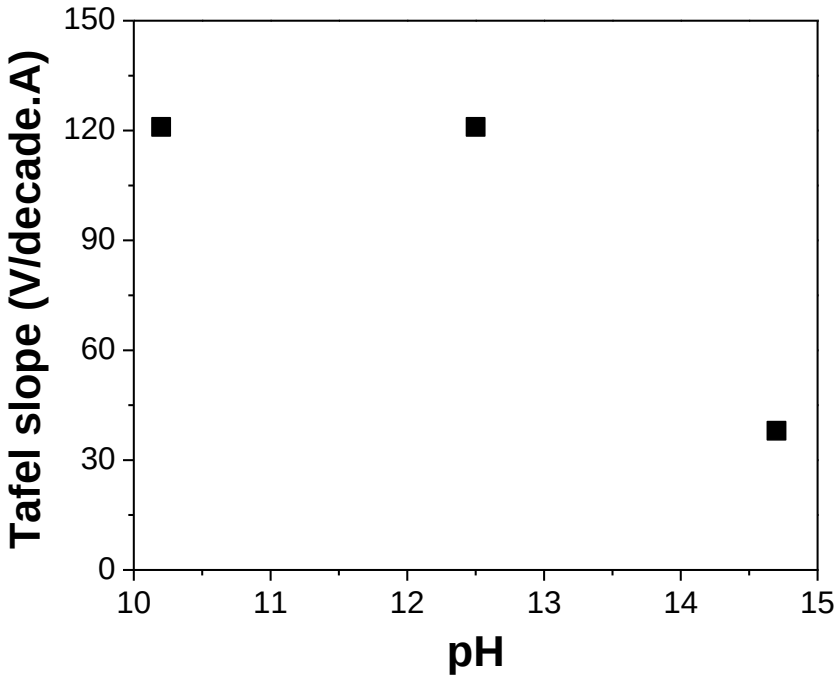

Figure 5.11 Tafel slope of Te reduction reaction in alkaline solutions with different pH: 10.2, 12.5 and 14.7 (calculated value). The experiments were conducted using Te as a substrate at [TeO_3^{2-}] of 0 mM and temperature of 23 ^oC.

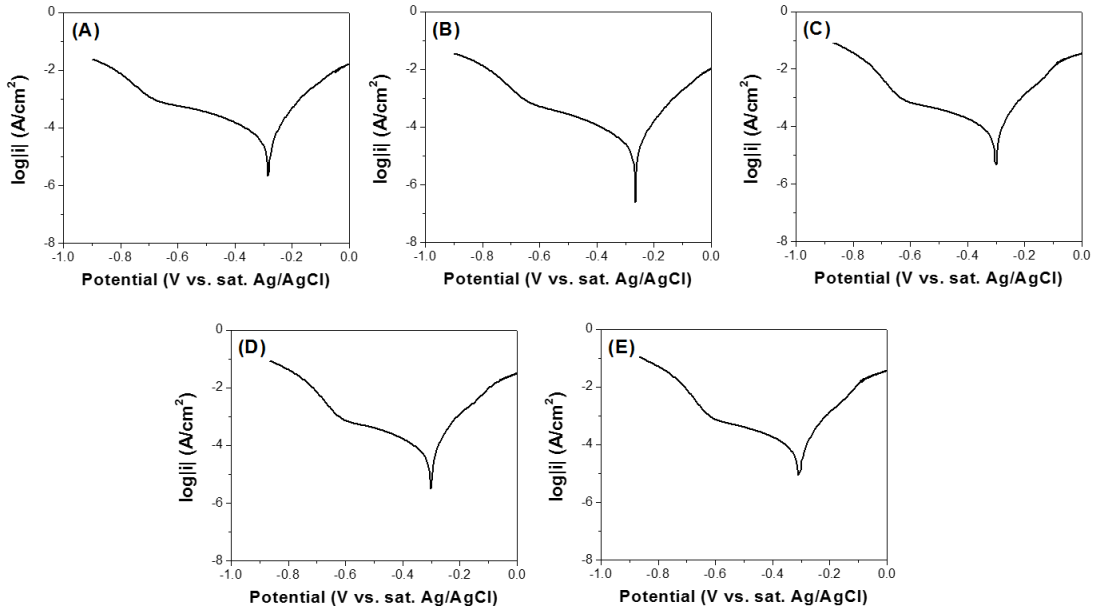

Figure 5.12 Tafel plot of TeO_3^{2-} in alkaline solutions with different [TeO_3^{2-}]. (A) 50, (B) 100, (C) 300, (D) 400, (E) 550 mM. The experiments were conducted using Te as a substrate at pH of 12.0 and temperature of 23 ^oC.

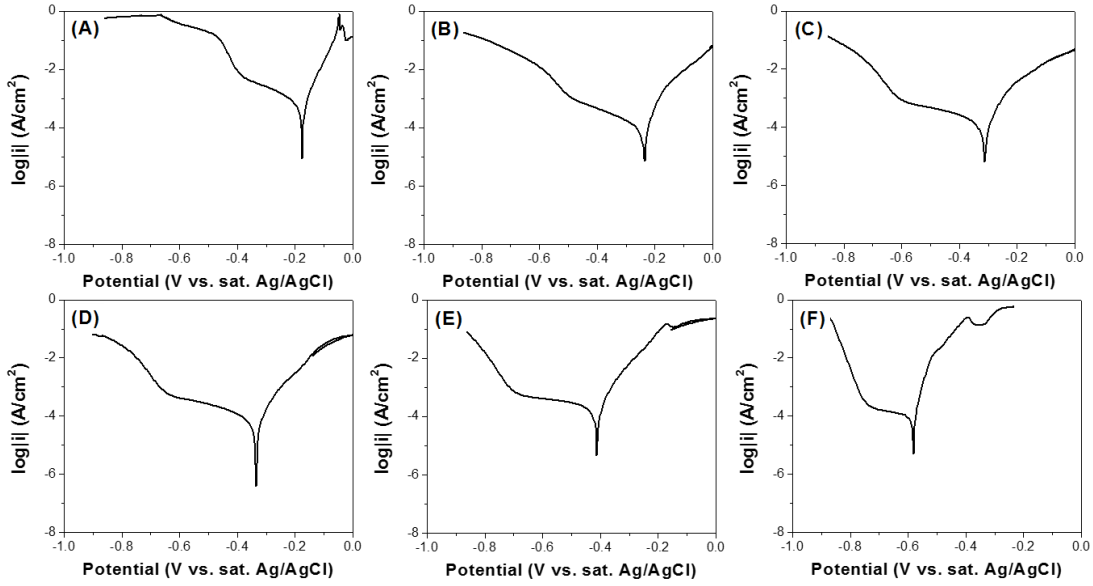

Figure 5.13 Tafel plot of TeO_3^{2-} in alkaline solutions with different pH: (A) 10.2, (B) 11.0, (C) 12.2, (D) 12.5, (E) 13.1, (F) 14.7 (calculated value). The experiments were conducted using Te as a substrate at [TeO_3^{2-}] of 550 mM and temperature of 23 ^oC.

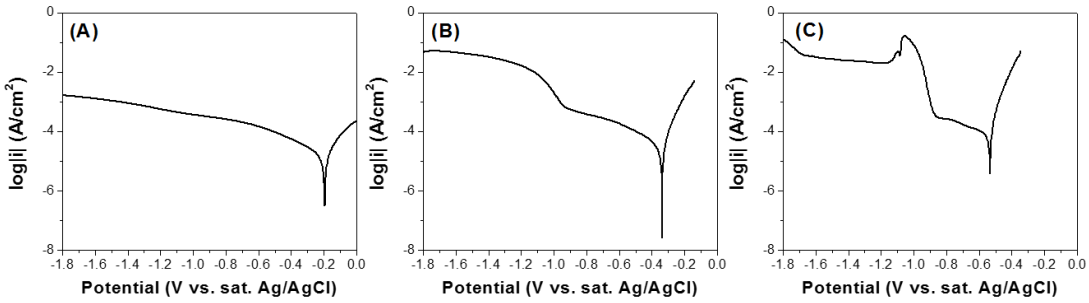

Figure 5.14 Tafel plot of Te dissolution in alkaline solutions with different pH: (A) 10.2, (B) 12.5 and (C) 14.7(calculated value). The experiments were conducted using Te as a substrate at [TeO_3^{2-}] of 550 mM and temperature of 23 ºC.

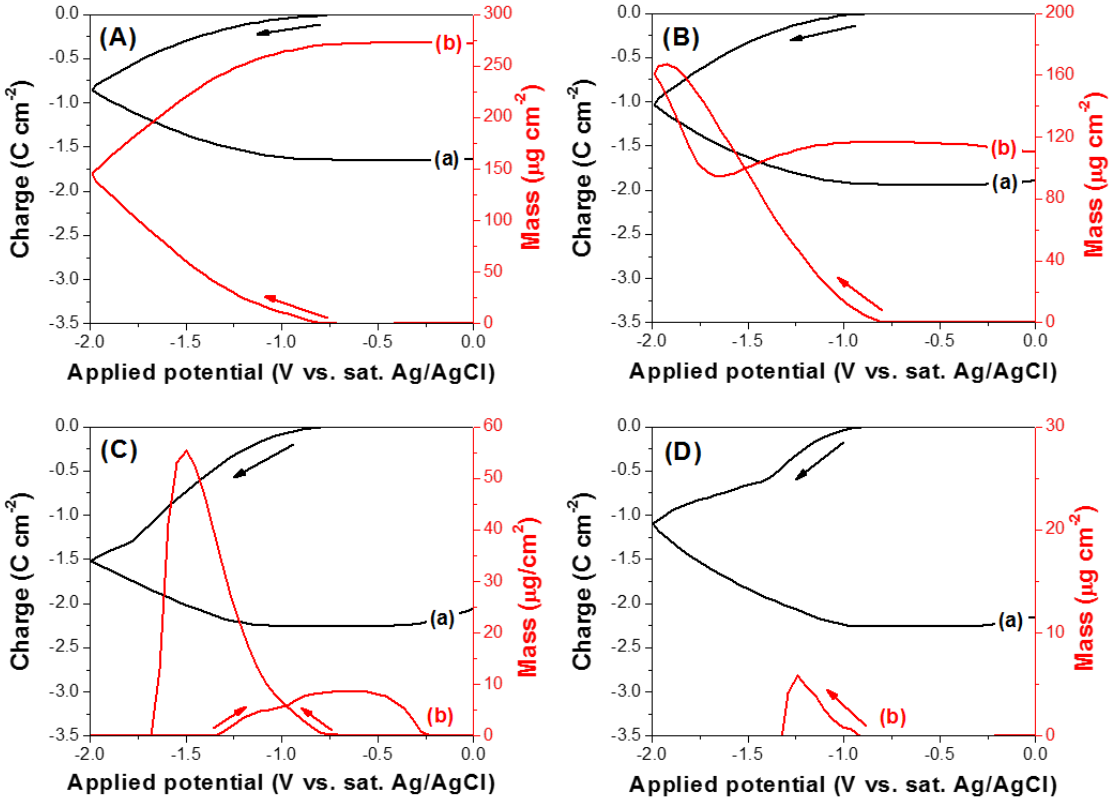

Figure 5.15 Charge curve (a) calculated from cyclic voltammogram and cyclic gravimetric curve (b) measured by EQCM. The experiments were conducted at different pH: (A) 10.2, (B) 12.5, (C) 13.1 and (D) 14.7 with 300 mM TeO_3^{2-} and scan rate of 50 mV/s at 23 ^{o}C.

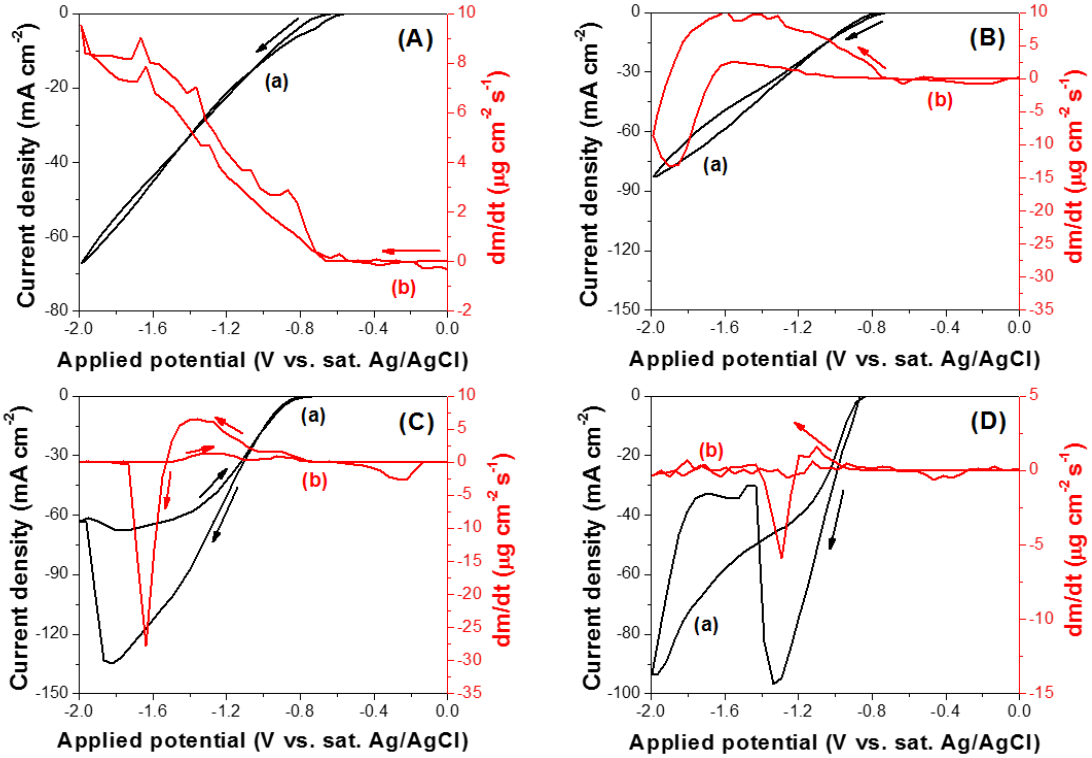

Figure 5.16 Cyclic voltammogram (a) and mass charge rate curve (b) measured by EQCM. The experiments were conducted at different pH: (A) 10.2, (B) 12.5, (C) 13.1 and (D) 14.7 with 300 mM TeO_3^{2-} and scan rate of 50 mV/s at 23 ^{o}C.

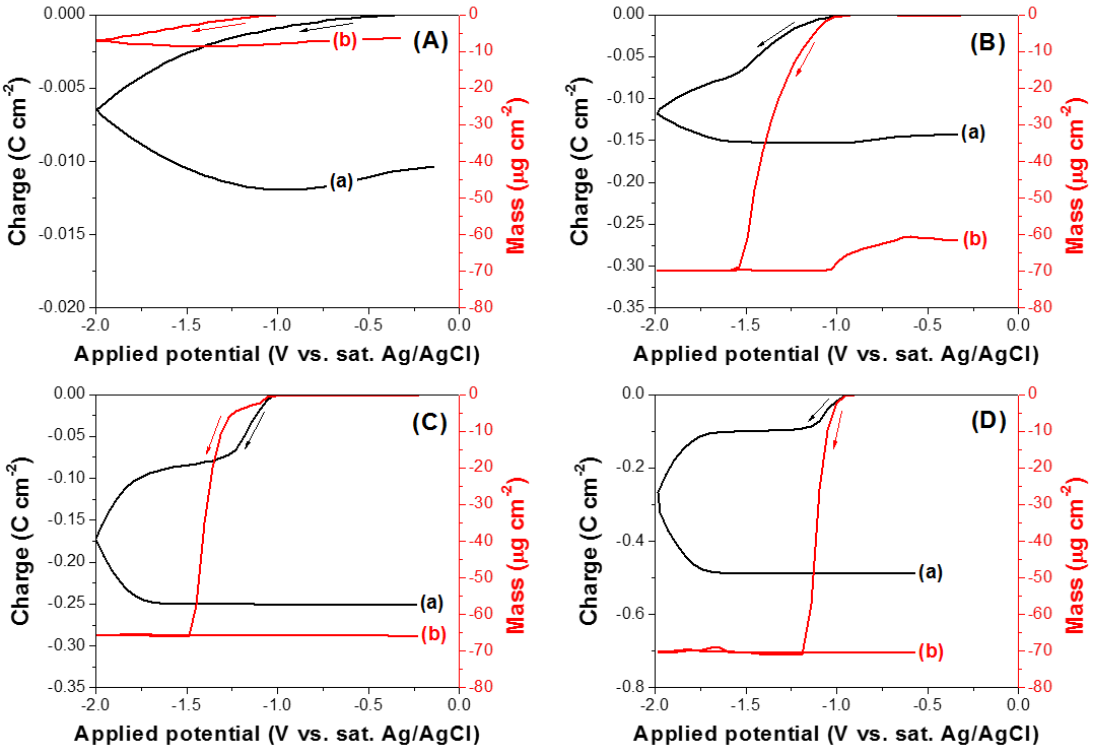

Figure 5.17 Charge curve (a) calculated from cyclic voltammogram and cyclic gravimetric curve (b) measured by EQCM. The experiments were conducted at different pH: (A) 10.2, (B) 12.5, (C) 13.1 and (D) 14.7 with 0 mM TeO_3^{2-} and scan rate of 50 mV/s at 23 ºC. The work electrode is commercialized Au/Cr crystal coated with a 70 ± 3.5 µg cm^{-2} Te thin film.

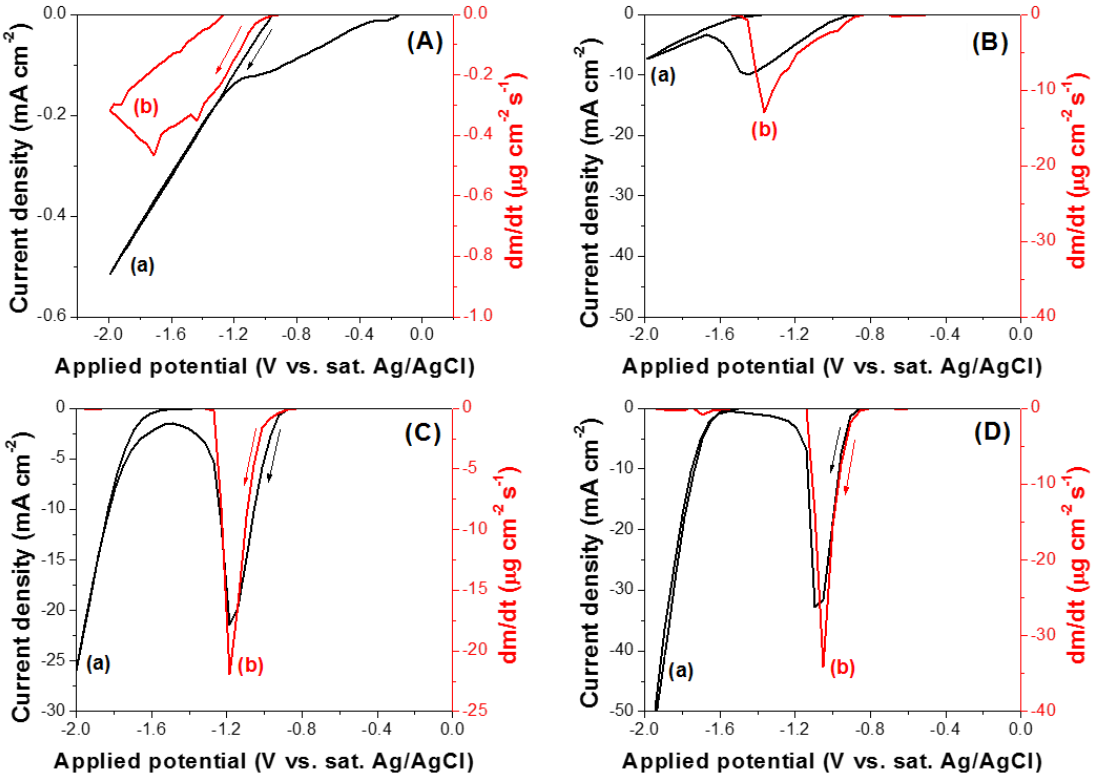

Figure 5.18 Cyclic voltammogram (a) and mass charge rate curve (b) measured by EQCM. The experiments were conducted at different pH: (A) 10.2, (B) 12.5, (C) 13.1 and (D) 14.7 with 0 mM TeO_3^{2-} and scan rate of 50 mV/s at 23 ^{o}C. The work electrode is commercialized Au/Cr crystal coated with a 70 ± 3.5 µg cm^{-2} Te thin film.

6 Electrodeposition of Dense Thick PbTe Film in Alkaline Solution

6.1 Abstract

Dense thick PbTe films were electrodeposited in alkaline solutions by an underpotential deposition mechanism. The composition of the PbTe films was varied from being stoichiometric to Te-rich. Although the applied potential had no substantial effect on the Pb composition, it needs to be in the proper range (from -0.8 to -1.1 V) to avoid further reduction of Te to Te_2^{2-} or keep the reduction of Te to Te_2^{2-} at a low reaction rate. To deposit dense thick films the pH must be maintained in the range 10.5 to 12.3. Higher TeO_3^{2-} concentrations and lower pH values decreased the Pb composition but increased deposition rates. Varying the TeO_3^{2-} concentration changed the surface morphology of thick PbTe films, but all the thick films were found to be dense in the SEM cross section images. A high deposition rate (163 μm/h) was achieved by high TeO_3^{2-} concentrations and at the more negative applied potential.

6.2 Introduction

Lead telluride (PbTe) is a semiconductor with a narrow band-gap energy of 0.31 eV at room temperature and can be n- or p-type as a result of departures from stoichiometry (n-type when Pb-rich: p-type when Te-rich).[1] Furthermore, it has a rock-salt crystal structure. Commercially available, state-of-the-art PbTe-based thermoelectric (TE) devices have the highest ZT of ~ 0.8 at ~ 600 K. This makes PbTe one of the best material candidates for TE application in the middle-to-high temperature range. Furthermore, the

TE microdevice which based on thick film has drawn a significant attention.[2] Thick-film-based devices have advantages over conventional TE module because of its compact size. By shrinking the size of thermoelectric devices, it not only allows the device to operate under smaller temperature gradients, but by so doing it expands its capability to handle a wider range of thermal and power management microelectronic systems.[2-6]

The conventional methods to synthesize films are sputtering and evaporation.[7] Both of these methods are operated under vacuum conditions, which increases capital cost. Furthermore, sputtering has every slow growth rates, which make it unsuitable to growth a thick film (> 20 μm). On the other hand, evaporation cannot control material composition and crystal structure very well, and it need to be operated under high temperature, which further increases capital and energy cost. Additionally, source material utilization may be poor due to lack of spatial selectivity.[8]

In contrast, electrodeposition is a low cost synthesis method with spatial selectivity, by which material composition and crystal structures can be well controlled, and high deposition rate can be achieved.[9] PbTe films have been synthesized by electrodeposition in acidic media.[10-17] However, the acidic bath have its drawbacks when applied to deposit thick films. The solubility of TeO_3^{2-} in acidic solution is low (10 mM at pH of zero)[18], which makes it difficult to achieve high deposition rate, while maintain a dense morphology. Unlike acidic baths, the solubility of TeO_3^{2-} is high in alkaline solution (550 mM at pH of 10.5).[18] Additionally, in both acidic [17] and alkaline [19, 20] solution, the electrodeposition mechanism reported that can electrodeposit dense PbTe films is underpotential deposition mechanism, in which Te deposited first followed by deposition

of Pb on top of Te drive by the Gibbs free energy for PbTe crystal formation (-69.5 kJ/mol) [21]. Therefore, the deposition rate of PbTe depends on Te deposition rate. The higher solubility of TeO_3^{2-} in alkaline solution make it possible to achieve high electrodeposition rate. Electrodeposition of PbTe in alkaline solution was investigated. Saloniemi et al. reported electrodeposition of Te-rich thin PbTe films in alkaline solution based on underpotential deposition (UPD) mechanism, PbTe films with constant composition were deposited in certain potential range, and the potential range may shift depending on different substrate used.[19] Additionally, Saloniemi et al. further investigated the underpotential deposition mechanism of PbTe using an electrochemical quartz crystal microbalance.[20] Miranda et al. electrodeposited polycrystalline PbTe thin films in alkaline solution with the grain size of 100 nm.[22] Qiu et al. synthesized PbTe nanorods by sonoelectrochemictry in which the complex reagent to lead ion ratio was used to control the composition PbTe.[23] Yang et al. synthesized PbTe nanowire arrays using lithographically patterned nanowire electrodeposition.[24] Erdogan et al. reported the synthesis of PbTe thin films using electrodeposition by underpotential deposition mechanism.[25] However, there was few studies about electrodeposition of thick (~50 μm) PbTe film with controlled morphology and high deposition rate.

In this study, the electrodeposition of thick PbTe films was demonstrated. High electrodeposition rates were achieved because of the high solubility of TeO_3^{2-} in alkaline solution. Ethylenediaminetetraacetic acid (EDTA) was used to stabilize lead ions at high pH due to a high stability constant (about 18) of EDTA complex with lead ions.[26-30] The effect of Reaction parameters, including [TeO_3^{2-}], [Pb^{2+}], [EDTA4-]/[Pb^{2+}], pH,

applied potential and agitation on the morphology, composition and electrodeposition rate was systematically studied. Morphology and composition of thick PbTe films was examined by scanning electron microscopy (SEM) and energy Dispersive X-ray (EDS). The crystal structures of thick PbTe films was investigated by X-ray diffraction (XRD). Additionally, electrical and thermoelectric properties of thick PbTe films were characterized.

6.3 Experimental

All solutions were prepared by dissolving various amounts of lead nitrate ($Pb(NO_3)_2$, Fisher Chemical), ethylenediaminetetraacetic acid disodium salt (Na_2H_2EDTA, Fisher Chemical), tellurium dioxide (TeO_2, 99+%, Acros Organics) in sodium hydroxide solutions (NaOH, 10 N, Fisher Chemical) and pH of the solutions were adjusted by NaOH. All the electrodeposition experiments were performed in a conventional three-electrode cell using a rotating disk electrode (RDE) (6.4 mm in diameter gold coated copper rods embedded in a cylindrical Teflon holder) as working electrodes, platinum coated titanium stripe as counter electrode, and saturated Ag/AgCl as reference electrode. Linear sweep voltammograms (LSV) were conducted in the same three-electrode system as used in electrodeposition. All the solutions are deaerated by bubbling N_2 for 40 minutes. [31]

The effect of reaction parameter on electrodeposition of PbTe was investigated at agitation of 2000 rpm and temperature of 23 ^oC. The applied potential effect on PbTe composition and morphology was investigated by varying the applied potential from -0.8 to -1.2 V at TeO_3^{2-} concentration, $PbEDTA^{2-}$ concentration, $[EDTA^{4-}]/[Pb^{2+}]$ ratio, and pH

at 550 mM, 100 mM, 7.5, and 12.3, respectively. The effect of [TeO_3^{2-}] on PbTe electrodeposition was investigated by varying the [TeO_3^{2-}] from 25 to 550 mM while fixing $PbEDTA^{2-}$ concentration, [$EDTA^{4-}$]/[Pb^{2+}] ratio, pH, and applied potential at 100 mM, 1.2, 12.0, and -1.0 V, respectively. Additionally, the pH effect on PbTe electrodeposition was investigated by varying the pH from 10.5 to 13.1, while fixing TeO_3^{2-} concentration, $PbEDTA^{2-}$ concentration, [$EDTA^{4-}$]/[Pb^{2+}] ratio, and applied potential at 550 mM, 100 mM, 1.2, and -1.0 V, respectively.

All the LSV experiments were conducted at agitation of 2000 rpm and temperature of 23 ^{o}C. The effect of TeO_3^{2-} concentration on LSV of PbTe was investigated at the [TeO_3^{2-}] of 25, 50, 100 and 550 mM while fixing $PbEDTA^{2-}$ concentration, [$EDTA^{4-}$]/[Pb^{2+}] ratio, and pH at 100 mM, 1.2, and 12.0 respectively. Additionally, the pH effect on LSV was investigated at pH of 10.5, 12.0, 12.3, 12.5 and 13.1, while fixing while fixing the TeO_3^{2-} concentration, $PbEDTA^{2-}$ concentration, and [$EDTA^{4-}$]/[Pb^{2+}] ratio at 550 mM, 100 mM, and 1.2, respectively. The current efficiency during electrodeposition of thick Te films was calculated using the action measured mass of electrodeposited thick Te films divided by the mass calculated from charge based on chronoamperograms. The morphology, composition and crystal orientation of the thick Te films were studied by field emission-scanning electron microscopy (FE-SEM, FEI NNS450), energy Dispersive X-ray (EDS, FEI NNS450) and X-ray diffraction (XRD, PANalytical Empyrean).

The current efficiency during electrodeposition of PbTe thick films was calculated using the actual measured mass of electrodeposited PbTe thick films divided by the mass calculated from charge based on chronoamperograms. The morphology, composition and

crystal orientation of the thick Te films were studied by field emission-scanning electron microscopy (FE-SEM, FEI NNS450), energy Dispersive X-ray (EDS, FEI NNS450) and X-ray diffraction (XRD, PANalytical Empyrean).

6.4 Results and discussion

The LSV curves of reduction reactions of TeO_3^{2-} (curve a), $PbEDTA^{2-}$ (curve b) and both TeO_3^{2-} and $PbEDTA^{2-}$ (curve c) in alkaline solutions are shown in Figure 6.1A. According to the Pourbaix diagram, in alkaline solution TeO_3^{2-} can be reduced to Te (reaction 6.1), then to Te_2^{2-} (reaction 6.2). Furthermore, Te_2^{2-} can be finally reduced to Te^{2-} (reaction 6.4). [18] However, the only reduction of Pb(II) in alkaline solution is the one step reaction from Pb(II) to Pb.[18] According to the LSV (figure 6.1A), the onset potentials for Te and Pb electrodeposition are -0.66 and -1.18 V, respectively. Additionally, the current density of PbTe LSV (figure 6.1A curve c) started to increase at -1.18 V. Based on the onset potential of Pb electrodeposition, at applied potential of -0.8 V, Pb was not supposed to be deposited. However, the Pb content data showed that at applied potential of -0.8 V, the deposited PbTe film have a Pb content of 45 % (figure 6.3A), which meant that Pb was electrodeposited at -0.8 V with the presence of Te. Therefore, the electrodeposition mechanism of PbTe is an underpotential deposition mechanism (UPD), where Te electrodeposit first followed by the deposition of Pb on top of Te, driven by the Gibbs free energy of PbTe formation (-69.5 kJ/mol) [21]. This UPD mechanism of PbTe was previously reported by Saloniemi et al., in which the electrodeposition mechanism of PbTe was investigated by a combination of electrochemical quartz crystal microbalance and cyclic voltammetry at pH of 9. Saloniemi et al. presented that before the

electrodeposition of PbTe occurred, the increase in current and mass was caused by the electrodeposition of Te. [20] However, in our experiments, the electrodeposition of Te was not observed. According to the UPD mechanism, the deposition current of PbTe should be about 1.5 times of the deposition current of PbTe.[17] However, based on figure 6.1A, when the applied potential is more positive than -1.0 V the current density of PbTe LSV is almost the same as the current of Te LSV. What is more, when the applied potential is more negative than -1.0 V, the current density of Te LSV was even higher than the current density of PbTe. This was probably due to the change of actual surface area of the working electrode because the current density calculation was based on the assumption that the surface area of the working electrode did not change during the electrodeposition. The LSV of Pb electrodeposition only showed one reduction wave because only one reduction reaction occurred. The further increase in current density at potential more negative than -1.8 V was probably caused by hydrogen gas evolution (reaction 6.3). In case of Te, multiple reduction waves were expected because of the multiple step reduction reactions mentioned above. However, the LSV of Te showed only one reduction wave. This is because high TeO_3^{2-} concentrations and well agitated solutions resulted in the quick replenishing of TeO_3^{2-} during LSV, which was reported in another publication from our group about thick Te film.

The chronoamperograms (CA) during PbTe electrodeposition were shown in figure 6.1B. The current density increased as applied potential which is expected based on the Butler-Volmer equation. At applied potential from -0.8 to -1.1 V, the current density (figure 6.1B curve a-d) was relatively stable as a function of time. However, at -1.2 V the current

density increased as a function of time after 2 mins, which may be because of the porous morphology (figure 6.2E).

Figure 6.2. shows the SEM images of PbTe films electrodeposited at different applied potentials, and the [TeO_3^{2-}], [Pb^{2+}], [$EDTA^{4-}$]/[Pb^{2+}], pH and temperature were fixed at 550 mM, 100 mM, 7.5, 12.3 and 23 ^oC, respectively. According to the cross-section view images (top row), when the applied potential is more positive than -1.1 V, dense PbTe films were deposited. However, when the applied potential increased to -1.2 V, porous PbTe films were deposited. There are three possible reasons which may cause the porous morphology: the overpotential deposition (OPD) of Pb; mass transfer control at more negative applied potential; and the further reduction of Te to Te_2^{2-}. When the applied potential (-1.2 V) was more negative than the onset potential of Pb (-1.18 V), the overpotential deposition of Pb started to occur. The change in the electrodeposition mechanism may cause the deterioration of morphology. If the OPD of Pb was triggered, the Pb composition of PbTe films would be more than 50 %.[17] However, the composition results (figure 6.3A) showed that the Pb composition maintained at 47 % at applied potential of -1.2 V; thus OPD of Pb should not be the reason for the change of morphology. Furthermore, at high overpotential the electrodeposition may shift from kinetics control to mass transfer control, which would result in dendritic growth. However, the PbTe LSV (figure 6.1) did not show the diffusion current and the SEM image (figure 6.2E) did not show dendritic structures, which meant that the change of morphology was not caused by mass transfer control. As a consequence, the porous morphology at -1.2 V was caused by further reduction of Te to Te_2^{2-}, which was mentioned in our previous publication about

electrodeposition of thick Te film. Because Te_2^{2-} is a solvable specie in the basic solutions, it would deteriorate the film morphology dramatically. However, during Te electrodeposition, the porous morphology started to occur at potential of -1.0 V instead of -1.2 V in PbTe. This may be because the PbTe crystal structure helped to stabilize Te, where a higher driving force is needed to reduce Te to Te_2^{2-}. Additionally, the applied potential had an effect on the residual stress for the dense films. For example, at applied potential of -0.8 and -1.1 V the PbTe films were cracked, which meant that the films had a high residual stress. However, at applied potentials of -0.9 and -1.0 V the PbTe films were not cracked with metallic color, which meant that the films had a relatively low residual stress.

Figure 6.3A shows that the Pb composition of PbTe film electrodeposited at different applied potentials varied from 45 to 47 %. This is expected because of the UPD mechanism.[19] Additionally, the deposition rate increased as the applied potential became more negative (figure 6.3B). The highest deposition rate yielding a dense morphology without cracks is 163 μm/h with a current efficiency higher than 95 % (figure 6.3C) achieved at applied potential of -1.05 V.

Figure 6.4 A-D shows the LSV curve of Pb (curve a), Te (curve b) and PbTe (curve c). The LSV curve of Pb was conducted at the same condition, which shows a single reduction wave representing the reduction of Pb(II) to Pb(0). The LSV curve of Te was conducted at different TeO_3^{2-} concentrations: 25, 50, 100, and 550 mM. The current density of LSV curve increased at higher TeO_3^{2-} concentrations. For example, at applied potential of -0.9 V, the current densities of Te LSV were 8.2, 11.4, 14.7 and 33.5 mA cm^{-2}, when

TeO_3^{2-} concentrations were 25, 50, 100 and 550 mM, respectively. The TeO_3^{2-} concentration influenced the current density of PbTe as well. At TeO_3^{2-} concentrations of 25, 50, 100 and 550 mM, current densities of PbTe were 13.0, 19.3, 26.8 and 58.5, respectively. This meant that the rate for electrodeposition of PbTe was limited by electrodeposition of Te instead of UPD of Pb. Additionally, the deposition mechanism of PbTe was UPD at different TeO_3^{2-} concentrations, which was confirmed by the Pb content data shown in figure 6.6A. The CA curves (figure 6.4E) during electrodeposition showed that at low TeO_3^{2-} concentration (i.e., 25 and 50 mM) the current density did not change significantly as a function of time, but at high TeO_3^{2-} concentration (i.e., 100, 300 and 550 mM) the CA curves fluctuated, which was probably caused by cracking.

Figure 6.5 shows the SEM images of thick PbTe films electrodeposited at different TeO_3^{2-}concentrations. Varying the TeO_3^{2-} concentration would not change the morphology of PbTe films significantly. According to the SEM images, all the films electrodeposited at different TeO_3^{2-} concentrations had dense morphology. However, the top view SEM images showed that the surface morphology were different: at high TeO_3^{2-} concentrations, the SEM images showed large nanostructures on the surface. Additionally, the residual stress increased at higher TeO_3^{2-} concentration. According to the observation when TeO_3^{2-} concentration was higher than 100 mM, the thick PbTe films were cracked, indicating relatively large residual stress. When the TeO_3^{2-} concentration was lower than 50 mM, the thick PbTe film was not cracked, which meant that the films had relatively small residual stress. In addition, the TeO_3^{2-} concentration affected the film composition and deposition rate. When TeO_3^{2-} concentration increased from 25 to 550 mM, the Pb composition (figure

6.6A) decreased from 50 to 30 %, and the deposition current density (figure 6.6B) increased from 25.9 mA/cm^2 to 82.5 mA/cm^2. (The current density was used to describe the deposition rate because thickness measurements are inaccurate for porous or severely cracked films.) The increase in the current density at higher TeO_3^{2-} concentrations was also shown in the PbTe LSV (figure 6.4 A-D). LSV of Pb, Te and PbTe showed that at different TeO_3^{2-} concentrations, the electrodeposition of PbTe followed the same UPD mechanism, i.e. Te was deposited on the substrate followed by the deposition of Pb on top of Te, where the onset potential of PbTe electrodeposition was the same as that of the Te electrodeposition.

LSV of Pb, Te and PbTe at different pH (i.e., 10.5 to 13.1) are presented in figure 6.7 A-E. At pH of 10.5, the current density of Te LSV curve was even higher than the current density of PbTe LSV. This was probably caused by a porous morphology of Te during LSV. Based on the LSV curves and Pb content (figure 6.9A), the electrodeposition of PbTe at different pH were UPD. The CA curves (figure 6.7 F) for electrodeposition of PbTe showed that at higher pH the current density would be lower. Figure 6.8 shows the thick PbTe films electrodeposited at different pH (10.5 to 13.1). In the pH range (i.e., 10.5 to 12.3), the thick PbTe films had a dense morphology. The residual stress of the film increase when pH increase. Based on the observation, PbTe film synthesized at pH of 10.5 had no cracks. When pH was from 11.3 to 12.3, the synthesized films were cracked because of large residual stress. Additionally, the films deposited at pH (11.3 to 12.3) (figure 6.8 B-D) had microstructure on the top of film, while the film synthesized at pH of 10.5 (figure 6.8A) showed small nodules. When pH increased to 12.5 and 13.1, the PbTe films became

porous. Furthermore, pH also influenced the Pb composition (figure 6.9A) and deposition rate (figure 6.9B). When pH increased from 10.5 to 12.3, the Pb composition varied from 31 to 37 %. However, when pH further increased to 12.5 and 13.1, the Pb composition increased dramatically. At pH of 13.1, the Pb composition is 96 %, which meant that the film was basically Pb instead of PbTe. According to the LSV curves of Pb, Te and PbTe (figure 6.7 A-E), the LSV curves of PbTe generally follows the LSV of Te, even at pH of 13.1, in which the composition of Pb is 96 %. Additionally, pH had effects on LSV of both Te and Pb. According to the Pourbaix diagram, the reduction reactions that happened at different pH are the same, but with different onset potentials. For LSV of Pb, the pH had an effect on the dissociation of EDTA, therefore pH may influence the complex between EDTA and Pb ions. Additionally, the LSV of Pb showed that when pH was higher than 12.5, further increasing pH would push the onset potential of Pb to the positive side, which facilitated electrodeposition of Pb and triggered the overpotential deposition of Pb. This may be the reason why at pH of 13.1 the Pb composition is 96 %. Additionally, the solution pH had a negative effect on the deposition rate of PbTe. When pH increased from 10.5 to 13.1, the average current density decreased from 121.6 to 76.3 mA/cm^2. Furthermore, current efficiency increased from 72 to 86 % when pH increased from 10.5 to 12.0, but it decreased to 71 % when pH was further increased to 12.3.

$TeO_3^{2-}(aq) + 3H_2O(l) + 4e^- \rightarrow Te(s) + 6OH^-(aq)$ (E_0 = - 0.45 V vs. Ag/AgCl)

Reaction 6.1

$HPbO_2^-(aq) + H_2O(l) + 2e^- \rightarrow \mathrm{Pb}(s) + 3OH^-(aq)$ (E_0 = - 0.90 V vs. Ag/AgCl)

Reaction 6.2

$2H_2O(l) + 2e^- \rightarrow H_2(g) + 2OH^-(aq)$ (E_0 = - 0.90 V vs. Ag/AgCl)

Reaction 6.3

$2Te(s) + 2e^- \rightarrow Te_2^{2-}(aq)$ (E_0 = -0.91 V vs. Ag/AgCl)

Reaction 6.4

$Te_2^{2-}(aq) + 2e^- \rightarrow 2Te^{2-}(aq)$ (E_0 = -1.47 V vs. Ag/AgCl)

Reaction 6.5

$PbEDTA^{2-}(aq) + Te(s) + 2e^- \rightarrow PbTe(s) + EDTA^{4-}(aq)$ (ΔG^O = - 69.5 kJ/mol)

Reaction 6.6

Electrodeposited thick PbTe films with different Pb composition were analyzed by XRD (figure 6.10). The results show that at Pb composition of 40 %, the XRD data (figure 6.10) included both PbTe and Te peaks, and the preferred orientation of PbTe was (220), based on reference data of Te (JCPDS, No. 36-1452) and PbTe (JCPDS, No. 38-1435). According to the phase diagram of PbTe, the solubility of Te in PbTe is less than 0.005 %.[32] Therefore, when the Pb composition is 40, 47 or 49 %, the film was Te embedded in the PbTe film instead of a solid solution of Te in PbTe. When the Pb composition increased to 47 %, the XRD data also showed both PbTe and Te peaks, but the preferred orientation of PbTe was (222). However, when the Pb composition was further increased to 49 %, only PbTe peak was seen and the preferred orientation of PbTe was (222).

Seebeck coefficient of PbTe thick films with different Pb content was measured at room temperature (figure 6.11 A). The PbTe thick films were electrodeposited at same applied potential of -1.0 V, but different baths. PbTe films with Pb content of 40 % was

electrodeposited in the solution with TeO_3^{2-} concentration, $PbEDTA^{2-}$, $EDTA^{4-}$ and pH of 50 mM, 100 mM, 120 mM and 12.0. PbTe films with Pb content of 47 % was electrodeposited in the solution with TeO_3^{2-} concentration, $PbEDTA^{2-}$, $EDTA^{4-}$ and pH of 550 mM, 100 mM, 750 mM and 12.3. PbTe films with Pb content of 49 % was electrodeposited in the solution with TeO_3^{2-} concentration, $PbEDTA^{2-}$, $EDTA^{4-}$ and pH of 50 mM, 100 mM, 120 mM and 10.5. The PbTe films with Pb content of 47 % has the highest Seebeck coefficient 641 µV/K. The PbTe films with Pb content of 49 % have a Seebeck coefficient of 524 µV/K. Compared to the Seebeck coefficient of bulk PbTe (220 µV/K) [1], the electrodeposited PbTe thick films have relatively high Seebeck coefficient, because the as-deposited PbTe thick films have crystal defects, including grain boundaries and embedded tellurium, which increases effective mass of the charge carriers, leading to high Seebeck coefficient.

Electrical conductivity of PbTe thick films with different Pb content was measured by Van der Pauw method (figure 6.11 B). The electrical conductivity of PbTe films at room temperature with Pb content of 47 and 49 % is 0.005 and 0.14 S/cm, respectively. Compared to the electrical conductivity of bulk PbTe (820 S/cm) [1], the as-deposited PbTe thick films have low electrical conductivity, which may be caused by crystal defects. Power factor of as deposited PbTe thick films was calculated (figure 6.11 C), As-deposited PbTe thick film with Pb content of 49 % has the highest power factor (3.9 $\mu W/K^2/m$).

6.5 Conclusion

In summary, electrodeposition of dense thick PbTe films in alkaline solution were demonstrated. The electrodeposition mechanism of PbTe was UPD. The composition of PbTe films were from Te-rich to stoichiometry. To achieve a dense morphology, the applied potential was controlled from -0.8 to -1.1 V to minimize the effect of reduction reaction (Te to Te_2^{2-}) on morphology. Lowing pH led to higher deposition rates and lower Pb composition in the whole pH range, while the proper pH to form a dense thick film (~50 μm) is from 10.5 to 12.3. TeO_3^{2-} concentration had a significant effect on deposition rate, and had a minor effect on the composition. The high deposition rate of 163 μm/h was achieved with dense morphology and composition close to stoichiometry. The as-deposited PbTe thick films have relatively high Seebeck coefficient but low electrical conductivity.

6.6 Reference

1. Dughaish, Z.H., *Lead telluride as a thermoelectric material for thermoelectric power generation.* Physica B: Condensed Matter, 2002. **322**(1–2): p. 205-223.
2. Fleurial, J.P., et al. *Power density-length of leg _ Thick-film thermoelectric microdevices*. in *Thermoelectrics, 1999. Eighteenth International Conference on*. 1999.
3. Semeniouk, V. and J.-P. Fleurial. *Temperature diff - thickness _ Modeling and Minimization of Intercascade Thermal Resistance in Multi-Stage Thermoelectric Cooler*. in *XVI Int. Conf. Thermoelectrics*. 1997. Dresden, Germany: IEEE.
4. Anatychuk, L.I., O.J. Luste, and L.N. Vikhor. *Optimal functions as an effective method for thermoelectric devices design*. in *Thermoelectrics, 1996., Fifteenth International Conference on*. 1996.
5. Anatychuk, L.I. and O.J. Luste. *Thickness limitation- lower limit_ Physical principles of microminiaturization in thermoelectricity*. in *Thermoelectrics, 1996., Fifteenth International Conference on*. 1996.
6. Snyder, G.J., et al., *Thermoelectric microdevice fabricated by a MEMS-like electrochemical process.* Nat Mater, 2003. **2**(8): p. 528-531.

7. Mattox, D.M., *Handbook of Physical Vapor Deposition (PVD) Processing (Second Edition)*2010, Boston: William Andrew Publishing. 1-24.

8. Mattox, D.M., *Physical vapor deposition (PVD) processes.* Metal Finishing, 2001. **99, Supplement 1**: p. 409-423.

9. Dini, J.W., *Electrodeposition - the materials science of coating and substrates*1993, Westwood, New jersey: Noyes Publications.

10. Xiao, F., et al., *Recent progress in electrodeposition of thermoelectric thin films and nanostructures.* Electrochimica Acta, 2008. **53**(28): p. 8103-8117.

11. Beaunier, L., et al., *PbTe - acid _ Cd ion effect on morphology _ current limit because of Te ion mass transfer.* Journal of Electroanalytical Chemistry, 2002. **532**(1–2): p. 215-218.

12. Li, G.-R., et al., *Facile and Efficient Electrochemical Synthesis of PbTe Dendritic Structures.* Chemistry of Materials, 2008. **20**(10): p. 3306-3314.

13. Ni, Y., Y. Zhang, and J. Hong, *Potentiostatic Electrodeposition Route for Quick Synthesis of Featherlike PbTe Dendrites: Influencing Factors and Shape Evolution.* Crystal Growth & Design, 2011. **11**(6): p. 2142-2148.

14. Mondal, A., et al., *PbTe -acidic- electrodeposition - temperature effect&morphology - thickness saturation&time.* Thin Solid Films, 2006. **515**(4): p. 1255-1259.

15. Li, X. and I.S. Nandhakumar, *Direct electrodeposition of PbTe thin films on n-type silicon.* Electrochemistry Communications, 2008. **10**(3): p. 363-366.

16. Ivanova, Y.A., D.K. Ivanou, and E.A. Streltsov, *Electrochemical deposition of PbTe onto n-Si(1 0 0) wafers.* Electrochemistry Communications, 2007. **9**(4): p. 599-604.

17. Xiao, F., et al., *Electrodeposition of PbTe thin films from acidic nitrate baths.* Electrochimica Acta, 2006. **52**(3): p. 1101-1107.

18. Pourbaix, M., *Atlas of electrochemical equilibria in aqueous solutions*1966, Long Island City, N.Y.: Pergamon Press Inc.

19. Saloniemi, H., et al., *PbTe alkaline _ underpotential deposition _ potential&composition.* Thin Solid Films, 1998. **326**(1–2): p. 78-82.

20. Saloniemi, H., et al., *PbTe alkaline bath _ underpotential deposition.* Journal of Electroanalytical Chemistry, 2000. **482**(2): p. 139-148.

21. *CRC Handbook of Chemistry and Physics*2002, Cleveland: CRC Press.

22. Renata, C., B. Mirandaa, and P.G. Abramof, *PbTe _ alkaline _ stress increase because of smaller crystallites.* Materials Research, 2004. **7**: p. 619-623.

23. Qiu, X., et al., *PbTe Nanorods by Sonoelectrochemistry.* Angewandte Chemie International Edition, 2005. **44**(36): p. 5855-5857.

24. Yang, Y., et al., *Synthesis of PbTe Nanowire Arrays using Lithographically Patterned Nanowire Electrodeposition.* Nano Letters, 2008. **8**(8): p. 2447-2451.

25. Erdoğan, İ.Y., et al., *PbTe alkaline _ co-deposition.* Thin Solid Films, 2009. **517**(18): p. 5419-5424.

26. Schwarzenbach, G. and E. Freitag, *Complexons. XX. Stability constants of heavy metal complexes of ethylenediaminetetraacetic acid.* Helvetica Chimica Acta, 1951. **34**: p. 1503-8.

27. Schwarzenbach, G., R. Gut, and G. Anderegg, *Complexons. XXV. Polarographic study of exchange equilibria. New data on the formation constants of metal complexes of ethylenediaminetetraacetic acid and 1,2-diaminocyclohexanetetraacetic acid.* Helvetica Chimica Acta, 1954. **37**: p. 937-957.

28. Schmid, R.W. and C.N. Reilley, *A Rapid Electrochemical Method for the Determination of Metal Chelate Stability Constants.* Journal of the American Chemical Society, 1956. **78**(21): p. 5513-5518.

29. Stary, J., *The solvent extraction of metal 8-quinolinolates.* Analytica Chimica Acta, 1963. **28**: p. 132-49.

30. Ogino, H., *The stability constants of ethylenediaminetetraacetato, trimethylenediaminetetracetato, and propylenediaminetetraacetato complexes of some divalent metal ions.* Bulletin of the Chemical Society of Japan, 1965. **38**: p. 771-7.

31. Butler, I.B., M.A.A. Schoonen, and D.T. Rickard, *Removal of dissolved oxygen from water: A comparison of four common techniques.* Talanta, 1994. **41**(2): p. 211-215.

32. Gomez, M.P., D.A. Stevenson, and R.A. Huggins, *Self-diffusion of Pb and Te in lead telluride.* Journal of Physics and Chemistry of Solids, 1971. **32**(2): p. 335-344.

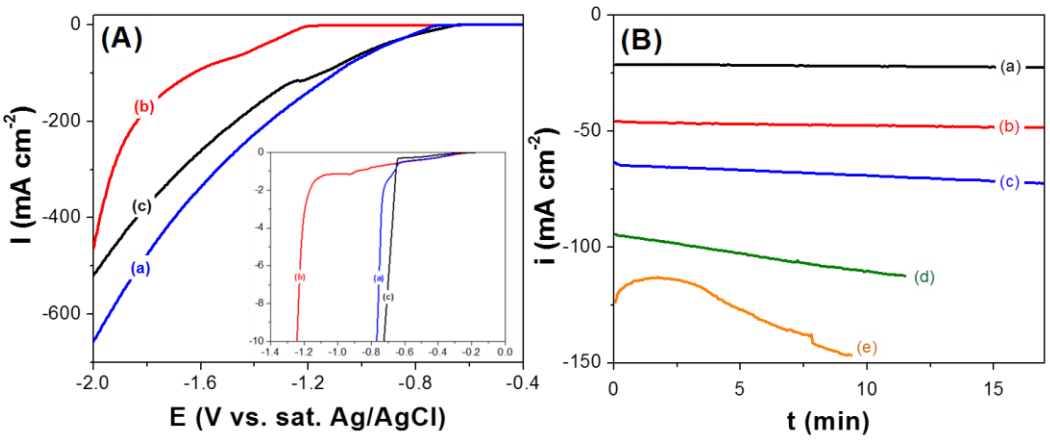

Figure 6.1 (A) LSV curves for Pb, Te and PbTe electrodepositions in alkaline solutions with (a) 550 mM [TeO_3^{2-}], (b) 100 mM [Pb^{2+}], and (c) 550 mM [TeO_3^{2-}] + 100 mM [Pb^{2+}] at pH of 12.3. Temperature and [$EDTA^{4-}$] concentration were fixed at 23 ^oC and 750 mM, respectively. (B) Chronoamperograms of PbTe electrodeposition at different applied potentials: (a) -0.8, (b) -0.9, (c) -1.0, (d) -1.1, and (e) -1.2 V. The electrolyte consisted of 550 mM [TeO_3^{2-}] + 100 mM [Pb^{+2}] + 750 mM [$EDTA^{4-}$]. The agitation rate and solution pH were fixed at 2000 rpm and 12.3, respectively. The substrates were gold coated copper rods.

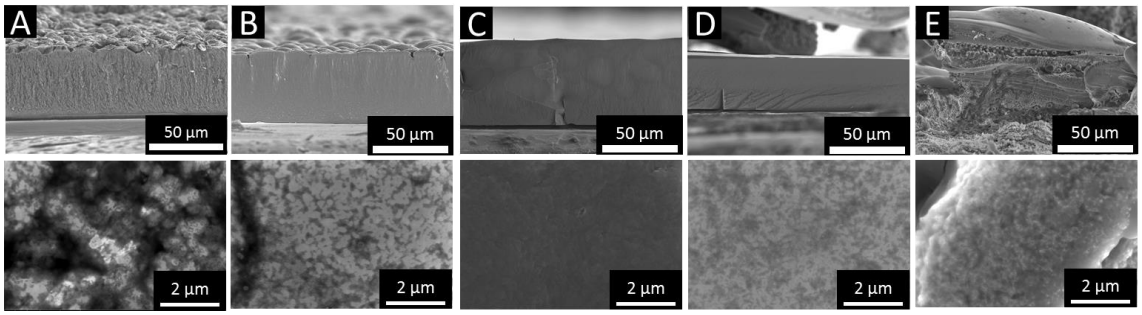

Figure 6.2 SEM images of PbTe electrodeposits at different applied potentials: (a) -0.8, (b) -0.9, (c) -1.0, (d) -1.1, and (e) -1.2 V vs sat. Ag/AgCl. The electrolyte consisted of 550 mM [TeO_3^{2-}] + 100 mM [Pb^{2+}] + 750 mM [$EDTA^{4-}$]. The solution pH was kept constant at 12.3 with fixed solution pH and temperature at 12.3 and 23^{o}C, respectively. The top row images are cross-section view, and the bottom row images are top view.

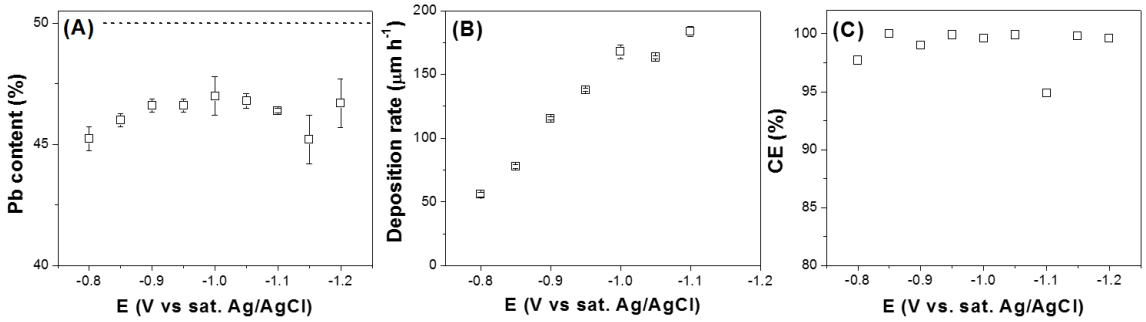

Figure 6.3 Deposited Pb content (A), film deposition rate (B) and current efficiency (C) of PbTe film electrodeposited at different applied potential. The electrolyte consisted of 550 mM [TeO_3^{2-}] + 100 mM [Pb^{2+}] + 750 mM [$EDTA^{4-}$]. The solution pH was kept constant at 12.3 with fixed solution pH and temperature at 12.3 and 23^{o}C, respectively.

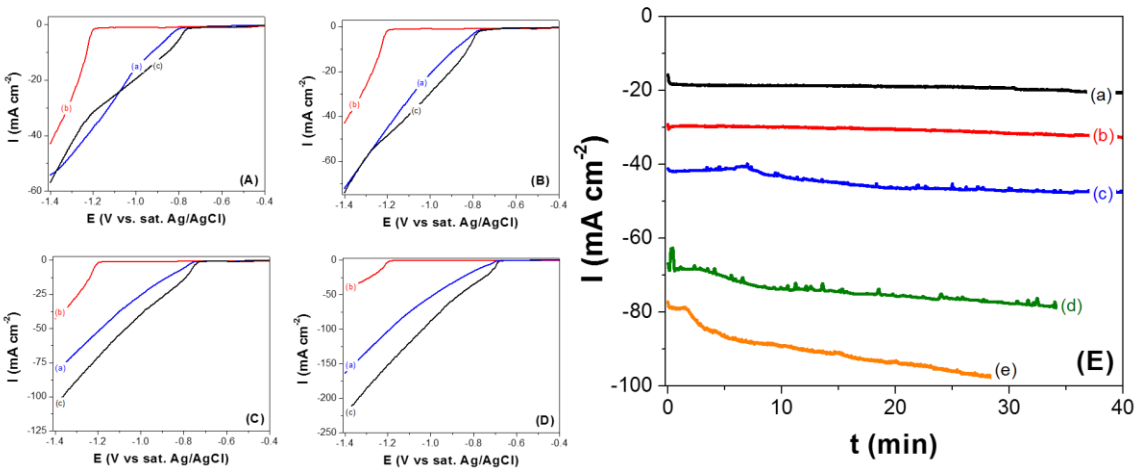

Figure 6.4 LSV curve for Pb, Te and PbTe electrodepositions in alkaline solutions with different (a) [TeO_3^{2-}], (b) 100 mM [Pb^{2+}], and (c) different [TeO_3^{2-}] + 100 mM [Pb^{2+}] at pH of 12.0 and temperature of 23 ºC. [TeO_3^{2-}] is: (A) 25, (B) 50, (C) 100, and (D) 550 mM. [$EDTA^{4-}$] was fixed at 120 mM. The substrates were gold coated copper rods. (E) Chronoamperograms of PbTe electrodeposition in alkaline solutions at different TeO_3^{2-} concentration: (a) 25, (b) 50, (c) 100, (d) 300, and (e) 550 mM with 100 mM [$PbEDTA^{2-}$], [$EDTA^{4-}$]/[Pb^{2+}] of 1.2 at pH of 12.0 and applied potential of -1.0 V.

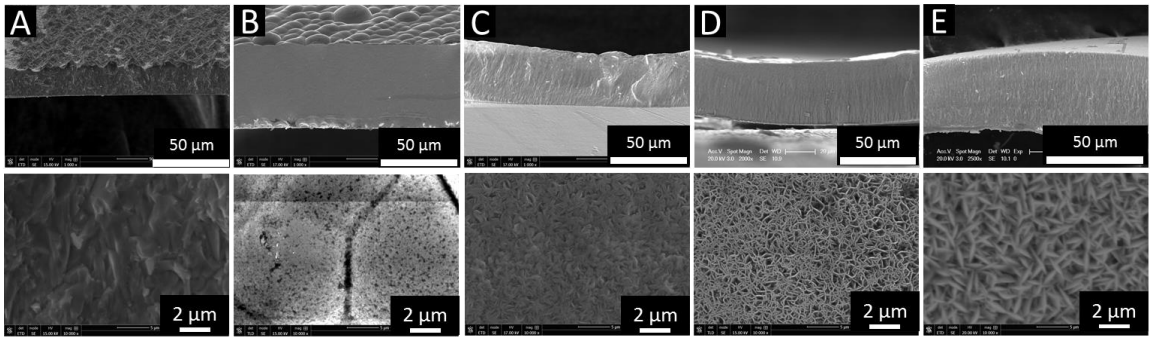

Figure 6.5 SEM images of PbTe electrodeposited at different [TeO_3^{2-}]: (A) 25, (B) 50, (C) 100, (D) 300, and (E) 550 mM at applied potential of -1.0 V, pH of 12.0 and temperature of 23 ºC, with 100 mM [Pb^{2+}] and [$EDTA^{4-}$]/[Pb^{2+}] of 1.2. The top row images are cross-section view, and the bottom row images are top view. The small images at top right corner are the low magnification images.

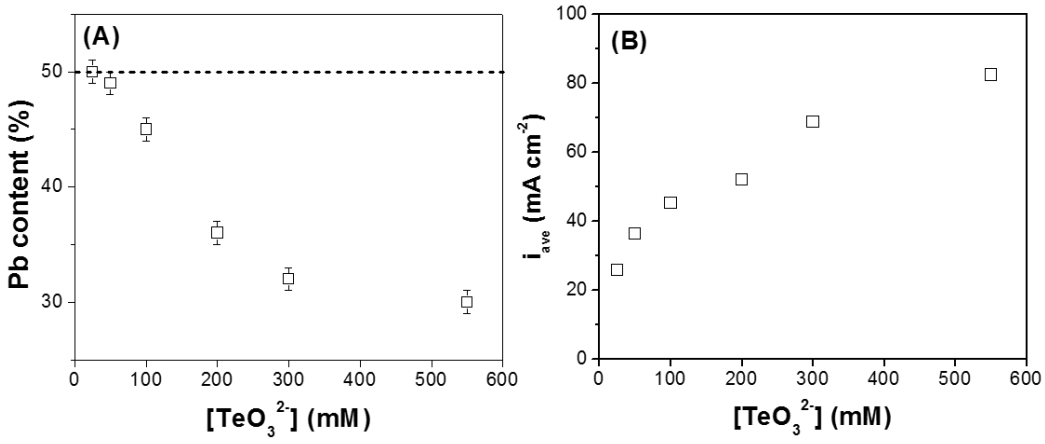

Figure 6.6 Pb composition (A) and growth rate (B) of PbTe film electrodeposited at different $[TeO_3^{2-}]$: 25, 50, 100, 300, and 550 mM with 100 mM $[Pb^{2+}]$, and $[EDTA^{4-}]/[Pb^{2+}]$ of 1.2 at applied potential of -1.0 V, pH of 12.0 and temperature of 23 ^{o}C.

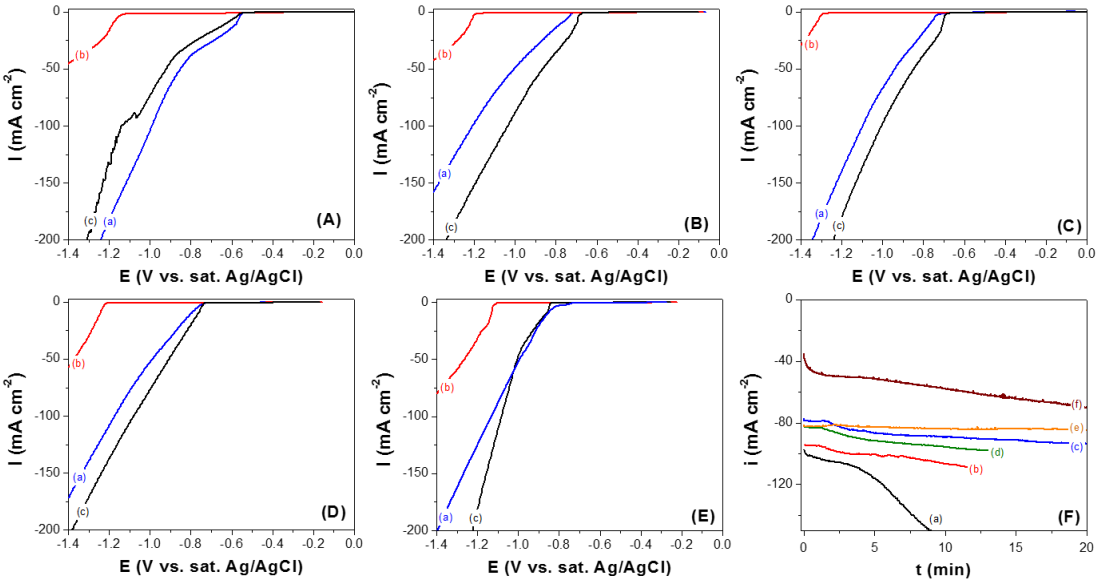

Figure 6.7 LSV curve for Pb, Te and PbTe electrodepositions in alkaline solutions with (a) 550 mM [TeO_3^{2-}], (b) 100 mM [Pb^{2+}], and (c) 550 mM [TeO_3^{2-}] + 100 mM [Pb^{2+}] at different pH: (A) 10.5, (B) 12.0, (C) 12.3, (D) 12.5, and (E) 13.1. Temperature was fixed at 23 ^oC. [$EDTA^{4-}$]/[Pb^{2+}] was fixed at 1.2. The substrates were gold coated copper rods. (F) Chronoamperograms of PbTe electrodeposition in alkaline solutions at different pH: (a) 10.5, (b) 11.3, (c) 12.0, (d) 12.3, (e) 12.5, and (f) 13.1 with 550 mM [TeO_3^{2-}], 100 mM [$PbEDTA^{2-}$], [$EDTA^{4-}$]/[Pb^{2+}] of 1.2 at applied potential of -1.0 V.

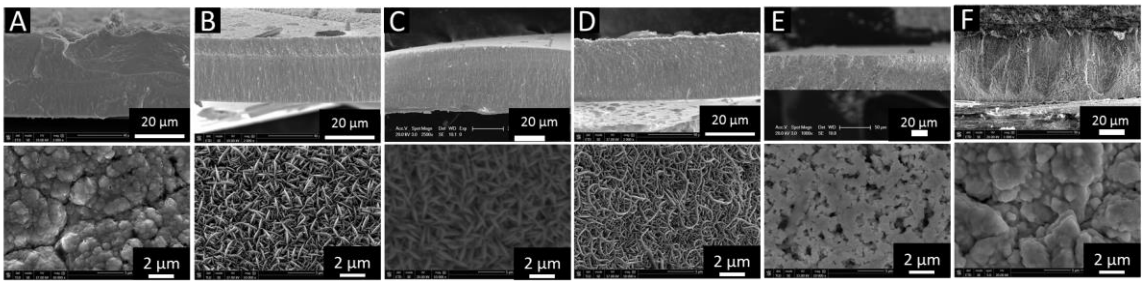

Figure 6.8 SEM images of PbTe electrodeposited at different pH: (A) 10.5, (B) 11.3, (C) 12.0, (D) 12.3, (E) 12.5, and (F) 13.1 with 550 mM [TeO_3^{2-}], 100 mM [Pb^{2+}], and [$EDTA^{4-}$]/[Pb^{2+}] of 1.2 at applied potential of -1.0 V and temperature of 23 ºC. The top row images are cross-section view, and the bottom row images are top view. The small images at top right corner are the low magnification images.

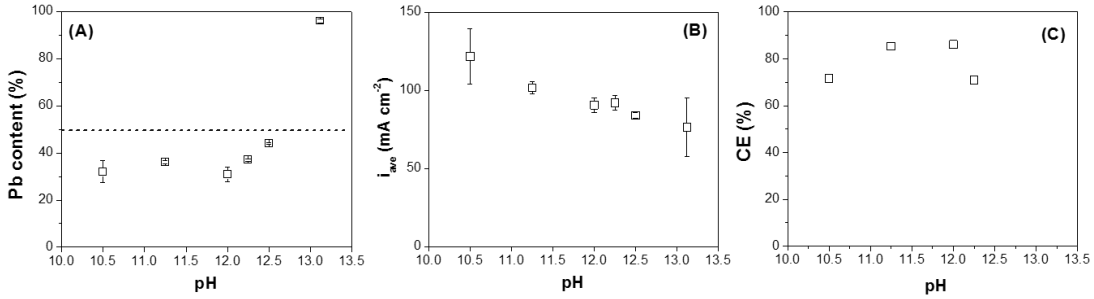

Figure 6.9 Pb composition (A), growth rate (B) and current efficiency (C) of PbTe film electrodeposited at different pH: 10.5, 11.3, 12.0, 12.3, 12.5 and 13.1 with 550 mM [TeO_3^{2-}], 100 mM [Pb^{2+}], and [$EDTA^{4-}$]/[Pb^{2+}] of 1.2 at applied potential of -1.0 V and temperature of 23 ºC.

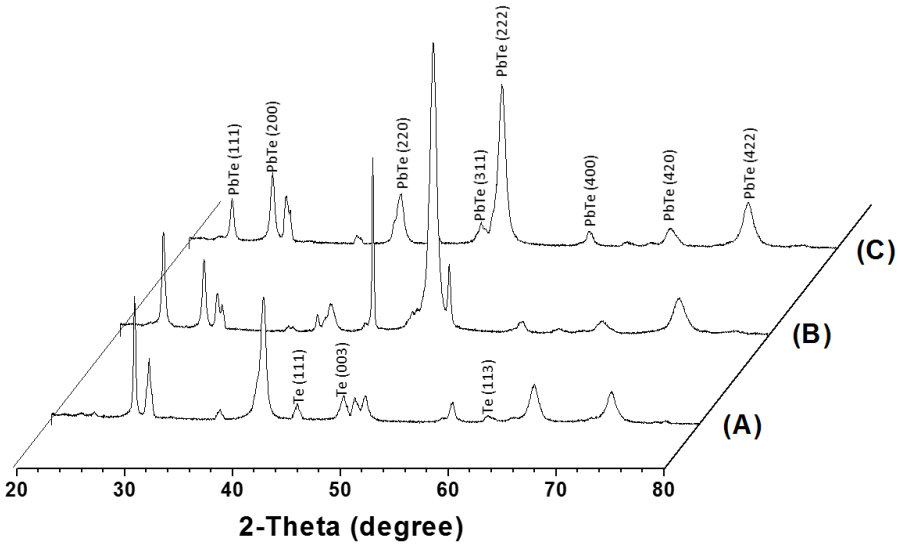

Figure 6.10 XRD of PbTe thick film with different Pb content: (A) 40, (B) 47 and (C) 49 %. D, E and F are the reference data of Te, Pb and PbTe.

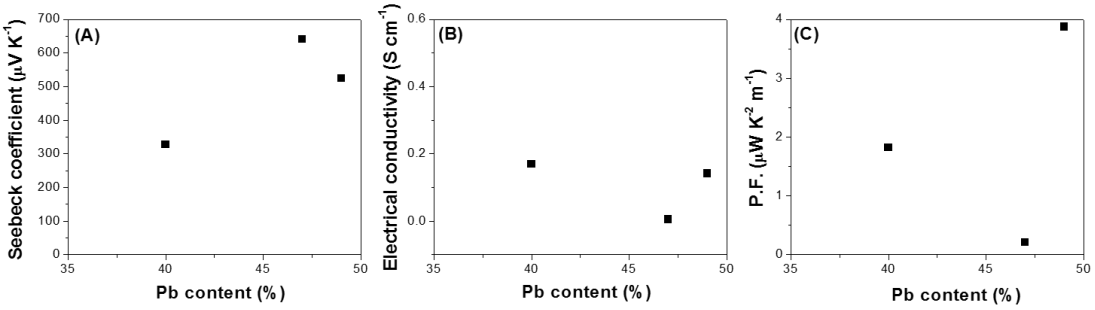

Figure 6.11 (A) Seebeck coefficient, (B) electrical conductivity and (C) power factor of as-deposited PbTe films with different Pb content: 40, 47 and 49 %.

7 Optimizing Thermoelectric Properties of Te-rich PbTe Thick Films by Tuning Energy Barrier

7.1 Abstract

Te-rich thick PbTe films were electrodeposited. Crystal grain boundary and Te nanoinclusion was controlled by tailoring by composition and crystal structures of the thick PbTe films. PbTe grain size was from 26 to 120 nm and the size of Te nanoinclusion was from 35 to 87 nm. The thermoelectric property of thick PbTe films were optimized by introducing energy barriers from crystal grain boundary and tellurium nanoinclusion. Increasing the diffraction percent and grain size of PbTe decreased the energy barrier. However, Increasing the size of Te nanoinclusion increased the energy barrier. Higher energy barrier resulted in higher Seebeck coefficient but lower electrical conductivity. The highest P.F. was 531 $\mu w\ K^{-2}\ cm^{-1}$, achieved at energy barrier of 0.023 eV.

7.2 Introduction

Heat is the natural by-product of energy conversion processes. Of the 4.25×10^{20} J of energy the United States consumes every year, more than 60% is wasted in the form of heat. Therefore, waste heat recovery is a crucial step to improve the energy generation and utilization efficiency. Thermoelectric (TE) materials, which can directly convert rejected or waste heat into usable electric power, has been extensively developed for this issue. The efficiency of a thermoelectric device can be presented by the thermoelectric figure of merit defined by $ZT=S^2\sigma T/\kappa$, where S, σ, T, and κ are the Seebeck coefficient, electrical conductivity, temperature, and thermal conductivity, respectively. However, these key

parameters in a bulk thermoelectric material would offset one another, which makes it difficult to further enhance the ZT value. Therefore, it is essential to decouple thermoelectric parameters namely, decouple S and σ, κ and σ, and κ and S. The energy filtering effect is able to enhance the average charge carrier energy by blocking low energy carriers at grain boundaries or material interfaces induced by nanoinclusion, which makes it possible to increase the Seebeck coefficient without depress the electrical conductivity significantly.

Lead telluride (PbTe) is a semiconductor with a narrow band-gap energy of 0.31 eV at room temperature and it has a rock-salt crystal structure. PbTe can be n- or p-type as a result of departures from stoichiometry (n-type when Pb-rich: p-type when Te-rich).[1] Commercially available, state-of-the-art PbTe-based thermoelectric devices have the highest ZT of ~ 0.8 at ~ 600 K. This makes PbTe one of the best material candidates for thermoelectric application in the middle-high temperature range. Furthermore, microdevice for thermoelectric application which based on thick film has drawn a significant attention.[2] Thick-film-based devices have advantages over conventional TE module because of its compact size. By shrinking the size of thermoelectric devices, it not only allows the device to operate under smaller temperature gradients, but by so doing it expands its capability to handle a wider range of thermal and power management microelectronic systems.[2-6]

Electrodeposition is a low cost synthesis method with spatial selectivity, by which material composition and crystal structures can be well controlled, and high deposition rate can be achieved.[7] PbTe films have been synthesized by electrodeposition in acidic

media.[8-15] However, the acidic bath have its drawbacks when applied to deposit thick films. The solubility of TeO_3^{2-} in acidic solution is low (10 mM at pH of zero)[16], which makes it difficult to achieve high deposition rate, while maintain a dense morphology. Unlike acidic baths, the solubility of TeO_3^{2-} is high in alkaline solution (550 mM at pH of 10.5).[16] Additionally, in both acidic [15] and alkaline [17, 18] solution, the electrodeposition mechanism reported that can electrodeposit dense PbTe films is underpotential deposition mechanism, in which Te deposited first followed by deposition of Pb on top of Te drive by the Gibbs free energy for PbTe crystal formation (-69.5 kJ/mol) [19]. Electrodeposition of PbTe in alkaline solution was investigated by several groups. Saloniemi et al. reported electrodeposition of Te-rich thin PbTe films in alkaline solution based on underpotential deposition (UPD) mechanism, PbTe films with constant composition were deposited in certain potential range, and the potential range may shift depends on different substrate.[17] Additionally, Saloniemi et al. further investigated the underpotential deposition mechanism of PbTe using electrochemical quartz crystal microbalance.[18] Miranda et al. electrodeposited polycrystalline PbTe thin films in alkaline solution with the grain size of 100 nm.[20] Qiu et al. synthesized PbTe nanorods by sonoelectrochemictry in which the complex reagent to lead ion ratio was used to control the composition PbTe.[21] Yang et al. synthesized PbTe nanowire arrays using lithographically patterned nanowire electrodeposition.[22] Erdogan et al. reported the synthesis of PbTe thin films using electrodeposition by underpotential deposition mechanism.[23] However, there are only a few papers reported to systematically study the thermoelectric properties of electrodeposited PbTe.

In this study, PbTe thick films were electrodeposited with different crystal structure and composition. The crystal structure of the PbTe films was further tuned by post-annealing process. Morphology and composition of thick PbTe films was examined by scanning electron microscopy (SEM) and energy Dispersive X-ray (EDS). The crystal structures of thick PbTe films was investigated by X-ray diffraction (XRD). Electrical and thermoelectric properties of PbTe thick films were characterized. The effect of crystal structure and composition on electrical and thermoelectric properties was discussed.

7.3 Experimental

All solutions were prepared by dissolving various amounts of lead nitrate ($Pb(NO_3)_2$, Fisher Chemical), ethylenediaminetetraacetic acid disodium salt (Na_2H_2EDTA, Fisher Chemical), tellurium dioxide (TeO_2, 99+%, Acros Organics) in sodium hydroxide solutions (NaOH, 10 N, Fisher Chemical) and pH of the solutions were adjusted by NaOH. All the electrodeposition experiments were performed in a conventional three-electrode cell using a rotating disk electrode (RDE) (6.4 mm in diameter gold coated copper rods embedded in a cylindrical Teflon holder) as working electrodes, platinum coated titanium stripe as counter electrode, and saturated Ag/AgCl as reference electrode. Linear sweep voltammograms (LSV) were conducted in the same three-electrode system as used in electrodeposition. All the solutions are deaerated by bubbling N_2 for 40 minutes. [24]

For electrical and thermoelectric characterization, the thin films were transferred from the Au/Cu substrate to a non-conductive epoxy substrate (Loctite, epoxy instant mix).

The entire film was successfully transferred without cracking.[25] The final dimensions of the sample for characterization were 0.16 cm^2.

The morphology, composition and crystal orientation of the thick Te films were studied by field emission-scanning electron microscopy (FE-SEM, FEI NNS450), energy Dispersive X-ray (EDS, FEI NNS450) and X-ray diffraction (XRD, PANalytical Empyrean). The samples were annealed at 200 ^oC for 2 and 10 hours in a nitrogen atmosphere with 5% hydrogen present. The electrical conductivity, Hall mobility, and carrier concentration of the film were examined using a custom-made Hall measurement system by the van der Pauw configuration with four-point probes. The Seebeck coefficient was investigated by a custom-made Seebeck measurement system

7.4 Results and discussion

PbTe thick film with the same composition but different crystal structure was electrodeposited in the solution with 550 mM [TeO_3^{2-}], 100 mM [Pb^{2+}], and [$EDTA^{4-}$]/[Pb^{2+}] of 7.5 at pH of 12.3 and temperature of 23 ^oC at different applied potential of -0.9 and -0.95 V (figure 7.1). Figure 7.1 showed that both of the thick film have a dense morphology. The crystal structure of the films were further tuned by post-annealing process for 2 and 10 hours. Figure 7.2 and 7.3 show the XRD data of the thick PbTe films before and after annealing, and the XRD patterns of the PbTe thick films match with the standard reference data (JCPDS-International Center for Diffraction Data, for Te No. 36-1452 and PbTe No. 38-1435). The un-indexed peak at 29.5 degree is attributed to the reflection of a frequency doubling radiation wave.[26]. According to the XRD data, there are crystallized

Te and PbTe in the thick film. After annealed for 2 and 10 hours, the thick films were further crystallized based on the higher intensity XRD peaks.

The diffraction percentage of crystallized PbTe over both crystallized PbTe and Te was calculated, as well as grain size of both PbTe and Te. Figure 7.4 shows that when annealing time increased, the diffraction percentage and grain size of PbTe increased but the grain size of Te decreased. For example, when annealing time increased from 0 to 10 hours, the diffraction percentage of PbTe increased from 66 to 86 % for the film electrodeposited at applied potential of -0.9 V (film 1), and 74 to 90 % for the film electrodeposited at applied potential of -0.95 V (film 2); the grain size of PbTe increased from 26 to 117 nm and 27.3 to 97.9 nm; but the grain size of Te decreased from 76 to 35 nm and 87 to 79 nm for film 1 and film 2, respectively. The increase of PbTe grain size is expected because of crystal growth during the annealing. Te grain, which was relatively small amount, was embedded in the PbTe crystals. Therefore, when the PbTe grains started to growth, it may consume the Te grains. This may be the reason why grain size of Te decreased during the annealing process.

The energy barrier of thick films was calculated using temperature dependent resistance data. According to figure 7.5 A-C, the energy barrier was influenced by diffraction percentage and grain size of PbTe and grain size of Te. The increase of diffraction percent and grain size of PbTe resulted in decrease of energy barrier, but the increase of Te grain size lead to increase of energy barrier.

Figure 7.6 shows that the Seebeck coefficient increased from 79 to 422 μV K^{-1} (125 to 545 μV K^{-1}), when energy barrier increased from 0.02 to 0.11 eV (0.023 to 0.04 eV). This may be caused by the energy filtering effect, in which the energy barrier filtering out cool (have lower energy) charge carriers to increase the average energy of charge carriers, leading to the enhancement of Seebeck coefficient. However, the energy barrier have a negative effect on the mobility of charge carriers (figure 7.7A) and have no significant effect on the carrier concentration (figure 7.7B). As a result, higher energy barrier would result in lower electrical conductivity (figure 7.8). The highest electrical conductivity (141 S cm^{-1}) was achieved at energy barrier of 0.02 eV. The power factor (P.F.) of PbTe films was calculated using Seebeck coefficient and electrical conductivity. According to figure 7.9, lower energy barrier resulted in higher power factor. The highest power factor (183 μW K^{-2} m^{-1}) was achieved at energy barrier of 0.023 eV. To better compare the effect of the energy barrier and Pb content on the thermopower, Pisarenko plot was applied with the bulk PbTe literature data shown in (figure 6.10). It clearly show that at same carrier concentration, as-deposited PbTe thick films have relatively highest thermopower and high effective mass. After annealing the PbTe thick films have relative lower thermopower compared to the as-deposit film, but getting closer to the thermopower of bulk materials, which means that the films have the tendency to get to the thermodynamically stable PbTe crystal structure. According to figure 7.11, the enhancement of power factor came from the enhancement of electrical conductivity at low energy barrier. Although lower energy barrier would result in lower thermopower, the enhancement in electrical conductivity could compensate the reduction of thermopower and further enhance the power factor.

PbTe film with composition ranged from 40 to 49 % with dense morphology was electrodeposited (figure 7.15). The crystal structure of the films were further tuned by post-annealing process for 2 and 10 hours. Figure 7.16 (40 %), 17 (47 %) and 18 (49 %) show the XRD data of the thick PbTe films before and after annealing, and the XRD patterns of the PbTe thick films match with the standard reference data (JCPDS-International Center for Diffraction Data, for Te No. 36-1452 and PbTe No. 38-1435). At Pb content of 40 % and 47 %, the XRD data showed both Te peaks and PbTe peaks, and the preferred orientation of PbTe was (220). According to the phase diagram of PbTe, the solubility of Te in PbTe is less than 0.005 %.[27] Therefore, when the Pb composition is 40 %, the film was Te embedded in PbTe film instead of solid solution. However, when the Pb content increased to 49 %, the XRD data shows PbTe peaks and the Te peaks are barely detectable.

Based on the XRD data, the diffraction percentage and grain size of PbTe and grain size of Te were calculated, and their relationship with annealing time was plotted. Figure 7.19 shows that diffraction percentage and grain size of PbTe increased when annealing time increase from 0 to 10 hours. However, the grain size of Te have different trend after annealing. At Pb content of 49 %, the grain size of Te decreased after annealing, this may be caused by the reason that Te was consumed during the process of PbTe crystal growth. At Pb content of 47 %, the grain size of Te did not change significantly. However, at Pb content of 40 %, the grain of Te crystal grew larger during the annealing process. This was probably caused by the reason that in the film with Pb content of 40 % there are large amount of Te, although some Te atoms may be consumed by PbTe crystal growth, the amount of Te atoms was still large enough to support the growth of Te crystal grains.

Figure 7.20 shows that energy barrier was influenced by diffraction percent and grain size of PbTe and grain size of Te. Higher diffraction percent of PbTe would lead to lower energy barrier (figure 7.20A). Larger grain size of PbTe would also lead to lower energy barrier (figure 7.20 A). However, Te grain size has different effect on energy barrier depending on the Pb content of PbTe films. When the Pb content of PbTe films was 49 %, increase the Te grain size would lead to increase of energy barrier. When the Pb content of PbTe films was 47 %, the changed of Te grains size during annealing is minor, so the trend was not obvious. However, when the Pb content of PbTe films was 40 %, increase the Te grain size would decrease the energy barrier.

Energy barrier has significant effect on Seebeck coefficient and the trend was the same at different Pb content (figure 7.21). Higher energy barrier resulted in higher Seebeck coefficient. When the energy barrier increase from 0.009 to 0.16 eV, the Seebeck coefficient increased from 64 to 641 $\mu V\ K^{-1}$.

Carrier concentration of the films was independent on energy barrier (figure 7.22 A). However, the mobility of the charge carrier increased from 0.0014 to 16.9 $cm^2\ V^{-1}\ s^{-1}$ when energy barrier decreased from 0.16 to 0.009 eV (figure 7.22). As a consequence, the electrical conductivity was influenced by energy barrier significantly. Lower energy barrier resulted in higher electrical conductivity. Additionally, Pb content also have effect on the electrical conductivity. The higher electrical conductivity that achieved was 204 $S\ cm^{-1}$ at energy barrier of 0.041 eV and Pb content of 49 % (figure 7.23). Power factor was calculated using the electrical conductivity and Seebeck coefficient. Both energy barrier and Pb content have significant effect on the power factor. The highest P.F. was 532.48

$\mu W/ K^{-2} m^{-1}$, achieved at Energy barrier of 0.041 eV and Pb content of 49 %, which was very close to stoichiometry.

To better compare the effect of the energy barrier and Pb content on the thermopower, Pisarenko plot was applied with the bulk PbTe literature data shown in (figure 7.25). It clearly show that at same carrier concentration, as-deposited PbTe thick films have relatively highest thermopower and high effective mass. After annealing the PbTe thick films have relative lower thermopower compared to the as-deposit film, but getting closer to the thermopower of bulk materials, which means that the films have the tendency to get to the thermodynamically stable PbTe crystal structure. According to figure 7.26, the enhancement of power factor was directly related to electrical conductivity. Higher electrical conductivity resulted in higher power factor. The enhancement of electrical conductivity after annealing is attributed to the reduction of energy barrier. Although lower energy barrier would result in lower thermopower, the enhancement in electrical conductivity could compensate the reduction of thermopower and further enhance the power factor. However, for the three samples presented in figure 7.15, after annealing copper was diffused in the PbTe thick films from the substrate. Therefore, further analysis is needed to separate effect of copper on electrical and thermoelectric properties of PbTe.

7.5 Conclusion

Electrodeposition of Te-rich thick PbTe films were demonstrated. Diffraction percentage and grain size of PbTe and size of Te nanoinclusion was controlled by

electrodeposition and post-annealing process. Crystal grain boundary and tellurium nanoinclusion introduced an energy barrier, which played a critical role on the electrical and thermoelectrical properties of PbTe thick film. Higher diffraction percentage and larger grain size of PbTe would resulted in lower energy barrier. However, the effect of Te grain size on energy barrier was dependent on Pb composition. Decrease the energy barrier would reduce the Seebeck coefficient, however lower energy barrier would enhance the electrical conductivity. The increase in electrical conductivity compensated the reduction of Seebeck coefficient, then power factor was improved by higher electrical conductivity due to low energy density. The highest power factor was 531 μw K^{-2} cm^{-1}, achieved at energy barrier of 0.023 eV with Pb content of 49 %.

7.6 Reference

1. Dughaish, Z.H., *Lead telluride as a thermoelectric material for thermoelectric power generation.* Physica B: Condensed Matter, 2002. **322**(1–2): p. 205-223.
2. Fleurial, J.P., et al. *Power density-length of leg _ Thick-film thermoelectric microdevices*. in *Thermoelectrics, 1999. Eighteenth International Conference on*. 1999.
3. Semeniouk, V. and J.-P. Fleurial. *Temperature diff - thickness _ Modeling and Minimization of Intercascade Thermal Resistance in Multi-Stage Thermoelectric Cooler*. in *XVI Int. Conf. Thermoelectrics*. 1997. Dresden, Germany: IEEE.
4. Anatychuk, L.I., O.J. Luste, and L.N. Vikhor. *Optimal functions as an effective method for thermoelectric devices design*. in *Thermoelectrics, 1996., Fifteenth International Conference on*. 1996.
5. Anatychuk, L.I. and O.J. Luste. *Thickness limitation- lower limit_ Physical principles of microminiaturization in thermoelectricity*. in *Thermoelectrics, 1996., Fifteenth International Conference on*. 1996.
6. Snyder, G.J., et al., *Thermoelectric microdevice fabricated by a MEMS-like electrochemical process.* Nat Mater, 2003. **2**(8): p. 528-531.

7. Dini, J.W., *Electrodeposition - the materials science of coating and substrates*1993, Westwood, New jersey: Noyes Publications.

8. Xiao, F., et al., *Recent progress in electrodeposition of thermoelectric thin films and nanostructures.* Electrochimica Acta, 2008. **53**(28): p. 8103-8117.

9. Beaunier, L., et al., *PbTe - acid _ Cd ion effect on morphology _ current limit because of Te ion mass transfer.* Journal of Electroanalytical Chemistry, 2002. **532**(1–2): p. 215-218.

10. Li, G.-R., et al., *Facile and Efficient Electrochemical Synthesis of PbTe Dendritic Structures.* Chemistry of Materials, 2008. **20**(10): p. 3306-3314.

11. Ni, Y., Y. Zhang, and J. Hong, *Potentiostatic Electrodeposition Route for Quick Synthesis of Featherlike PbTe Dendrites: Influencing Factors and Shape Evolution.* Crystal Growth & Design, 2011. **11**(6): p. 2142-2148.

12. Mondal, A., et al., *PbTe -acidic- electrodeposition - temperature effect&morphology - thickness saturation&time.* Thin Solid Films, 2006. **515**(4): p. 1255-1259.

13. Li, X. and I.S. Nandhakumar, *Direct electrodeposition of PbTe thin films on n-type silicon.* Electrochemistry Communications, 2008. **10**(3): p. 363-366.

14. Ivanova, Y.A., D.K. Ivanou, and E.A. Streltsov, *Electrochemical deposition of PbTe onto n-Si(1 0 0) wafers.* Electrochemistry Communications, 2007. **9**(4): p. 599-604.

15. Xiao, F., et al., *Electrodeposition of PbTe thin films from acidic nitrate baths.* Electrochimica Acta, 2006. **52**(3): p. 1101-1107.

16. Pourbaix, M., *Atlas of electrochemical equilibria in aqueous solutions*1966, Long Island City, N.Y.: Pergamon Press Inc.

17. Saloniemi, H., et al., *PbTe alkaline _ underpotential deposition _ potential&composition.* Thin Solid Films, 1998. **326**(1–2): p. 78-82.

18. Saloniemi, H., et al., *PbTe alkaline bath _ underpotential deposition.* Journal of Electroanalytical Chemistry, 2000. **482**(2): p. 139-148.

19. *CRC Handbook of Chemistry and Physics*2002, Cleveland: CRC Press.

20. Renata, C., B. Mirandaa, and P.G. Abramof, *PbTe _ alkaline _ stress increase because of smaller crystallites.* Materials Research, 2004. **7**: p. 619-623.

21. Qiu, X., et al., *PbTe Nanorods by Sonoelectrochemistry.* Angewandte Chemie International Edition, 2005. **44**(36): p. 5855-5857.

22. Yang, Y., et al., *Synthesis of PbTe Nanowire Arrays using Lithographically Patterned Nanowire Electrodeposition.* Nano Letters, 2008. **8**(8): p. 2447-2451.

23. Erdoğan, İ.Y., et al., *PbTe alkaline _ co-deposition.* Thin Solid Films, 2009. **517**(18): p. 5419-5424.

24. Butler, I.B., M.A.A. Schoonen, and D.T. Rickard, *Removal of dissolved oxygen from water: A comparison of four common techniques.* Talanta, 1994. **41**(2): p. 211-215.

25. Yoo, I.-J., et al., *Thermoelectric characteristics of Sb2Te3 thin films formed via surfactant-assisted electrodeposition.* Journal of Materials Chemistry A, 2013. **1**(17): p. 5430-5435.

26. Mo, M., et al., *Controlled Hydrothermal Synthesis of Thin Single-Crystal Tellurium Nanobelts and Nanotubes.* Advanced Materials, 2002. **14**(22): p. 1658-1662.

27. Gomez, M.P., D.A. Stevenson, and R.A. Huggins, *Self-diffusion of Pb and Te in lead telluride.* Journal of Physics and Chemistry of Solids, 1971. **32**(2): p. 335-344.

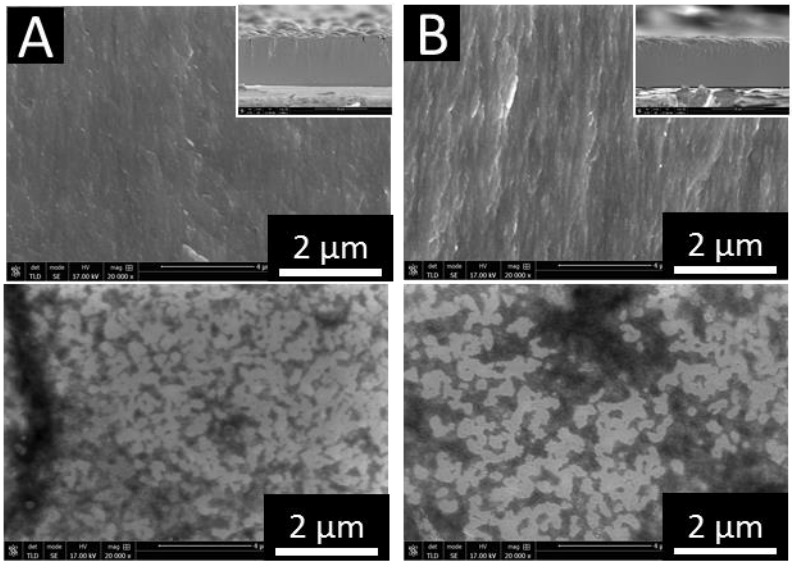

Figure 7.1 SEM images of PbTe electrodeposited at different applied potential: (A) -0.9 and (B) -0.95 V with 550 mM [TeO_3^{2-}], 100 mM [Pb^{2+}], and [$EDTA^{4-}$]/[Pb^{2+}] of 7.5 at pH of 12.3 and temperature of 23 ºC. The top row images are cross-section view, and the bottom row images are top view. The small images at top right corner are the low magnification images. Pb content of the four samples are 47%

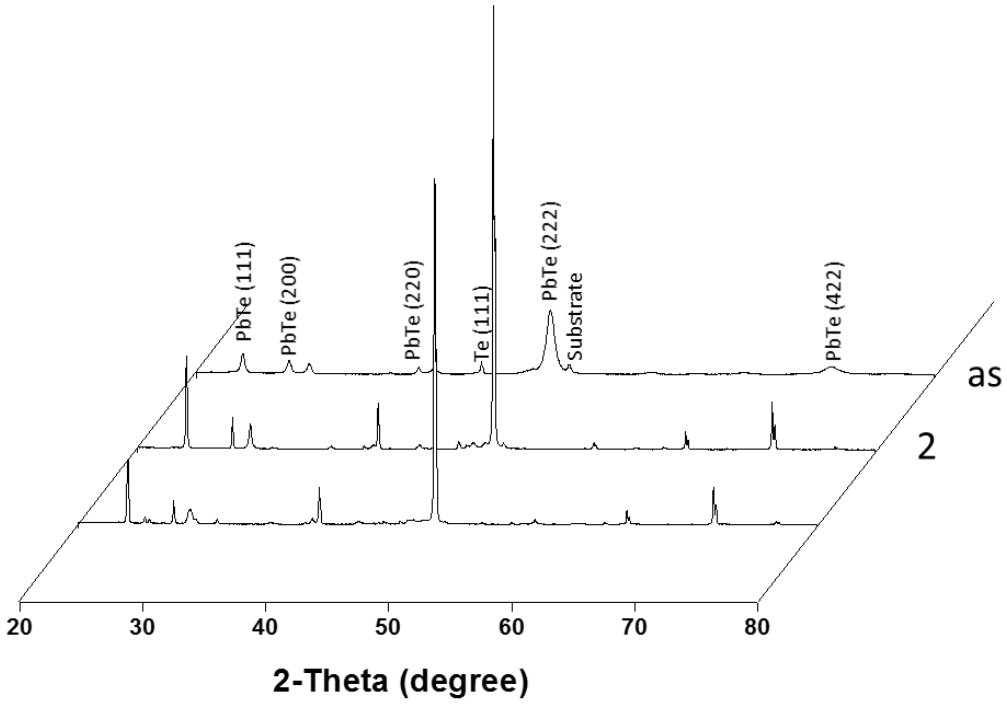

Figure 7.2 XRD analysis of as deposited and annealed for 2 and 10 h at 200 ºC PbTe thick film. PbTe with Pb content of 47 % was electrodeposited at different applied potential of -0.9 V with 550 mM [TeO_3^{2-}], 100 mM [Pb^{2+}], and [$EDTA^{4-}$]/[Pb^{2+}] of 7.5 at pH of 12.3 and temperature of 23 ºC.

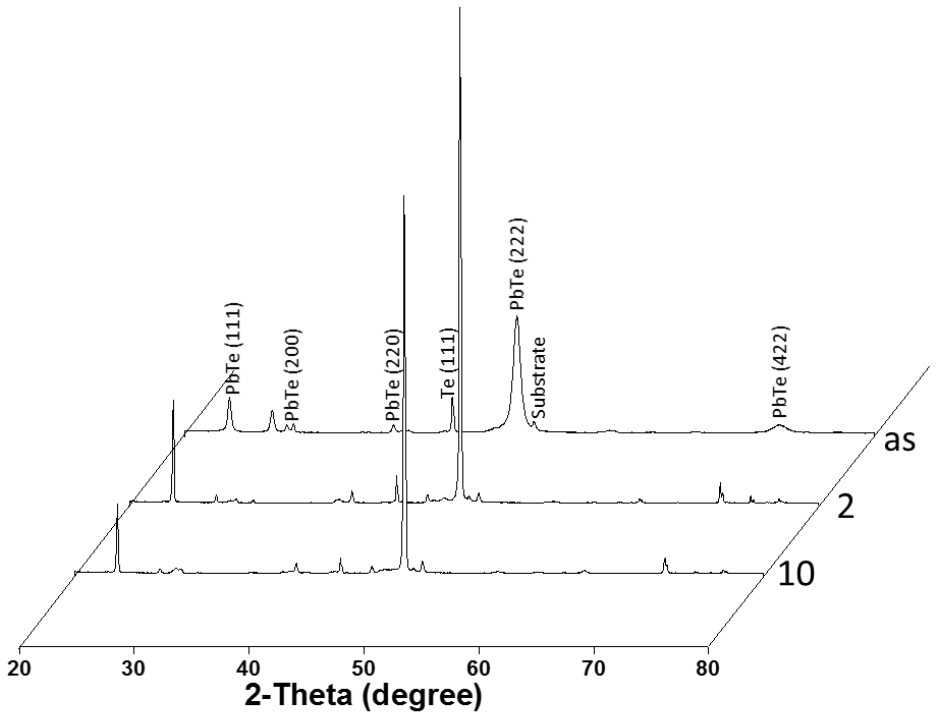

Figure 7.3 XRD analysis of as deposited and annealed for 2 and 10 h at 200 ºC PbTe thick film. PbTe with Pb content of 47 % was electrodeposited at different applied potential of -0.95 V with 550 mM [TeO_3^{2-}], 100 mM [Pb^{2+}], and [$EDTA^{4-}$]/[Pb^{2+}] of 7.5 at pH of 12.3 and temperature of 23 ºC.

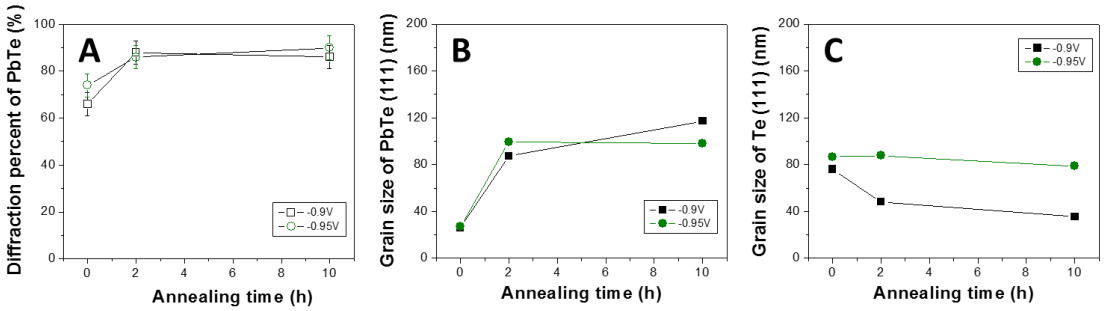

Figure 7.4 Diffraction percent (A) and grain size (B) of PbTe, and grain size of Te (C) as a function of annealing time (0, 2 and 10 h) The PbTe film electrodeposited at different applied potential: -0.9 and -0.95 V with 550 mM [TeO_3^{2-}], 100 mM [Pb^{2+}], and [$EDTA^{4-}$]/[Pb^{2+}] of 7.5 at pH of 12.3 and temperature of 23 ^{o}C as shown in figure 7.1.

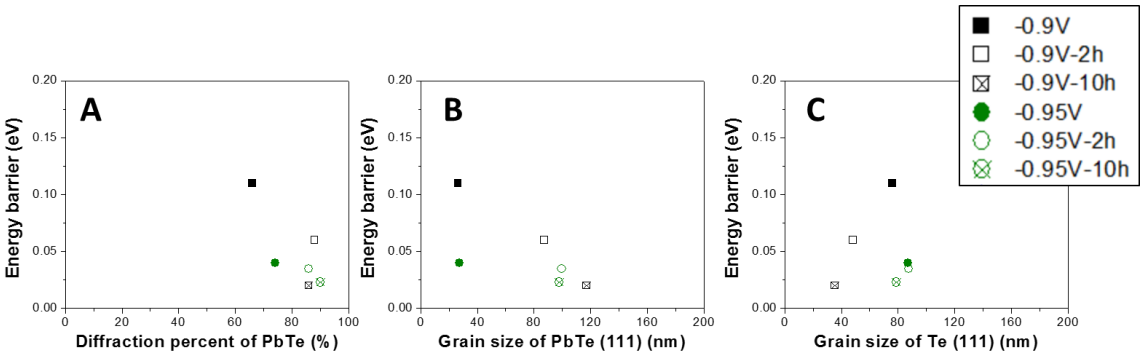

Figure 7.5 Energy barrier as a function of diffraction percent (A) and grain size (B) of PbTe, and grain size of Te (C) as-deposited and annealed for 2 and 10 hours PbTe films. The PbTe film electrodeposited at different applied potential: -0.9 and -0.95 V with 550 mM [TeO_3^{2-}], 100 mM [Pb^{2+}], and [$EDTA^{4-}$]/[Pb^{2+}] of 7.5 at pH of 12.3 and temperature of 23 ^oC as shown in figure 7.1.

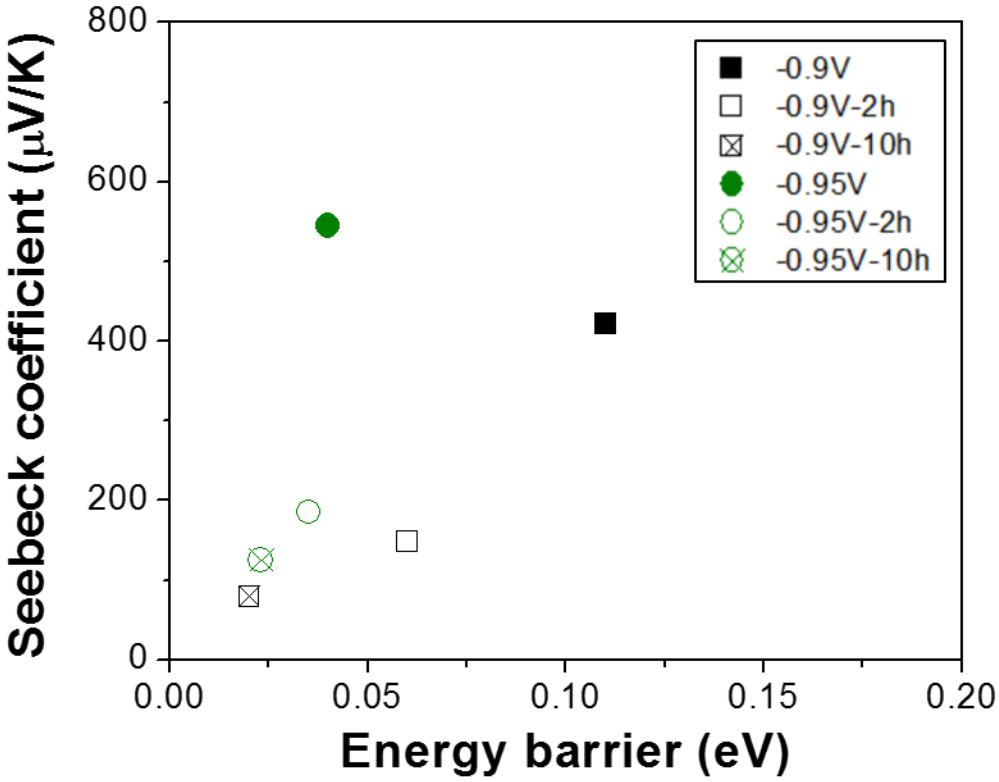

Figure 7.6 Seebeck coefficient as a function of energy barrier of as-deposited and annealed for 2 and 10 hours PbTe films. The PbTe film electrodeposited at different applied potential: -0.9 and -0.95 V with 550 mM [TeO_3^{2-}], 100 mM [Pb^{2+}], and [$EDTA^{4-}$]/[Pb^{2+}] of 7.5 at pH of 12.3 and temperature of 23 ^{o}C as shown in figure 7.1.

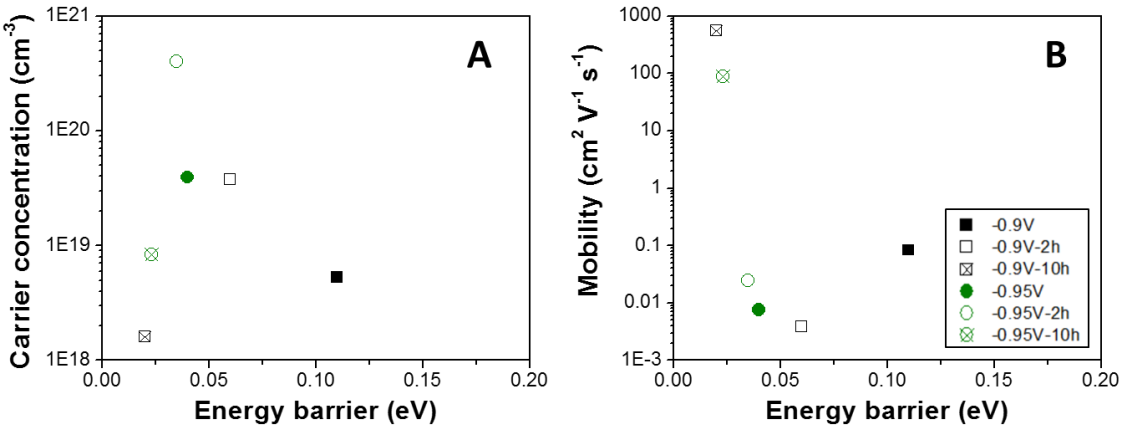

Figure 7.7 Carrier concentration (A) and mobility (B) as a function of energy barrier of as-deposited and annealed for 2 and 10 hours PbTe films. The PbTe film electrodeposited at different applied potential: -0.9 and -0.95 V with 550 mM [TeO_3^{2-}], 100 mM [Pb^{2+}], and [$EDTA^{4-}$]/[Pb^{2+}] of 7.5 at pH of 12.3 and temperature of 23 ºC as shown in figure 7.1.

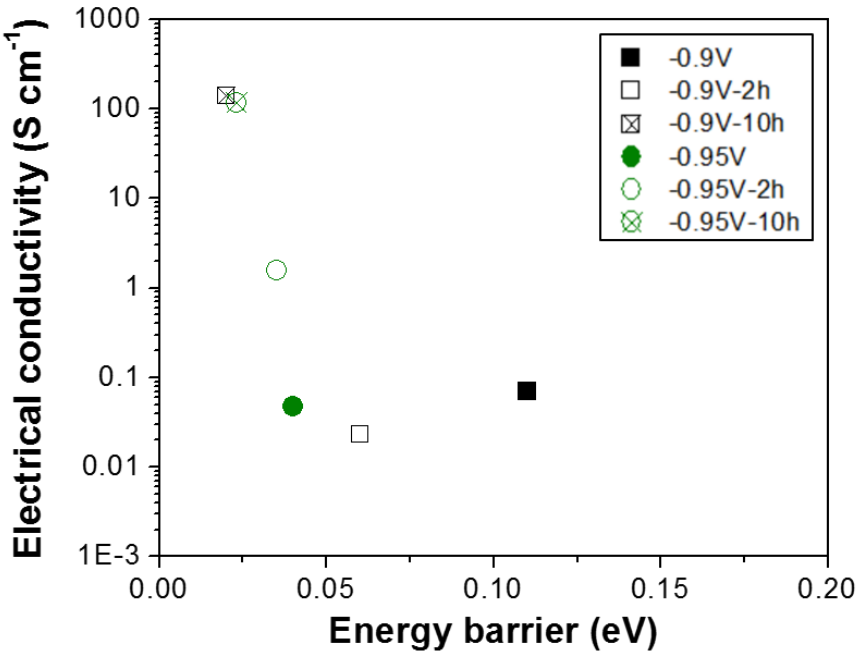

Figure 7.8 Electrical conductivity as a function of energy barrier of as-deposited and annealed for 2 and 10 hours PbTe films. The PbTe film electrodeposited at different applied potential: -0.9 and -0.95 V with 550 mM [TeO_3^{2-}], 100 mM [Pb^{2+}], and [$EDTA^{4-}$]/[Pb^{2+}] of 7.5 at pH of 12.3 and temperature of 23 ºC as shown in figure 7.1.

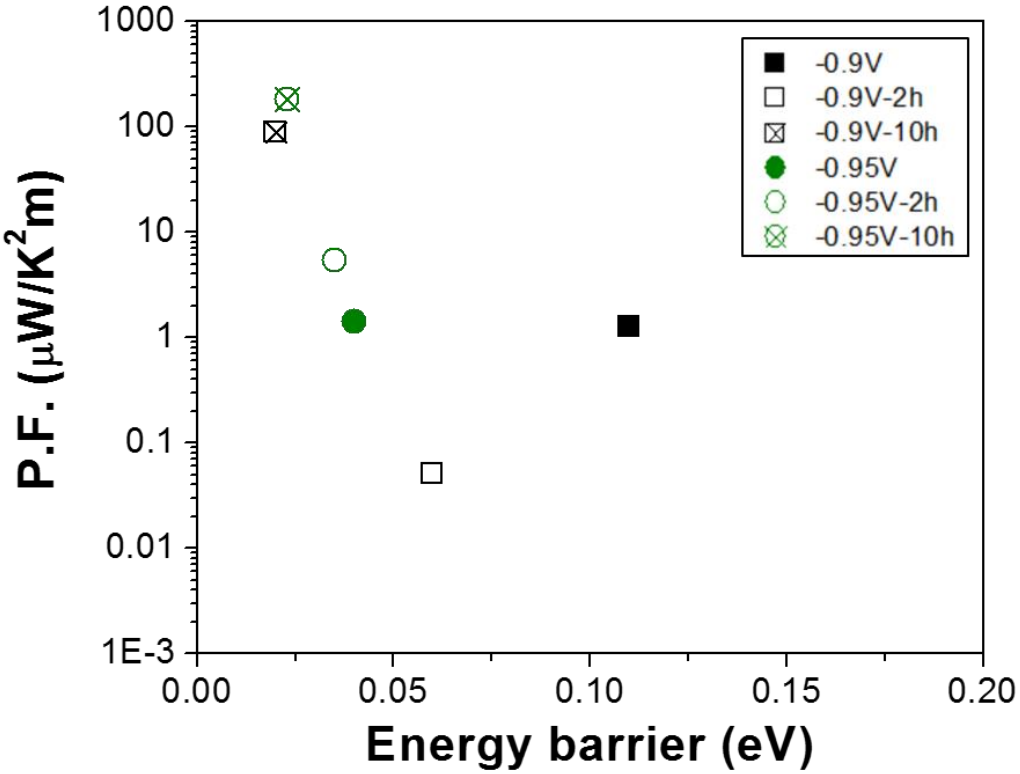

Figure 7.9 Electrical conductivity as a function of energy barrier of as-deposited and annealed for 2 and 10 hours PbTe films. The PbTe film electrodeposited at different applied potential: -0.9 and -0.95 V with 550 mM [TeO_3^{2-}], 100 mM [Pb^{2+}], and [$EDTA^{4-}$]/[Pb^{2+}] of 7.5 at pH of 12.3 and temperature of 23 ^{o}C as shown in figure 7.1.

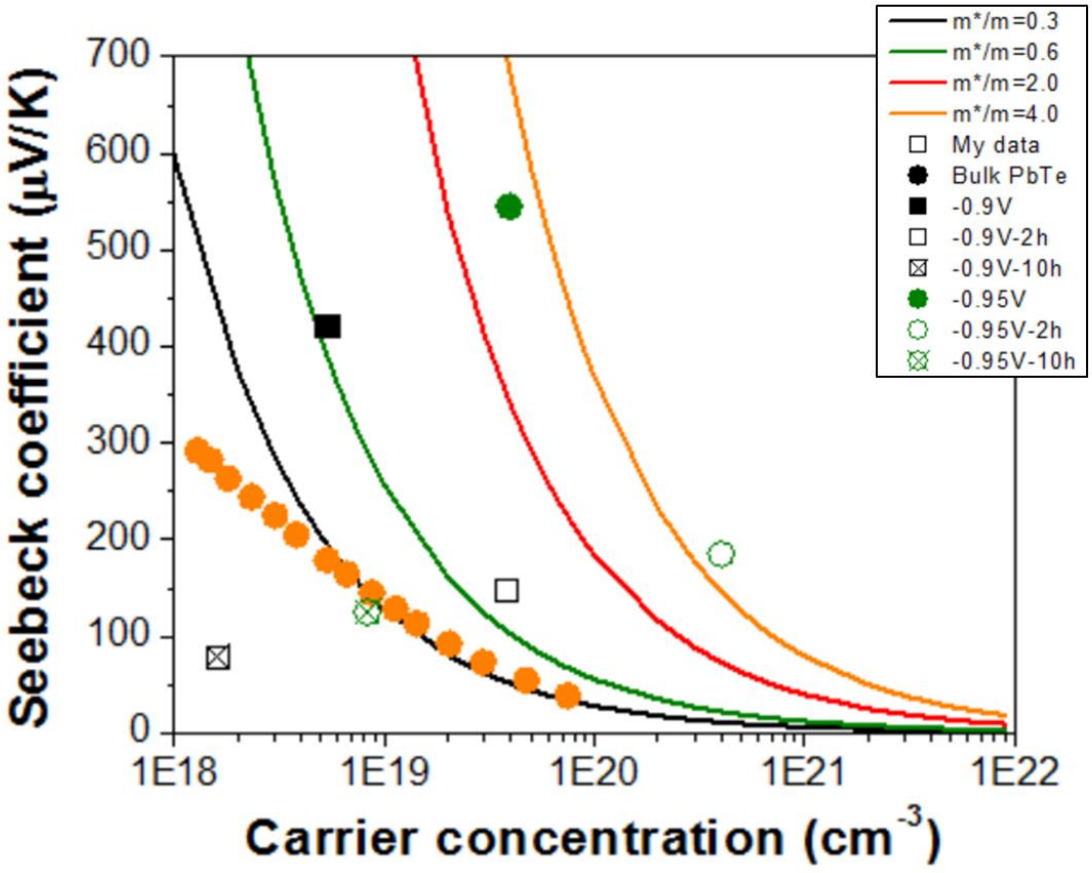

Figure 7.10 Seebeck coefficient as a function of carrier concentration at room temperature. The compared results are from studies of PbTe thick films with Bulk PbTe. The color lines are the theoretical fitting by Mott-relation.

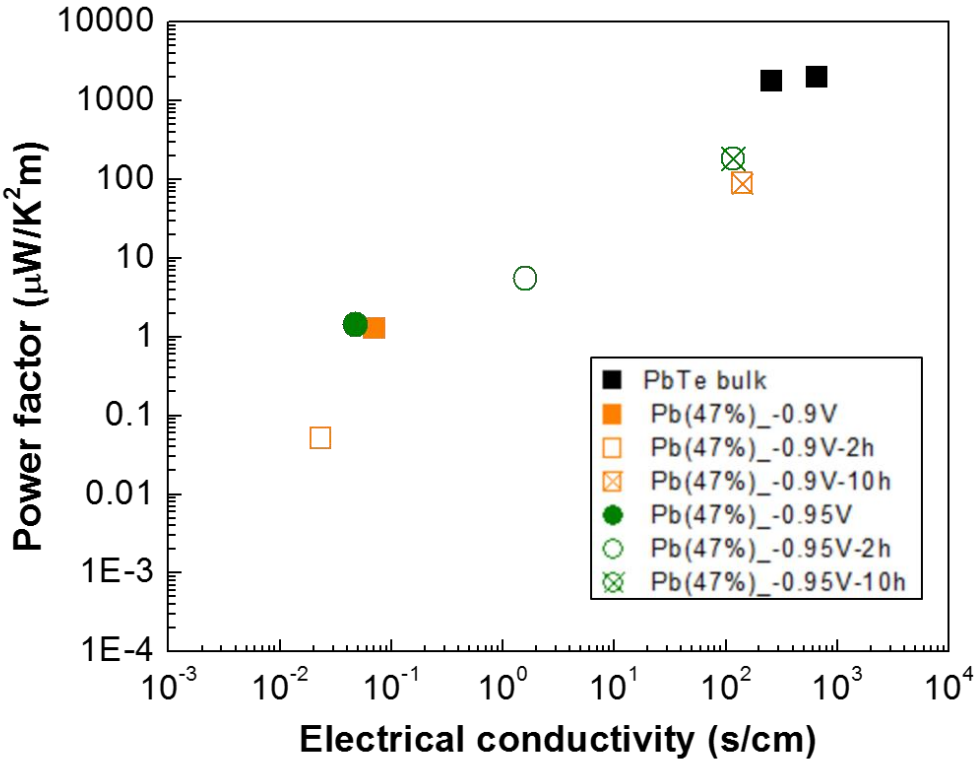

Figure 7.11 Power factor as a function of electrical conductivity of as-deposited and annealed for 2 and 10 hours PbTe films. The PbTe film electrodeposited at different applied potential: -0.9 and -0.95 V with 550 mM [TeO_3^{2-}], 100 mM [Pb^{2+}], and [$EDTA^{4-}$]/[Pb^{2+}] of 7.5 at pH of 12.3 and temperature of 23 ºC as shown in figure 7.1.

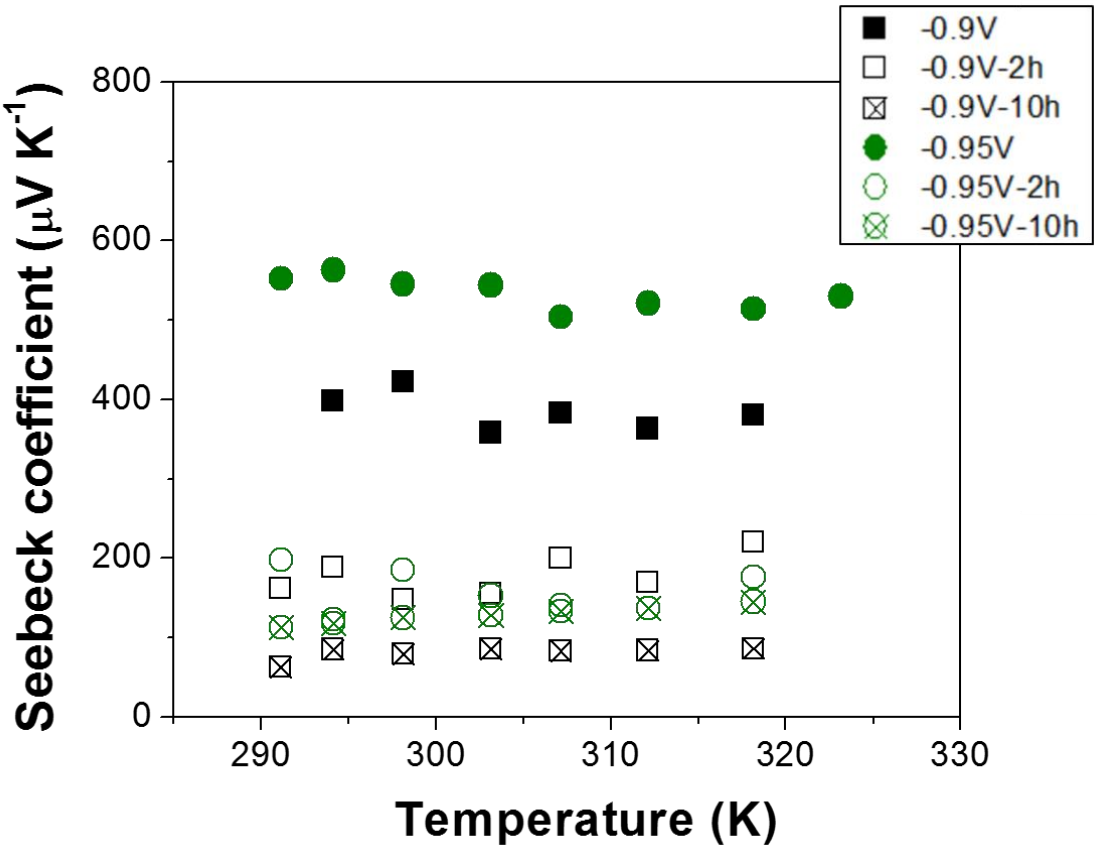

Figure 7.12 Seebeck coefficient measurement of as-deposited and annealed for 2 and 10 hours PbTe films. The PbTe film electrodeposited at different applied potential: -0.9 and -0.95 V with 550 mM [TeO_3^{2-}], 100 mM [Pb^{2+}], and [$EDTA^{4-}$]/[Pb^{2+}] of 7.5 at pH of 12.3 and temperature of 23 ºC as shown in figure 7.1.

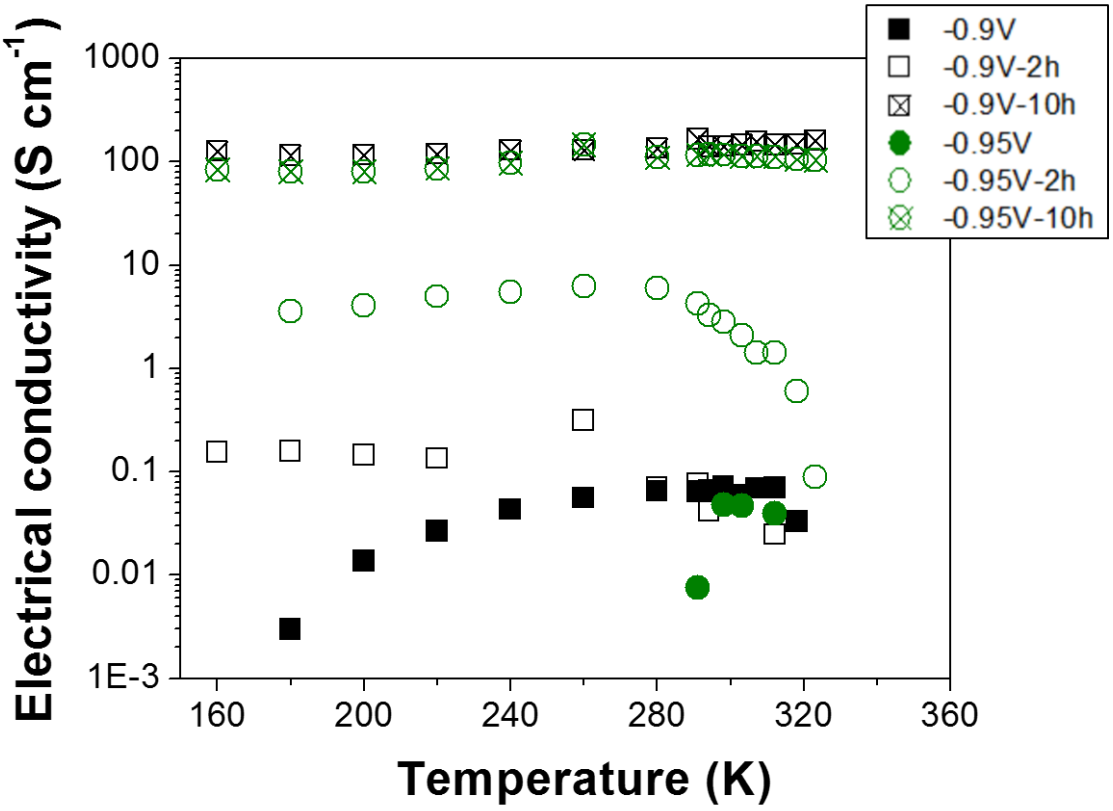

Figure 7.13 Electrical conductivity measurement of as-deposited and annealed for 2 and 10 hours PbTe films. The PbTe film electrodeposited at different applied potential: -0.9 and -0.95 V with 550 mM [TeO_3^{2-}], 100 mM [Pb^{2+}], and [$EDTA^{4-}$]/[Pb^{2+}] of 7.5 at pH of 12.3 and temperature of 23 ºC as shown in figure 7.1.

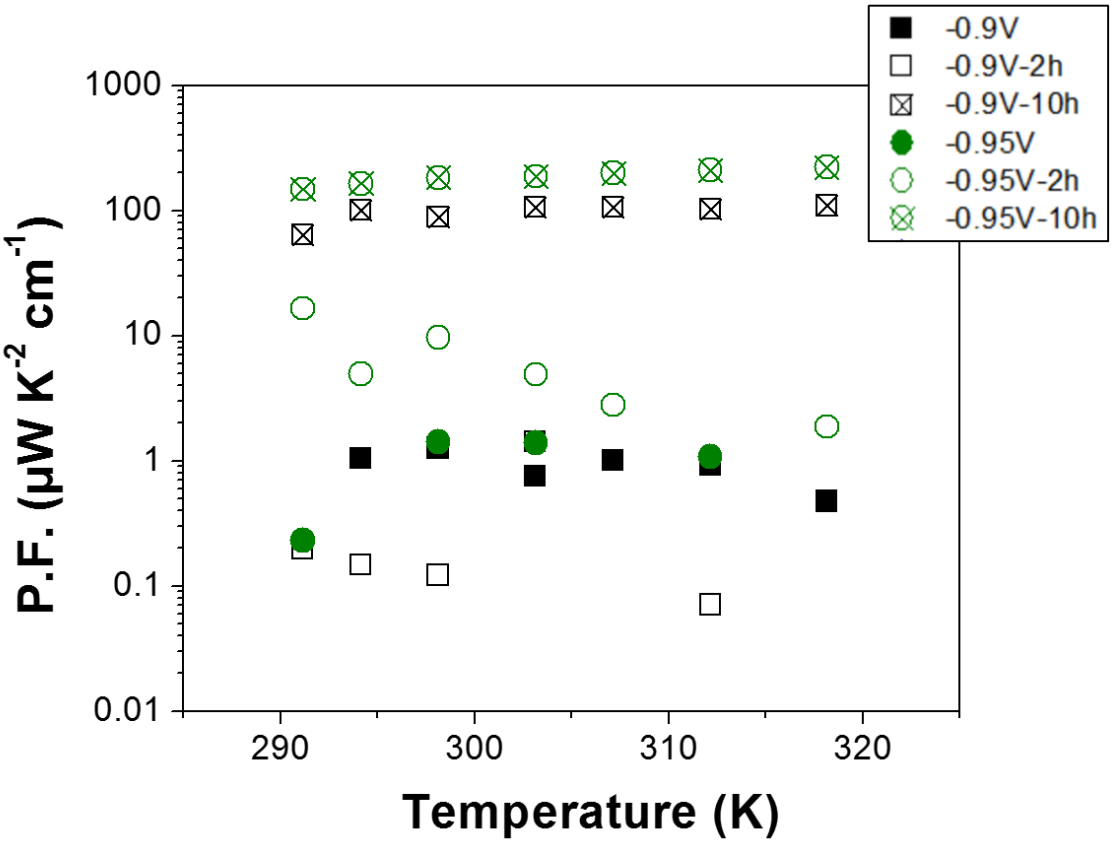

Figure 7.14 Thermoelectric power factor of as-deposited and annealed for 2 and 10 hours PbTe films. The PbTe film electrodeposited at different applied potential: -0.9 and -0.95 V with 550 mM [TeO_3^{2-}], 100 mM [Pb^{2+}], and [$EDTA^{4-}$]/[Pb^{2+}] of 7.5 at pH of 12.3 and temperature of 23 ºC as shown in figure 7.1.

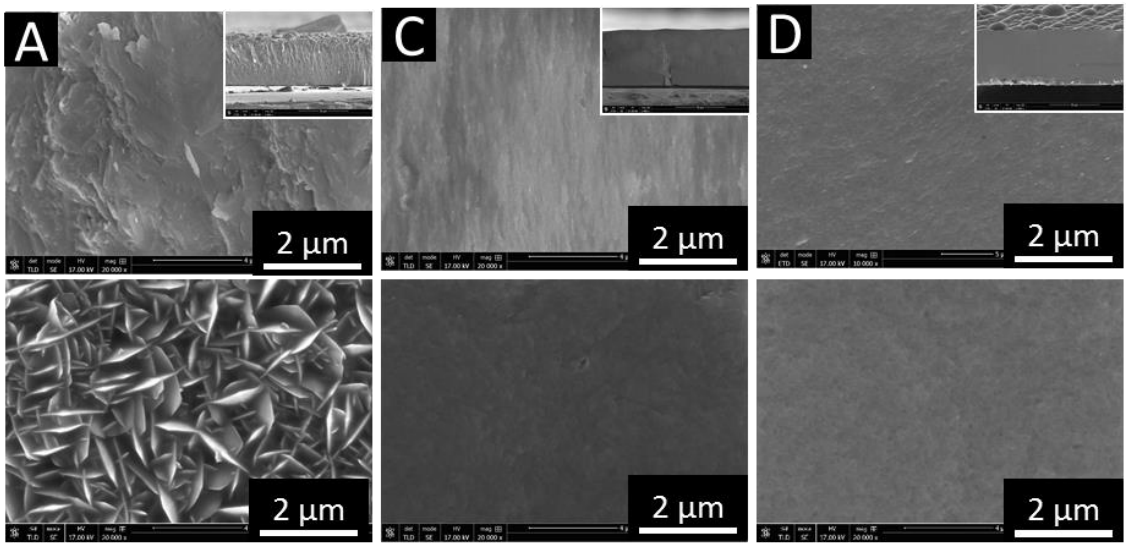

Figure 7.15 SEM images of PbTe with different Pb content: (A) 40%, (B) 47% and (C) 49%. The top row images are cross-section view, and the bottom row images are top view. The small images at top right corner are the low magnification images.

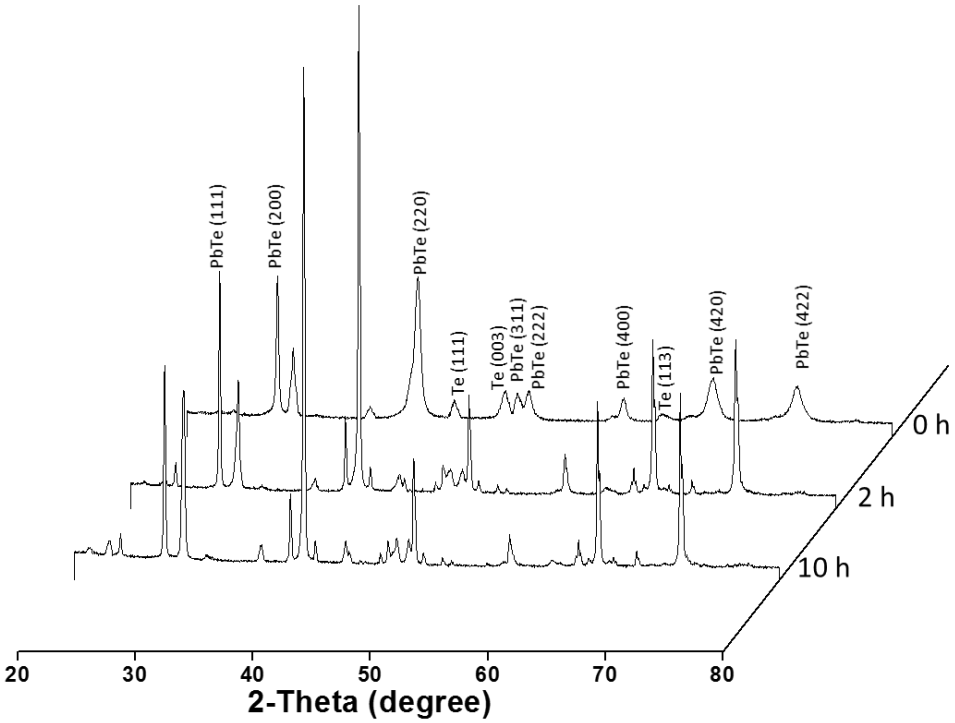

Figure 7.16 XRD analysis of as deposited and annealed for 2 and 10 h at 200 ^{o}C PbTe thick film. PbTe with Pb content of 40 % was electrodeposited at different applied potential of -1.0 V with 50 mM [TeO_3^{2-}], 100 mM [Pb^{2+}], and [$EDTA^{4-}$]/[Pb^{2+}] of 1.2 at pH of 10.5 and temperature of 23 ^{o}C.

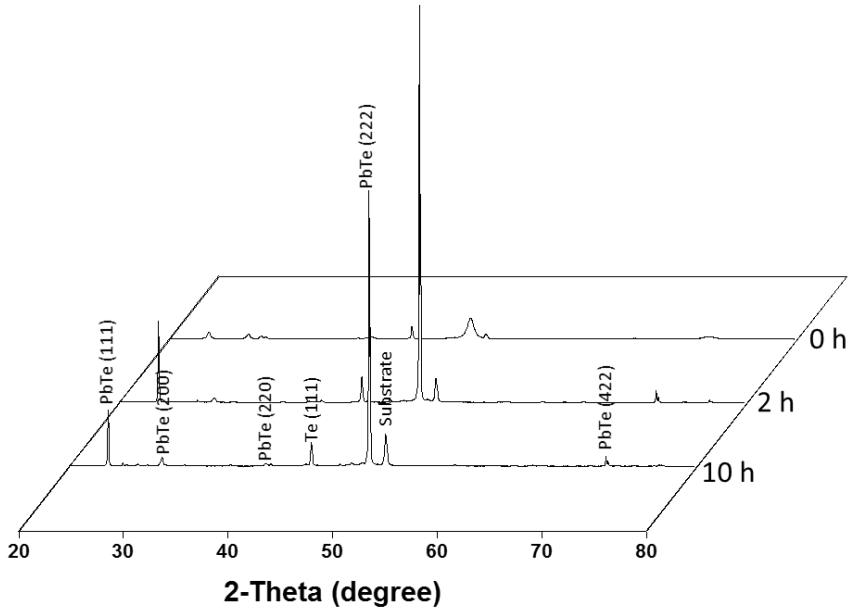

Figure 7.17 XRD analysis of as deposited and annealed for 2 and 10 h at 200 ^{o}C PbTe thick film. PbTe with Pb content of 47 % was electrodeposited at different applied potential of -1.0 V with 550 mM [TeO_3^{2-}], 100 mM [Pb^{2+}], and [$EDTA^{4-}$]/[Pb^{2+}] of 7.5 at pH of 12.3 and temperature of 23 ^{o}C.

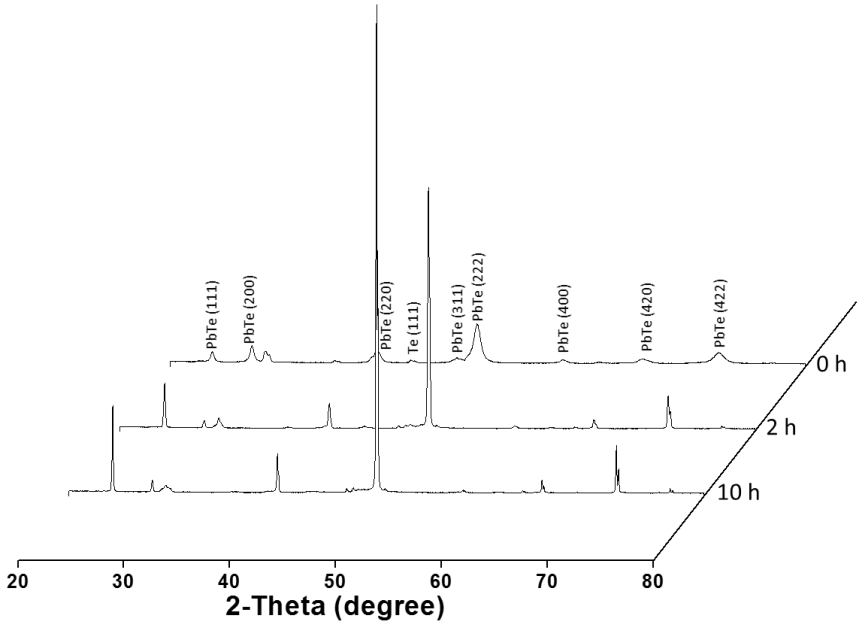

Figure 7.18 XRD analysis of as deposited and annealed for 2 and 10 h at 200 ^{o}C PbTe thick film. PbTe with Pb content of 49 % was electrodeposited at different applied potential of -1.0 V with 50 mM [TeO_3^{2-}], 100 mM [Pb^{2+}], and [$EDTA^{4-}$]/[Pb^{2+}] of 1.2 at pH of 12.0 and temperature of 23 ^{o}C.

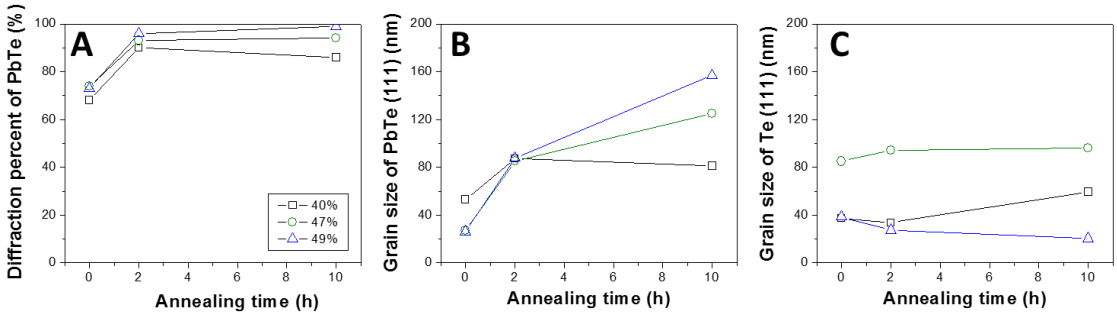

Figure 7.19 Diffraction percent (A) and grain size (B) of PbTe, and grain size of Te (C) as a function of annealing time (0, 2 and 10 h). The Pb content of PbTe films are: 40, 47 and 49 %.

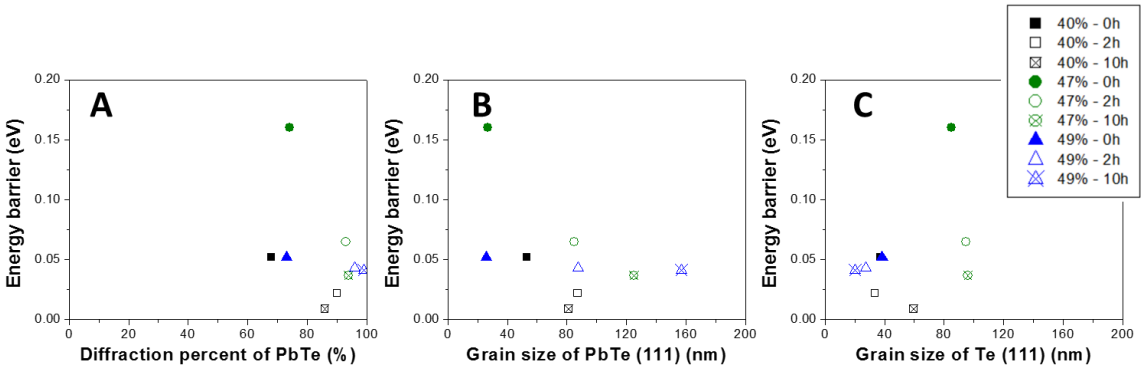

Figure 7.20 Energy barrier as a function of diffraction percent (A) and grain size (B) of PbTe, and grain size of Te (C) as-deposited and annealed for 2 and 10 hours PbTe films. The Pb content of PbTe films are: 40, 47 and 49 %.

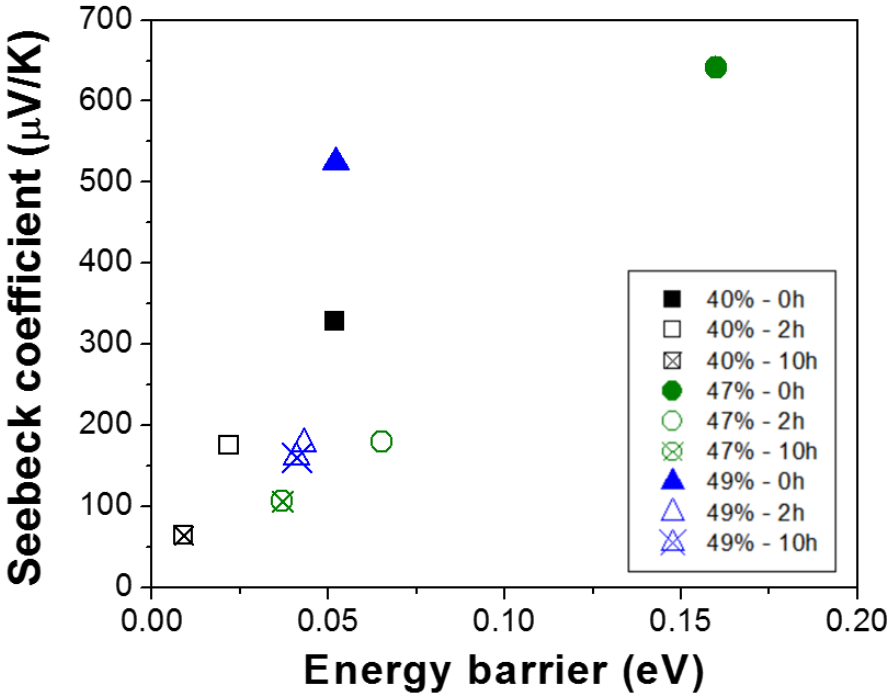

Figure 7.21 Seebeck coefficient as a function of energy barrier of as-deposited and annealed for 2 and 10 hours PbTe films. The Pb content of PbTe films are: 40, 47 and 49 %.

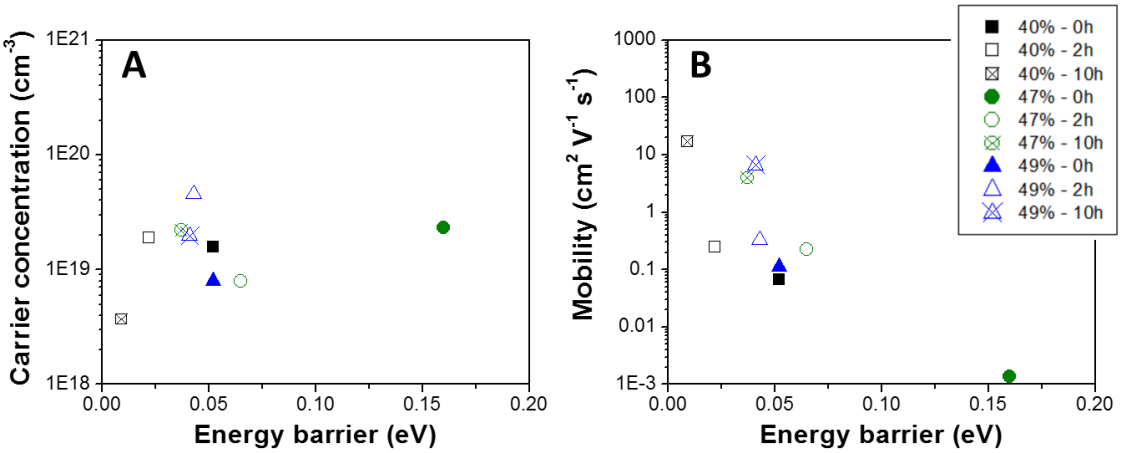

Figure 7.22 Carrier concentration (A) and mobility (B) as a function of energy barrier of as-deposited and annealed for 2 and 10 hours PbTe films. The Pb content of PbTe films are: 40, 47 and 49 %.

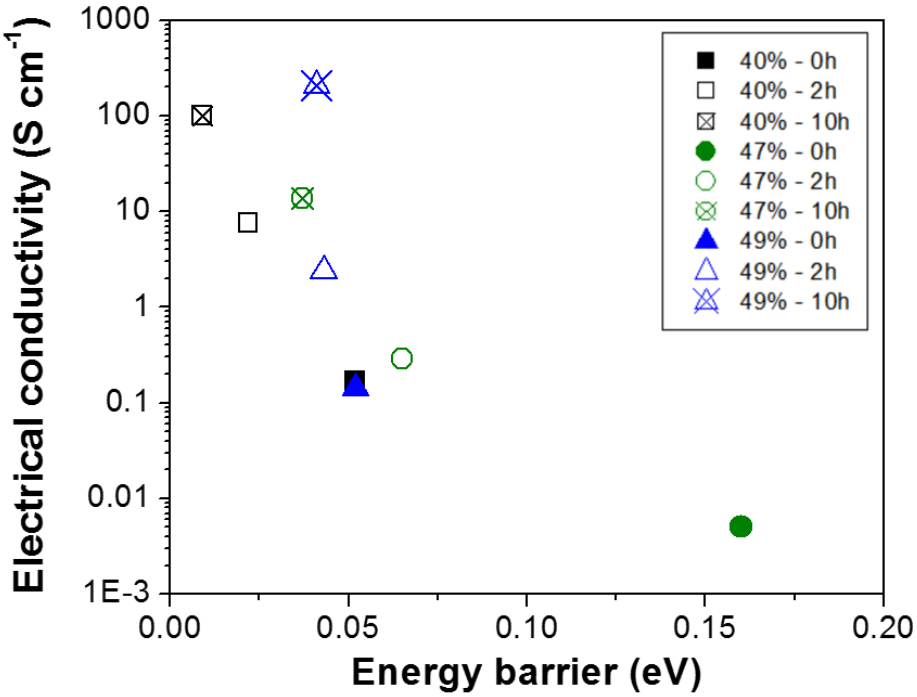

Figure 7.23 Electrical conductivity as a function of energy barrier of as-deposited and annealed for 2 and 10 hours PbTe films. The Pb content of PbTe films are: 40, 47 and 49 %.

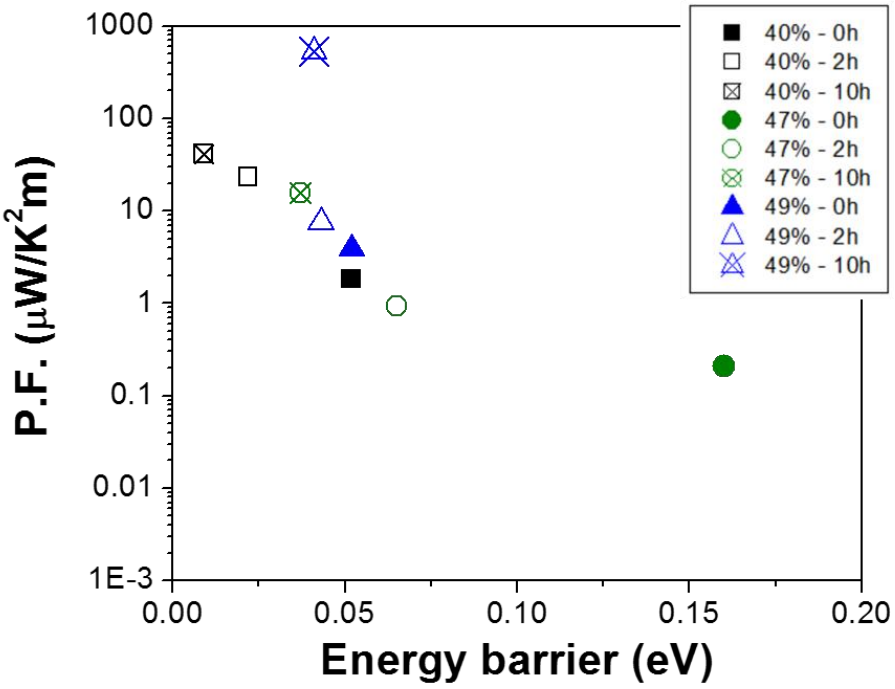

Figure 7.24 Electrical conductivity as a function of energy barrier of as-deposited and annealed for 2 and 10 hours PbTe films. The Pb content of PbTe films are: 40, 47 and 49 %.

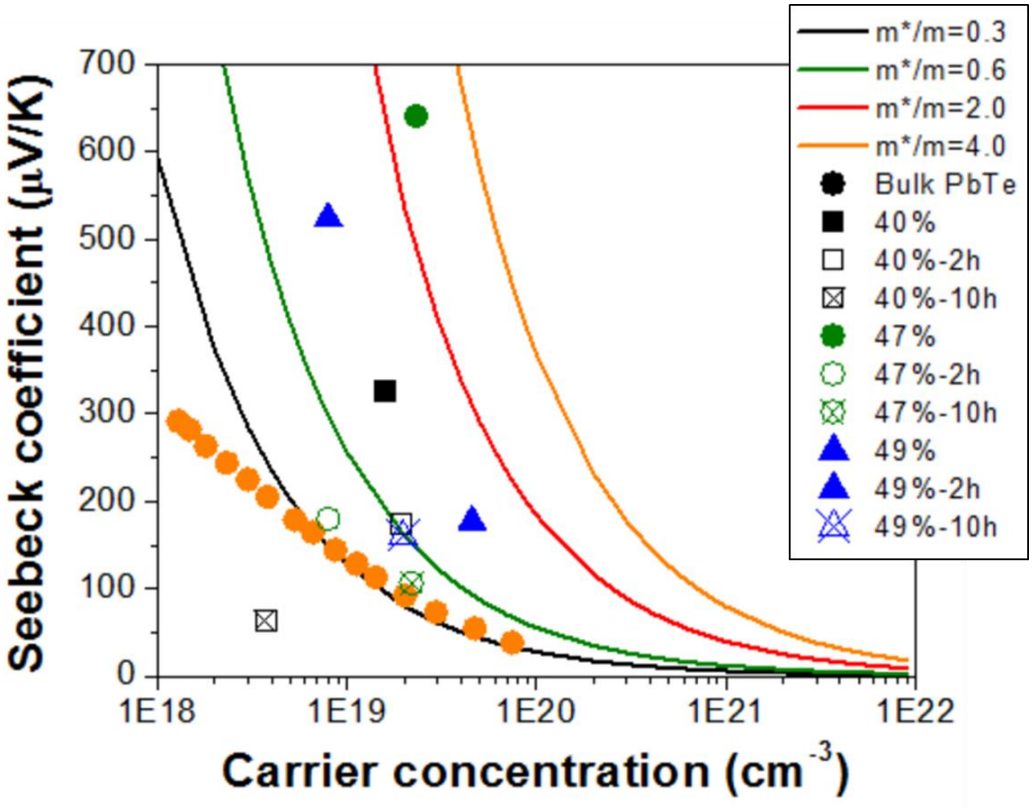

Figure 7.25 Seebeck coefficient as a function of carrier concentration at room temperature. The compared results are from studies of PbTe thick films with different Pb content: 40, 47 and 49 % to Bulk PbTe. The color lines are the theoretical fitting by Mott-relation.

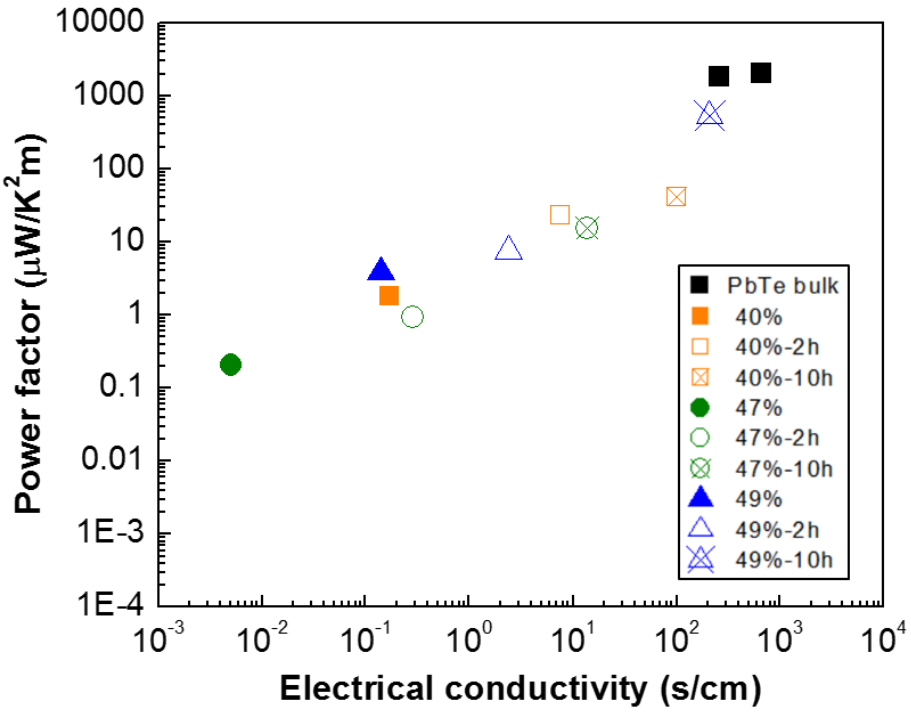

Figure 7.26 Power factor as a function of electrical conductivity of as-deposited and annealed for 2 and 10 hours PbTe films with different Pb content: 40, 47 and 49 %.

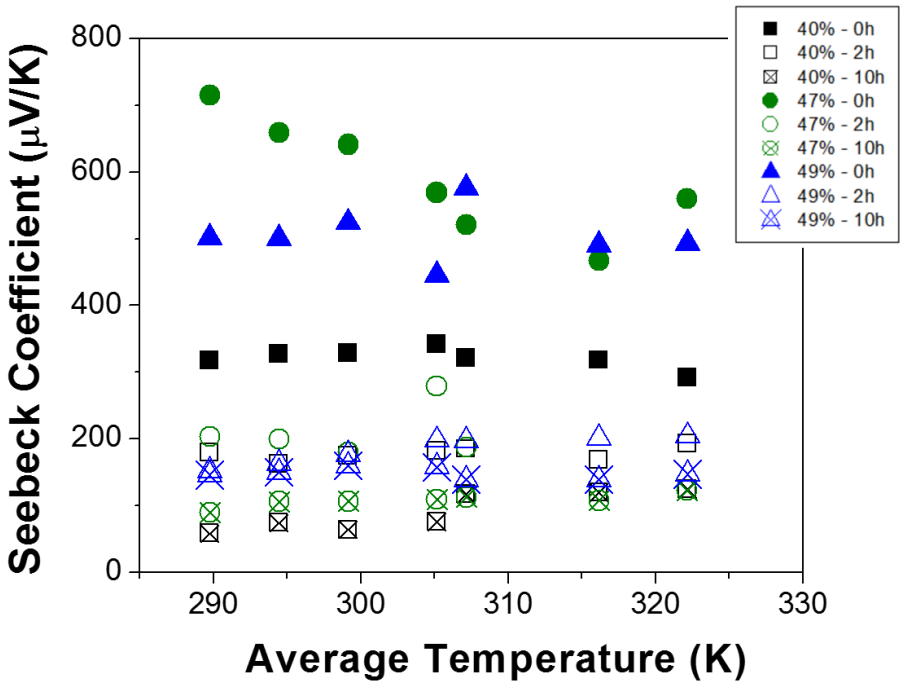

Figure 7.27 Seebeck coefficient measurement of as-deposited and annealed for 2 and 10 hours PbTe films. The PbTe films have different Pb content: 40, 47 and 49 %.

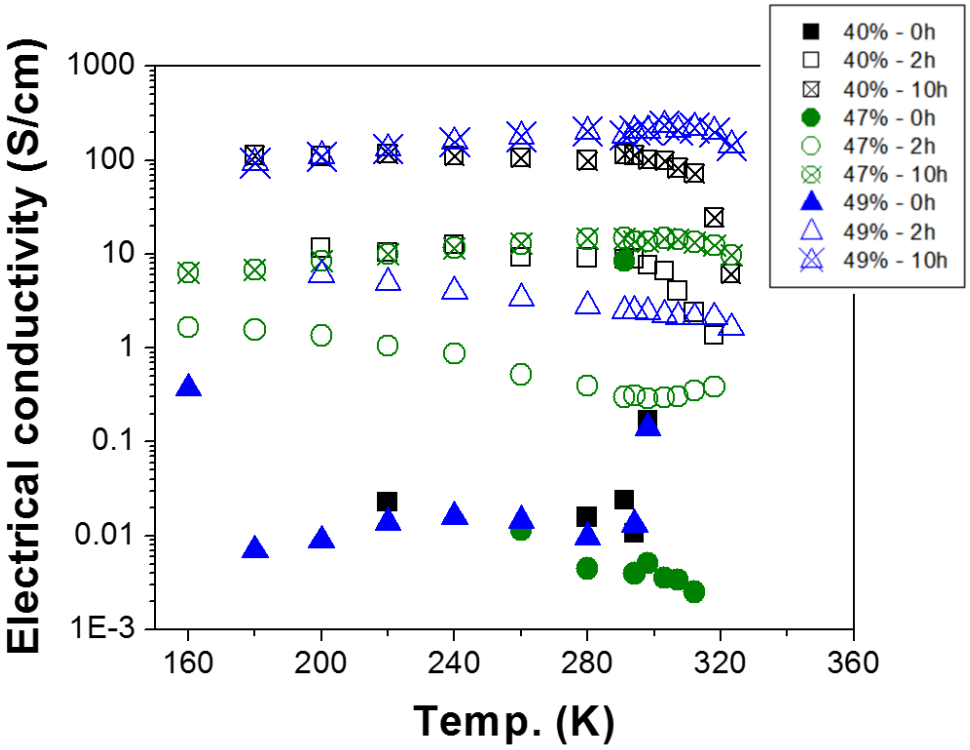

Figure 7.28 Electrical conductivity of as-deposited and annealed for 2 and 10 hours PbTe films. The PbTe films have different Pb content: 40, 47 and 49 %.

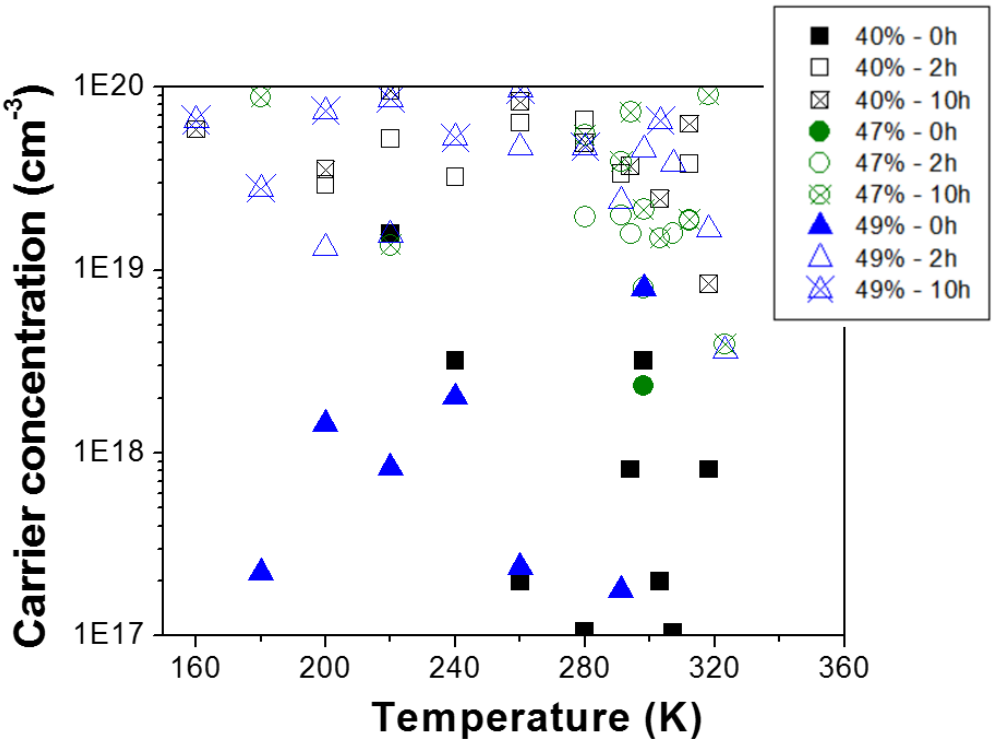

Figure 7.29 Carrier concentration of as-deposited and annealed for 2 and 10 hours PbTe films. The PbTe films have different Pb content: 40, 47 and 49 %.

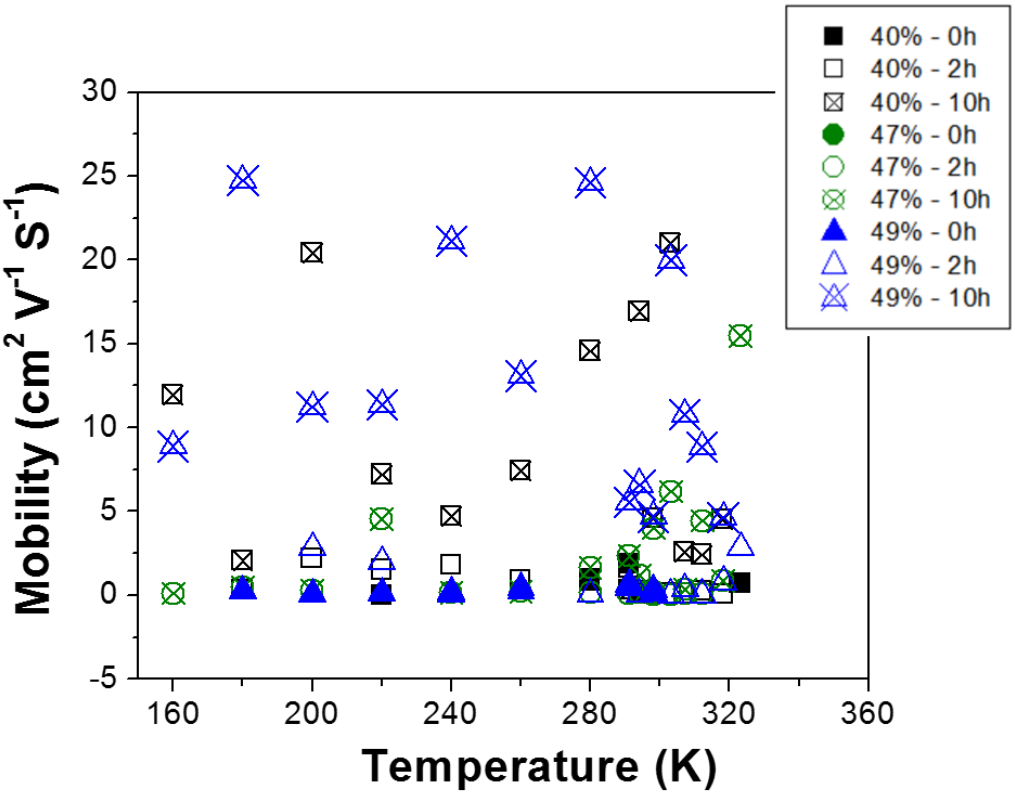

Figure 7.30 Mobility of as-deposited and annealed for 2 and 10 hours PbTe films. The PbTe films have different Pb content: 40, 47 and 49 %.

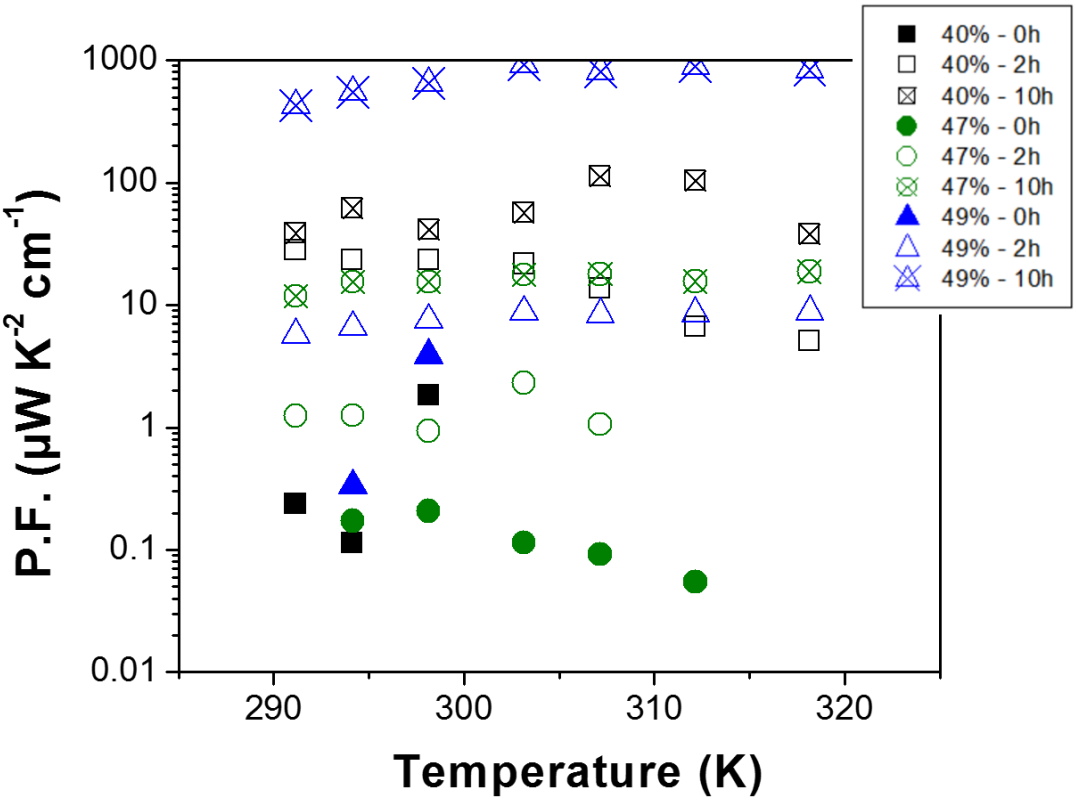

Figure 7.31 Power factor of as-deposited and annealed for 2 and 10 hours PbTe films. The PbTe films have different Pb content: 40, 47 and 49.

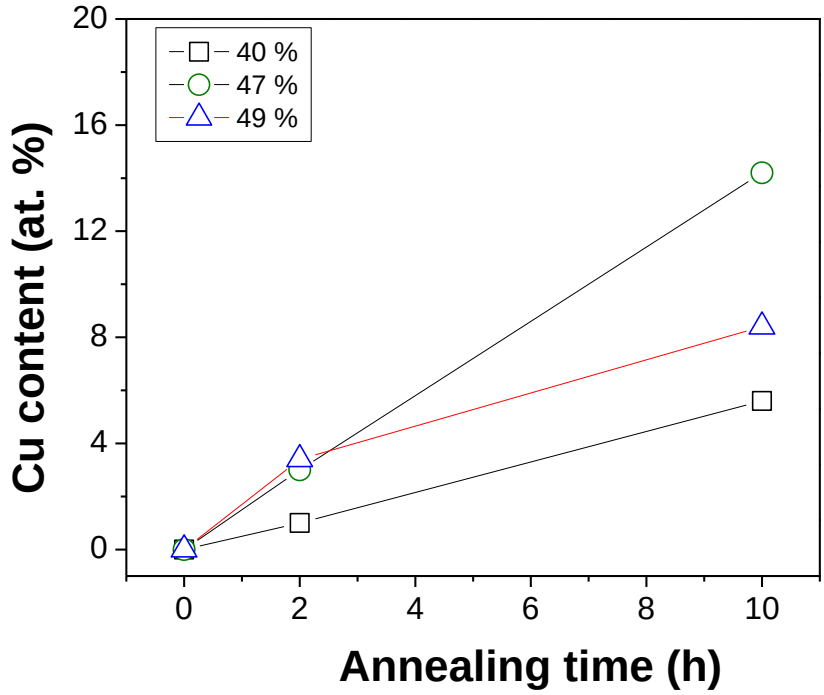

Figure 7.32 Cu content of as-deposited and annealed for 2 and 10 hours PbTe films. The PbTe films have different Pb content: 40, 47 and 49.

8 Conclusions

This work demonstrated Electrochemical Synthesis of Tellurium & Lead Telluride from Alkaline Baths and Their Thermoelectric Application.

Chapter 2 demonstrated that Te hetero-structures, including 1D and 3D nanostructures, were synthesized by galvanic displacement reaction in an alkaline bath using zinc foil as sacrificial material. Single crystal Te nanowires were synthesized at TeO_3^{2-} concentration of 2 mM. The diameter of Te nanowires were controlled from 200 ± 94 nm to 49 ± 23 nm by reducing temperature from 50 ^oC to 4 ^oC The morphology of the Te nanostructures were successfully modulated from nanowire to branched structures through varying the TeO_3^{2-} concentration from 2 to 10 mM, while fixing pH at 13.1. The HRTEM images of branched structure showed that the branches and the trunk had the same growth direction (i.e. [001]). The morphology were tuned from nanowires to branched structures as pH reduced from 14.7 to 13.1, while fixing the TeO_3^{2-} concentration at 10 mM. The electrochemical analysis together with the SEM and TEM results indicated that the transition from nanowires to branched structure was attributed to secondary nucleation at high Te reduction rate and sufficient Te source.

Chapter 3 elucidated that Te "rice-like" nanostructures with controlled dimensions were synthesized by galvanic displacement reactions of aluminum in alkaline baths. The Te "rice-like" nanostructures were deposited in the solution via chemical reaction between Te_2^{2-} (-I) or Te^{2-} (-II) and TeO_3^{2-} (IV). The formation of sharp tips may be attributed to the high density of surface charges at the tips. The morphology of the Te evolved from

branched nanostructures together with some “rice-like” nanostructures to only “rice-like” nanostructures as the reaction time (10 to 90 min) and temperature (4 to 50 ^{o}C) increased. The nanostructures peaked in dimensions after 30 min. At pH < 11.9 the deposited Te film was amorphous.

Chapter 4 described the synthesis of thick, dense Te films by electrodeposition in alkaline solution. To achieve dense morphology, applied potential should be more positive than -1.0 V to avoid further reduction of Te to Te_2^{2-} or keep the reduction of Te to Te_2^{2-} at a low reaction rate, because this reduction reaction would deteriorate the film morphology significantly. The proper pH range to deposit dense thick film is 11.3 to 12.5. Sufficient agitation (2000 rpm) is necessary to electrodeposit a dense film. Grain size of the thick Te films was from 66 to 135 nm, which is controlled by applied potential, TeO_3^{2-} concentration and pH. The Highest deposition rate was 130 μm/h achieved by high TeO_3^{2-} concentration (550 mM) and more negative applied potential (-1.0 V). The Current efficiency for electrodeposition of Te thick films was higher than 85% in alkaline solution.

Chapter 5 presented the kinetics of Te reduction reactions in alkaline solution. The TeO_3^{2-} concentration affected the mass transfer and reaction rate, but it did not influence the reaction rate limiting step. The solution pH, however, was essential to control the rate limiting step. When the solution pH was 11.0 and 12.5, in which the discharge of $Te(OH)_3^{+}$ (reaction 5.8) was the rate limiting step. For the reduction of Te(0) to Te_2^{2-} at relatively weak alkaline solutions the second discharge reaction was the rate limiting step. At strong alkaline solutions (i.e., pH = 14.7), the second electrochemical reaction was the rate limiting step.

Chapter 6 studied the electrodeposition of dense thick PbTe films in alkaline solution. Electrodeposition mechanism of PbTe was UPD. The composition of PbTe films were from Te-rich to stoichiometry. To achieved dense morphology, the applied potential was controlled from -0.8 to -1.1 V to minimize the effect of reduction reaction (Te to Te_2^{2-}) on morphology. The proper pH to form a dense thick film is from 10.5 to 12.3. TeO_3^{2-} concentration had a significant effect on deposition rate, and had a minor effect on composition compared with Pb^{2+} concentration. Tailoring Pb^{2+} concentration would vary the film from Te-rich to Pb-rich, but when the electrodeposited film was Pb-rich the morphology became porous, due to OPD of Pb. Additionally, at $[EDTA^{4-}]/[Pb^{2+}]$ of 7.5, dense thick PbTe films were electrodeposited without cracks, which meant low residual stress. The high deposition rate of 163 μm/h was achieved with dense morphology and composition close to stoichiometry.

Chapter 7 demonstrated electrodeposition of Te-rich thick PbTe films. Diffraction percentage and grain size of PbTe and size of Te nanoinclusion was controlled by electrodeposition and post-annealing process. Crystal grain boundary and tellurium nanoinclusion introduced an energy barrier, which played a critical role on the electrical and thermoelectrical properties of PbTe thick film. Higher diffraction percentage and larger grain size of PbTe would resulted in lower energy barrier. However, the effect of Te grain size on energy barrier was dependent on Pb composition. Decrease the energy barrier would reduce the Seebeck coefficient, but would enhance the electrical conductivity. The increase in electrical conductivity compensated the reduction of Seebeck coefficient, then

further improve the power factor. The highest power factor was 531 μw K^{-2} cm^{-1}, achieved at energy barrier of 0.023 eV with Pb content of 49 %.